Quantum-Dot-Based Optoelectronics for Spectral Conversion

Zur Erlangung des akademischen Grades eines

Doktors der Ingenieurwissenschaften (Dr.-Ing.)

von der KIT-Fakultät für
Elektrotechnik und Informationstechnik
des Karlsruher Instituts für Technologie (KIT)

genehmigte

Dissertation

von

M.Sc. Junchi Chen

geb. in Chaozhou, V.R. China

Tag der mündlichen Prüfung:	31. 10. 2024
Erster Gutachter:	Prof. Dr. Uli Lemmer
Zweiter Gutachter:	Prof. Dr. Hendrik Hölscher

Abstract

Currently, people's lifestyles and industrial production are heading into the era of digitalization and intelligence. In this process, optoelectronic devices play a critical role in the aspects of detection, signal transmission, and information presentation. To meet the high demands of complex electronic systems, such as high efficiency, high integration, and low energy consumption, implementing effective light management schemes is an essential step to optimize the performance of optoelectronics. Furthermore, the discovery and development of colloidal quantum dots (QDs) have led to tremendous innovations and promotions in optoelectronics. Owing to their superior optical and electrical properties, QDs demonstrate a broad prospect in the fabrication of high-performance optoelectronics devices, including light-emitting diodes (LEDs), lasers, solar cells, and photodetectors. However, at this stage, the industrialization of QD-based optoelectronics still faces challenges of insufficient long-term stability and device efficiency. Addressing these issues, integrating appropriate light management into QD-based optoelectronics can improve the device efficiency and reduce power consumption significantly. On the other hand, the reduced power applied to the devices further facilitates long-term stability. These effects are conducive to advancing the commercialization of QD-based optoelectronics.

This thesis presents light management schemes to enhance the performance of various QD-incorporating optoelectronic devices. These schemes are implemented through three strategies: improving light extraction of the backward emission from QDs by back reflectors, increasing light absorption and photoluminescence intensity of QDs by microporous structures, and suppressing diffuse light of QD layer for X-ray imaging system by developing compact encapsulation matrix. Fabrication processes for nano-/micro- structures as well as synthesis methods for new ligand molecules are developed to realize photon management of the devices.

For QD-based LEDs, this work develops a metallo-dielectric composite reflector to acquire an effective utilization of the backward emission of QDs. The reflector comprises a monolayer of silver nanoparticles coated with a titanium dioxide layer. It exhibits unique wavelength-dependent transmittance and reflectance spectra. Moreover, the optical properties of the reflectors can be controlled by manipulating the morphology of the silver nanoparticles and the titanium dioxide layer. The tailoring of wavelength-dependent characteristics allows a high transmission of excitation light for the QDs and a high reflection of the emitted light of QDs. By incorporating this back reflector between the excitation chip and QD layer, a radiant flux enhancement of 19.5% is demonstrated for a UV-pumped white LED.

In display technologies, QDs commonly serve as color conversion layers. The photoluminescence intensity of QDs is limited by the insufficient absorptance of the excitation light due to the lack of scattering capability. This thesis introduces volumetric microporous structures to QD color converters as effective light-scattering media. A phase-separation method based on the polymer blends is investigated for the self-assembly fabrication of the microporous structures. The proposed method shows good control of the morphology of the micropores, enabling fine

adjustment to the light scattering capability. By optimizing the microporous structure, the photoluminescence intensity of the QD film is enhanced by 110%. Besides, along with the rapid development of micro-LED and organic LED display technologies, the demand for cost-effective fabrication of QD pixels is growing. As the phase separation method is a solution-based process, this work adapts the solution of QDs and polymer blends as the ink for inkjet printing technique. Mask-free fabrication of microporous QD pixels is achieved. The inkjet-printed QD pixel arrays achieve a photoluminescence enhancement of 35.3% and show high uniformity in pixel size and good reproducibility.

Recently, perovskite QDs (PQDs) have been testified as promising materials for X-ray scintillation. To pursue a high spatial resolution for the X-ray imaging system, the diffused light of PQD scintillators needs to be suppressed to minimize the blurring of the obtained image. With this goal, this thesis demonstrates a new ligand system based on organosilicon molecules for the compact encapsulation of PQDs. Owing to the better affinity of the ligand system, PQD films with improved surface morphology and remarkable photoluminescence quantum yield are achieved. The reduced surface roughness and porosity lessen the light scattering of the scintillator film, providing a clearer fluorescent pattern for the camera. As a result, the PQD-integrated X-ray imaging system demonstrates a high spatial resolution of over 20 line pairs per millimeter. In addition, the robust encapsulation facilitates the long-term stability of PQDs in various harsh conditions, showing vast potential for commercial applications.

Kurzfassung

In der heutigen Zeit bewegen sich der Lebensstil der Menschen und die industrielle Produktion in Richtung Digitalisierung und künstliche Intelligenz. In diesem Prozess spielen optoelektronische Geräte eine entscheidende Rolle in den Bereichen Erkennung, Signalübertragung und Informationsdarstellung. Um die hohen Anforderungen komplexer elektronischer Systeme in Bezug auf Effizienz, Integration und geringer Energieverbrauch zu erfüllen, ist die Implementierung effektiver Lichtmanagementverfahren ein wesentlicher Schritt zur Optimierung der Leistung von optoelektronischer Bauteile. Darüber hinaus hat die Entdeckung und Entwicklung kolloidaler Quantenpunkte (QPe) zu enormen Innovationen und Fortschritten in der Optoelektronik geführt. Aufgrund ihrer überlegenen optischen und elektrischen Eigenschaften bieten QPe ein breites Spektrum an Möglichkeiten für die Herstellung hochleistungsfähiger optoelektronischer Bauelemente, darunter Leuchtdioden (LEDs), Laser, Solarzellen und Fotodetektoren. Die Industrialisierung der Optoelektronik auf der Basis von QPe steht jedoch noch vor dem Problem der unzureichenden Langzeitstabilität und Effizienz der Bauelemente. Durch die Integration eines geeigneten Lichtmanagements in QP-basierter Optoelektronik kann die Effizienz der Geräte verbessert und der Stromverbrauch erheblich gesenkt werden. Andererseits wird durch die geringere Leistungsaufnahme der Bauelemente die Langzeitstabilität weiter verbessert. Diese Effekte tragen dazu bei, die Kommerzialisierung der QP-basierten Optoelektronik voranzutreiben.

In dieser Arbeit werden Lichtmanagementkonzepte zur Verbesserung der Leistung verschiedener optoelektronischer QP-basierter Bauelemente vorgestellt. Diese Verbesserungen werden durch drei Strategien umgesetzt: Erhöhung der Lichtextraktion der Rückwärtsemission von QPe durch Rückreflektoren, Steigerung der Lichtabsorption und Photolumineszenzintensität von QPe durch mikroporöse Strukturen und Unterdrückung des diffusen Lichts der QP-Schicht für Röntgenbildgebungssysteme durch die Entwicklung einer kompakten Verkapselungsmatrix. Dabei werden Herstellungsverfahren für Nano-/Mikrostrukturen sowie Synthesemethoden für neue Ligandenmoleküle entwickelt, um das Photonenmanagement der Geräte zu realisieren.

Für QP-basierte LEDs wird in dieser Arbeit ein metallisch-dielektrischer Kompositreflektor entwickelt, um die Rückwärtsemission von QPe ausreichend zu nutzen. Der Reflektor besteht aus einer Monoschicht aus Silbernanopartikeln, die mit einer Titandioxidschicht überzogen ist. Er weist einzigartige wellenlängenabhängige Durchlässigkeits- und Reflexionsspektren auf. Darüber hinaus können die optischen Eigenschaften der Reflektoren durch Manipulation der Morphologie der Silbernanopartikel und der Titandioxidschicht gesteuert werden. Die wellenlängenabhängige Charakteristik ermöglicht eine hohe Transmission des Anregungslichts und eine hohe Reflexion des emittierten Lichts der QPe. Durch den Einbau dieses Rückreflektors zwischen dem Anregungschip und der QP-Schicht wird für eine UV-gepumpte weiße LED eine Erhöhung des Strahlungsflusses um 19,5 % nachgewiesen.

In der Displaytechnologie dienen QPe in der Regel als Farbumwandlungsschichten. Die Photolumineszenzintensität von QPe wird durch die unzureichende Absorption des Anregungslichts aufgrund der fehlenden Streuungsfähigkeit begrenzt. In dieser Arbeit werden volumetrische

mikroporöse Strukturen in QP-Farbkonvertern als effektive Lichtstreuungsmedien eingeführt. Eine auf Polymermischungen basierende Phasentrennungsmethode wird zur selbstorganisierenden Herstellung der mikroporösen Strukturen untersucht. Mit der vorgeschlagenen Methode lässt sich die Morphologie der Mikroporen gut kontrollieren, was eine Feineinstellung der Lichtstreuungsfähigkeit ermöglicht. Durch die Optimierung der mikroporösen Struktur wird die Photolumineszenzintensität des QP-Films um 110% erhöht. Mit der raschen Entwicklung von Mikro-LEDs und organischen LED-Display-Technologien steigt auch die Nachfrage nach einer kostengünstigen Herstellung von QP-Pixeln. Da die Phasentrennungsmethode ein Lösungsmittelprozess ist, kann ein Gemisch aus QPe und Polymermischungen in Lösungsmitteln als Tinte für das Tintenstrahldruckverfahren verwendet und damit eine maskenfreie Herstellung von mikroporösen QP-Pixeln erreicht werden. Die im Tintenstrahldruckverfahren hergestellten QP-Pixel-Arrays erreichen eine Photolumineszenz-Verbesserung von 35,3 % und weisen eine hohe Homogenität der Pixelgröße und eine gute Reproduzierbarkeit auf.

Kürzlich wurden Perowskit-QPe (PQPe) als vielversprechende Materialien für die Röntgenszintillation getestet. Um eine hohe räumliche Auflösung für das Röntgenbildgebungssystem zu erreichen, muss das Streulicht der PQP-Szintillatoren unterdrückt werden, um die Unschärfe des erhaltenen Bildes zu minimieren. Zu diesem Zweck wird in dieser Arbeit ein neues Ligandensystem auf der Basis von Organosiliziummolekülen für die kompakte Verkapselung von PQPe vorgestellt. Dank der besseren Affinität des Ligandensystems werden PQP-Filme mit verbesserter Oberflächenmorphologie und bemerkenswerter Photolumineszenz-Quantenausbeute erzielt. Die geringere Oberflächenrauhigkeit und Porosität verringern zusätzlich die Lichtstreuung des Szintillatorfilms und sorgen für ein klareres Fluoreszenzmuster für die Kamera. Infolgedessen weist das PQP-integrierte Röntgenbildgebungssystem eine hohe räumliche Auflösung von über 20 Linienpaaren pro Millimeter auf. Darüber hinaus ermöglicht die robuste Verkapselung die Langzeitstabilität der PQPe unter verschiedenen rauen Bedingungen, was ein großes Potenzial für kommerzielle Anwendungen darstellt.

Table of Contents

List of Publications

Peer-reviewed publications (first author)

- <u>Chen, J.</u>, Jin, Q., Donie, Y. J., Perales, O. T., Busko, D., Richards, B. S., Lemmer, U. "Enhanced photoluminescence of a microporous quantum dot color conversion layer by inkjet printing." *Nano Research*, 2024, 1-9.
- <u>Chen, J.</u>, Jiang, G., Hamann, E., Mescher, H., Jin, Q., Allegro, I., Brenner, P., Li, Z., Gaponik, N., Eychmüller, A., Lemmer, U. "Organosilicon-Based Ligand Design for High-Performance Perovskite Nanocrystal Films for Color Conversion and X-ray Imaging." *ACS nano*, 2024, 18(14), 10054-10062.
- <u>Chen, J.</u>, Zhao, Q., Yu, B., Lemmer, U. "A Review on Quantum Dot-Based Color Conversion Layers for Mini/Micro-LED Displays: Packaging, Light Management, and Pixelation." *Advanced Optical Materials*, 2024, 12(2): 2300873.
- <u>Chen, J.</u>, Yu, S., Fu, T., Xu, L., Tang, Y., Li, Z. "The kapok petal: superhydrophobic surface induced by microscale trichomes." *Bioinspiration & Biomimetics*, 2022, 17(2): 026007.
- <u>Chen, J.</u>, Theobald, D., Shams, A. B., Jin, Q., Mertens, A., Gomard, G., Lemmer, U. "Silver-Nanoparticle-Based Metallodielectric Wavelength-Selective Reflectors for Quantum-Dot-Enhanced White-Light-Emitting Diodes." *ACS Applied Nano Materials*, 2021, 5(1): 87-93.

Peer-reviewed publications (co-author)

- Jin, Q., Zhang, Q., Rainer, C., Hu, H., <u>Chen, J.</u>, Gehring, T., Dycke, J., Singh, R., Paetzold, U. W., Hernández-Sosa, G., Kling, R., Lemmer, U. "Inkjet-printed optical interference filters." *Nature Communications*, 2024, 15(1), 3372.
- Yu, S., <u>Chen, J.</u>, Gomard, G., Hölscher, H., Lemmer, U. "Recent progress in light‐Scattering porous polymers and their applications." *Advanced Optical Materials*, 2023, 11(13): 2203134. (co-first author)
- Jin, Q., Zhang, Q., <u>Chen, J.</u>, Gehring, T., Eizaguirre, S., Huber, R., Gomard, G., Lemmer, U., Kling. R. "High dynamic range smart window display by surface hydrophilization and inkjet printing." *Advanced Materials Technologies*, 2022, 7(5): 2101026.

Contributions to conferences

- <u>Chen, J.</u>, Donie, Y. J., Lemmer1, U. "Light management via disordered porous structure in micro- and nano- scales (Oral-Poster-Presentation)." *International School and Conference on Disorder in Materials Science (DisoMAT 2023)*, Bavaria, Germany, 19. 06. 2023 - 21. 06. 2023.

- Reza, K. M. S., Borgmann, L., <u>Chen, J.</u>, Thelen, R., Gomard, G., Lemmer, U., Hölscher, H. "Nanopores generate broadband reflecting structures in snakes and bees." *Bioinspiration, Biomimetics, and Bioreplication XIV. SPIE,* 2024, S, PC1294408.

- Lemmer, U., <u>Chen, J.</u>, Donie, Y. J. "Light management and color conversion for micro-LEDs using self-assembled nanostructures." *Nanoengineering: Fabrication, Properties, Optics, Thin Films, and Devices XX. SPIE*, 2023, S, PC1265307.

- Jin, Q., Zhang, Q., <u>Chen, J.</u>, Gehring, T., Eizaguirre, S., Huber, R., Gomard, G., Lemmer, U., Kling. R. "Pixelated Smart Window for High Dynamic Range Signage Displaying Applications." *6th Smart Materials and Surfaces (SMS 2021), Mailand, Italien*, 20. 10. 2021 - 22. 10. 2021. 2021.

1   Introduction

Quantum dots (QDs) are nanometer-scale semiconductor particles that show unique properties with quantum mechanical effects.[1], [2] These tiny particles, typically comprised of materials such as cadmium selenide and metal halide perovskite, demonstrate the advantages of a narrow emission spectrum, size-dependent fluorescence, and high quantum efficiency. Owing to the quantum confinement effect, the size-dependent electronic structures of QDs allow fine control over their electronic and optical properties by simply adjusting the particle size. These distinct characteristics are promising for a wide range of applications in optoelectronics, including light-emitting diodes (LED), displays, photovoltaics, photodetectors, and biosensors.[3] Moreover, from a manufacturing perspective, solution-processing approaches, such as inkjet printing and roll-to-roll processing, exhibit good potential for the industrial fabrication of electronics due to their cost-effectiveness and good scalability.[4] The nanoscale particle size of QDs enables excellent compatibility for the solution process. It significantly increases the prospects for the commercialization of QDs. In light of the profound advancement of QDs, Moungi G. Bawendi, Louis E. Brus, and Aleksey Yekimov have been awarded the Nobel Prize in Chemistry 2023 for their significant contribution to the discovery and development of QDs.[5]

Today, a few QD-based electronics, such as QD-enhanced televisions, have reached industrial production requirements and made their way into people's lives. The market size of QDs was evaluated at over USD 5.5 billion in 2023 and is estimated to register a compound annual growth rate of over 15.5% in the period of 2024 to 2032,[6] as shown in **Figure 1.1**. The main contributor to the growing market is the rapid development of high-end display devices incorporating QDs. Compared to conventional liquid crystal display devices, QD-enhanced display technologies provide higher brightness, better color purity, and a broader color gamut.[7] These appealing merits are desirable in high-end televisions, monitors, and mobile devices that require high color accuracy. More technical solutions, such as QD/organic LED displays, QD/micro-
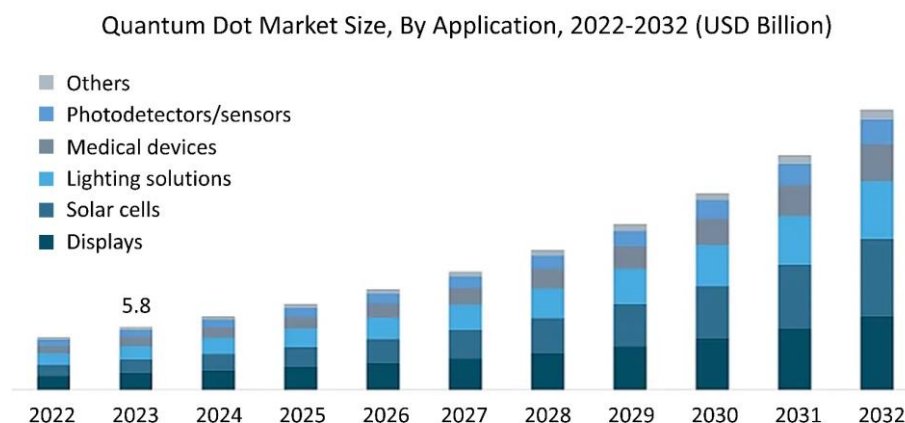

Figure 1.1 Histogram of valued (2022-2023) and estimated (2024-2032) market size of quantum dots (QDs) with segments of different applications. (Source: www.gminsights.com)

LED displays, and electroluminescent QD displays have been proposed and developed for high-performance displays.[8] The demand for QD-based displays is expected to increase. Other electronic devices like QD-incorporating solar cells, lighting devices, medical devices, and photodetectors all show a rising tendency in the market size. Besides, the development of emerging applications of QDs has accelerated the growth of the QD market as well. In 2020, UbiQD Inc. (a specialist in advanced materials for agriculture) settled down a partnership with Nanosys, Inc. (a leading company in developing QD products) to promote QD-based luminescent greenhouse films for commercial application in agriculture.[9] The market of greenhouse cover film was evaluated to be more than 50 billion square feet globally with a comparable size to the display industry. In recent years, perovskite QDs have been testified as ideal scintillation material for X-ray detection and imaging and attracted massive attention.[10] Commercially available X-ray scintillators based on perovskite QDs were subsequently released to the market.[11]

Despite the huge potential for the growth of the market, the commercialization of QDs and QD-based optoelectronics is still in its infancy. On the one hand, the light extractions of QD-incorporating devices are yet insufficient, limiting their efficiency and performance to meet the demand of high-end applications. On the other hand, the inadequate long-term stability of QDs against environmental stimuli is a common obstacle that inhibits their commercialization.[12] For photoluminescent applications, QDs are generally encapsulated in a barrier matrix to minimize degradation and elongate the longevity of QDs. However, the introduction of the encapsulating matrix normally deteriorates the light extraction of the devices. Extensive recent studies have demonstrated that proper light management schemes enable significant enhancement in the efficiency and performance of optoelectronic devices.[13, 14] Light managing strategies, including applying photonic structure, surface engineering, and introducing back reflectors or diffusers, can realize higher light extraction efficiency and lower energy consumption for the devices. They provide more dimensions for tailoring the optical properties of the devices. In addition, the lifetime of the QD-based electronics can be extended by minimizing the electric consumption as well, due to the reduced electric loading and heat generation. Thus, designing and optimizing light management solutions for QD-based optoelectronics is an essential step in advancing the industrialization of QDs.

Aiming at the photoluminescent applications, the work in this dissertation is dedicated to improving the light management of QD-based optoelectronics. Based on the in-depth analysis of the photoluminescence mechanism, three strategies are proposed to boost the light extraction and performance of the QD layers. These approaches demonstrate remarkable enhancing effects in various QD-incorporating electronics, including light-emitting diodes, color-converting QD pixels, and X-ray detectors. The dissertation is structured as follows:

- Chapter 2 presents the fundamentals of QDs regarding the electronic structures and the quantum confinement effect. Besides, a brief outline of the development of QDs and an introduction of perovskite QDs are provided.
- Chapter 3 shows the recent advancements in QD-based material development and optoelectronics for photoluminescent applications. Specifically, the aspects of encapsulation, light management, and patterning methods of QDs are covered. This chapter offers an overview of the state of the art of the research on QDs.

- Chapter 4 presents the materials, experimental methods, and characterization techniques applied in this dissertation.
- Chapter 5 focuses on the fabrication of wavelength-selective reflectors and their application in QD-incorporating white light-emitting diodes. The fabrication of the reflectors made from silver nanoparticles and a titanium dioxide coating layer is demonstrated, with detailed manipulation of the processing parameters. The mechanism of the reflectors in extracting backward emission of QDs is illustrated by spectral characterizations. These wavelength-selective reflectors are eventually integrated into light-emitting diodes as back reflectors. The optical performance of the devices is characterized systematically.
- Chapter 6 introduces microporous structures to QD color conversion layers for enhancing light absorption and light outcouping. A phase-separation approach for fabricating microporous polymeric networks is explored. Microporous films with and without embedding QDs are characterized to investigate their performance of light scattering and light conversion. Equivalent studies on titanium dioxide nanoparticles are conducted as a comparison. With the validation of the enhancing effect, the latter part of the chapter focuses on the integration of the microporous structure into inkjet-printed QD pixels. Optical and morphological characterizations are performed on the QD pixels to evaluate their uniformity and reproducibility.
- Chapter 7 demonstrates a dual-organosilicon ligand system to encapsulate metal halide perovskite QDs for reduced light scattering and enhanced stability. The design and synthesis of the proposed ligand are first illustrated with the assistance of molecular simulation. Chemical characterizations are performed to certify the successful synthesis of perovskite QDs with the proposed ligand. Comprehensive morphological and optical measurements are followed to investigate the quality of the encapsulation and the photoluminescent performance of the QD films. The robustness of resulting QD films is studied in detail through a series of stability tests under harsh conditions. Eventually, an X-ray imaging test incorporating the optimized QD scintillators is carried out at the end of the chapter, achieving a high spatial resolution of over 20 line pairs per millimeter.
- Chapter 8 concludes the significance of the key advances of this dissertation and provides the outlook for future work on this topic.

2 Fundamentals of Quantum Dots

This chapter discusses the electronic band structure and optical properties of quantum dots along with the underlying mechanism. Specifically, the electronic structure of quantum dots and the quantum confinement effect are highlighted. Section 2.1 draws an overview of the history and recent development of quantum dots. Section 2.2 illustrates the formation and characteristics of the band structures of bulk semiconductors and quantum dots, respectively, to illustrate the quantum confinement effect. In Section 2.3, perovskite quantum dots are introduced, with a comprehensive interpretation of the advantages and obstacles originating from their unique band structure.

2.1 An overview of quantum dots

Quantum dots (QDs), also known as semiconductor nanocrystals (NCs), are semiconductor nanoparticles with diameters ranging from several nanometers to tens of nanometers.[15], [16] Due to the quantum confinement effect, electrons in these semiconductor nanostructures show behaviors that differ from those of bulk solids, resulting in distinctive optical and electronic properties, such as size-dependent light absorption and emission, narrow emission linewidth, and high fluorescence quantum yield.[17], [18] Given these promising characteristics, QD materials have been widely applied in various applications, including illumination, displays, energy harvesting, sensors, and biology.[19], [20], [21] Regarding the profound influence and broad potential of QDs in academic and industrial fields, the Nobel Prize in Chemistry 2023 was awarded to Louis E. Brus, Alexey Ekimov, and Moungi G. Bawendi for the discovery and synthesis of QDs.
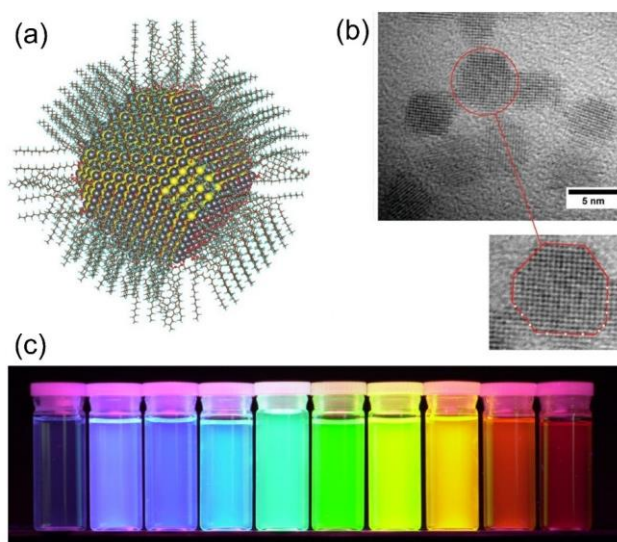

Figure 2.1 (a) Illustration of a QD capped with surface ligands. (b) TEM image and enlarged view of PbS QDs.[22] Reproduced with permission. Copyright 2014, AAAS. (c) The tunable emission color of QDs by adjusting their particle size.[25] Reproduced with permission. Copyright 2009, Elsevier.

Analogous to metal ions, which do not exist in a completely isolable form in a non-vacuum environment, inorganic QDs require a protective surface barrier when placed in a solvent host or atmosphere. Thus, colloidal QDs are commonly capped with ligand molecules for effective surface passivation with a typical configuration shown in **Figure 2.1** (a).[22] Core-shell designs are frequently employed for improving stability as well.[23], [24] Considering an individual QD is only composed of a few atoms in the crystal structure, as exhibited in **Figure 2.1** (b), its properties could be different from the corresponding bulk solid.[25] These phenomena are summarized as size-effect. The most unique size-effect of QDs is the quantum confinement effect.[26], [27] The quantum confinement effect is profound when the size of the semiconductor particle is smaller than the exciton Bohr radius which causes spatial confinement to the carriers (electrons, holes, and excitons). This spatial confinement leads to the discretization of the energy levels of the carriers and further affects the band gap of the QDs. By use of this phenomenon, the emission and absorption spectra of QDs can be adjusted by altering the particle size. For instance, in CdSe QDs, the shifting of energy gap caused by the change of particle size can reach up to 1.2 eV, specifically from 1.8 eV (the bulk value) to 3 eV, covering almost the entire visible wavelength range.[28]
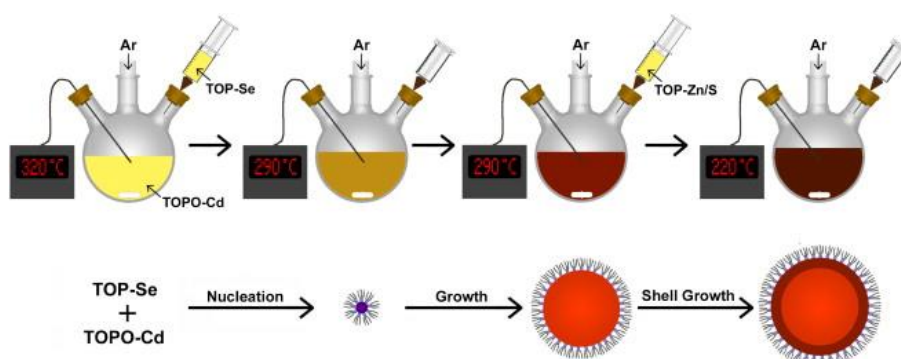

Figure 2.2 Illustration of the hot-injection synthesis process (upper row) and schematic of the formation (bottom row) of QDs.[32] Reproduced with permission. Copyright 2014, Elsevier.

The story of QDs started in the 1980s. In 1981, Alexei Ekimov and Alexander Efros, based at the S. I. Vavilov State Optical Institute and the A. F. Ioffe Institute in Russia, began exploring semiconductor-doped glasses and formulating theories to explain their properties.[29] At the same time, but on the other side of the globe, Louis Brus at Bell Laboratories, US, was studying semiconductor particles in liquid colloids.[30] Despite the geographic and political separation caused by the Iron Curtain, these parallel lines of research led to the independent development of QDs and the underlying theory of their size-dependent optical properties by both groups. Since their invaluable discovery in the 1980s, QD materials have attracted increasing attention. In 1993, Moungi G. Bawendi proposed an efficient hot-injection method for synthesizing QDs with well-defined size and high optical quality.[31] To better explain the hot-injection methods, we take the synthesis process of CdSe QDs as an example.[32] As illustrated in **Figure 2.2**, the cadmium compound is first dissolved in an organic solvent at 320°C. Selenium compound is dissolved in another solvent at room temperature and then injected into the reaction vessel, leading to supersaturation of CdSe solution and the start of nucleation. When the temperature decreases to 290°C, nucleation of new crystals ceases and the existing crystals continue to grow. After a certain time, the solution is cooled to 220°C to stop the growth. A small amount of zinc

sulfide is then injected into the reaction vessel to form a coating shell. This method enabled the large-scale fabrication and technological applications of QDs, significantly promoting their industrialization. In 1994, Paul Alivisatos reported the first electroluminescent QD light emitting diode (LED) based on CdSe QDs combining semiconducting polyphenylene vinylene polymer.[33] In the early 2000s, Xiaogang Peng and his research group introduced multiple benign reagents to the synthesis system of QDs for replacing toxic and unstable precursors (such as Cd(CH$_3$)$_2$), improving the safety of the fabrication process.[34] Lately, benefiting from the tremendous progress in the field of metal halide perovskite solar cells, perovskite QDs (PQDs) have emerged as one of the most promising QD materials.[35], [36] Following the pioneers, nowadays, vast efforts from researchers have been contributing to the development of QDs with better performance, such as cost-efficient synthesis, low toxicity composition, high emission efficiency, and high long-term stability.

Table 2.1 Optical properties of several common types of QDs

	Peak Emission [nm]	FWHM [nm]	PLQY [%]	Reference
CdSe	Tunable (Red)	28–32	~99.6 ± 0.2	[37]
CdSe	532 (Green)	26	75	[38]
ZnCdSe	630 (Red)	17.1	99	[39]
CdZnS	455 (Blue)	17.2	92	[40]
InP	~535 (Green)	37	95	[41]
InP （InP/ZnSe/ZnS）	630 (Red)	35	~100	[42]
InP (InP/ZnS)	~425 (Blue)	~72	~25	[43]
Perovskite (MAPbBr$_3$)	526 (Green)	20	~100	[44]
Perovskite (CsPbBr$_x$Cl$_{3-x}$)	463 (Blue)	15	98	[45]
Perovskite (CsPbI$_3$)	680 (Red)	33	96	[46]

To demonstrate the current state of the optical properties of QDs, we summarize the recent progress regarding the basic performances of various common types of QDs, as shown in **Table 2.1**. Among the existing types of QDs, those based on CdSe/CdS, InP, and perovskite material, are the most used in optoelectronic applications. Generally, QD materials exhibit a narrow full width at half maximum (FWHM) of the emission spectrum and high photoluminescence quantum yield (PLQY), which are the key performances to evaluate QDs. Cd-based QDs, which have been developed over two decades, are more mature than other types and are well-suited for

commercial applications due to their high stability and excellent PLQY, reaching nearly 100% in solution.[37], [38], [39], [40] Core-shell structures (e.g. CdSe/CdS core-shell QDs) have been widely applied for the passivation of Cd-based QDs. Nevertheless, the high toxicity of Cd-based QDs poses significant challenges for commercial applications. Consequently, substantial efforts have been directed towards developing cadmium-free QDs as alternatives. InP-based QDs have emerged as the most promising candidates.[41], [42], [43] The PLQYs of InP-based QDs have been promoted to near 100%, which shows good potential for commercial display applications. However, it is still challenging to develop high-performance blue-emitting InP QDs, due to the poor controllability of nucleation and growth during synthesis, especially in the deep blue wavelength range.

PQDs offer straightforward low-temperature synthesis processes and low manufacturing costs. Additionally, PQDs typically have a small FWHM of less than 20 nm and a near unity PLQY, garnering extensive attention in recent years.[44], [45], [46] For the three fundamental colors, PQDs have achieved remarkable fluorescence efficiency and high color purity, showing good potential in display and color conversion applications. However, different from II−VI, and III−V semiconductors, metal halides PQDs contain more ionic bonding, leading to poorer stability when exposed to water and oxygen. Designing robust encapsulation and dense surface passivation for PQDs to elongate their lifetime in practical applications is still a challenge at this stage.
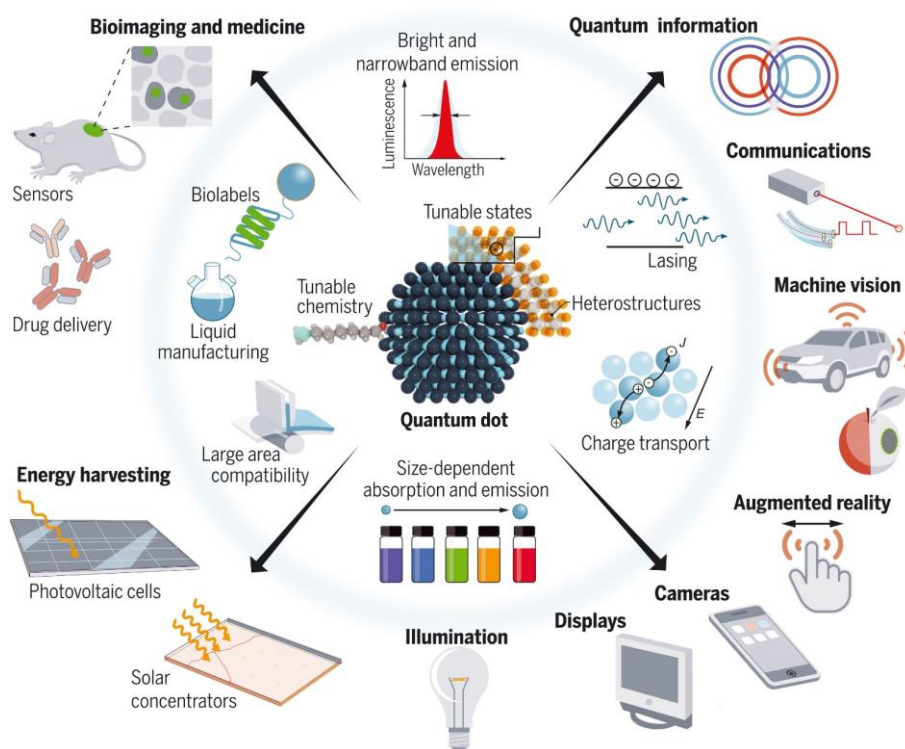

Figure 2.3 Characteristics and applications of QDs.[3] Reproduced with permission. Copyright 2021, AAAS.

Research and development in QD-related technology continue with strong momentum. This interdisciplinary field lies at the intersection of chemistry, physics, and materials science. The evolution of QD materials science over the past 20 years parallels the development of bulk

semiconductor technology in the mid-20th century. Currently, hundreds of scientists and engineers are working on improving QD designs, synthesis methods, and prototype devices. Various novel applications, including micro-LED displays, single-photon sources, quantum information science, and many other possibilities are being explored along with the rapid development of QDs.[3] The field is still in its early stages.

2.2 Electronic structure of quantum dots

From the perspective of a chemist, QDs might be regarded as large molecules with ordered assembly of a few atoms. For a physicist, QDs are more likely described as tiny powders of semiconductor crystals. As nanoscale materials, QDs with intermediate dimensions between individual atoms and macroscopic bulk exhibit physical and chemical behaviors distinct from the corresponding bulk material or single molecule.[47], [48] For bulk semiconductors, their physical properties are mainly determined by the elements or atoms they contain and the crystalline structure formed by these atoms.[49], [50] However, for semiconductor nanocrystals, the size of the material brings in another dimension to adjust the properties of semiconductor materials.[51] As an example, in carbon-based materials, unique performances, and band structures are observed in various low-dimension carbon materials, such as two-dimension graphene sheets, one-dimension carbon nanotubes, and zero-dimension carbon dots, which are notably diverse with bulk graphite.[52], [53] These phenomena are called the size effect of nanoscale particles.

To understand the distinct properties of QDs, details about their band structure and the behaviors of the charge carriers within them need to be elaborated. For a comprehensive explanation, in this section, a top-down strategy is used, which starts from bulk semiconductor material and then adapts the principles to quantum-confined semiconductor nanocrystals.[54], [55], [56] In a bulk system, the motion of the charge carriers can be described by a linear combination of a series of plane waves, as the free charges and holes can travel through the whole crystal. However, the charge carriers in a QD are spatially confined in three dimensions since the size of QD is comparable to the wavelength of the carriers. In this situation, the solutions of the Schrödinger equation are a series of standing waves with discrete energies confined in the potential well. This discretization of the energy level of QDs is the so-called quantum confinement effect, further leading to the unique optical and electrical properties. Understanding this effect is the key to entering the fascinating world of QDs.

2.2.1 Bulk luminescent semiconductor

A characteristic of the electronic behavior in crystal solids is the presence of energy bands and the band gaps interspersing in between. The bands are energy ranges that allow occupation with charge carriers while the band gaps are the energy ranges where no electronic states exist. The band gap between the valence band and conduction band of semiconductors is of moderate size compared to insulators (large band gap) and conductors (almost no band gap). For instance, silicon with a band gap energy of 1.12 eV is regarded as a semiconductor, while silicon dioxide with a band gap energy exceeding 9 eV is recognized as an insulator.
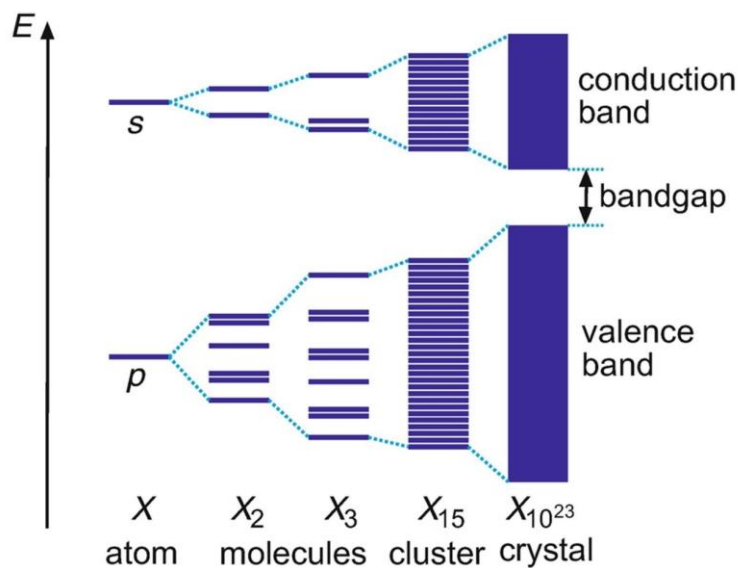
Figure 2.4 Schematic illustration of the formation of energy bands of an element X, from single atomic orbitals to continuous bands with increasing atom amount.[55] Reproduced with permission. Copyright 2022, Springer Nature.

To learn the formation of the energy band, a simple first step is to consider the electron behavior of a single atom. Based on the quantum mechanics model, the charge distribution of the electrons around a nucleus is described by atomic orbitals, which correspond to different energy states of the electrons. Namely, the electrons within an atom feature only specific and discrete energy levels, and each energy level can hold a maximum of two electrons with opposite spins. With more atoms bound together, the orbitals of different atoms with the same eigenstate split slightly due to the Pauli exclusion principle. When the energy levels are close enough, the distinction between the individual levels is no longer permitted by Heisenberg's uncertainty principle, discrete energy levels merge into energy bands. Meanwhile, the exchange or sharing of electrons between atoms happens, forming molecular orbitals. With further increasing the number and reducing the distance of coupling atoms, the molecular orbitals split into bonding orbitals and anti-bonding orbitals, corresponding to localization and delocalization states.[57], [58] The conduction band and valence band are formed correspondingly from bonding orbital and anti-bonding orbitals. The illustration of the formation of energy bands is shown in **Figure 2.4**. This model emphasizes the collective behavior in atom clusters that share electrons among atoms, causing the aggregation of discrete energy levels. Considering the number of atoms in solids is tremendous with densities in the order of $10^{28}/m^3$, bulk semiconductors possess quasi-continuous energy band structure.

The lattice structure is another critical feature of semiconductor crystals. With a regular arrangement of atoms, the electrons experience a series of potential wells created by the fixed atom nucleus when propagating in the crystal solid. For a single atom, as shown in **Figure 2.5**, an energy potential well with a funnel shape is exhibited with the discrete energy levels filled inside. The electrons in the bottom level are restricted toughly due to the higher Coulomb attraction while the outer shell electrons are easier to escape from the atom. For a small crystal, numerous atoms are involved in the system and the figure of the energy potential is demonstrated as the superimposition of many potential wells of adjacent atoms. Electrons in the conduction
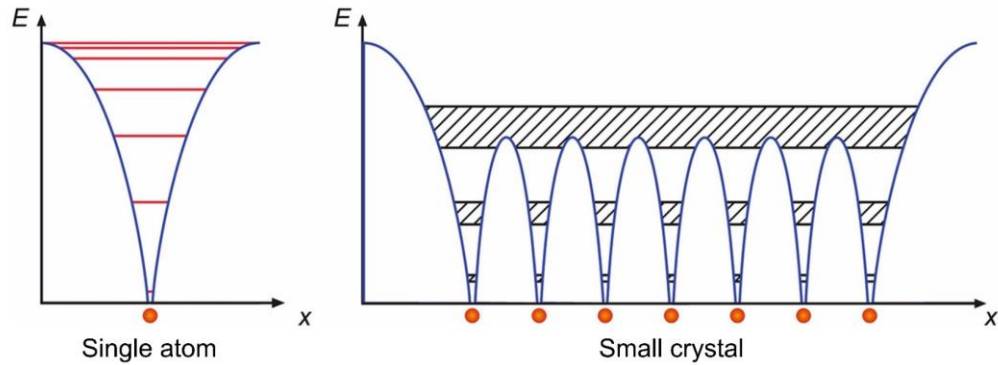
Figure 2.5 Potential energy and energy levels/bands of electrons in a single atom and a small crystal, respectively. The red dots represent the nucleus and the blue lines represent the potential wells.[55] Reproduced with permission. Copyright 2022, Springer Nature.

band can move across potential barriers and propagate among the crystal, while electrons in lower energy bands are bonded. Excitation with energy larger than the band gap is needed to excite an electron from the valence band to the conduction band. As the energy potential is provided by the attraction of the atom nucleus, in a specific semiconductor crystal, the band structure is significantly dependent on the element of the atom and the interatomic distance. The lattice constant is a fundamental parameter for describing the geometry (interatomic distance and angle) of the basic unit cells in a crystal lattice. This parameter is crucial to the band structure of the crystal.[59]
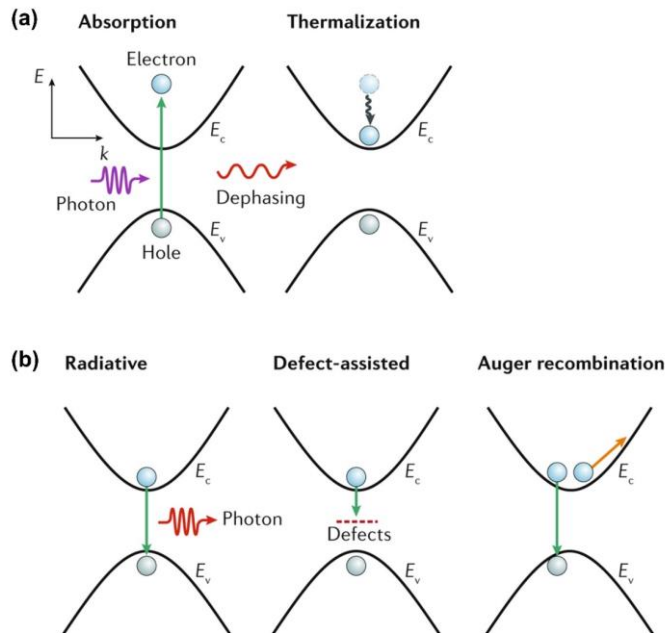

Figure 2.6 Schematics of the fundamental process of (a) electron transition and thermalization, and (b) three types of carrier recombination.[60] Reproduced with permission. Copyright 2020, Springer Nature.

Luminescent semiconductors are a type of semiconductor with band gap energies lying in the range of visible light. For luminescent semiconductors, light emission is accomplished through carrier generation and recombination processes.[60] These fundamental processes can be illustrated via a simplified two-level system with the interaction between photons and electrons, as shown in **Figure 2.6**. The carrier generation refers to the process of an electron in the valence band (with energy E_v) absorbing an incident photon with sufficient energy and transiting to the conduction band with a higher energy state (conduction band, E_c), leaving an electron hole in the valence band. After transiting, this hot carrier with energy larger than E_c exchanges energy with other electrons or the lattice and starts cooling down. It finally cools down to the minimum of the conduction band after a certain time of thermalization or dephasing. Following the cooling of the hot carrier, the recombination process occurs. The carrier recombination can be divided into radiative recombination and non-radiative recombination. In radiative recombination, the transited electron recombines with an electron hole and emits a photon with the wavelength corresponding to the band gap energy. The non-radiative recombination is mainly attributed to the defect state in the band gap that traps charge carriers as well as the Auger recombination which involves a third carrier taking the released energy from the electron-hole pair. This recombination increases with the increasing concentration of carriers normally.[61], [62] In these two cases, no photon is emitted through the recombination process. For luminescent semiconductors, trap-state and Auger recombination should be restrained to obtain a high efficiency of radiative combination.
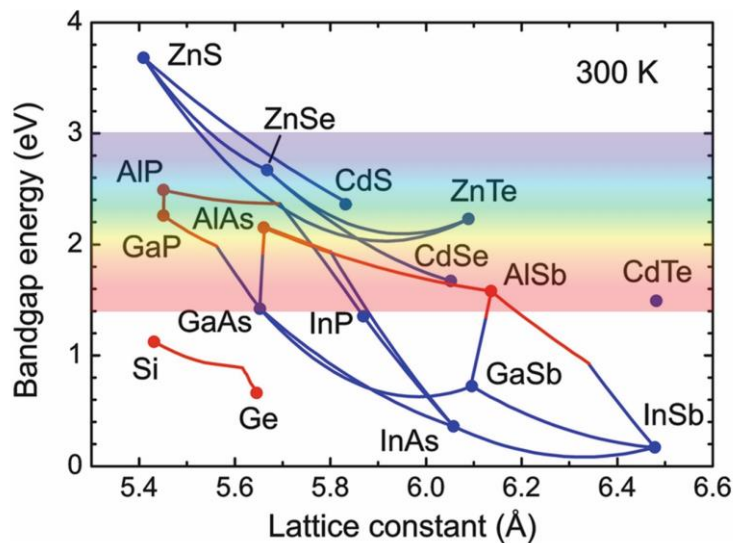

Figure 2.7 Band gap energy as a function of lattice constant for various common semiconductors at the temperature of 300k. The dots represent pure semiconductors and the lines denote alloyed semiconductors. The semiconductors with a direct band gap are marked as blue while those with an indirect band gap are marked as red.[55] Reproduced with permission. Copyright 2022, Springer Nature.

In the dynamic process of carrier generation and recombination, the emission wavelength of the luminescent semiconductor is directly determined by the band gap energy. The band gap energy further refers to the geometry of the crystal and the elements of the atoms that form the crystal. Based on it, a typical approach of mixing or doping multiple elements to acquire compounds with different lattice constants is broadly applied for band gap engineering and emission manip-

ulation.[55] In **Figure 2.7**, a summary graph of band gap energy as a function of lattice constant for common pure (shown as dots) and alloyed (shown as lines) semiconductors at a temperature of 300K is shown. In this graph, the blue lines represent the semiconductors with a direct band gap and the red lines denote an indirect band gap. The compound design enables the adjustment of the emission wavelength of the semiconductors across the visible wavelength range. For instance, by altering the ratio between ZnS and CdS compounds in the crystal, emission wavelength from green to ultraviolet range can be obtained. However, challenges remained for achieving full-color emissions with a single type of semiconductor compound.

The size effect offers another compelling solution to realize the more versatile and effective band gap engineering of the luminescent semiconductor. The miniaturization of the semiconductor materials to a certain extent leads to the quantum confinement effect, introducing additional dimensions for tuning their absorption and emission features.

2.2.2   From bulk to quantum dots

A fundamental aspect of quantum mechanics is the particle-wave duality, known as matter wave from Louis de Broglie. It refers to the behavior of the particle that shows properties of both particle and wave more profoundly when their size becomes comparable to its wavelength.[54], [63] Moreover, to study the behavior of electrons or charge carriers, one can solve its Schrödinger equation with corresponding boundary conditions for obtaining the necessary information. The solutions of this equation indicate the possible physical states that can be found in the system. In this section, we will utilize this approach to demonstrate the evolution of the behavior of charge carriers in a semiconductor crystal when shrinking its dimension from bulk crystal to quantum dots.
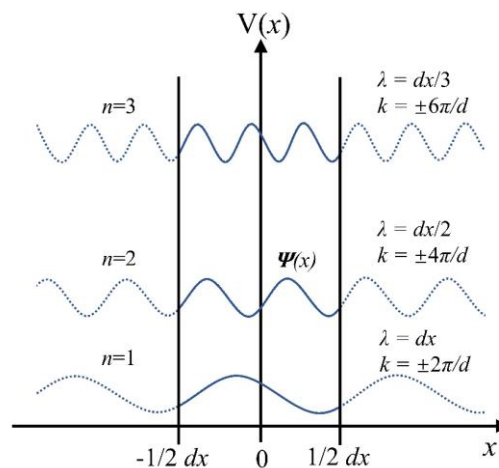

Figure 2.8 Two-dimensional illustration of periodic boundary conditions for a free electron in bulk semiconductor and the wavefunctions with different wave numbers. In this situation, there is nearly no potential formed at the boundary.[54] Reproduced with permission. Copyright 2010, Wiley-VCH.

For bulk semiconductors, electrons in the conduction band are free to move throughout the crystals. In the approximate model, an assumption that the interactions between electrons and

crystal atoms are neglected is made and this model is so-called free electron gas.[64] It is sufficient to handle many cases by replacing electron mass with effective mass, which denotes the electron-crystal and electron-electron interactions as a collection for the calculation. In the free electron gas model, the periodic boundary condition is applied to describe the environmental condition of carriers, as the semiconductor size is much larger than the wavelength of carriers. Thus, the electron that is close to the boundaries is not affected by the boundary conditions as both sides of the boundary are identical, as shown in **Figure 2.8**. The solution of the stationary Schrödinger equation in this situation can be described as a linear combination of plane waves, meaning all the possible electronic states in the momentum space (or *k*-space) are evenly distributed. It highlights that the electrons in the conduction band of bulk semiconductors act more like free electrons.
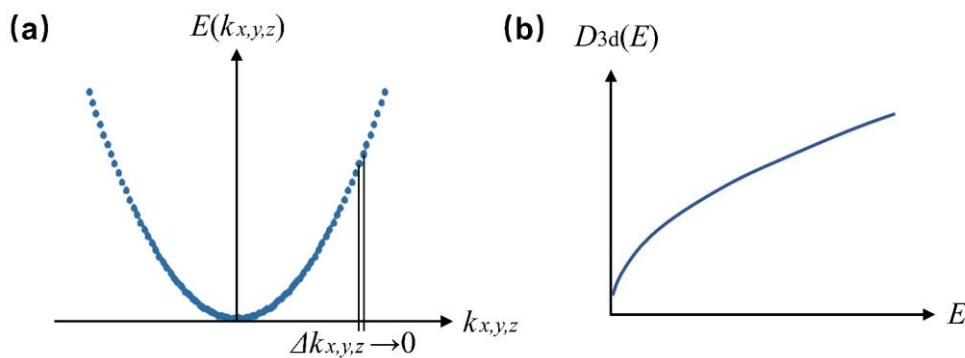

Figure 2.9 (a) Dispersion relation, and (b) density of states of free electrons in a bulk semiconductor.[54] Reproduced with permission. Copyright 1976, Thomsom Learning Inc.

To describe the energy distribution of the electrons, a useful concept of the density of states *D(k)*, which is the number of states per unit interval of wavenumbers, should be involved. Based on the definition, *D(k)Δk* represents the number of electrons with a wavenumber within the range of *k* to *k+Δk*. As the behavior of the electrons is like the free electron, the energy of the electrons in the conduction band is a square relation to the momentum *k*, exhibiting a parabola shape, as shown in **Figure 2.9**. Since the conduction band of bulk semiconductors is quasi-continuous, the dispersion curve can be regarded as quasi-continuous as well. As the density of states *D(k)* is proportional to wavenumber *k* and electron energy *E(k)* is proportional to k^2, *D(k)* is proportional to the square root of *E(k)*. Similarly, the corresponding curve is quasi-continuous.

We now consider the situation of shrinking the bulk semiconductor to QD with a diameter of a few nanometers. The dimension of QD is comparable to the de Broglie wavelength of the electrons in the conduction band. These electrons can no longer propagate freely in the crystal as the energy potential at the border of the QD nanocrystal is extremely high. The excitation energy needs to be greater than the working function for ejecting the electron from the QD. Thus, it is extremely difficult for the electrons to escape from the QD and they are spatially restricted inside, like a particle trapped in a box.[65] The spatial restriction leads to the localization and the quantization of the energy states of the free electrons, namely the quantum confinement effect. In the mathematical model, the boundary condition in this situation is described by an infinitely high potential well instead of a periodic boundary without potential, as shown in **Figure 2.10**. The solution of the Schrödinger equation in this condition is a series of stationary waves with

different energies. The wavenumber *k* can only take the value of certain integers, resulting in the discrete energy states.
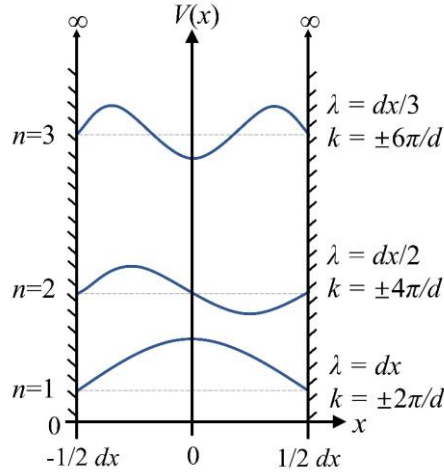

Figure 2.10 Two-dimensional illustration of the boundary condition for a free electron in a QD and the wavefunctions with different wave numbers. The potential boundary is assumed as infinitely high.[54] Reproduced with permission. Copyright 2010, Wiley-VCH.

As there are a few wavenumbers allowed for the electrons in a QD system, the parabolic dispersion relation of free electrons is still valid but only some discrete positions with certain *k* values are occupied, as exhibited in **Figure 2.11**. The available individual states in *k*-space are represented by dots and the distances between the separated dots are determined by the diameter of the QD.[66] The calculated density of states diagram shows a distribution of a series of s delta peaks. It indicates the energy bands converge to atom-like energy states. This phenomenon is more profound at the edges of the bands and thus affects semiconductor materials more than metals. Moreover, the electronic properties of luminescent semiconductors are significantly related to the electron transition and recombination between the edges of the valence band and the conduction band. Due to the discreteness of the energy levels, the ground-state electrons in the conduction band of a QD have higher energy than that of a bulk semiconductor. Compared to bulk semiconductors, the band structure of QD has changed by the quantum confinement
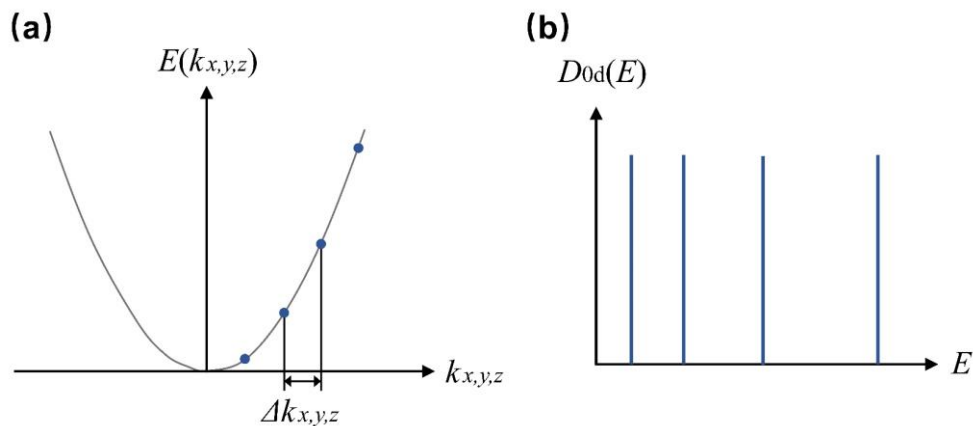

Figure 2.11 (a) Discrete energy levels, and (b) density of states of free electrons in semiconductor QD.[54] Reproduced with permission. Copyright 1976, Thomsom Learning Inc.

15

effect, further resulting in the unique property of size-dependent absorption and emission.

In **Figure 2.12**, the band structures of bulk semiconductors and QDs with different particle sizes are illustrated for comparison.[67] The energy levels of bulk semiconductors merge into continuous bands while the transition and recombination of charge carriers happen among the band gap (energy difference between the edges of the conduction band and valance band). The emission wavelength of the semiconductor is determined by the energy difference of the band gap. When the size of the semiconductor reduces to the nanometer scale, the quantum confinement effect leads to the discretization of the allowed energy states of electrons. Stronger spatial restriction generates larger discreteness. Consequently, the band gaps of the QDs are increased with the reduction of the particle size. The absorption spectrum (related to the carrier transition process) and the emission spectrum (related to the electron-hole recombination process) of QDs can be adjusted by controlling their diameter. Specifically, the decrease of the particle size causes blue-shifting of the absorption and emission spectra of QDs. Moreover, as the density of states diagram is a series of lines, the free electrons distribute in the discrete energy levels more concentratedly, resulting in the narrow emission peak of QD materials. In brief, regarding the band structure, the quantum confinement effect can be regarded as a reverse process of the formation of energy bands. Instead of merging individual energy levels into continuous bands, it leads to discrete energy levels and larger energy differences than the intrinsic band gap of the material. Besides, the tiny particle size of QDs increases the exciton binding energy as well, resulting in a higher density of excitons in the QDs.[68], [69]
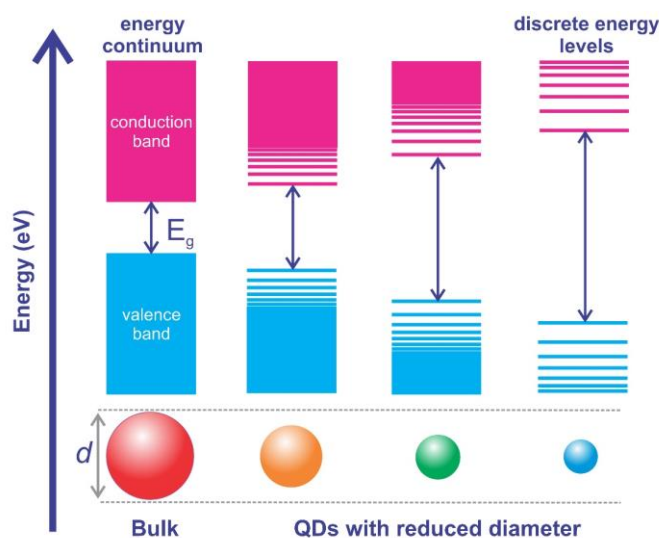

Figure 2.12 Illustration of the band structures of bulk semiconductors and QDs against the size.[67] Reproduced with permission. Copyright 2024, Royal Society of Chemistry.

The evidence for the quantum confinement effect of QDs is the size-dependent absorption spectrum.[70] **Figure 2.13** shows the absorption spectra of colloidal CdSe, CdTe, PbS, and PbSe QDs with different diameters. The first absorption peaks of the curves indicate the corresponding lowest band gap energies of the QDs. A clear tendency of blue-shifting is shown from the graphs with the decrease of the particle diameter. Taking CdSe QDs as an example, the absorption peak can be altered across almost the whole visible wavelength range by simply changing

the size, covering a broad wavelength span that bulk semiconductors can hardly achieve. The same tendency can be found in the emission spectrum of QDs.
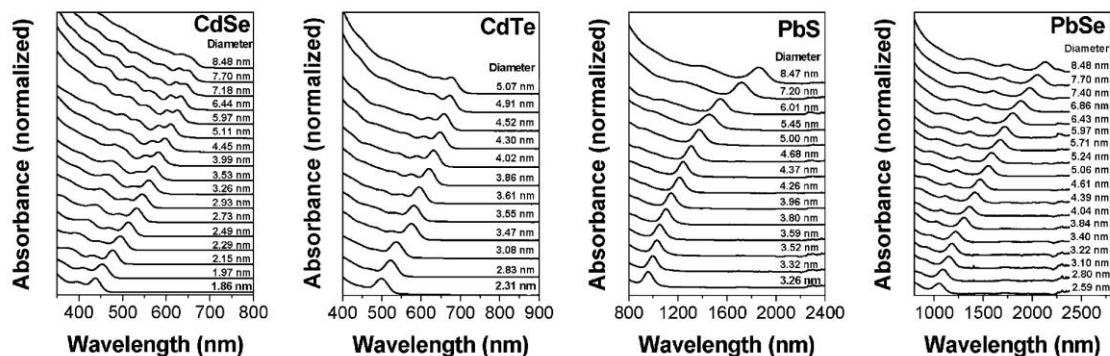

Figure 2.13 The size-dependent absorption spectra of CdSe, CdTe, PbS, and PbSe QDs. With decreasing particle size, the absorption peak of every material shows blue shifting.[70] Reproduced with permission. Copyright 2011, American Chemical Society.

The size-dependent characteristics of QDs are beneficial to various fields, including full-color display technology, white-light illumination, photodetection, and bio-sensing. Based on the mechanism of quantum confinement introduced above, massive efforts have been devoted to the band gap engineering and synthesis method with good size and shape control of QDs. Till now, QDs with emission wavelengths spanning from the ultraviolet range to the infrared range have been achieved.[71], [72], [73]

2.3 Perovskite quantum dots

In recent years, metal halide PQD materials have attracted tremendous attention from scientific and industrial fields, owing to their unique advantages of good defect tolerance, high PLQY, and low-cost fabrication at room temperature.[36], [74] Compared to classical semiconductors (e.g. Si, GaN, InP), metal halide perovskite materials with high quality can be synthesized at room temperature and under ambient conditions by conveniently mixing precursor solutions with corresponding ratios, due to their ionic bonding character.[75] It demonstrates a great potential for commercial mass production with high efficiency.

Perovskite materials refer to a category of crystalline compounds fitting the general chemical formula of ABX_3, where the "B" site is surrounded by six neighboring "X" anions and "A" cation sites at the center of eight corner-sharing BX_6 octahedra, as shown in **Figure 2.14**. Based on the element of "A" site, perovskites are classified into organic-inorganic hybrid perovskite and all-inorganic perovskite.[76] Cesium, methylammonium, formamidinium, and mixtures thereof, are common components for the "A" site, while halide elements are normally employed for the "X" sites. Moreover, perovskite materials demonstrate high defect tolerance that originates from their unique bonding character. The band structures of many conventional semiconductors are generated by the bonding and antibonding molecular orbitals, while the band gaps of perovskite materials are formed between two antibonding orbitals.[77] Taking $MAPbI_3$ perovskite as an example, the valence band maximum is formed by antibonding orbitals of Pb (6s)
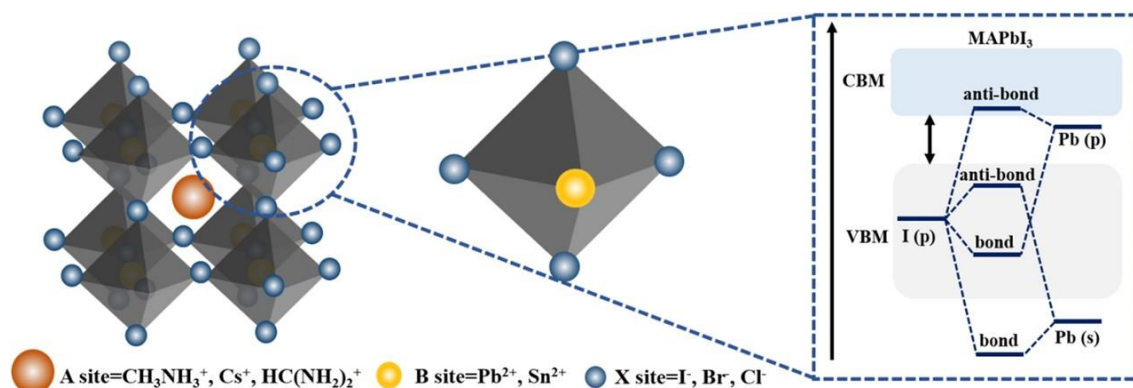
Figure 2.14 Illustration of the crystal structure of metal halide perovskite (left) and the molecular orbitals of MAPbI$_3$ material as an example (right).The valence band of MAPbI$_3$ perovskite is formed by the antibonding hybridization of Pb (6s) and I (5p) orbitals, while the conduction band is formed by the antibonding hybridization of Pb (6p) and I (5s) orbitals.[76] Reproduced with permission. Copyright 2023, Springer Nature.

and I (5p) atomic states, while antibonding Pb (6p) and I (5s) orbitals form the conduction band minimum. In addition, the strong antibonding coupling of the orbitals results in large curvature at the valence band maximum, representing a light effective mass for hole carriers.

Intrinsic point defects, such as vacancies or external impurities, are crucial and detrimental for traditional semiconductors (e.g. Si and GaAs) even in low concentrations, as they act as deep electronic traps.[78] For perovskites, despite their abundance of point defects due to low formation energy and high surface-to-volume ratio, defects in PQDs are benign to the electronic and optical properties and hardly form deep trap states in the mid-gap region. This defect tolerance is significantly beneficial to the photoluminescence efficiency of PQDs.[79], [80] A comparative illustration of the defects in the electronic properties of conventional semiconductors and
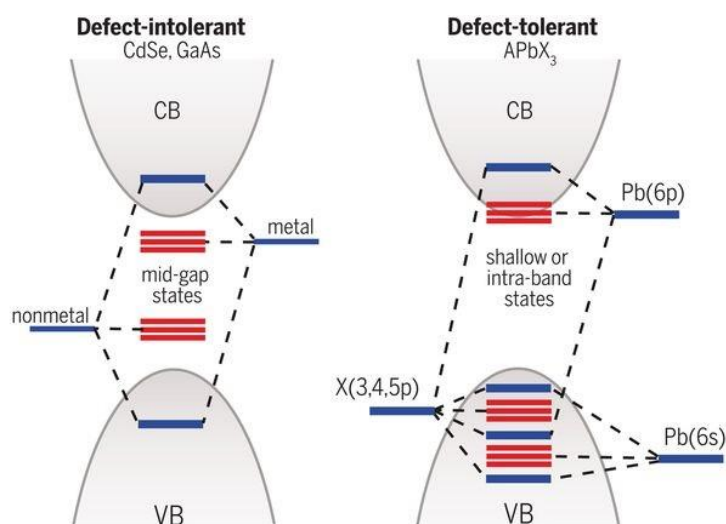

Figure 2.15 Schematics comparison of electronic structures of conventional semiconductors and perovskites, regarding the defect states. The atom with defect fails to form hybridized orbital and remains original atomic orbital with energy level marked as red lines. The defect states of conventional semiconductors locate at the middle of the band gap, while those of perovskite semiconductors lay on the shallow region of the band gap.[81] Reproduced with permission. Copyright 2017, AAAS.

perovskite materials is shown in **Figure 2.15**.[81] The defect states are depicted as red lines in the illustration. In conventional semiconductors, localized nonbonding or weakly bonding orbitals are generated when vacancies or displacements of atoms occur. The defect states are located at the mid-gap region forming trap-states in semiconductors. As the band gap of perovskite originates from two sets of anti-bonding orbitals, the defect states normally reside within or close to the conduction band and valance band. The mechanism applies to the defect states caused by the dangling bonds on the surface of PQDs. These shallow trap states cause minor impairment to the optoelectrical performance of perovskite materials, empowering them with a high defect tolerance.

Perovskite oxides normally demonstrated characteristics of rigid and thermally stable. However, unlike perovskite oxides, metal halide perovskite shows much lower lattice energy due to the fewer charges of the halide ions, resulting in lower formation energy and melting point (e.g. $T_m \approx 570°C$ for $CsPbBr_3$).[82] On the one hand, the ionic bonding feature and low formation energy of metal halide perovskite are favorable for the fabrication process as they enable facile synthesis with the solution process at room temperature. On the other hand, these features are detrimental to the long-term stability of the perovskites in practical applications as it is hard to maintain structural integrity. Moisture and polar solvents can easily lead to decomposition of perovskite or PQDs. Moreover, the bonding between PQD and capping ligand is highly ionic as well, resulting in faster ligand desorption compared to conventional QDs with static covalent ligand binding.[83] Exposing metal halide perovskites or PQDs into ambient conditions comprising oxygen and moisture can also lead to structural decomposition, resulting in a total failure of their optical and optoelectronic behaviors. The low melting point of PQDs limits their applications at high temperatures as well. Therefore, the long-term stability problem is the main obstacle for PQD materials at the present stage. Designing appropriate capping ligands for effective surface passivation and developing a robust barrier matrix with good compatibility for encapsulation are prospective strategies for enhancing the long-term stability of PQDs.

3 State of the Art: Quantum Dots for Color Conversion

This chapter provides an overview of the recent advancements in quantum-dot-based materials and optoelectronic devices, especially for color conversion applications. Focusing on the color conversion of QD materials, a thorough summary and discussion covering the aspects of encapsulation, light management, and patterning methods are carried out. Section 3.1 introduces the challenges and concerns in the practical applications of quantum dots. Section 3.2 delves into the solid-state encapsulation approaches for high-performance QD color converters. In Section 3.3, typical strategies for enhancing luminescence efficiency and light extraction of quantum dots are illustrated. Lastly, patterning methods for the fabrication of quantum dot pixels in micrometer and nanometer scales are introduced and compared.

Acknowledgements and Contributions

3.1   Introduction

As a type of luminescence material, QDs are broadly applied as color and light conversion media in various fields, including illuminations,[85], [86] displays,[87], [88] bio-sensing,[89] luminescent solar concentrators,[90] and farming.[91] In practical applications, QDs are commonly packaged in polymer or inorganic matrixes for enhancing the stability of the materials against environmental stimuli, such as oxygen and moisture.[92], [93] This emitter-in-matrix configuration brings shortages of ligand desorption, aggregation-induced luminescence quenching, and light trapping.[94], [95], [96] Moreover, in the integration of QD materials to optoelectronic devices, film deposition, and patterning methods need to be involved appropriately to meet the demands of fabrication and application. Thus, comprehensive design and engineering covering the aspects of encapsulation, light management, and patterning processes are essential to achieve high-performance optoelectronic devices based on QDs.

Taking display technology as an example, QDs have been adapted into commercial television products as color conversion film in the back-lighting module, resulting in a wide color gamut and high efficiency. Moreover, micro-LEDs, specifically miniaturized gallium-nitride-based LEDs, have seen significant development for high-performance displays in recent years, expected to have widespread applications in active indoor displays and small-sized screens for smart devices.[8], [97], [98], [99], [100] However, efforts are needed to develop efficient approaches for giant transfer and adequate red-green-blue (RGB) colorization solutions for micro-LED display technology.[101], [102], [103] Combining blue-emitting micro-LEDs with QD-based color conversion layers is a promising strategy to achieve full-color display with high manufacturing efficiency.[104] On the one hand, blue GaN LEDs have high luminous efficiency, and manufacturing display panels with a single type of LED chip reduces the technical demands for a giant transfer process, reducing the fabrication cost. On the other hand, incorporating QDs as color converters in micro-LED display panels improves the color accuracy and overall performance of the devices.[105], [106] For realizing high-performance micro-LED displays with the assistance of QDs, several concerns should be addressed. First, from a materials perspective, appropriate solid-state encapsulation is needed for maintaining the luminescence efficiency and stability of QDs. Second, additional strategies for enhancing light conversion and outcoupling are beneficial to the overall efficiency of the devices. Third, to meet the demands of high-resolution display technology, productive and high-precision fabrication methods are demanded for the deposition of RGB QD pixel arrays.

Focusing on the color conversion of QD materials, we here summarize and discuss the up-to-date research on QDs from three perspectives: encapsulation, light management, and patterning method.

3.2   Solid-state encapsulation of quantum dots

Due to the poor resistance of QD materials to water and oxygen, encapsulating QD nanoparticles in a solid-state matrix composed of materials such as polymers, ionic crystals, or inorganic particles for protection is necessary for practical applications. In the encapsulating process, the

surface ligands capping on QDs normally exhibit poor compatibility with the solid-state matrices. Directly mixing or embedding QD materials into these matrices tends to result in uneven dispersion and aggregation due to the detachment of surface ligands, leading to luminescence quenching and degradation of optical properties. It has been demonstrated that reducing the amino ligands on the surface of CdSe QDs causes a significant drop in PLQY from 70% to 18%.[107] Therefore, the uniform encapsulation of QDs within a suitable solid-state matrix is the foundation for QD-incorporated optoelectronic devices.
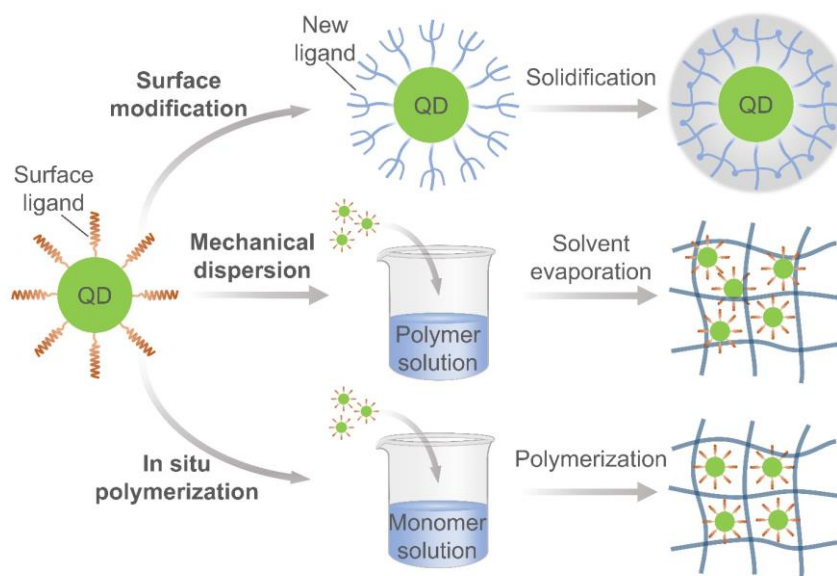
Figure 3.1 Schematic illustration of the solid-state encapsulating strategies of QDs.[84] Reproduced with permission. Copyright 2023, Wiley-VCH.

The existing encapsulating strategies of QDs can be divided into three categories: surface modification, mechanical dispersion, and in situ polymerization. As shown in **Figure 3.1**, the schematics of the three packaging strategies are illustrated. Surface modification methods focus on ligand engineering for improving the affinity between QDs and the hosting matrix or directly employing cross-linkable ligands to create a coating shell. Mechanical dispersion methods directly mix the QD dispersion into a polymer solution via mechanical processes, such as magnetic stirring or sonication. In situ polymerization methods first blend QD dispersion with the monomer solution, followed by a polymerization process of the monomer to form the polymer matrix.

Surface ligands protect QDs from aggregation in the synthesis and enable further bonding connection with encapsulating materials. Surface modification and ligand design are frequently involved in the encapsulation of QDs. Appropriate surface modifications of QDs, such as forming a coating shell or introducing specific functional groups, can enhance the capability of the hosting matrix. Dong et al. developed a QD/polymer composite ink with good dispersibility in water for inkjet printing.[108] As shown in **Figure 3.2** (a-b), a dual-functional group polymer, mercaptopropionic polyethyleneimine (MPPEI), which combines the thiol group of 3-mercaptopropionic acid and the amine group of polyethyleneimine, was introduced to modify the surface of CdSe/CdS/ZnS core/shell/shell QDs. MPPEI minimized the oxidation of the thiol

group and improved the binding affinity of the amino group, thereby providing adequate protection for the QDs. The resulting QD material exhibited excellent resistance to acids, as well as high photostability and thermostability, making it suitable for applications in anti-counterfeiting and identification.
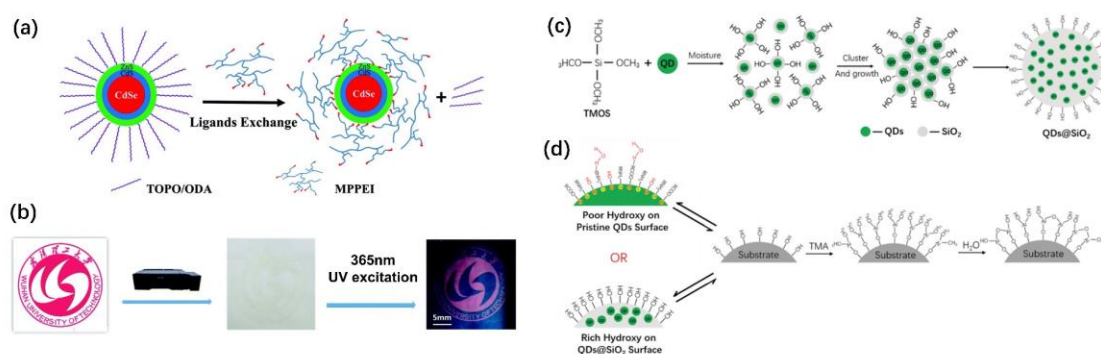

Figure 3.2 (a) Synthesis process of MPPEI-capped QDs, and (b) inkjet printing of MPPEI-capped QDs.[108] Repro-duced with permission. Copyright 2013, Royal Society of Chemistry. (c) Hydrolysis process of QDs@SiO2 composite, and (d) schematic of the deposition of Al2O3 layer.[109] Reproduced with permis-sion. Copyright 2020, Wiley-VCH.

Moreover, the direct crosslinking of the capping ligand can provide compatible encapsulation as well. Wang et al. proposed a packaging method that combines the sol-gel process and atomic layer deposition (ALD) technique to create ultra-stable $QD/SiO_2/Al_2O_3$ luminescent microspheres (QLuMiS).[109] Schematics of this method are shown in **Figure 3.2** (c-d). First, they produced QD/SiO_2 particles by hydrolyzing methoxysilane precursors (also acted as surface ligands of QDs) in a CdZnSeS QD dispersion. An Al_2O_3 coating layer was then grown on the surface of the QD/SiO_2 particles using the ALD technique to obtain QLuMiS. The resulting QLuMiS retained more than 86% of its PLQY after aging for 1000 hours under blue light irradiation at 450 nm with an optical power density of 2000 mW/cm², demonstrating excellent stability. The exceptional stability was attributed to the hydroxyl groups on the surface of the SiO_2 coating, which provided numerous chemisorption sites and facilitated the formation of a dense Al_2O_3 layer during the ALD process, forming robust protection.

Mechanical dispersion is the simplest method for incorporating QDs into a hosting medium. This approach involves using organic solvents that effectively disperse the QDs and dissolve the packaging matrix, serving as intermediates between the QD particles and the protective matrix. After thorough stirring to ensure homogeneous mixing and sufficient evaporation of the organic solvent, the QDs become embedded in the resulting solid-state matrix. There are two types of mechanical dispersion methods: one without the QD synthesis process and one along with QD synthesis.

Mechanical dispersion without QD synthesis is the most straightforward strategy. Kuo et al. utilized toluene and methylene chloride as intermediate solvents to prepare the mixture of $CsPbBr_3$ PQDs with three commonly used polymers: poly(styrene-butadiene-styrene) (SBS), polystyrene (PS), and PMMA.[110] Polymers were directly added into PQD dispersions with common solvents followed by sufficient stirring. Fiber network films were then fabricated from these PQD/polymer composites via electrospinning, as illustrated in **Figure 3.3** (a). The CsP-

bBr$_3$/SBS composite exhibited the best compatibility, with uniform QD dispersion and the highest PLQY. The CsPbBr$_3$/PMMA film demonstrated the greatest thermal stability due to the high glass transition temperature of PMMA. Additionally, the CsPbBr$_3$/PS film showed the best water resistance, retaining 83% of its PLQY value after three months of water immersion.
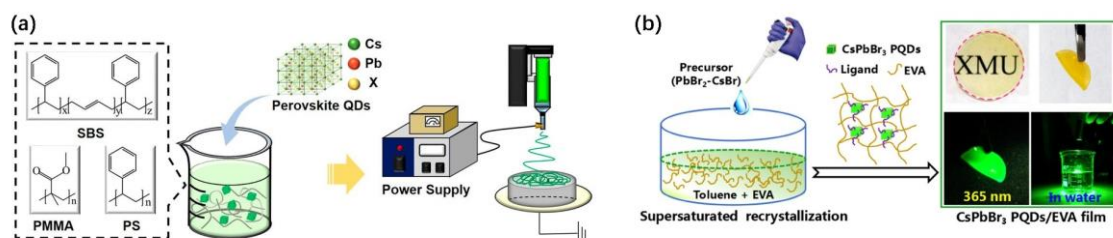

Figure 3.3 (a) Schematic of the fabrication of CsPbX$_3$ (X = Cl, Br, I) nanofiber films.[110] Reproduced with permission. Copyright 2019, The Authors. (b) Fabrication of CsPbBr$_3$ PQD/EVA films incorporating the synthesis process of PQDs.[111] Reproduced with permission. Copyright 2020, Wiley-VCH.

Another strategy that incorporates the synthesis process of QDs into the mechanical encapsulation enables better dispersibility. Chen et al. developed CsPbBr$_3$ PQD/ethylene vinyl acetate (EVA) composite films using a one-step method.[111] As shown in **Figure 3.3** (b), the preparation involved dissolving the EVA polymer in toluene and quickly mixing it with a precursor solution containing PbBr$_2$, CsBr, specific ligands, and DMF solvent. During natural drying, the CsPbBr$_3$ QDs underwent supersaturation and recrystallization, while the EVA matrix solidified simultaneously. The resulting composite films demonstrated excellent performance with a high color purity and a PLQY of 40.5%. Additionally, the PQD/EVA films showed high flexibility and stability, maintaining nearly constant photoluminescence intensity after 1000 cycles of repeated bending.
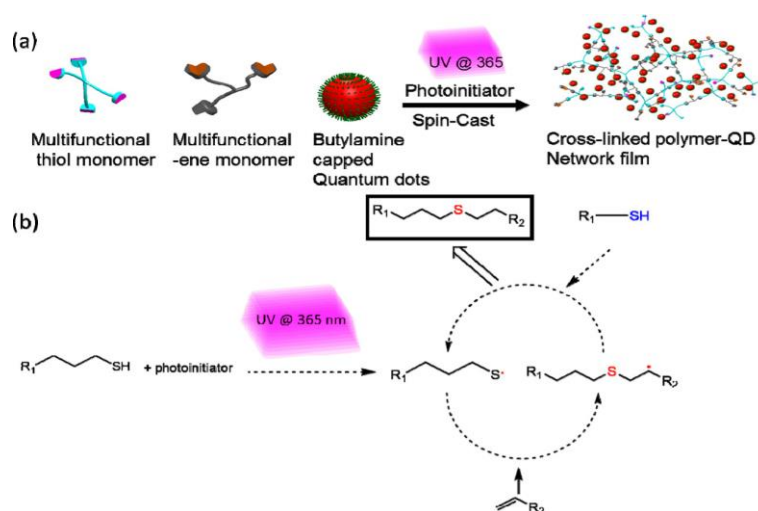

Figure 3.4 (a) Mechanism for fabrication of BAQD/polymer composite, and (b) details of UV-initiated thiol-ene reaction.[112] Reproduced with permission. Copyright 2017, American Chemical Society.

The principle of the in situ polymerization method is to first mix the precursor of polymer with QDs homogeneously, then conduct polymerization of the monomers to form a QD/polymer composite. Thiol-ene photopolymerization is a well-established method for QD encapsulation as

the polymerization is initiated by UV light, which allows for integration with the photolithography process. Tsukruk et al. proposed highly loaded nanocomposite films by combining butylamine-capped CdSe/ $Cd_{1-x}Zn_xSe_{1-y}S_y$ QDs (BAQDs) with high stability using thiol-ene photopolymerization reaction for packaging.[112] The schematic of the packaging method is shown in **Figure 3.4**. The BAQDs have only amine functional groups on their surface, which do not interfere with photopolymerization. Furthermore, the rapid UV polymerization forms extensive crosslinked polymer networks that prevent QD aggregation, allowing for high QD loading of up to 30 wt.%. The resulting composite demonstrated good flexibility, elasticity, and tunable mechanical and thermal properties due to the controllable crosslinking while maintaining excellent optical performance. These composite films were also compatible with nanoimprinting techniques.

3.3 Light management of quantum dot composites

Besides optimizing the solid-state encapsulation for QDs, introducing appropriate microstructures or configurations to QD composites can facilitate their optical performance. A high photoluminescence efficiency originates from the enhanced light outcoupling and better stability can be achieved by optimal configuration of the device.[113], [114] These benefits highlight the importance of light management for the performance of the devices. In addition, different optoelectronic devices raise diverse demands on the QD layers, requesting specific light-manipulating
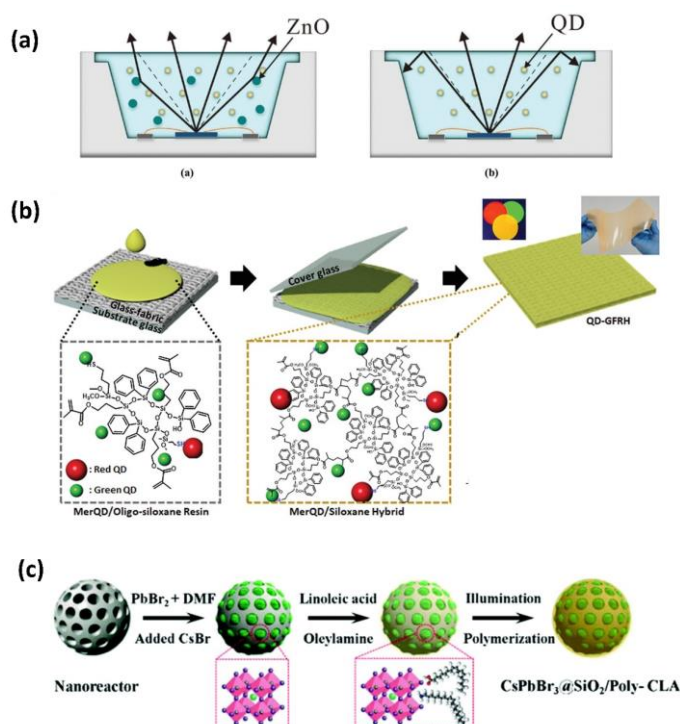

Figure 3.5 (a) Schematic of LEDs with and without ZnO incorporation.[115] Reproduced with permission. Copyright 2018, IEEE. (b) Fabrication procedure of QD-GFRH film via vacuum filling and UV-driven solidification.[116] Reproduced with permission. Copyright 2020, Wiley-VCH. (c) Illustration of the fabrication of $CsPbBr_3/SiO_2$/polymer composite with conjugated linoleic acid.[117] Reproduced with permission. Copyright 2021, Royal Society of Chemistry.

solutions. For instance, display screens for TVs require a broad viewing angle, while some of the screens for cell phones tend to reduce view angles for privacy protection. The introduction of microstructures or surface textures is an effective way for the light management of QD composites. Here, we summarize and divide the relevant studies into three categories: internal scatterers, internal porous structures, and surface structures, for a comprehensive introduction to the existing light management approaches for QD layers.

Internal scatterers make use of the light scattering effect via the embedded materials, such as metal oxide microparticles, and microfibers. The enhanced light scattering elongates the optical path of the excitation light propagating in the QD composite, thus increasing the light absorption and usage rate of QDs. Li et al. embedded ZnO particles in the QD/polymer layer and incorporated them into QD-converted LEDs.[115] **Figure 3.5** (a) illustrates the schematic of QD-converted LEDs with and without ZnO particles, showing that the scattering effect improved blue light utilization and outcoupling of the emitted light. However, they observed a decrease in total radiant flux with excessive ZnO nanoparticle doping, as the ZnO particles oversaturated the absorption enhancement and blocked the emission light. After optimization, a luminous flux enhancement of 3.37% was achieved with QD-converted LEDs containing 0.1 wt.% of ZnO particles. Moreover, a better angular uniformity of the correlated color temperature of the LED within the angular range of -70° to 70° was obtained. Besides, TiO_2 particles and SiO_2 particles have been tested in analogous configurations as well.

Another process that embeds glass fibers into QD/polymer composites was designed by Bae et al. By impregnating thermally and chemically stable QD/siloxane resins into porous glass fibers, a QD-embedded glass-fiber-reinforced siloxane hybrid (QD-GFRH) composite with a high haze value and high stability was fabricated.[116] The fabrication process is illustrated in **Figure 3.5** (b). The haze value of the composite is based on the refractive index mismatch between the siloxane resin matrix and the glass fibers. This approach can effectively improve the light extraction of the QD-GFRH composite. The hazy QD-GFRH composite showed a twofold improvement in light extraction and enhancements in various mechanical properties such as thermal expansion and deformation resistance. In addition, the QDs were chemically dispersed inside the composite via covalent crosslinking with the siloxane matrix, exhibiting superb long-term stability under high temperature (85°C) and high relative humidity (85%) conditions.

Li et al. proposed a method of synthesizing $CsPbBr_3$ QDs mesoporous silica microspheres with conjugated linoleic acid as the ligand for the QDs,[117] as shown in **Figure 3.5** (c). The synthesized QDs could be used as photo-initiators to initiate the polymerization of conjugated linoleic acid to form a hydrophobic polymer coating on the surface of mesoporous silica microspheres to achieve higher stability. The mesoporous silica microspheres acted as scatterers in the system as well as limited the growth and agglomeration of the $CsPbBr_3$ QDs through spatial confinement, resulting in a narrow FWHM of 20 nm and a high PLQY of 79.16%. Owning to the protection of the hydrophobic polymer coating, the improved water resistance of the $CsPbBr_3$ QDs enabled a photoluminescence retention of 77% after soaking in water for a week.

Intense light scattering can be generated by microporous networks as well. Compared to the strategy of mixing scattering particles, the microporous network enables light scattering by the refractive index contrast between the matrix and air void, minimizing the extra light absorption.

27

For instance, when embedding TiO_2 particles as scatterers in a QD film, the excitation light for QDs in the blue or UV wavelength range would be partly absorbed by TiO_2 particles. This part of absorbed excitation cannot be converted to the desired emission light and causes low efficiency. In contrast, a microporous structure hardly brings additional light absorption while creating a sufficient scattering effect.
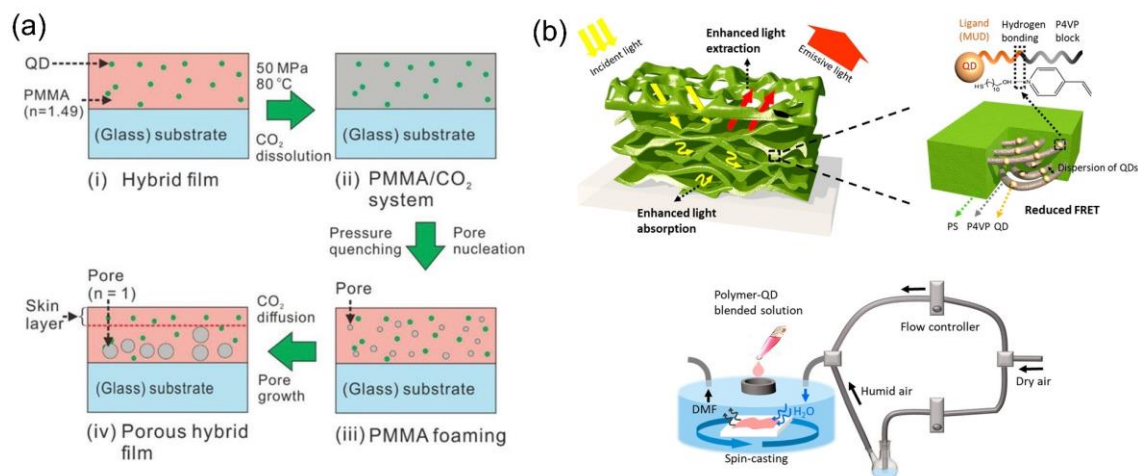

Figure 3.6 (a) Fabrication of microporous QD/PMMA hybrid film by supercritical CO_2 foaming approach.[118] Reproduced with permission. Copyright 2019, Wiley-VCH. (b) Illustration of a randomly porous BCP-QD film with structural features at nano- and micro-scales, as well as the humidity-controlled spin-casting equipment.[119] Reproduced with permission. Copyright 2019, American Chemical Society.

For fabricating the internal porous structure, Yu et al. developed a supercritical CO_2 foaming technique to create a microporous network in PMMA composite film with embedding CdSe/ZnS QDs.[118] The micropores significantly boosted the overall photoluminescence intensity of the QD-based color conversion film compared to a non-porous composite. **Figure 3.6** (a) illustrates the details of the foaming process. With optimization on the porosity, the porous QD film maintained a high transmittance of up to 80% in the visible range and achieved a maximum photoluminescence intensity enhancement factor of 6.6 compared to the non-foamed QD/PMMA film. Ray-tracing simulations indicated that this enhancement results from the extended optical path length of the UV/blue photons in the conversion medium, leading to increased absorption by the QD material. Additionally, the PLQY of the QD composite film was enhanced as the porous network improved light extraction and reduced reabsorption compared to the planar non-foamed composite film.

Moreover, Jung et al. introduced another approach using a poly-(styrene-b-4-vinylpyridine) (PS-b-P4VP) block copolymer (BCP) with an internal porous structure created via a phase separation method.[119] As depicted in **Figure 3.6** (b), controlling humidity allowed the generation of multiscale phase separation features, including micrometer-scale spinodal decomposition between polymer-rich and water-rich phases and sub-10-nm-scale phase separation between polymer blocks. The QD-BCP composite film, featuring a random and hierarchical porous structure, showed a significant improvement in both light absorption and extraction efficiency

due to the scattering properties of the porous structure. A 21-fold enhancement in photoluminescence intensity for the QD-BCP composite film was achieved compared to the pure QD film.

The surface structure strategy involves either adding an extra functional layer or directly creating a micro-/nano-texture on the QD composite. The enhancing mechanism is diverse depending on the specific function of the surface layer. Yang et al. proposed a surface plasmon resonances (SPR) enhanced method, incorporating silica-coated Au nanoparticles and nanorods as fluorescence-enhancing structures into a QD/poly(diallyl dimethylammonium chloride) (PDDA) composite.[120] An electrostatic self-assembly technique was applied for the deposition of the Au plasmon. The configuration of the Au-enhanced QD composites is illustrated in **Figure 3.7** (a). Manipulating the overlap between the SPR wavelength of the Au nanostructure and the absorption band of the QD material brings significant photoluminescence enhancement. By optimizing the size of the Au nanoparticles and the thickness of the silica coating, they achieved fluorescence enhancements of 17.8-fold for the sample with Au nanoparticles and 24.7-fold for the sample with nanorods.
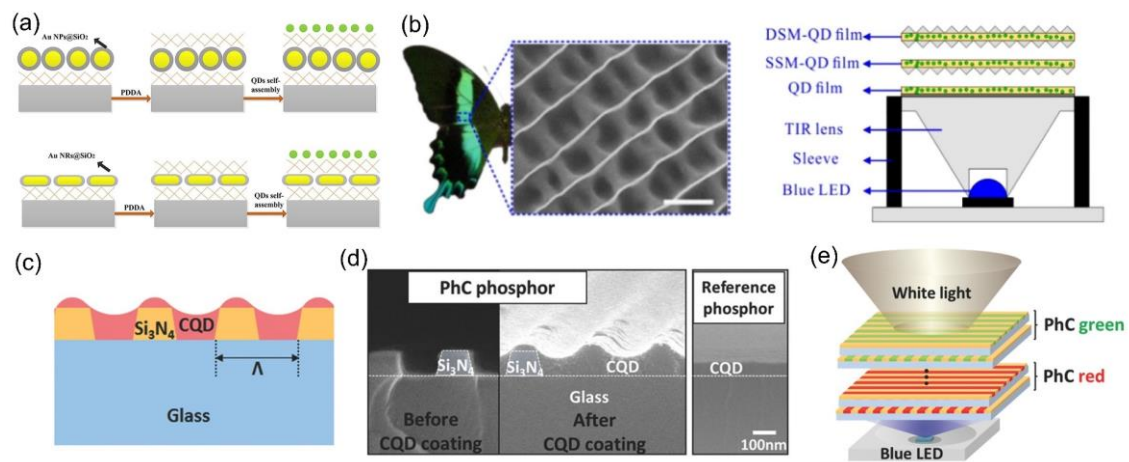

Figure 3.7 (a) Schematics of the assembly of CdSe@ZnS QDs on gold nanoparticles and gold nanorods, respectively.[120] Reproduced with permission. Copyright 2019, Elservier. (b) SEM image of the micro-concave cone structure of Papilio blumei butterfly (scale bar: 10 μm) and the architecture of the LED device.[121] Reproduced with permission. Copyright 2016, Springer Nature. (c) Schematic, and (d) SEM image of QD/PhC structure. (e) White LED built with QD/PhC luminescent layers.[122] Reproduced with permission. Copyright 2017, Wiley-VCH.

Inspired by nature, Yu et al. designed a micro-concave-cone array (MCA) that mimics the surface texture of the wings of a phoenix butterfly.[121] They incorporated this structure into a QD composite film with single-sided and double-sided configurations, as shown in **Figure 3.7** (b), to enhance the color conversion efficiency of QD-LEDs. The MCA composite demonstrated higher reflectance and lower transmittance (21% and 75%, respectively) when light impinged from the plane side compared to light impinging from the textured side (5% and 95%, respectively). Consequently, the color conversion efficiencies of the single-sided and double-sided LEDs increased from 20.0% to 21.6% and 21.8%, respectively. This improvement is attributed to the scattering effect and light recycling effect of MCA.

A more delicate structure was developed by Jeon's research group. A 1D photonic crystal (PhC) composed of silicon nitride as the high-index medium was introduced, filled with dense colloi-

dal QDs as the fluorescent low-index material.[122] They fabricated the PhC structure through photolithography and reactive ion etching. CdSe colloidal QDs were subsequently spin-coated onto the PhC structure. The design details are shown in **Figure 3.7** (c-e). By stacking red and green PhC phosphor plates to build a white LED, they achieved an 8% increase in total emission intensity while using 33% less QD material compared to the reference device.

3.4   Patterning approaches for quantum dots

Thin film deposition, patterning, and pixelation of QD composites are commonly needed when being employed in optoelectronics. Particularly, multiple deposition methods might be utilized for fabricating a QD-incorporated device. Compared to conventional phosphors, the superior solution processibility of QD material contributes to good compatibility with various patterning or film depositing processes. It largely broadens the potential of applying QDs in commercial products. In this stage, the printing method, lithography method, and transfer printing method are the most general patterning approaches for QDs.
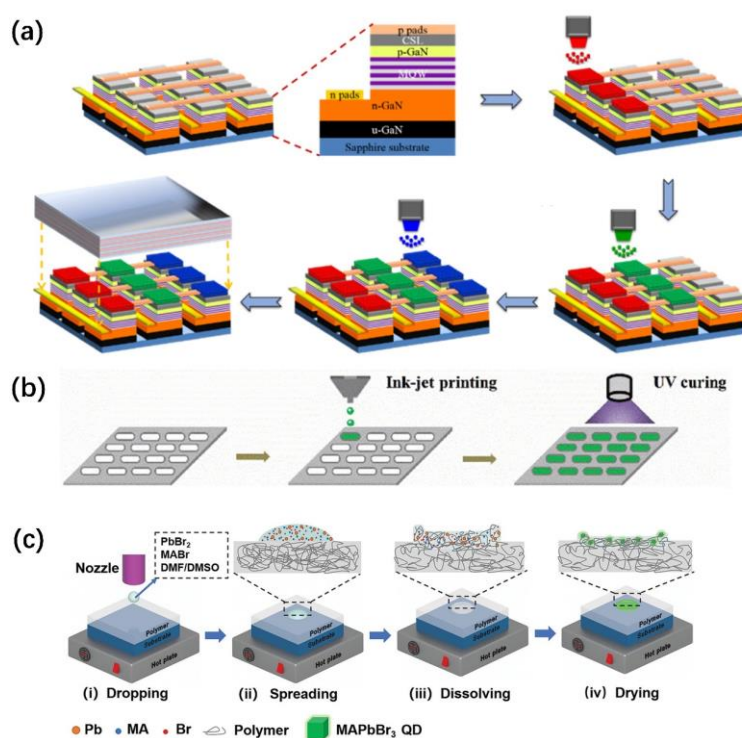
Figure 3.8 (a) Fabrication process of full-color micro-LED display via aerosol-jet printing QDs.[123] Reproduced with permission. Copyright 2015, Optica Society. (b) Illustration of inkjet printing PQD color conversion pixels using UV-curing ink.[124] Reproduced with permission. Copyright 2019, Wiley-VCH. (c) Schematics of the in-situ inkjet printing strategy for PQDs.[125] Reproduced with permission. Copyright 2019, Wiley-VCH.

Aerosol-jet printing and inkjet printing are two types of promising printing technologies, which have been successfully used to produce various electronic devices. In 2015, Kuo et al. introduced a backlight-free full-color LED display strategy by combining UV micro-LED technology with aerosol-jet printing QDs.[123] As illustrated in **Figure** 3.8 (a), printing parameters includ-

ing working distance, stage speed, and gas flow rate, were optimized for successfully spraying RGB QDs onto a micro-LED array with a line width of 35 μm. This process resulted in a full-color display panel with a resolution of 282 pixels per inch. In device building, a photolithography process was introduced to create a rectangular micro-well array structure to confine the printed QDs, reducing optical crosstalk and the coffee ring effect. This modification decreased the crosstalk rate of the micro-LED panel from 32.8% to nearly zero.

Instead of applying gas flow for spraying QD ink, inkjet printing technology ejects QD ink by use of the piezoelectric effect, causing less gas turbulence. Duan et al. prepared printable PQD inks by dispersing $CsPbBr_3$ PQDs in a UV adhesive and used a mold-assisted inkjet printing process to prepare the color conversion layer.[124] The fabrication process is depicted in **Figure 3.8** (b). This technique produced a 6.6-inch active matrix PQD display prototype with a resolution of 384×300, combined with a blue OLED backlight. The device demonstrated high stability, with light conversion efficiency decreasing by only 1.4% after 30 days of exposure to air and moisture without additional protection. To obtain better dispersibility of QDs, Zhong et al. combined in situ synthesis with inkjet printing that directly deposits a perovskite precursor solution onto polymeric substrates to create PQD pixels.[125] As illustrated in **Figure 3.8** (c), the PQD precursors were dissolved in DMF or DMSO solvents to form the ink, which was then printed onto the heated polymer film. After the solvent evaporated, PQD pixels were formed. This cost-effective, large-area printing technique achieved PQD patterns with a PLQY of up to 80%. This method demonstrated broad applicability across various PQD materials and polymers, such as polyacrylonitrile, PMMA, polystyrene, polyvinyl chloride, and polyvinylidene fluoride.
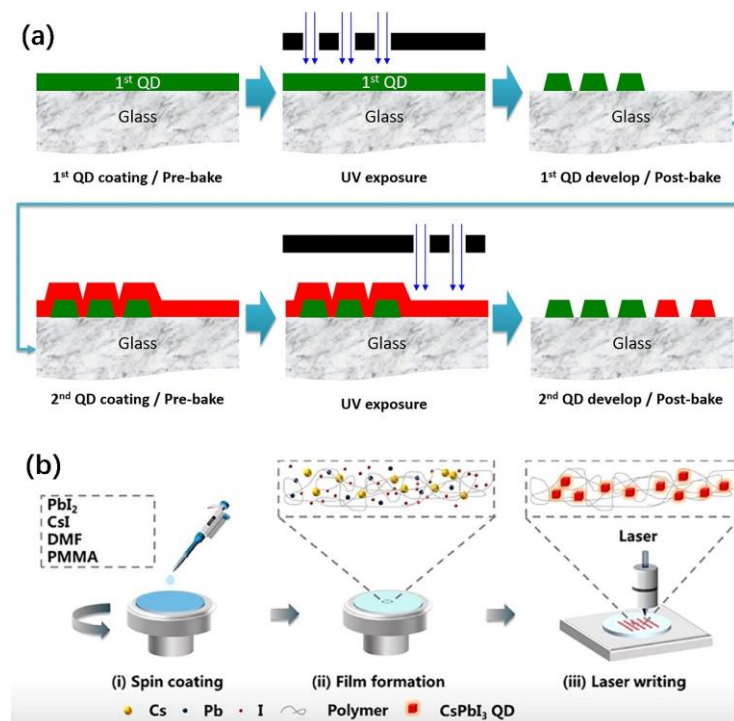

Figure 3.9 (a) Fabrication process of green and red QD pixel arrays on the same substrate via repeating photolithography.[126] Reproduced with permission. Copyright 2019, Society for Information Display. (b) Laser writing fabrication integrated with in situ synthesis of pixelated $CsPbI_3$ PQDs.[127] Reproduced with permission. Copyright 2021, American Chemical Society.

In 2019, Jang et al. developed a UV-curable QD photoresist using the mechanical dispersion method. They mixed QDs with resin, curing agent, additives, and a photo-initiator in a common solvent. Through sequential photolithography processes, as shown in **Figure 3.9** (a), they fabricated a full-color QD color conversion layer with high pixel resolution for a micro-LED display.[126] By optimizing the QD photoresist formulation, they achieved pixelated QD patterns with dimensions of 10 μm × 10 μm and a minimum thickness of 12 μm. Besides, many other types of lithography methods, including X-ray lithography and laser lithography, have been adopted for fabricating QD pixels. For example, leveraging the difference in thermal conductivity between PQDs and polymer encapsulation matrix, Shi et al. used a 405 nm nanosecond laser as a light source to perform direct laser writing on a polymer film containing the precursors of $CsPbI_3$ PQDs,[127] as illustrated in **Figure 3.9** (b). This process resulted in a fluorescent PQD grating with a period of 4 μm and a PLQY of up to 92%. By adjusting the laser power and scanning speed, the line width of the pixelated $CsPbI_3$ PQDs could be controlled, achieving a minimum line width of 900 nm.
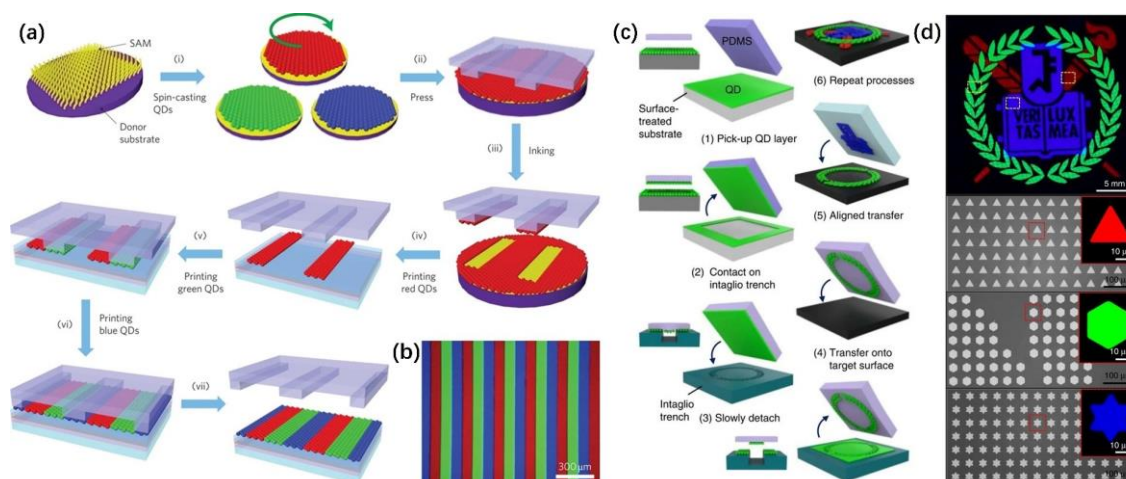
Figure 3.10 (a) Illustration of the transfer-printing process for QD pixelation, and (b) fluorescence micrograph of transfer-printed QD stripes under UV light.[128] Reproduced with permission. Copyright 2011, Springer Nature. (c) Schematic of the intaglio transfer-printing process, and (d) SEM and fluorescence images of RGB QD pixels created through multiple aligned transfer printing.[129] Reproduced with permission. Copyright 2015, The Authors.

Transfer printing encompasses a set of techniques that involve assembling a material onto a pre-structured surface or into a specific spatial arrangement, followed by transferring the patterned material layer to the final substrate. For QD pixelation, the critical aspect of this process is developing effective assembly and transfer strategies with good control of the affinity between the master template and the substrate for QD materials. Choi and Kim et al. demonstrated a full-color, large-scale transfer printing technique for QD-based displays using a relief printing form.[128] The process flow and obtained QD micropattern are shown in **Figure 3.10** (a-b). In this process, a uniform QD layer was spin-coated on a substrate with low surface energy, which had been chemically modified to facilitate delamination at the interface. Since the surface energy of PDMS is slightly lower than that of the modified substrate, the QD layer is partially picked up by the protruding stripes of the textured PDMS stamp. Then the QD stripes are transferred and horizontally stacked onto a receiving substrate to form full-color QD micro-strips.

This solvent-free transfer printing process can create large-scale QD-based optoelectronic devices with well-ordered micropatterns. Based on another mechanism, Hyeon et al. introduced an intaglio transfer printing technology to fabricate RGB QD pixels with a resolution of up to 2460 pixels per inch.[129] As illustrated in **Figure 3.10** (c-d), the QD material was initially spin-coated onto a pre-treated silicon substrate. A planar PDMS stamp was then used for the rapid pickup (10 cm/s) of the QD layer. This layer was transferred and pressed onto a structured intaglio trench at low pressure and slowly detached, leaving a patterned QD layer on the PDMS stamp. This QD pattern was then transferred to the target substrate. By repeating the transfer printing process, a full-color pixelated QD layer was achieved. Compared to the relief printing form, the intaglio transfer printing process showed superior printing accuracy and transfer yield.

Tremendous efforts have been dedicated to developing high-efficiency QD materials and promoting QDs to commercial products. The research works mentioned above are only some representative spots of the full picture of QDs. Demanding challenges, such as inadequate long-term stability, high toxicity of some QDs and organic solvents, and low production efficiency of QD patterning, yet remain unsolved and need to be particularly addressed in the future.

4 Materials, Methods, and Characterizations

In this chapter, the materials, methods, and characterizations applied in the dissertation are demonstrated and discussed. In Section 4.1, detailed information about the materials, including formulations of quantum dot (QD) dispersions, is provided. Section 4.2 outlines the methods employed to fabricate the samples and devices in the dissertation. In Section 4.3, the principles and operations of the characterization approaches used investigation are explained.

4.1 Materials

QD materials applied in *Chapter 5* were CdSe/ZnS core-shell QD powders bought from Beida-Jubang Science and Technology, with emission peak wavelengths at 465 nm, 545 nm, and 627 nm, respectively. Poly (methyl methacrylate) (PMMA) powders with a mean molecular weight of 350,000 Da and toluene solvent (anhydrous, 99.8%) were purchased from Sigma-Aldrich. A UV-emitting LED chip was bought from Nichia (NCSU276A) with an emission peak wavelength of 365 nm.

For the fabrication of microporous QD/polymer composite in *Chapter 6*, polystyrene (PS) with a mean molecular weight of 100,000 Da, polyethylene glycol (PEG) with a mean molecular weight of 200 Da, chloroform (anhydrous, 99%), 1,2-dichlorobenzene (anhydrous, 99%), and titanium dioxide nanoparticles (mean diameter: 200 nm) were brought from Sigma-Aldrich. CdSe/ZnS core-shell QD from Beida-Jubang Science and Technology were applied. Dispersant (DISPERBYK 2190) was utilized for the surface modification of titanium dioxide nanoparticles. Polydimethylsiloxane (PDMS, SYLGARD 184) material was purchased from SYLGARD. UV-emitting LED chip (UV-SMD-LED 3535) with a peak at 365nm was obtained from LG Inc.

For the preparation of PQD scintillators in *Chapter 7*, cesium bromide (CsBr, 99%), lead bromide (PbBr$_2$, 99%), pentanedioic anhydride (PA, 95%), aminopropyltriethoxysilicone (APTES, 95%), oleic acid (OA, 90%), oleyl amine (OLA, 90%), and polystyrene (PS, 96000 Da) were ordered form Sigma Aldrich. Solvents including N, N-dimethylformamide (DMF), tetrahydrofuran (THF), methylene chloride (DCM), and toluene were of analytical grade. All the chemical reagents were directly used in the synthesis process without additional purification. In the imaging tests, a standard X-ray line-pair test pattern (PTW L659035), objectives from Newport Corporation, and a monochrome CMOS camera (DMK21BZU04) from Imaging Source were used.

4.2 Methods

Preparation of QD/polymer mixture solutions

A mechanical dispersing method was applied to prepare the mixture solutions by composing QD nanoparticles, polymer, and organic solvent. QD powders were first weighed with the desired amount and then added into an organic solvent (e.g. toluene, chloroform). By conducting 2h of magnetic stirring, a dispersion of colloidal QDs was obtained. Polymer materials (e.g. PMMA, PS, PEG) with corresponding amounts were added to the QD dispersion followed by 4h of magnetic stirring to mix QDs and polymers in the solution homogeneously. In this process, multiple types of QDs (e.g. red, green, and blue QDs) can be mixed in one solution for white-light color conversion. Different polymers can be blended in the same solution as well. In *Chapter 6*, polymer blends of PS and PEG were added to common solvents for generating porous QD composites. Moreover, an excessive concentration of QDs could lead to aggregations in the mixture solution, which should be prevented.

Drop-casting

To obtain the color conversion films, a drop-casting method was applied for the film deposition. Before drop-casting, glass substrates were pre-cut to the desired size, followed by sequential ultrasonic baths for 10 min in acetone and isopropanol, respectively. O_2 plasma treatment was conducted on the cleaned glass substrates to increase their surface energy and wettability. For the film deposition, the prepared QD/polymer solution was dropped directly on the glass substrate by pipette and left in a fume hood for 6 h for solvent volatilization and solidification. Petri dishes were employed as covers on the samples during solvent volatilization to prevent turbulence from ambient gas flow. By varying the casting volume and the concentration of polymer in the solution, the thickness of the consequent QD films can be well adjusted. In some cases, high temperatures need to be introduced to accelerate solvent volatilization. It can be achieved by simply performing the solvent volatilization process on a hotplate or conducting the volatilization in an oven.

Inkjet printing of QD pixels

The mixture solution of QDs and polymer can be conveniently adapted to the inkjet printing process. An inkjet printer (PixDro LP50) was applied here for the printing. Different from the drop-casting process for film deposition, due to the miniatured size of the ink droplets and high jetting speed, the solidification of the QD/polymer solution would be largely accelerated in the inkjet printing process. To prevent nozzle clogging, organic solvents with a high boiling point (e.g. 1,2-dichlorobenzene with a high boiling point of 180.2 °C) were preferred for ink preparation. To reduce the surface energy of the substrate, a thin PDMS layer was spin-coated on a glass substrate with a spinning speed of 2000 rpm for 30 seconds and then solidified on a hot plate at 100 °C for 10 min. During the inkjet printing process, the nozzle was maintained at a temperature of 27°C, while the substrate was kept at 25°C. The printing resolution was set to 200 dots per inch. To reach the desired thickness and size of the QD pixels, each sample underwent multiple printing passes.

Fabrication of CsPbBr3 PQD films

The fabrication of CsPbBr$_3$ PQD film consists of three parts: the synthesis of APTES-PA ligands, the synthesis of CsPbBr$_3$ PQD dispersion, and the deposition of CsPbBr$_3$ PQD film. In synthesizing APTES-PA ligands, 5 mmol of glutaric anhydride was first dissolved in 10 mL of tetrahydrofuran. Then, 5 mmol of APTES was gradually added while stirring at 65 °C. After 12 h of reaction time, the red crude product was obtained and extracted using a rotary evaporator. The red product is the APTES-PA ligands and could be used directly. This amidation reaction exhibited a high yield of over 95%, eliminating the need for further purification.

For synthesizing CsPbBr$_3$ PQD dispersion, precursors of CsBr and PbBr$_2$, as well as ligands of APTES and APTES-PA, were dissolved in DMF solvent with 30 min of magnetic stirring. Subsequently, the obtained solution was rapidly injected into a nonpolar solvent (toluene) to recrystallize CsPbBr$_3$ QDs at room temperature. The injection process was conducted during continuous magnetic stirring to ensure sufficient mixing of good and poor solvents. The PQDs were stabilized and passivated by the capping ligands in the solution with nice dispersibility.

The prepared PQD dispersion was then applied for the film formation without an additional centrifuge process. The PQD dispersion was drop-cast on clean glass substrates and subsequently heated in a vacuum environment at 65 °C for 10 min. During the heating, the solvent evaporated and the trace water in the solution triggered hydrolysis reactions among the ligands, forming the organosilicon matrix spontaneously. After the heating process, CsPbBr$_3$ PQD films were coated on the substrate.

White LED devices

White LED devices comprise an LED pumping chip (UV- or blue-emitting), QD color conversion layers, and a holder to package the whole devices. The fabrication of the holder can be achieved by a Prusa 3D printer with polylactic acid filament. The commercially available LED chip with UV or blue emission was first fixed on the bottom of the holder as a pumping source. The cable of the LED chip was guided out through the holes on the holder for the connection with the electric source. The prepared QD films were then mounted onto the holder to form a remote phosphor configuration. Normally, the UV LED chip was combined with red, green, and blue (RGB) QD films and the blue LED chip was coupled with red and green (RG) films to generate white light, as shown in **Figure 4.1**. The arrangement of the QD films with multiple colors can be vertical or horizontal stacking. Directly mixing multi-color QDs in a film is feasible as well.
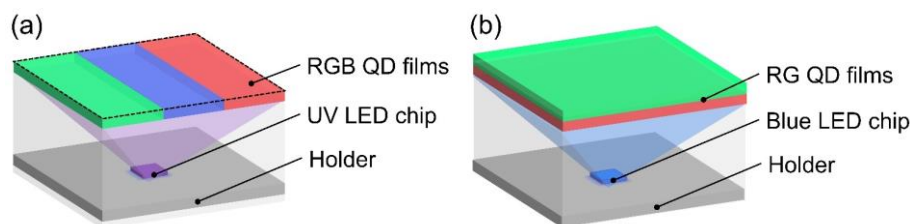

Figure 4.1 Configurations of white LED devices with the combination of (a) UV LED chip with RGB QD films, and (b) blue LED chip with RG QD films.

4.3 Characterizations

UV-vis-NIR spectrometer

A UV-vis-NIR spectrometer (Lambda 1050, PerkinElmer Inc.) equipped with a 150 mm integrating sphere was applied to characterize the transmittance, absorption, reflectance, and haze spectrum of the samples. In this system, the light source (e.g. halogen lamp) is first spectrally divided by an optical grating and selected through a slit. The selected light is then split into two beams. The sample to be measured is placed in the path of one of the beams, while the other beam serves as a reference. With the photodetector in the integrating sphere, the transmittance or reflectance values are obtained by calculating the ratio of the detected intensities of the sample beam to the reference beam. The absorptance of the samples was then calculated using the transmittance and reflectance values. Transmittance and reflectance spectra within the wavelength range from 175 nm to 3300 nm are measurable using this system.

Besides, diffuse transmittance can be obtained by allowing the direct transmittance to escape from the integrating sphere (by opening the back lid). Haze value is acquired by calculating the ratio of the diffuse transmittance to the total transmittance. By introducing a rotatable sample holder and fixing the sample in the center of the integrating sphere, angle-resolved reflectance measurement can be conducted. The back side of the sample should be painted black to absorb the transmitted light when measuring angle-resolved reflectance.

Integrating sphere

The luminous fluxes of the LED devices were measured using an integrating sphere system with a diameter of 20 cm. The inner surface of the integrating sphere is coated with a white barium sulfate layer to provide effective diffuse reflectance within the spectral range of 350-2400 nm. In the measurement, the LED device is positioned at the entrance opening with a designed holder and manipulated electrically by a current source. The emission of the device is collected and homogenized by the integrating sphere and detected by an external spectrometer (CAS140CT, Instrument Systems GmbH) through glass fiber. Calibration with a luminous flux standard (halogen lamp, Techno Team GmbH) has been conducted to measure the absolute value of the luminous flux of the sample.

PLQY measurement system

The PLQY and light absorption of QD samples were characterized using a custom-built optical system based on a 3M procedure.[130], [131] The principle of the measurement system is illustrated in **Figure 4.2**. A laser diode (DL-7146-101S, Roithner Lasertechnik GmbH) with a peak wavelength of 405 nm serves as the excitation source. The emitting power of the laser diode is adjusted by a controller (ITC4001, Thorlabs GmbH) and the laser power is set to 101 µW for the measurements. An integrating sphere with a diameter of 150 mm (Lab sphere) and a CCD spectrometer (AvaSpec-ULS2048x64-TEC, Avantes BV) are employed for detecting the spectrum and light power in the integrating sphere. A variable density filter is placed between the laser diode and the integrating sphere to adjust the laser power that enters the sphere. During measurements, the QD sample is positioned in the center of the integrating sphere using a white

holder, which can be rotated to meet the requirements of the 3M measuring procedure. Light absorption and PLQY value of the QD sample can be calculated using the detected spectra.
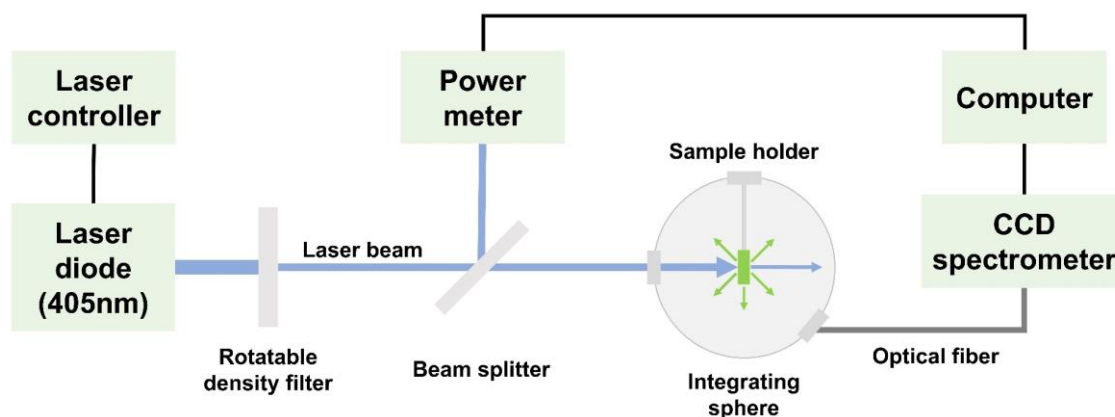

Figure 4.2 Illustration of the measurement system for PLQY and light absorption of QD samples.

Angular light intensity measurement system

For characterizing the angular intensity distribution of the transmitted light through a solid thin film, a measurement system was built consisting of a UV-vis-NIR spectrometer (HR2000CG-UV-NIR, Ocean Optics), a red laser diode (peaks at 640 nm), and a rotary stage driven by a motion controller (SMC 100PP, Newport). The schematic illustration of the system is shown in **Figure 4.3**. In the measurement, the sample film is fixed at the center of the rotary stage, which also holds the red laser diode. The laser beam is pointing at the sample film vertically. The spectrometer, positioned outside the rotary stage and fixed, collects the intensity of the transmitted light at each rotation step. During the measurements, the stage rotated in 2.5° increments from 0 to 90 degrees for the off-axis angle. The laser diode, sample film, and spectrometer are carefully aligned before measurement and the entire measurement is conducted in a dark environment. By integrating the spectra detected at different angles, an angular distribution curve of the intensity of the transmitted light can be plotted to demonstrate the scattering capability of the sample film.
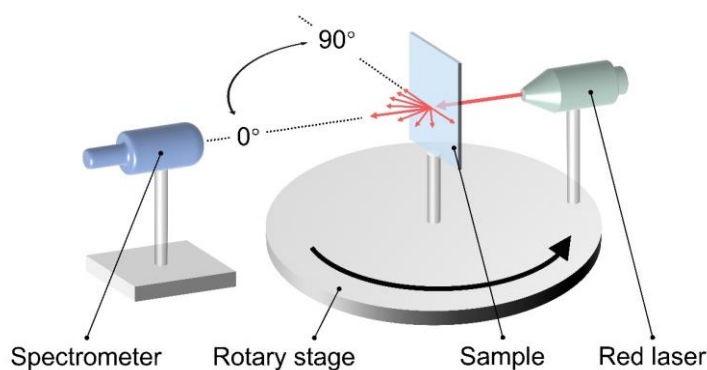
Figure 4.3 Illustration of the measurement system for angular intensity distribution of transmitted light.

X-ray imaging system

The X-ray imaging system was built with an indirect configuration for detection. In this configuration, the scintillator film serves as a functional layer to convert X-ray to visible light that is detectable for CMOS cameras. In this imaging system, as demonstrated in **Figure 4.4**, a 3D-printed holder is applied to fix the scintillator film. X-ray radiation hits the scintillator film first in the measurement. An objective lens (4× or 10×, Newport Corporation) is mounted on a linear stage behind the sample holder for magnification. The liner stage is applied to adjust the focus position, enabling a precise focus on the scintillator film. A mirror was fixed behind the objective lens to reflect the converted visible light to a monochrome CMOS camera (DMK21BZU04, Imaging Source) to accomplish the imaging process. The camera has a pixel size of 5.6 μm × 5.6 μm. The introduction of the mirror avoids the direct hitting of the X-ray on the camera, inhibiting the noisy flashing dots on the obtained image significantly. The camera is fixed on another linear stage for aligning and finding focus. As the X-ray imaging test would be conducted in a dark room, additional cover is unnecessary.
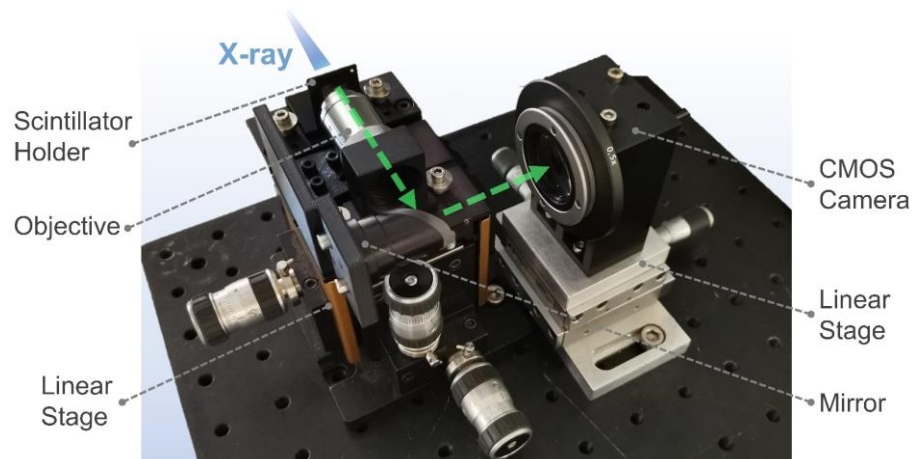
Figure 4.4 Photograph and annotations of the X-ray imaging system.

Optical microscopy

An optical microscope (Axioplan 2, Zeiss) is employed to take images of microstructure. The objectives of the microscope with the desired magnification can be chosen. Images are captured by a CCD camera (AT AxioCam ICc R3, Zeiss). The exposure time and image contrast of the microscope are automatically controlled by the ZEN core software. In brightfield microscopy, a white light source is applied to illuminate the sample. For taking fluorescent microscope images, an additional light source (blue or UV) is equipped to excite the QD sample in a dark environment.

Atomic force microscopy

To characterize the surface morphology of the samples, atomic force microscopy (AFM) (nanoWizard II, JPK) was employed. A cantilever with an extremely sharp tip is equipped in the AFM system to probe the surfaces of samples. In the measurement, a laser beam is pointed at the cantilever and reflected to a CCD array. Owing to the atomic forces between the tip and the

sample surface, the cantilever deflects the path of the laser beam, which can be converted to electronic signals by the CCD array for reconstructing a 3D image of the surface. Quantitative analysis, such as the surface root-mean-square roughness, can be obtained by data processing software (Gwyddion). Thus, both qualitative and quantitative information on various physical properties, including size, morphology, surface texture, and roughness are approachable by this method.

5 Wavelength-selective Reflector for Light Extraction of Quantum Dot Layers

This chapter focuses on the fabrication of wavelength-selective reflectors based on silver nano-particles and the integration of the reflectors into quantum-dot-enhanced white light-emitting diodes to improve light extraction. By manipulating the structure and morphology of the silver nanoparticles, the optical response of the reflector, such as the reflection spectrum, can be adjusted to fit the demand of the optoelectronic device. First, Section 5.1 discusses the obstacles of high-performance white light generation with quantum dots and the mechanism of enhancing light outcoupling. Section 5.2 introduces the fabrication process of the reflector and the influence of the critical parameters in the fabrication. In Section 5.3, the optical properties of the reflectors are characterized. Subsequently, the investigation of the reflector into white light-emitting diodes is illustrated and discussed in Section 5.4. Lastly, Section 5.5 draws a conclusion and summary to the whole chapter.

Acknowledgements and Contributions

5.1 Introduction

Light-emitting diodes (LEDs) have garnered significant attention from both the scientific and commercial sectors due to their high efficiency, long lifetime, and compact design.[85] White LEDs (WLEDs) that combine UV or blue LEDs with color conversion phosphors have been widely applied in illumination and display applications.[133] The configuration that applies blue LEDs with red and green phosphors for white light generation is the most common, due to the high efficacy of blue LED chips. However, this design contains intense blue emission, which poses a risk of retinal injury.[134] Moreover, it is relatively difficult to achieve a proper balance between red, green, and blue emissions with this configuration, limiting its optical performance.[135] Conversely, UV-pumped WLEDs can provide superior color rendering indices and more balanced emission spectra, thereby mitigating the hazards caused by excessive blue light.[136] Nonetheless, UV-pumped WLEDs exhibit lower luminous efficiency compared to blue-pumped WLEDs. The key to increasing the efficiency of UV-pumped WLEDs lies in optimizing the performance and light extraction of the color conversion layer.

QD color conversion layer is an ideal option for UV-pumped WLEDs owing to their high PLQY, high color purity, and superior processability.[3], [137] In practical applications, QDs are normally encapsulated by a polymer matrix or sandwiched between barrier layers to enhance their environmental stability and lifetime.[86] Despite significant advancements in QD materials, effective light management in the QD film remains a challenge that limits the optical performance. For illumination and display applications, isotropic emitting light of QDs is difficult to extract to the forward direction, thereby diminishing the luminous efficiency of the devices.[138], [139] Consequently, facilitating efficient excitation of the QD color conversion layer becomes imperative for QD-enhanced WLEDs.

Various approaches, including utilizing surface plasmon resonance,[120], [140] introducing micro-porous structure,[118], [119], [141] and particle doping,[115], [142] have been explored to enhance the color conversion efficiency of QD layers. Recently, distributed Bragg reflectors have been investigated for their potential to improve light management by recycling backward emissions from QD films.[143] These distributed Bragg reflectors were engineered to permit high transmittance of the excitation light while maintaining high reflectance of the backward converted light. However, the sequential deposition of DBR stacks is time-consuming and costly.[144], [145] In addition, DBRs exhibit angle-dependent reflection spectra, potentially inhibiting the angular uniformity of the emission of WLEDs. Similarly, by utilizing the wavelength-selective reflection, a thin silver film was employed to confine QD-converted light within the QD-based solar concentrator.[142] Nevertheless, the wavelength selectivity of a flat silver film was not optimal. Alternatively, plasmonic color filters have higher compactness and tolerance for viewing angle.[146] Several low-cost fabrication methods, such as nanoimprinting and solid-state dewetting, have emerged to produce economical plasmonic color filters, showing good potential to be integrated into QD-enhanced WLEDs.[147], [148]

In this chapter, we develop wavelength-selective reflectors (WSRs) based on the nanocomposite structure comprising silver and titanium dioxide (Ag/TiO$_2$) for enhancing the forward emission of QD color conversion layers. This reflector demonstrates high optical transmittance in the UV-blue spectral ranges, along with high reflectance among the green and red wavelength

ranges. Initially, we focus on optimizing the solid-state dewetting process for forming a mono-layer of Ag nanoparticles. Subsequently, we demonstrate that by adjusting both the size of the formed Ag nanoparticles and the thickness of the TiO$_2$ coating layer, the transmission and reflection characteristics can be altered. This property is utilized to enhance the excitation of QDs and the extraction of the emitted long-wavelength photons. Consequently, this approach is applied to a QD-enhanced WLED based on UV excitation, which shows a remarkable enhancement in forward emission intensity compared to the reference devices.

5.2 Fabrication of wavelength-selective reflectors

The origin of the wavelength-dependent response of the reflector lies on the localized surface plasmon resonance of the metal medium. To obtain localized surface plasmon, the metal layer is commonly patterned into nano- and micro-structures, including grating structure, nanodisk array, nanohole array, and hybridized nanodisk/nanohole array.[146], [149], [150] The optical performances of the WSR can be altered by manipulating the morphology of the nanopattern. However, the fabrication of a metal layer with an ordered and periodic nanostructure is time-consuming and costly. As we are aiming at applying the WSRs in QD-enhanced illumination or display devices with relatively large sizes, the fabrication approach for WSRs needs to be large-scale and cost-effective, while maintaining adequate control for the optical properties. Recently, disordered metallic structures have gained wide attention and show great potential, due to their lower production cost for generating vivid plasmonic color.[151], [152], [153] Fabrication approaches, such as laser writing,[148] self-assembly method,[154], [155] and solid-state dewetting,[156], [157] have been applied for the fast formation of the disordered metallic nanostructure. Moreover, the optical properties of the plasmon layer can be regulated by tailoring the disordered structure. Thus, a disordered plasmonic structure is an ideal solution for the design and fabrication of WSRs.

5.2.1 Configuration and fabrication process

As a cost-effective method, solid-state dewetting is selected to fabricate the metallic nanostructure of the WSR. Typically, solid metallic thin films are metastable or unstable when they are in the as-deposited state. At a high temperature, the solid thin films tend to undergo a dewetting or agglomeration process to form island structures, driven by the minimization of surface energy. This process can be achieved through the surface diffusion phenomenon at a temperature significantly below the melting point of the material, particularly when the films are rather thin. Silver is a widely applied material for localized surface plasmon resonance plasmon.[158] By thermally dewetting a flat Ag thin film, a monolayer of separated Ag nanoparticles with disordered distribution can be obtained. Besides, coating a dielectric material on top, such as titanium dioxide (TiO$_2$), enables the adjustment of the refractive index of the surface of Ag nanoparticles, offering the second dimension to regulate the optical performance of the WSR. Based on this strategy, we propose a method for the low-cost fabrication of the WSRs.

The schematics of the fabrication processes of the WSR are illustrated in **Figure 5.1** (a)-(c). First, a flat Ag layer with a thickness of several to tens of nanometers is deposited on a glass substrate via the thermal evaporation method. Subsequently, the sample is annealed at 400°C for 5 minutes in a nitrogen atmosphere, inducing solid-state dewetting of the flat Ag layer to form a monolayer of disordered Ag nanoparticles with varying diameters, driven by surface energy minimization. Lastly, a thin TiO_2 coating layer with a higher refractive index is deposited onto the surface via electron beam evaporation, resulting in a core-shell structure for the Ag/TiO_2 composite. The used glass substrates have been sequentially cleaned in ultrasonic baths with acetone and isopropanol for 10 min, followed by 3 min of oxygen plasma treatment before the fabrication.
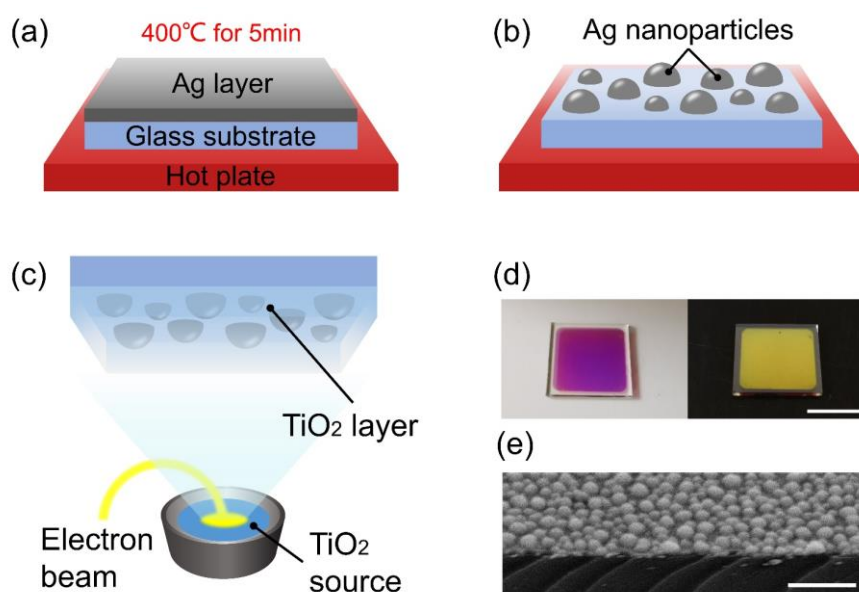
Figure 5.1 (a)-(c) Scheme of the fabrication process of WSR. (d) Photographs of a WSR sample placed on both white (left) and black backgrounds (right). The scale bar represents 10 mm. (e) Scanning electron microscopy (SEM) image of the cross-section of a WSR sample. The scale bar represents 400 nm.[132] Reproduced with permission. Copyright 2022, American Chemical Society.

The photographs in **Figure 5.1** (d) show a WSR placed on white and black backgrounds under natural sunlight conditions, respectively. When placed on a white background, the sample displays a purple color. Owing to the strong scattering of the white background, we can see a mixture of the transmitted blue light and the reflected yellow light of the WSR, resulting in a purple color. On the black background, as the transmitted blue light is absorbed by the background, only the reflected light of the WSR can be observed, therefore, it exhibits a yellow appearance. The details of the transmittance and reflectance spectra are depicted in **Figure 5.9**. The photographs of the WSR sample on different backgrounds visually demonstrate its wavelength-selective response and adequate uniformity. Moreover, **Figure 5.1** (e) shows a cross-sectional scanning electron microscope (SEM) image of a WSR with a tilting angle of 60°. In this image, the self-assembled Ag nanoparticles with disordered arrangement are uniformly coated by the thin TiO_2 layer, forming a nano-corrugated surface for the WSR. The scale bar in the image represents 400 nm. The diameters of the nanoparticles show a certain extent of variety in the image.

5.2.2 Morphology manipulation of silver nanoparticles

Localized surface plasmon resonance is significantly affected by the morphology of the metal layer, including the size and geometry of the nanostructures, and the distance between them. Therefore, to achieve the fine adjustment of the optical performances of the WSRs, good control of the morphology of the monolayer of Ag nanoparticles is crucial.
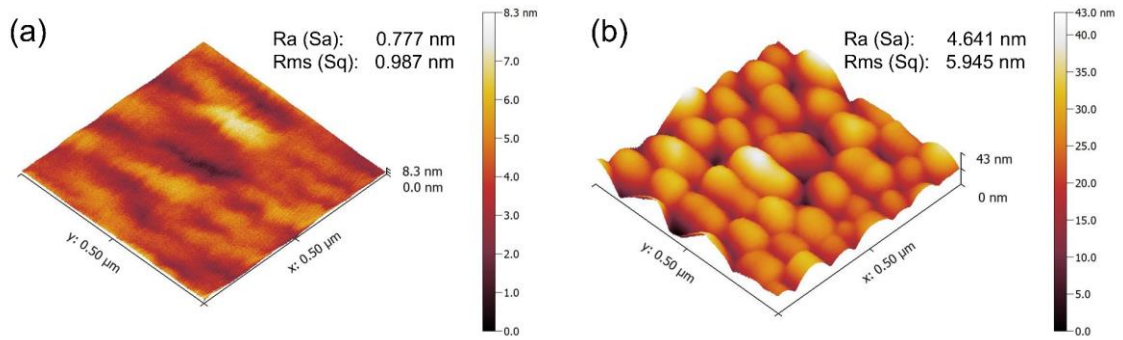

Figure 5.2 Morphology of an Ag layer before and after solid-state dewetting. (a) Atomic force microscopy (AFM) image of a flat as-deposited Ag layer. (b) AFM image of a monolayer of Ag nanoparticles generated by the dewetting of a plane Ag layer. The initial thickness of the flat Ag layer is 14 nm and the thermal annealing temperature is 400 °C.

A morphological comparison is shown here to demonstrate how the dewetting process transforms a flat Ag layer into a monolayer of Ag nanoparticles. The surface morphology of an as-deposited Ag layer with a thickness of 14 nm is shown in **Figure 5.2** (a). The flat surface of the Ag layer exhibits a height deviation of 8.3 nm and low surface roughness with a root mean square (Rms) roughness of 0.987 nm. After the solid-state dewetting process at 400 °C in a
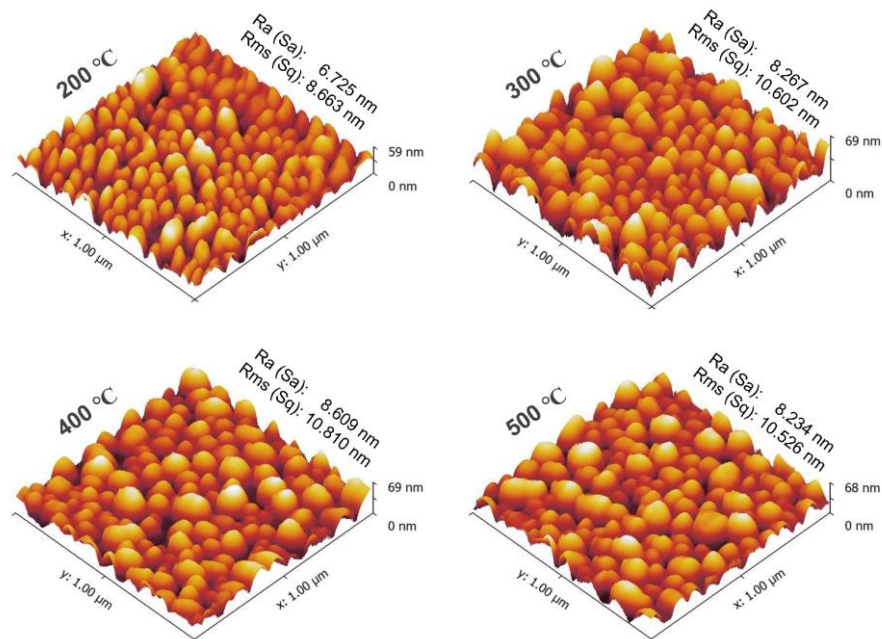
Figure 5.3 AFM images of the monolayers of Ag nanoparticles after thermal annealing at different temperatures for 5 min.

nitrogen environment, the plane Ag thin film transforms into a monolayer of Ag nanoparticles. The nanoparticles are separated from each other and their geometries show certain randomness of the size and distribution. The height difference of the layer increases to 43 nm and the surface roughness is significantly higher than the initial flat Ag layer.

In the solid-state dewetting process, parameters including annealing temperature, annealing time, ambient atmosphere, and surface texture of the substrate, are effective in the topography of the Ag nanoparticle layer. In this research, to minimize the production cost of the WSRs, plane glass substrates without surface structures were applied for fabrication. To avoid oxidation of the Ag material during annealing, the dewetting process was conducted in a glovebox with nitrogen. To determine an appropriate annealing temperature for the dewetting process of WSRs, flat Ag films with a thickness of 16 nm were heated for 5 min at different temperatures. In the experiment, the samples deposited with the Ag layer were directly put on the hotplate with the corresponding temperature without pre-heating. **Figure 5.3** shows the AFM images of the samples prepared with annealing temperatures ranging from 200 °C to 500 °C. The sample prepared at 200 °C exhibits a narrower surface structure than the samples with higher annealing temperatures, indicated by its smaller height difference and surface roughness. The samples with annealing temperatures higher than 200 °C show similar morphology and surface roughness. It suggests that temperature effects rarely the geometry of the Ag nanoparticle layer when it is higher than 200 °C.
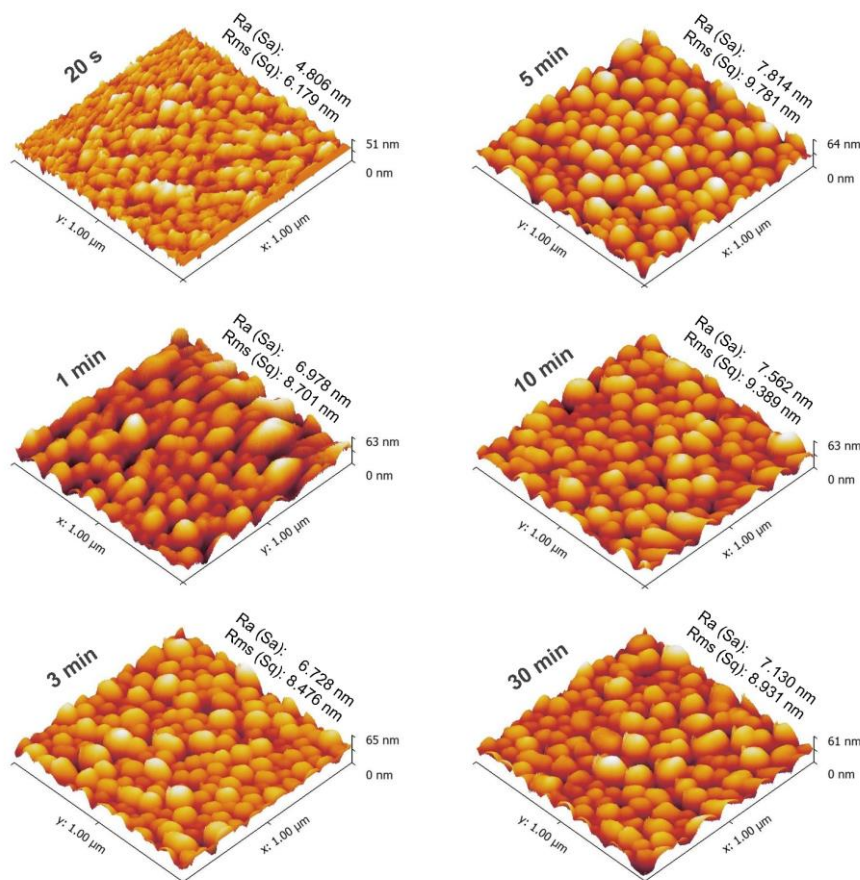
Figure 5.4 AFM images of the monolayers of Ag nanoparticles after thermal annealing at 400 °C for different durations, respectively.

To evaluate the influence of the annealing time on the surface morphology of the Ag layer, flat Ag layers with a thickness of 14 nm were deposited on glass substrates, followed by a thermal annealing process at 400 °C for different annealing time. The AFM images of the samples are shown in **Figure. 5.4**. When the annealing time is less than 3 min, the morphologies of the samples exhibit a lower height difference and poorer uniformity than the samples with longer annealing times. With the increase of the heating time, the morphologies of the Ag nanoparticle layers show high similarity. Thus, we speculate that the geometry of the Ag layer is stable and the dewetting process is accomplished after being heated for 5 min. On the other hand, a long annealing time could potentially bring more oxidation to the Ag nanoparticles. Therefore, an annealing time of 5 min and an annealing temperature of 400 °C are selected for the solid-state dewetting process of the Ag layer.
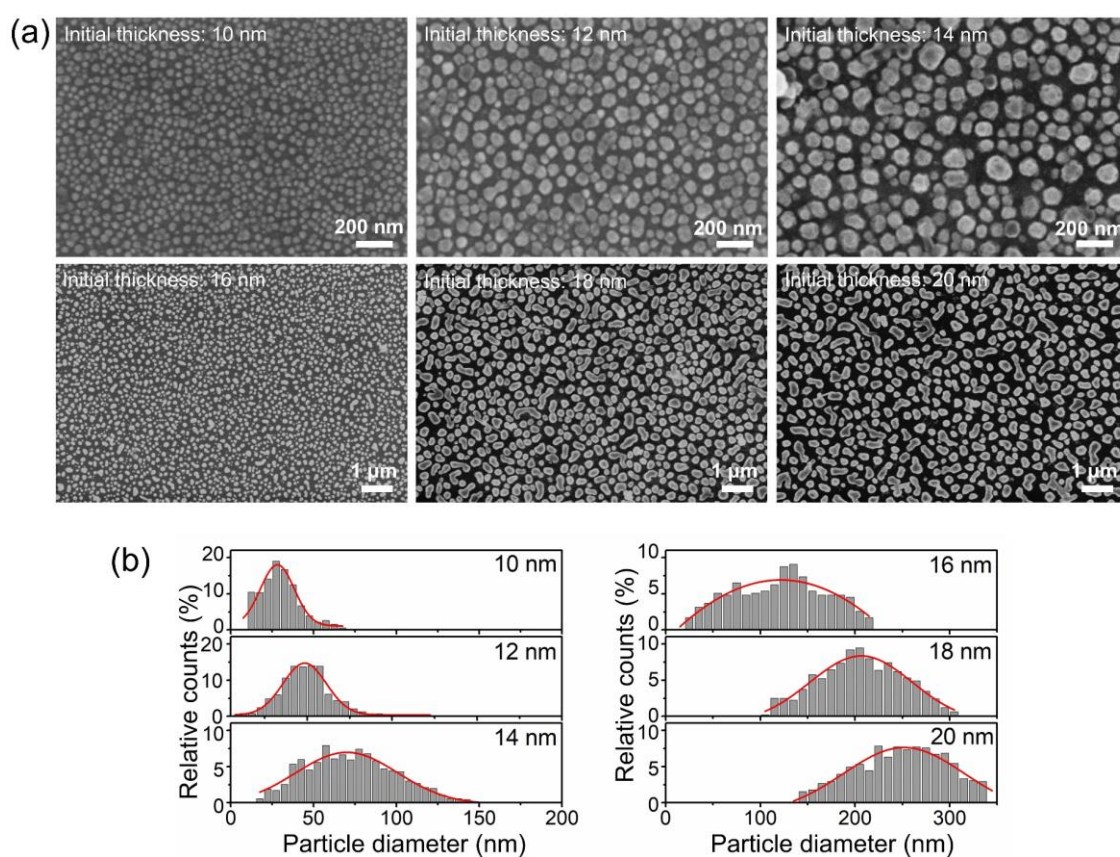
Figure 5.5 (a) Top-view SEM images, and (b) histograms of diameter distributions of solid-state dewetting Ag nanoparticles with initial Ag layer thickness of 10 nm, 12 nm, 14 nm, 16 nm, 18 nm, and 20 nm, respectively.[132] Reproduced with permission. Copyright 2022, American Chemical Society.

Besides the processing parameters, the initial thickness of the as-deposited planar Ag layer is a crucial factor for the structure of the resulting Ag nanoparticles, including the sizes of the particles and the gap between particles. To investigate the influence of the initial thickness, as-deposited Ag layers with thickness ranges from 10 nm to 20 nm were thermally annealed on the hot plate at 400 °C for 5 min. The top-view SEM images of the annealed samples are shown in **Figure 5.5** (a). The scale bars on the upper row are 200 nm, and the scale bars on the bottom row are 1 μm. In the SEM images, the sample with a larger initial Ag thickness obtains a larger

mean particle size. Moreover, with the increase of the initial thickness, the interparticle distance of the Ag nanoparticle increases gradually. For the samples with an initial Ag thickness lower than 16 nm, the Ag nanoparticles after dewetting appear in an individual round shape. When the initial thickness is higher than 16 nm, numerous Ag nanoparticles show a worm-like outline due to the coalescence of multiple nanoparticles. This coalescence potentially could diminish the plasmonic effect and cause impairment to the controllability of the optical property of the WSR.

To quantitatively evaluate the diameter of the dewetting Ag nanoparticles, histograms of diameter distribution were calculated based on the SEM images, as shown in **Figure 5.5** (b). The red lines in the figure represent the Gaussian fitting curves of the histograms. These histograms demonstrate that the mean diameter of the nanoparticles can be well adjusted by the initial Ag layer thickness. Increasing from 10 nm to 20 nm in 2 nm steps, the mean diameters of the nanoparticles were measured as 30 nm, 50 nm, 72 nm, 121 nm, 206 nm, and 249 nm, respectively. Moreover, the thinner Ag layers (for example 10 nm and 12 nm) generate nanoparticles with a relatively narrow diameter size distribution, indicating a better uniformity
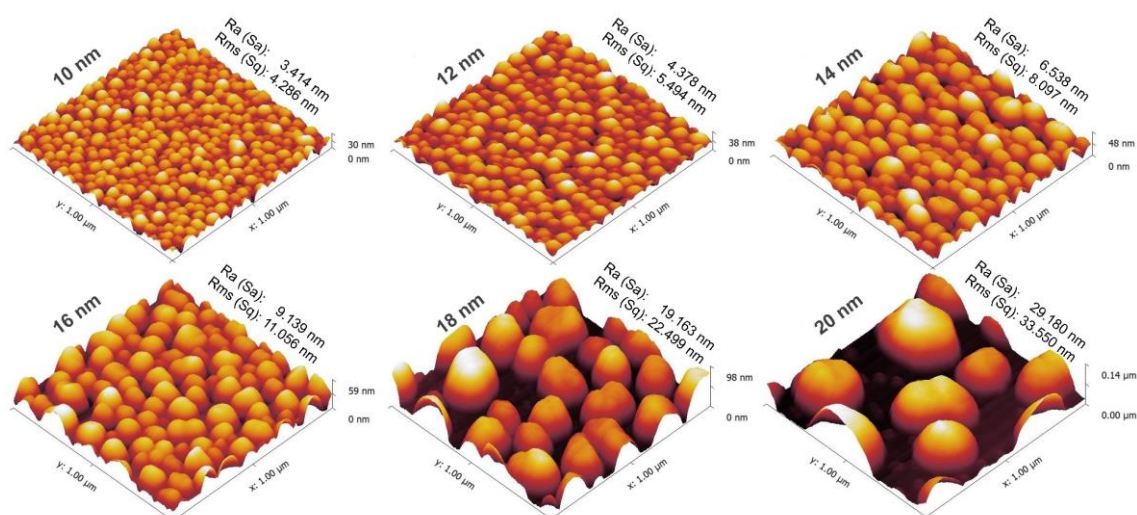
Figure 5.6 AFM images of solid-state dewetting Ag nanoparticle monolayers with different initial Ag layer thicknesses.[132] Reproduced with permission. Copyright 2022, American Chemical Society.

Figure 5.6 shows the AFM images of the Ag nanoparticle monolayers for initial Ag layer thicknesses ranging from 10 nm to 20 nm. The Ag nanoparticles show a nearly hemispherical profile with a high surface filling fraction. Upon increase of the Ag layer thickness, the mean diameter and mean height of the nanoparticles, as well as the nanoparticles' inter-distance increase gradually. When the initial thickness lies above 16 nm, a significant spacing among nanoparticles can be observed. The surface roughness of the 10 nm sample is 4.286 nm for Rms and gradually increases to 33.550 nm for the 20 nm sample. The increase in the height of nanoparticles can be visually observed from the enlarged height difference of the images as well. A comprehensive comparison is summarized in **Table 5.1** to demonstrate the significant effect of the initial Ag thickness on the morphology of the nanoparticles, based on the SEM and AFM measurements. Compared to the processing parameters, such as annealing temperature and annealing time, initial Ag layer thickness has a more prominent capability of manipulating the

geometry of the Ag nanoparticles. Therefore, it is applied as the key factor for the fabrication of the WSRs and the fine adjustment of their optical performance.

Table 5.1 Mean diameter, height, and surface filling fraction of the Ag nanoparticles.

Initial thickness (nm)	Mean diameter (nm)	Mean height (nm)	Filling fraction (%)
10	30	16	51.9
12	50	19	51.1
14	72	24	49.3
16	121	39	46.4
18	206	46	47.5
20	249	69	43.9

5.2.3 Deposition of titanium dioxide layer

Following the preparation of the monolayer of Ag nanoparticles, the deposition of the TiO_2 layer is another critical step for fabricating the WSRs. A high-refractive-index TiO_2 layer is desired to cover atop the Ag nanoparticles, resulting in a core-shell-like configuration for the metal-dielectric nanostructures.[159], [160] To obtain this coating layer, the spin-coating method and electron beam evaporation method are investigated.
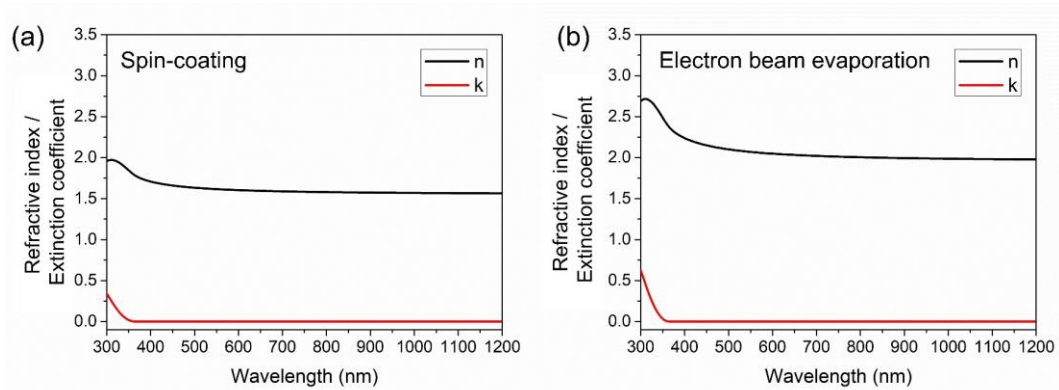
Figure 5.7 Refractive indexes and extinction coefficients of TiO_2 thin films with a thickness of 50 nm deposited on glass substrate prepared by (a) spin-coating, and (b) electron beam evaporation.[132] Reproduced with permission. Copyright 2022, American Chemical Society.

Characterizations for refractive index were conducted for the TiO_2 thin films deposited on glass substrates by spin-coating and electron beam evaporation, respectively. For the spin-coating method, ethanol dispersion of TiO_2 nanoparticles was spin-coated on a clean glass substrate and dried in an air atmosphere without an additional annealing process. For electron beam evaporation, an evaporator (Angstrom Engineering Inc.) was applied to deposit TiO_2 thin film in vacuum conditions. **Figure 5.7** shows the refractive indexes and extinction coefficients of the TiO_2 thin layers prepared with the two different approaches. The thickness of the thin layer is 50 nm. The spin-coating TiO_2 thin layer shows a lower refractive index with a mean value of 1.6 between 300 nm to 800 nm, while the evaporated layer obtains a mean refractive index of 2.2

among the same wavelength range. It should be attributed to the compactness difference and the phase difference of the TiO_2 layers fabricated by the two approaches. The spin-coated TiO_2 nanoparticles cannot generate a dense coating without an extra annealing process and the crystal phase of the TiO_2 materials for the two methods might be different. The air voids between nanoparticles reduce the total refractive index of the layer. Thus, the electron beam evaporation method was selected for the deposition of the TiO_2 coating layer.

In the fabrication process of the WSRs, the initial thickness of the as-deposited plane Ag layer and the thickness of the TiO_2 coating layer are crucial parameters affecting the morphology of the WSRs. In this chapter, these two critical parameters are denoted in brackets for different designs investigated; for example, $Ag(10)/TiO_2(20)$ signifies a WSR sample with an initial Ag layer thickness of 10 nm and a TiO_2 coating layer thickness of 20 nm.

5.3 Optical performances of wavelength-selective reflectors

The purpose of developing the WSR is to enhance the forward emission of QD color conversion layers in WLED devices. The optical optimization of the WSR should comply with the configuration of the device in the application and the goal of enhancing forward emission.
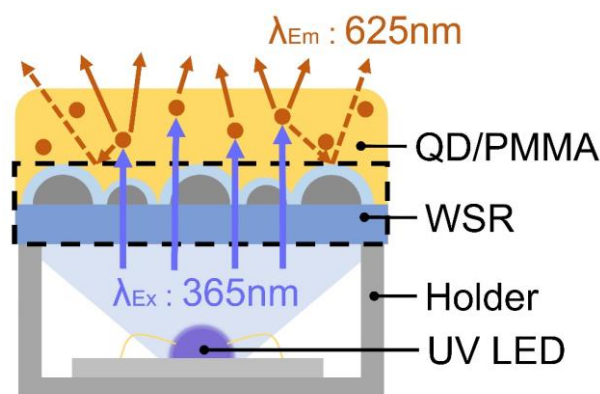
Figure 5.8 Illustration of the operational principle of a WSR integrated within a UV-pumped QD-LED with efficient forward extraction of the converted light (red arrows).[132] Reproduced with permission. Copyright 2022, American Chemical Society.

An illustration of the enhancing principle of a UV-pumped QD-LED integrating with a WSR is shown in **Figure 5.8**. In this configuration, the WSR is directly inserted between the UV light source (here with an excitation peak at 365 nm) and the QD conversion layer (red emission peak at 625 nm in this example) to foster the outcoupling of the converted photons and enhance the photoluminescence (PL) in the forward direction. This concept relies on the high transmittance of the WSR in the UV-blue range, such that most of the excitation light can reach the QD layer. Meanwhile, the WSR should obtain high reflectance in the green-red wavelength range for recycling the backward emission of the QD layer. These two characteristics are the guidelines for the optical optimization of WSRs.

To optimize the optical performance of the WSRs, samples with different Ag and TiO$_2$ layer thicknesses were fabricated and their overall (i.e., specular and diffuse) reflectance and transmittance spectra were measured over the 300-800 nm wavelength range with a UV-vis-NIR spectrometer. The transmittance spectra were acquired under vertical incidence, and the reflectance spectra were acquired under an angle of incidence of 8 degrees with unpolarized light. Transmittance measurements have been performed with illumination through the glass substrate, while reflectance measurement has been carried out with the excitation source on the opposing side to fit the configuration of the WLED. For comparison, two reference samples, a bare glass substrate and a glass substrate coated by a planar Ag layer (thickness: 14 nm) were measured as well. Thin planar Ag layers were notably used in the study of Song et al. [142] to retro-reflect the downward propagating emission in a solar concentrator device while ensuring a sufficient amount of excitation light transmitted through it. The comparison between the WSRs and the planar Ag layer is designed to exhibit the benefit of the wavelength-selective effect from the plasmonic Ag nanoparticles.
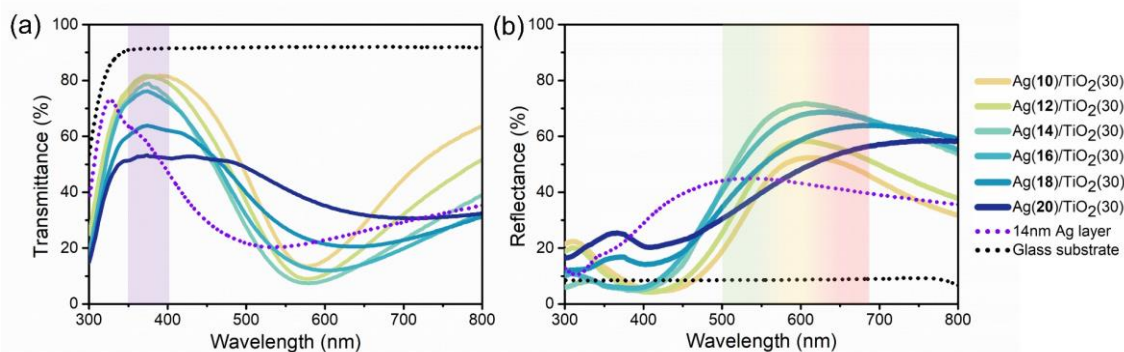
Figure 5.9 (a) Transmittance and (b) reflectance spectra of WSRs with an initial Ag layer thickness ranging from 10 nm to 20 nm. The thickness of the TiO$_2$ coating layer is 30 nm.[132] Reproduced with permission. Copyright 2022, American Chemical Society.

Figure 5.9 illustrates the corresponding transmittance and reflectance spectra of WSR samples with initial Ag layer thickness ranging from 10 nm to 20 nm (in 2 nm increments) and a 30 nm thick TiO$_2$ layer. These WSRs exhibit a main transmittance peak in the UV-blue range and a reflectance peak centered in the visible range. The spectral features of maximum intensity, peak wavelength, and peak width need to be tailored to fit the demand of the QD-WLEDs. Hence, for the transmittance spectra, particular attention should be given to the wavelength range around 365 nm, corresponding to the peak wavelength of the excitation light from the UV chip. Moreover, indium gallium nitride UV LED chips centered at emitting wavelengths longer than 365 nm demonstrate notably higher external quantum efficiency compared to those centered at shorter wavelengths.[161] Around this wavelength, the transmittance peak value gradually decreases with increasing initial Ag layer thickness. This decrease becomes more pronounced once the initial Ag layer thickness equals or exceeds 18 nm, likely due to stronger absorption and light scattering of the enlarged particle size, which enters the Mie scattering regime.[162] Multiple scattering among nanoparticles might alter the direction of incident light. The measured specular transmittance of the bare glass substrate approaches 91% at 365 nm, whereas the 14 nm thin planar Ag layer on glass exhibits a transmittance of only 60% at the same wavelength. One should note that all WSRs are fabricated on a glass substrate, leading to parasitic UV absorption within the

substrate. Reflectance spectra shown in the figure reveal that increasing the initial Ag layer thickness initially elevates the main peak value, which then decreases, reaching its maximum at an initial thickness of 14 nm. The peak of the reflectance spectrum of the Ag(10)/TiO$_2$(20) sample spans the entire green and red bands and is notably higher than that of the planar Ag layer.
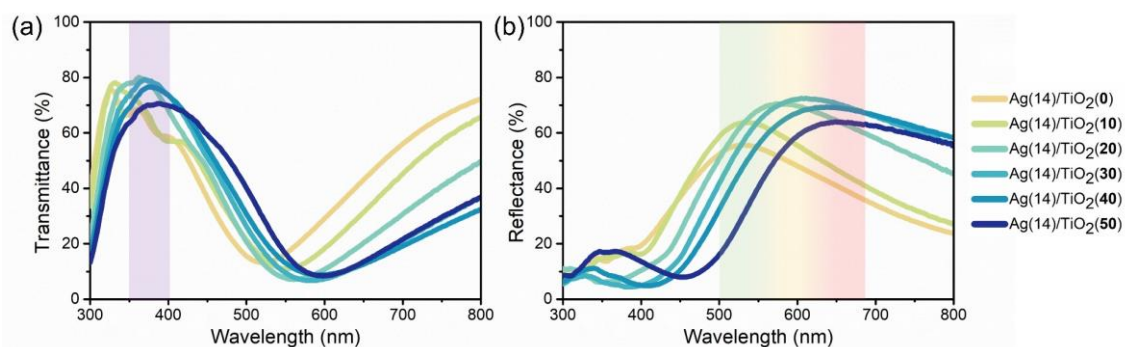

Figure 5.10 (a) Transmittance and (b) reflectance spectra of WSRs with TiO$_2$ layer thicknesses ranging from 0 nm to 50 nm. The initial thickness of the Ag layers of the samples is 14 nm.[132] Reproduced with permission. Copyright 2022, American Chemical Society.

The transmittance and reflectance spectra of WSR samples with TiO$_2$ coating layer thicknesses ranging from 0 nm to 50 nm are depicted in **Figure 5.10**. The samples have an initial Ag layer thickness of 14 nm. It is important to note that, differs from the flat Ag layer, the Ag(14)/TiO$_2$(0) sample signifies the dewetted Ag nanoparticles monolayer without TiO2 coating. These spectra illustrate a noticeable red-shift in both transmittance and reflectance peaks as the TiO$_2$ coating thickness increases. Specifically, the transmittance peak wavelength shifts from 326 nm to 386 nm, and the reflectance peak wavelength shifts from 530 nm to 648 nm, with TiO$_2$ layer thickness varying from 0 nm to 50 nm. This red-shift phenomenon is caused by the augmentation in the effective refractive index of the dielectric coating due to the increase of the TiO$_2$ layer thickness.[163] Additionally, the transmittance peak value of the WSRs remains relatively constant when the thickness is below 40 nm, whereas the reflectance peak value experiences more
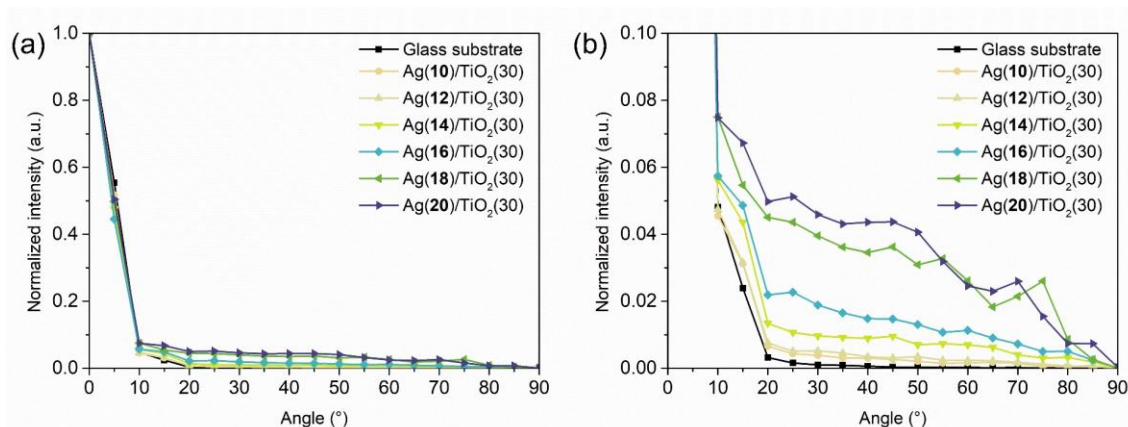
Figure 5.11 (a) Normalized angular intensity distribution of the transmitting light of the WSRs excited by a red laser beam centering at 640 nm. (b) An enlarged view of the normalized angular intensity distribution graph.[132] Reproduced with permission. Copyright 2022, American Chemical Society.

pronounced changes, reaching its maximum at a TiO_2 coating thickness of 30 nm. By adjusting the thickness of the TiO_2 layer, fine-tuning the peak wavelengths for both reflection and transmission peaks can be achieved. Following spectral characterization, the $Ag(14)/TiO_2(30)$ WSR sample is chosen for further application studies due to its superior optical performance in both transmittance and reflectance. Specifically, this sample exhibits a peak value of transmittance in the UV wavelength of 79% and a maximum reflectance of 72% in the visible wavelength range.

Figure 5.11 illustrates the normalized angular intensity distribution of the transmitted light from the WSRs, which are tested by a red laser beam with a central wavelength of 640 nm. In the measurement, the samples were mounted in front of a laser diode on a rotation stage vertically to the laser beam direction. The transmitted laser light was then detected by a spectrometer fixed behind the sample. By rotating the stage during the measurement, the angular distribution of the intensity of the transmitted laser light was obtained. In this figure, the WSRs show weak light scattering as the transmittance intensity is concentrated in small angles. It should be attributed to the small size of the core-shell nanoparticles in WSRs. The scattering effects become relatively stronger when the initial Ag layer thickness reaches 18 nm, as the particle size is larger and enters the Mie scattering regime. This phenomenon is in agreement with the morphological characterizations.
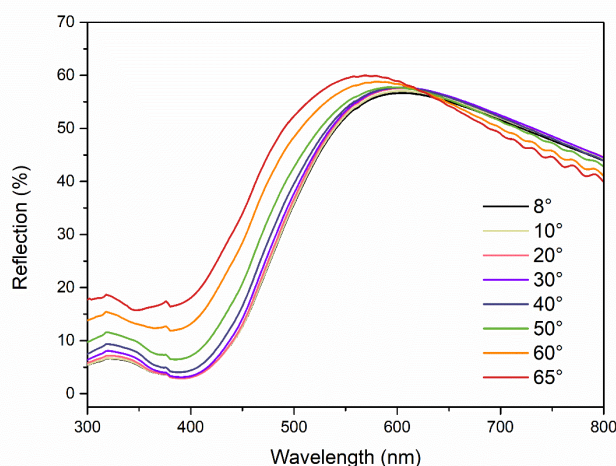
Figure 5.12 Specular reflectance spectra of an $Ag(14)/TiO_2(30)$ WSR with the testing light incidents from different angles range from 8° to 65°.[132] Reproduced with permission. Copyright 2022, American Chemical Society.

Compared to other types of wavelength-dependent reflectors, such as distributed Bragg mirrors and grating reflectors, plasmonic reflectors can achieve lower angular dependence. To demonstrate it, a spectral characterization was conducted for an $Ag(14)/TiO_2(30)$ WSR sample with testing light impinging from different angles ranging from 8° to 65°. In this characterization, the spectra were measured without integrating the sphere and only the specular reflecting light was collected, resulting in a relatively lower reflectance value. As shown in **Figure 5.12**, the reflectance spectra exhibit a similar shape among visible wavelengths, especially when the incident angle is lower than 50°. The peak value of the specular reflectance spectrum first maintains the same and slightly increases for larger angles of incidence. The low angular dependence of the

WSR benefits its performance when being applied in the QD-LED device, as a big portion of the backward emission from QDs hits the WSR with a large incident angle.

5.4 Integration of wavelength-selective reflectors into light-emitting diodes

To demonstrate the utility of WSRs in QD-based color conversion applications, red QDs/PMMA films were fabricated on three different substrates: a bare glass substrate, a planar Ag reflector (consisting of a 14 nm thick Ag film on a glass substrate), and an Ag(14)/TiO$_2$(30) WSR for comparison. As the WSRs are made of metal particles and inorganic coating layer which have high resistance to organic solvent, a direct solution casting method was selected for fabricating the QD films. In detail, 4.0 mg of QD powder and 1.0 g of PMMA powder were added into 10 ml of toluene solvent, followed by 4h of magnetic stirring to obtain a homogeneous mixture solution. Subsequently, 200 μl of the solution was drop-casted onto the surface of the Ag(14)/TiO$_2$(30) WSR sample (the Ag/TiO$_2$ composite side). After the total evaporation of the toluene solvent at room temperature, a solid QDs/PMMA film attached to the WSR sample was obtained. In the same way, identical QDs/PMMA films were deposited onto a glass substrate and a 14 nm flat Ag layer with the same solution and drop-casting volume.
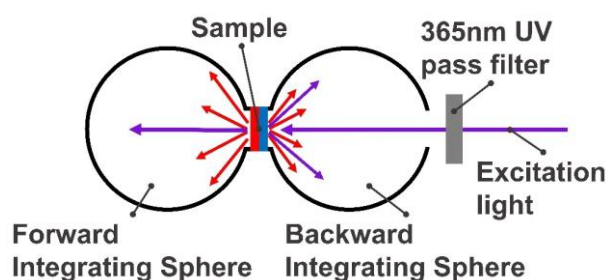
Figure 5.13 Schematic of double integrating sphere setup.[132] Reproduced with permission. Copyright 2022, American Chemical Society.

The obtained QD films with different substrates were then measured in a double-integrating sphere to characterize their forward and backward PL intensity. As shown in **Figure 5.13**, the double integration sphere system consists of two integration spheres and a testing beam. In the measurement, the QD/PMMA films were positioned between two integrating spheres, with the collimated excitation beam (UV LED centered at around 365 nm) directed onto the glass substrate side for all samples. The forward emission of the samples and the transmitted UV excitation were detected by the spectrometer in the forward integrating sphere, while the backward emission and the reflected UV excitation were collected in the backward integrating sphere.

The corresponding forward and backward PL spectra are shown in **Figure 5.14**. It is important to note that the excitation peaks and the emission peaks are represented on different scales. Forward emission measurements indicate a 40.3% increase in PL intensity for the QD color conversion film combined with the WSR compared to the reference QD film deposited on a bare glass substrate. The sample with a bare glass substrate exhibits the highest UV peak in the forward direction due to its high UV transmittance compared to the other two configurations.

The lowest PL intensity in the forward direction is measured for the planar Ag reflector, being 35.2% lower than for the bare glass substrate, as the planar Ag reflector shows relatively low transmittance to the excitation light. The recycled backward emission cannot compensate for the loss caused by low transmittance.
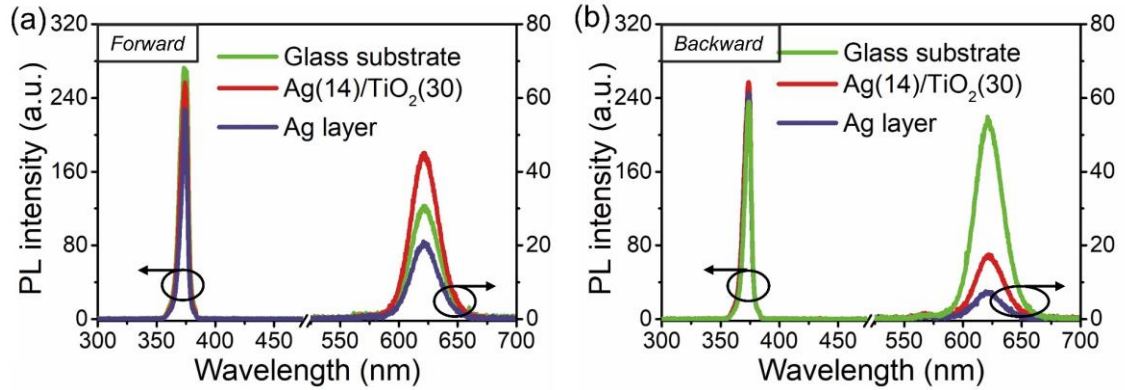

Figure 5.14 (a) Forward PL spectra and (b) backward PL spectra of QDs/PMMA films on different substrates under 365 nm UV excitation.[132] Reproduced with permission. Copyright 2022, American Chemical Society.

In the backward direction, the PL intensity peak of the bare glass substrate sample is significantly higher than for the other two samples (WSR and planar Ag layer), indicating that a large fraction of the light emitted by the QDs is directed backward without the reflector. The WSR and planar Ag reflector exhibit weak backward emission mainly attributed to their high reflectance values at the wavelength range around 627 nm (71% for the WSR sample and 42% for the planar Ag layer sample). The relatively lower transmittances of the WSR and the planar Ag reflector also reduce their PL intensity in the backward direction due to the attenuation of the effective excitation light that reaches the QD film. However, compared to the bare glass substrate sample, the reductions of the PL intensity to the backward sphere are disproportionate to their transmittance differences at the excitation wavelength, indicating the dominant effect of reflection.

To practically apply the WSRs in QD-based photoelectronic devices, WLEDs incorporating UV chips as well as red, green, and blue (RGB) QDs were built. For acquiring the white color conversion films, RGB QDs were embedded in PMMA film following the same procedure as the samples prepared for double integrating sphere measurement. Herein, the mass ratio of the RGB QDs in the QD/PMMA color conversion films was 1:5:12. The configuration of the QD-WLED is shown in **Figure 5.8**. The resulting electroluminescence (EL) spectra, obtained under a driving current of 120 mA for the UV chip (Nichia NCSU276A), are depicted in **Figure 5.15** (a). In the near UV region, the device incorporating a bare glass substrate exhibits the highest EL intensity, followed by those employing the WSR and the planar Ag reflector. It is consistent with their transmittance values in this wavelength range. In the red and green spectral ranges, the WSR demonstrates the highest EL intensity among the three QD-WLEDs, attributed to its effective extraction of converted photons in the forward direction. However, in the blue spectral range, the EL spectrum of the bare glass substrate mostly overlaps with the WSR sample. This parity arises from the WSR sample's lower transmittance for UV excitation light but higher

reflectance within the blue band, compensating each other and yielding similar overall emission intensity as the glass substrate sample.
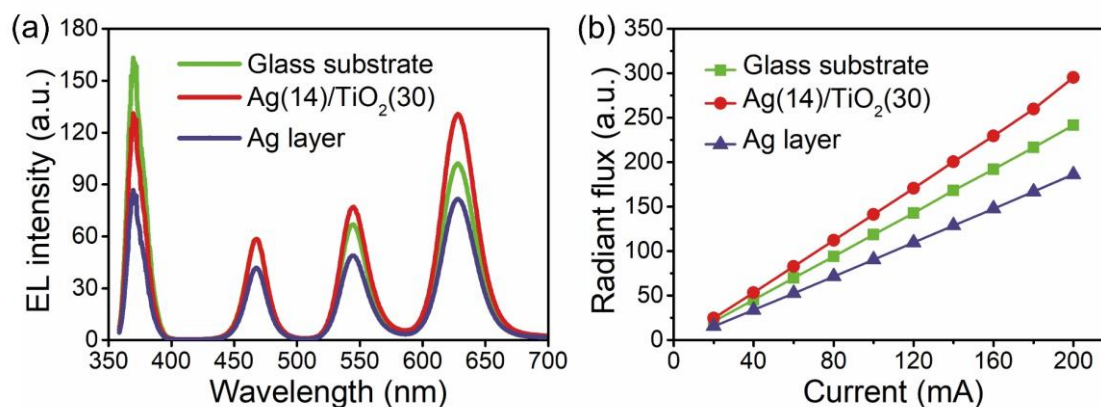

Figure 5.15 (a) Emission spectra of QD-WLEDs incorporating QD/PMMA films on various substrates under a driving current of 120 mA. (b) Radiant flux of QD-WLEDs with driving current ranging from 20 mA to 200 mA.[132] Reproduced with permission. Copyright 2022, American Chemical Society.

By integrating over the EL intensity of the entire visible spectrum, the WSR sample reveals a 19.5% increase in radiant flux compared to the device with the bare glass substrate. Specifically, this enhancement amounts to 28.2%, 15.6%, and 0.4% in the red, green, and blue bands, respectively. Conversely, devices utilizing a planar Ag reflector exhibit the lowest EL intensity in both the UV range and the visible range. **Figure 5.15** (b) illustrates the total radiant flux of the three QD-WLEDs as the driving current varies from 20 mA to 200 mA. All three samples exhibit a linear increase in radiant flux with increasing driving current. The WSR sample demonstrates the highest radiant flux value across all driving currents, underscoring the remarkable light extraction properties of WSRs incorporated into WLEDs across various operating conditions.
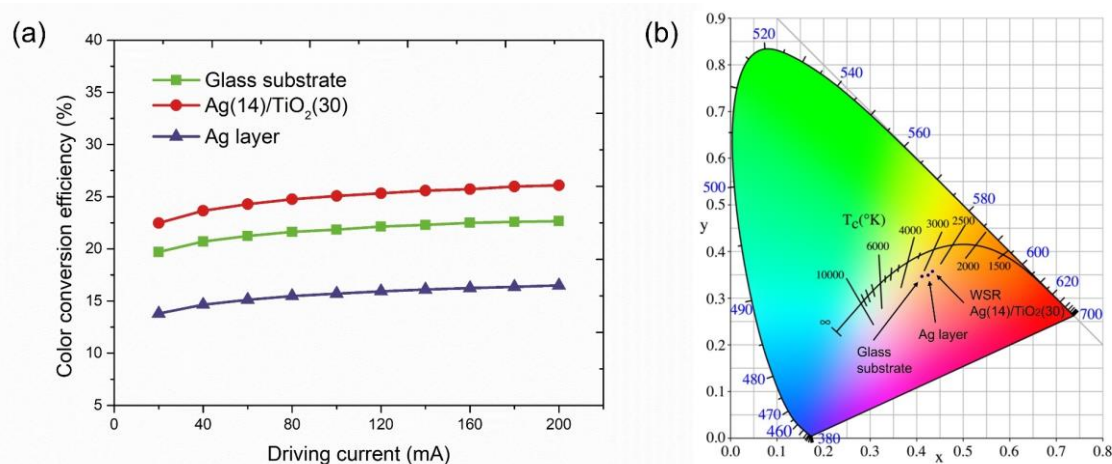
Figure 5.16 (a) Overall light conversion efficiency and (b) CIE color coordinates of QD-WLEDs integrated with QDs/PMMA films on different substrates.[132] Reproduced with permission. Copyright 2022, American Chemical Society.

Based on the EL spectra of the WLEDs with different substrates, by integrating the radiant power of the QD converted light among visible wavelength range and weighted to the absorbed power of the UV excitation light from the LED chip, the light conversion efficiencies of different devices under the driving current from 20 mA to 200 mA are calculated, as shown in **Figure 5.16** (a). The measurement was conducted in an integrating sphere system and only the forward emission of the device was collected. Among all the driving currents, the WSR sample shows the highest color conversion efficiency around 25%, followed by the device with a glass substrate. The Ag layer sample demonstrates the lowest color conversion efficiency. For a current of 120 mA, the color conversion efficiency of the bare glass substrate sample amounts to 22.1%, while the efficiency of the WSR sample is 25.3%. Due to the larger absorption of the UV excitation light, the planar Ag layer only obtains a light conversion efficiency of 15.9%. **Figure 5.16** (b) exhibits the CIE color coordinates of these three QD-WLEDs. The color coordinate of the WSR sample shows a light red shift compared to the sample with a bare glass substrate, as the PL enhancement of the WSR sample is mainly at a long wavelength region. The correlative color temperature of QD-WLEDs incorporated with the $Ag(14)/TiO_2(30)$ WSR, the Ag reflector, and the bare glass substrate are 2622 K, 2710 K, and 2956 K, respectively. It indicates the utilization of the WSR in the QD-WLED tends to reduce the correlative color temperature of the device.

5.5   Summary

In this chapter, we introduced a metallo-dielectric wavelength selective reflector (WSR) utilizing a monolayer of Ag nanoparticles and a TiO_2 coating layer. This reflector showcased high transmittance in the UV and blue spectrum, coupled with significant reflectance in the green and red ranges. The fabrication process of the reflector involved a solid-state dewetting technique to form a self-assembled monolayer of Ag nanoparticles, followed by the deposition of a thin TiO_2 layer. Processing parameters, including initial layer thickness, dewetting temperature, and dewetting time were investigated. Through precise control of the initial Ag layer thickness and the TiO_2 coating layer, we optimized the transmittance and reflectance spectra of the WSR. The most effective WSR sample achieved a peak transmittance of 79% in the UV and a peak reflectance of 72% in the visible spectrum. We evaluated the QD films deposited on the optimized WSR sample using a double-integrating sphere setup for forward and backward spectral measurements. Benefitting from the enhanced forward emission facilitated by the WSR, the forward emission intensity of the QD film demonstrated a notable improvement of 40.3%. Subsequently, we integrated these WSRs into QD-WLEDs to enhance luminescence, resulting in a notable enhancement of 19.5% in radiant flux.

We anticipate wide-ranging applications of this approach in lighting and display technologies. Potential micro-patterning techniques, such as photolithography, nanoimprinting, and inkjet printing, can be adapted to fabricate the patterned or pixelated WSRs. The WSR pixels can be further applied for enhancing the forward light extraction of the QD micro-pixels for organic LED display and micro-LED display.

6 Microporous Quantum Dot Color Converters

This chapter explores a self-assembly method for the fabrication of microporous polymeric networks based on the phase separation of polymer blends. Quantum dots are incorporated in the polymer blends and further adapted to the inkjet printing process for the deposition of microporous quantum dot pixels. In Section 6.1, the research background of quantum-dot-based displays and the motivation for introducing microporous structures are discussed. Detailed investigations of the fabrication and manipulation of the micropores are illustrated in Section 6.2. Section 6.3 shows the optical characterizations of the microporous films with and without embedding quantum dots, respectively. Section 6.4 demonstrates the integration of the phase-separating ink into the inkjet printing process for fabricating micro-pixels. Lastly, a comprehensive summary is concluded in Section 6.5.

Acknowledgements and Contributions

6.1 Introduction

Recently, quantum dots (QDs) have emerged as one of the most promising emissive materials with the potential to supplant traditional rare-earth phosphors in display and lighting applications.[3], [165] Due to their unique optical performances including adjustable band gap, narrow emission spectrum, and high photoluminescence quantum yield (PLQY), QD materials demonstrate good potential for enhancing color purity and improving the efficiency of display devices.[87], [166] Currently, the integration of QD color conversion layers with liquid-crystal-based display modules has commercially gained significant market share.[167] Meanwhile, micro-light emitting diodes (micro-LEDs) have rapidly developed and are regarded as transformative for display applications, especially for high-resolution near-eye displays.[168], [169] QD materials hold great promise as color conversion layers for achieving the full-color display of micro-LEDs. Compared to micrometer-scale rare-earth phosphors, QD materials possess significantly smaller particle sizes, falling within the nanometer range, allowing for more uniform coating on the micro-size chips. Additionally, their smaller size facilitates better adaptability to micro-patterning processes such as inkjet printing,[170], [171] and photolithography,[172], [173] thereby increasing the potential for mass production.

Typically, QD materials are encapsulated in a polymeric or inorganic matrix to enhance stability and lifetime in practical lighting and display applications.[141], [174] However, the introduction of the non-luminescent barrier material could potentially reduce the light outcoupling of the QD layer. Poor light extraction from the color conversion layer poses a challenge to achieving high efficiency.[175] Part of the emitted light from the QDs is trapped within the matrix due to total internal reflection, gradually diminishing due to the reabsorption of QDs. In addition, the overall photoluminescence (PL) intensity of the QD color conversion layer heavily relies on the absorption of excitation light. Due to their small particle size, QDs lack sufficient optical scattering, resulting in a short optical path length for excitation light within the layer and thus a low absorption probability by the QDs.[176]

To address these issues, diverse scattering media, including diffusing reflectors,[177], [178] surface scattering textures,[121], [179] scattering particles in nanometer or micrometer scales,[180], [181], [182] and porous structure,[183], [184] have been incorporated into QD color conversion layers to improve light absorption and light extraction. Among these, introducing a disordered porous scattering structure is a cost-effective and efficient method to achieve broadband light scattering by micropores with irregular sizes and distribution. To generate microporous structures in QD/polymer composite films, strategies based on the supercritical CO_2 foaming method and the humidity-induced phase-separation method have been explored.[118], [119] However, current approaches require complex equipment and detrimental stimuli for QD materials, such as high temperature or high humidity.[185], [186] Furthermore, these existing approaches have only been practically conducted on QD films rather than QD micro-pixels which are more essential in display technology. Thus, methods for fabricating porous structures for pixelated QD color converters are needed. Moreover, due to the advantages of high usage rate of material, mask-free, and contactless, inkjet printing has been widely investigated and applied to QD pixelation,[187], [188] as well as other optical components.[189], [190] It shows great potential for mass pro-

duction and commercialization. A fabrication approach for microporous structures with good adaptability to the inkjet printing method is in intense need.

In this chapter, we propose a phase-separating ink based on a polystyrene (PS) and polyethylene glycol (PEG) blend for inkjet printing to fabricate a microporous structure in QD/polymer composites. This self-assembly approach offers distinct advantages over directly embedding optically scattering particles (e.g. TiO_2 microparticles, ZnO microparticles), as these particles with relatively large sizes tend to block the inkjet printing nozzle. The microporous structure is spontaneously formed through the sequential solidification of PS-rich and PEG-rich domains during solvent volatilization.[191], [192] The morphology of the microporous network can be easily controlled by adjusting the weight ratio of PS and PEG, providing precise control over the optical scattering properties. Using this method, the microporous QD film prepared by drop-casting exhibits a substantial enhancement in photoluminescence (PL) intensity. Moreover, as a solution-based process, this phase separation approach is highly compatible with inkjet printing techniques for cost-efficient mass production of microporous QD pixels for display applications. With further optimization of the ink, a uniform QD pixel array with a microporous structure and a diameter of around 30 μm was fabricated by inkjet printing. The pixel array demonstrates a remarkable 35.3% enhancement in PL intensity.

6.2 Fabrication and optimization of microporous structure

Polymeric porous media are widely applied in the fields of energy storage and harvesting, biofilters, stretchable devices, thermal isolation, etc.[193], [194], [195] Polymeric porous media originates from the basic concept of generating pore structures in a compact polymer material with fine controllability. The introduction of pore structure brings unique properties such as permeability, light scattering, and thermal or acoustic insulation effects for polymer materials. The morphology and characteristics of the porous structure significantly affect the performance of polymeric porous media as well.[196], [197] To fabricate and tailor the porous structure, various fabricating approaches, including microcellular foaming,[198], [199], [200] electrospinning,[201], [202] direct templating,[203], [204] and phase separation,[205], [206], [207], [208] have been developed. Among the above approaches, the phase separation method as a self-assembly method can create disordered porous structures spontaneously without employing complex facilities or templates. This advantage largely benefits their adaptivity and the reduction of the fabrication cost.

Common polymer-based phase separation strategies can be categorized into non-solvent-induced phase separation,[205] polymerization-induced phase separation,[207] and polymer-blend phase separation.[209], [210] For non-solvent induced-phase separation, the polymer is dissolved in a mixture of good solvent and non-solvent. During the evaporation of the good solvent, phase separation occurs between the non-solvent and polymer, resulting in a porous structure. However, as QD materials are quite sensitive to the solvent environment, a mixture of different solvents could lead to the degradation of the QDs or debonding of the surface ligands.[211], [212] Polymerization-induced phase separation is based on the polymerization process of a mixture of monomers, initiators, and porogen. To trigger the polymerization, additional heating or UV

radiation processes need to be employed which increases the complexity of the method. Polymer-blend phase separation is based on the immiscibility of high-molecular-weight polymers. In this method, multiple polymers are first dissolved in a common solvent. Due to the solubility difference of the polymers in the solvent, phase separation appears during the solvent volatilization. Polymer-blend phase separation has the simplest requirement for the fabrication process and solution system among the methods above and thus is chosen as the fabricating approach for the porous QD/polymer composites.
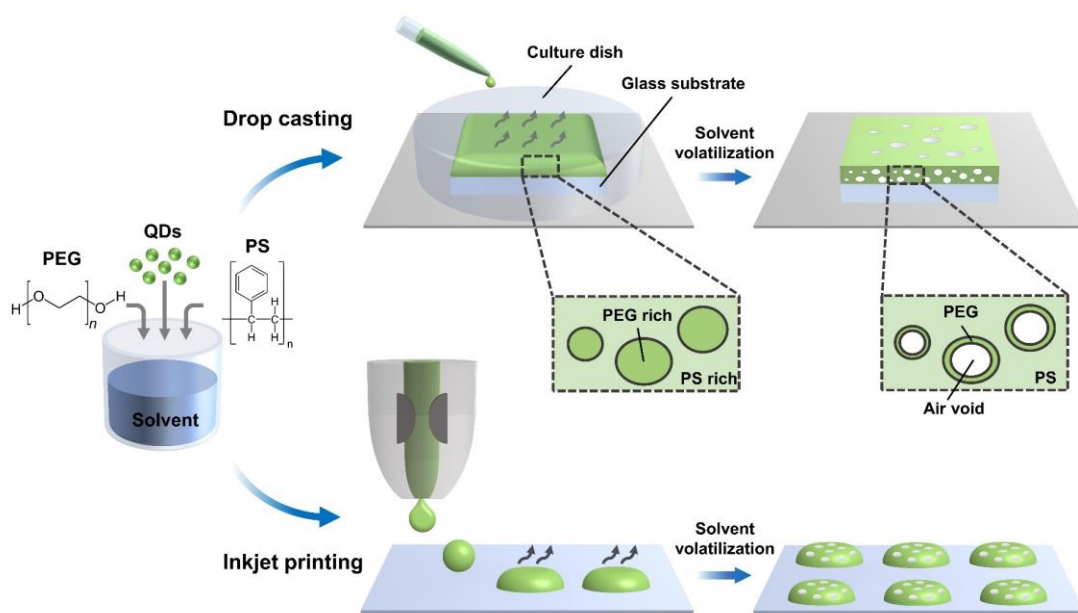
Figure 6.1 Schematics of the fabrication process for microporous QD films and inkjet-printed micropixels, respectively.[164] Reproduced with permission. Copyright 2024, Springer Nature.

The components of the polymer blend system should be able to form a tough barrier for QDs besides creating a microporous structure. PS polymer is one of the most common encapsulating materials for QDs and is here employed as the hosting matrix. Due to its inertness to QDs and immiscibility to PS polymer, PEG is selected as the porogen material in the polymer blend system. The procedure for fabricating microporous QD/polymer composites is depicted in **Figure 6.1**. In the fabrication, PS and PEG powder are mixed in a common solvent in the desired weight ratio, followed by 2 hours of magnetic stirring to obtain a polymer blend solution. Once the polymers completely dissolve, QD powder or dispersion is added into the solution and mixed homogeneously. For the fabrication of microporous QD films, the mixture solution is drop-cast onto a clean glass substrate which has been treated with oxygen plasma for 3 minutes. Subsequently, the solution is left for solidification through solvent volatilization. A glass cover is employed to prevent the influence of ambient gas flow. During solvent volatilization, PS-rich and PEG-rich domains gradually form, with PS-rich domains solidifying faster due to their lower solubility, establishing the outer framework. Meanwhile, the PEG-rich domains remain in a liquid phase, capsulated within the PS framework. After complete solvent evaporation, the PEG-rich domains solidify and collapse within the PS matrix, creating extensive air voids inside the film. On the other hand, for fabricating microporous QD pixels via inkjet printing, the obtained polymer blend solution is utilized as ink in the inkjet printing process, with the porosi-

ty formation mechanism identical to that of the drop-casting process. However, in inkjet printing, the jetting gas flow and reduced droplet size expedite solvent volatilization and polymer solidification. Hence, a solvent with lower vapor pressure is preferred for ink preparation. Notably, the micropore structure of the QD pixel is formed after being jetted out from the nozzle, preventing nozzle clogging by the polymer blend ink and turbulence to the printing process. In this chapter, we distinguish and name the samples by their mass fraction of PEG polymer in the total polymer blend. For instance, a sample that has a weight ratio between PEG and PS of 1:9 is named a PEG-10% sample.
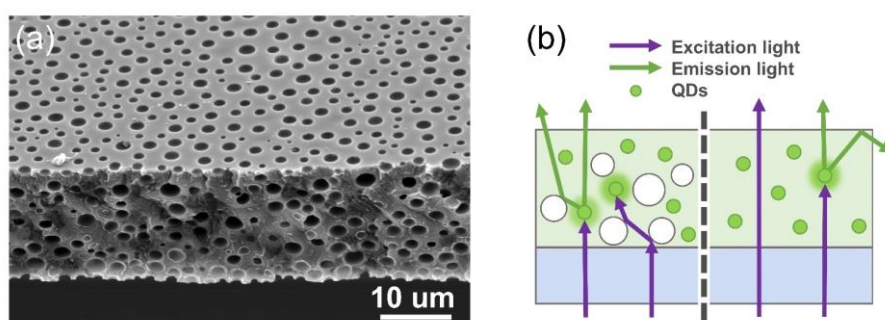
Figure 6.2 (a) SEM image of a microporous QD film with a PEG concentration of 20 wt.%. (b) Scheme of optical mechanisms: Scattering leads to an elongated optical path length of excitation light in QD/polymer composite and the enhanced light extraction caused by micropores.[164] Reproduced with permission. Copyright 2024, Springer Nature.

As an example, an SEM image of a microporous QD/polymer film (PEG-20%) captured at a tilt angle of 45° is shown in **Figure 6.2** (a). This image showcases the irregular volumetrically distributed micropores within the film, extending to its surface. The structure exhibits a diverse range of pore diameters. These micropores act as the primary scattering medium generated from the refractive index contrast between polymer and air, enhancing QD absorption and improving light extraction. The varied sizes of the micropores facilitate broadband scattering, minimizing wavelength dependence. In this magnification, the embedding QD nanoparticles are not discernible, leading to the conclusion that QD aggregations at the micro-scale do not occur in this composite matrix. **Figure 6.2** (b) illustrates the optical paths of the UV or blue excitation in the QD/polymer films with (left) and without (right) the interactions with microporous structure, respectively. The optical performance of QD film, as a color conversion medium, directly depended on its absorption to the excitation photons, PLQY, and the light outcoupling of the emitting photons. The presence of micropores enhances the PL intensity primarily through two mechanisms: Firstly, the scattering effect significantly elongates the optical path length of the excitation photons within the color conversion medium, thereby increasing the probability of absorption by the QD nanoparticles. Secondly, the micropores scatter portions of the emitted light that would otherwise be laterally waveguided and trapped, facilitating their outcoupling in the vertical direction. Notably, the enhancing effect of the micropore structure is closely tied to its scattering capability and morphology, including pore size and pore density. Therefore, a fabrication technique capable of producing porous scattering structures with fine control over their morphology is crucial for optimizing performance in practical applications within optical devices.

Before the fabrication, solubility, and dispersibility tests were conducted on different solvents to select the common solvent for the PS/PEG polymer blend and QD dispersion. Herein, nine organic solvents (chloroform, toluene, anisole, cyclohexanone, 1,2-dichlorobenzene, 2-butanone, tetrahydrofuran, acetophenone, hexane) were examined. For the solubility test, PS (average molecular weight: 100 000 Da) and PEG (average molecular weight: 4 000 Da) were applied and the concentration of the polymer solution was 100 mg/ml. For the dispersibility test, CdSe/ZnS core-shell QDs were used with a concentration of 10 mg/ml. Magnetic stirring for 4 h was conducted for all the solutions in the tests. The results are summarized in **Table 6.1**. To obtain a homogeneous solution of PS and PEG polymer blend, chloroform, and 1,2-dichlorobenzene can be chosen since they directly dissolve both polymers at room temperature. The rest of the solvents either cannot dissolve the polymers or need an additional heating process. Meanwhile, chloroform and 1,2-dichlorobenzene are good solvents for dispersing QD particles. Aiming at preparing a homogeneous ink containing PS, PEG, and QDs, chloroform and 1,2-dichlorobenzene are selected as the candidate solvents for the fabrication of microporous QD/polymer composite. Moreover, regarding reducing the production duration, chloroform with a boiling point of 61°C and relatively high volatilization speed is more suitable for the fabrication of QD films. 1,2-dichlorobenzene with a lower volatilization rate and higher boiling point (180.2 °C) can be employed for preparing inkjet printing ink, as the jetting process could largely accelerate the volatilization of the ink.

Table 6.1 The solubility of PS and PEG and the dispersibility of QDs in different solvents

	PS	PEG	CdSe/ZnS QDs
Chloroform	√	√	√
Toluene	√	○	√
Anisole	×	○	×
Cyclohexanone	√	○	×
1,2-Dichlorobenzene	√	√	√
2-Butanone (MEK)	√	○	×
Tetrahydrofuran	√	○	√
Acetophenone	√	○	×
Hexane	×	○	√

x: insoluble or not dispersible. √: soluble or dispersible. ○: soluble with heating.

As the porogen material in this polymer blend system, PEG plays a critical role in the formation and morphology of the pore structure. The average molecular weight of the PEG material affects directly the solubility of the polymer in solvent and the phase separation behavior during solvent volatilization. In **Figure 6.3**, SEM images of the cross sections of microporous films with PEG molecular weight ranging from 200 Da to 4000 Da. The mass fraction of the PEG for the sample films was 20 wt.%. Chloroform solvent was used for the tests and all the samples were solidified at 22 °C. PEG 200 sample and PEG 600 sample show relatively regular elliptical shapes for the cross-section. The PEG 4000 sample demonstrates an irregular shape for the

pores and a larger pore size as well, compared to the sample with a lower molecular weight. Since PEG with larger molecular weight shows poorer solubility in chloroform solvent, PEG-rich domains are formed earlier than samples with lower molecular weight. It allows a longer duration for the growth of the PEG pores and leads to an increase in the pore size. Coalescences of the PEG-rich domains occur in the period and cause the less regular morphology of the micropores. To achieve a higher density for the micropores, a molecular weight of 200 Da is selected for preparing the scattering microporous films.
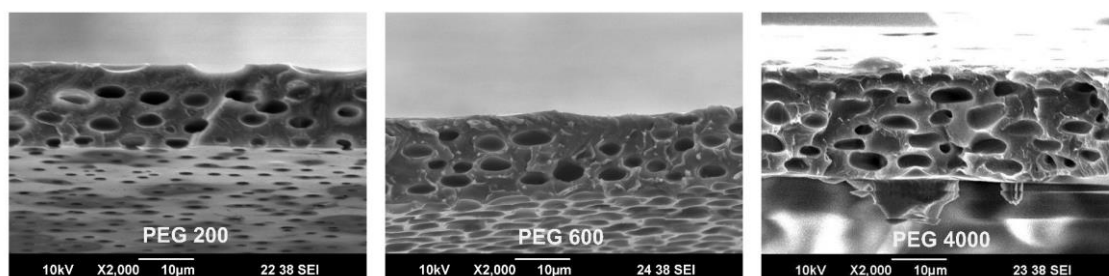
Figure 6.3 Cross-sectional SEM images of the microporous polymer films with different molecular weights for PEG.

The weight ratio of PEG in the polymer blend solution influences the final morphology of the porous structure more significantly. **Figure 6.4** shows the cross-sectional SEM images of the PS/PEG hybrid films with different mass fractions of PEG. As a reference, the PEG-0% sample (pure PS film without PEG composition) exhibits a smooth cross-section, attributed to the absence of PEG porogen. As the PEG mass fraction increases, the porosity of the samples gradually escalates, shown mainly by the enlargement of pore diameter. This phenomenon arises from the behavior during solvent volatilization, wherein the PEG-rich domains retain mobility within the polymer blend solution until the PS-rich domains solidify, allowing coalescence with neighboring domains to form larger droplets. Consequently, polymer blends with higher PEG mass fractions facilitate more coalescence due to the higher density of PEG-rich
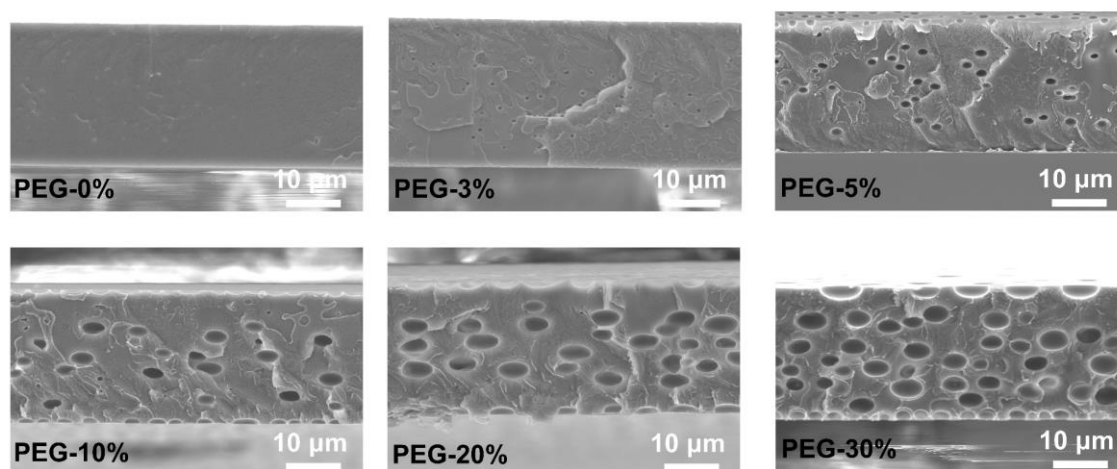
Figure 6.4 Cross-sectional SEM images of the microporous polymer films with PEG mass fraction ranging from 0% to 30%.[164] Reproduced with permission. Copyright 2024, Springer Nature.

domains, leading to increased pore size in the final structure.

The mean diameter of the micropore structures with different PEG mass fractions is calculated as 0.75 μm, 1.76 μm, 3.0 μm, 4.42 μm, and 4.57 μm for PEG-3%, PEG-5%, PEG-10%, PEG-20%, and PEG-30% samples, respectively. The irregular pore sizes and random distribution of micropores facilitate efficient broadband light scattering across visible wavelengths. Furthermore, the adequate geometric variability of the micropore structure underscores the PEG mass fraction as a convenient and effective parameter for controlling morphology.
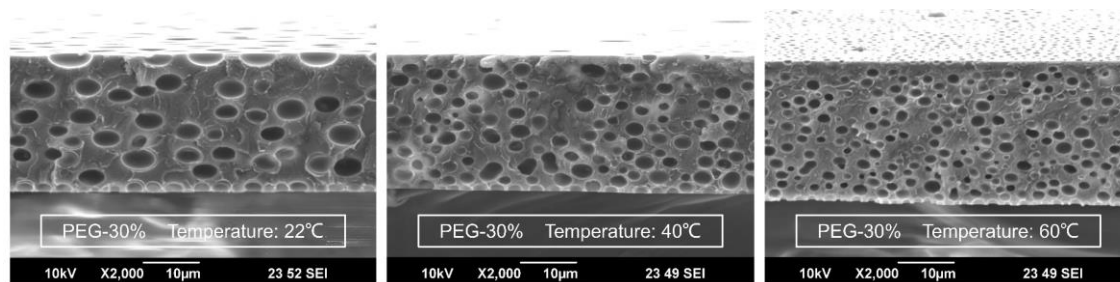
Figure 6.5 Cross-sectional SEM images of the microporous films cured at different temperatures ranging from 22 °C to 60 °C.[164] Reproduced with permission. Copyright 2024, Springer Nature.

Besides the mass fraction of PEG composition, the curing temperature can be utilized for adjusting and tailoring the micropore morphology as well. **Figure 6.5** exhibits the cross-sectional SEM images of microporous films formed from the same PS/PEG blend solution (PEG-30%) but cured at varying temperatures from 22 °C to 60 °C. As the curing temperature rises, the micropore size diminishes while the overall pore count gradually increases. In the phase separation, an elevated curing temperature accelerates the volatilization of the solvent and the solidification of the matrix. Duration for the pore growth is shortened leading to the reduction of the mean pore size and increasing pore amount. The pore distribution of the samples cured at higher temperatures shows adequate uniformity, indicating that thermal convection causes little effect on the porous morphology. Therefore, a heating process during the phase separation of the polymer blend can be introduced to adjust the porous morphology and reduce the producing duration of the porous films.

In the morphological investigations above, the influences of relevant factors, including solvent type, molecular weight of PEG, and weight ratio between polymer compositions, on the phase separation process are studied. It lays a foundation for the tailoring of the microporous structure and the manipulation of its optical properties. Among these factors, the mass fraction of PEG polymer affects the geometry of porous structure the most and provides a high controllability as well. Therefore, it is chosen as the main parameter for optimizing the optical performance of the microporous QD/polymer composite.

6.3 Optical performance of microporous films

The microporous films characterized in this section can be divided into two categories: microporous polymer films without embedding QDs and microporous QD/polymer composite

films with embedding QDs. The former type is investigated to demonstrate the transmittance and scattering properties of the porous structure, which should eliminate the interference of the light absorption and color conversion effects from QDs. The latter type incorporates QDs into the film for investigating the enhancing effect of microporous structure on the QD color conversion film. Besides, as a common type of scatterer, TiO_2 nanoparticles are embedded into PS polymer films and included in the investigation as a reference. For the preparation of the sample films, the molecular weight of PS polymer was 100 000 Da and the molecular weight of PEG was 200 Da. Chloroform solvent and drop-casting method were applied for the fabrication of the samples.

6.3.1 Optical characterizations for microporous films without quantum dots

The main purpose of introducing a microporous structure lies in generating sufficient light scattering capability in the polymer matrix. To validate the scattering capability, spectral measurements for haze value, defined as the portion of diffused transmittance ($> 5°$) to total transmittance through the films, were conducted. Meanwhile, the overall transmittance of the microporous film is a critical factor to light extraction in practical applications as well. The evaluation of the scattering films needs to be balanced between their transmittance and haze values.
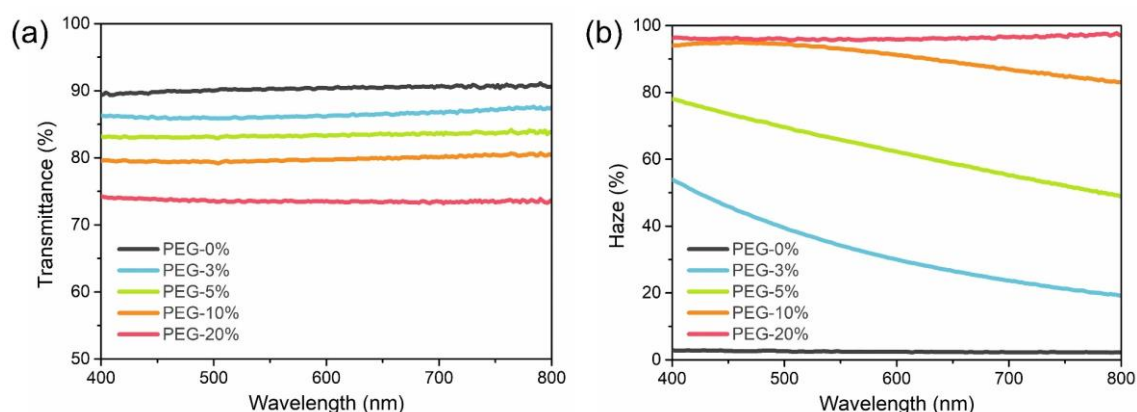
Figure 6.6 (a) Transmittance spectra and (b) haze spectra of the microporous polymer films with different PEG mass fractions.[164] Reproduced with permission. Copyright 2024, Springer Nature.

The transmittance and haze spectra of microporous films with varying PEG mass fractions within the 400-800 nm wavelength range are illustrated in **Figure 6.6**. These films were measured as freestanding samples using a UV–VIS–NIR spectrometer (Lambda 1050+ UV-vis-NIR, PerkinElmer). The transmittance spectra exhibit a gradual decline with increasing PEG mass fraction, from a mean transmittance of 90.3% for non-porous film to 73.6% for PEG-20% film. It is attributed to the dense micropore structure causing multiple light scattering and reflection. Conversely, average haze values rise from 2.4% to 96.3% with increasing PEG mass fraction, indicating enhanced scattering performance. The wide variation in haze values underscores the versatility of the porous structure in adjusting scattering capability. Balancing micropore density is crucial to avoid excessive scattering, which can reduce total transmittance, highlighting the

importance of morphology controllability of the fabrication method. Additionally, PEG-3%, PEG-5%, and PEG-10% samples exhibit wavelength-dependent haze spectra due to sub-micrometer pores, consistent with the morphological characterization.
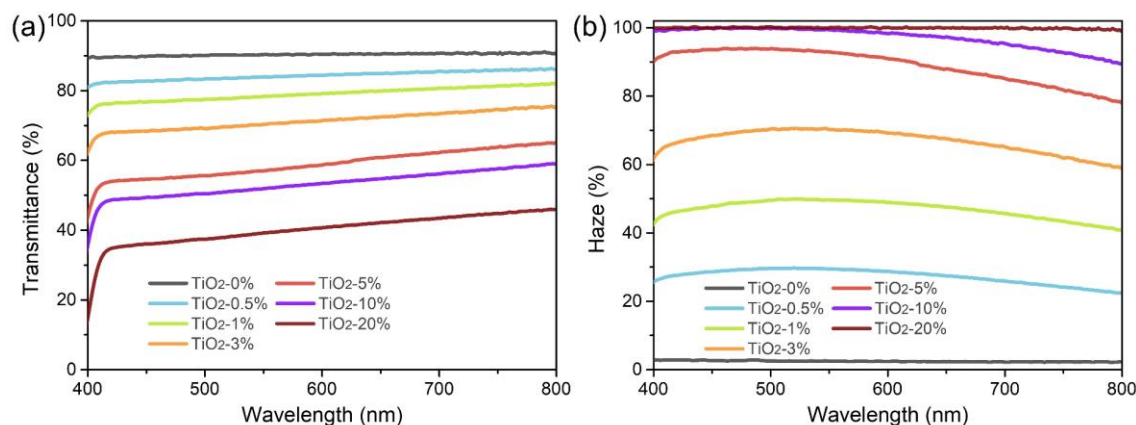
Figure 6.7 (a) Transmittance spectra and (b) haze spectra of the TiO_2/PS films embedding different mass fractions of TiO_2 nanoparticles.[164] Reproduced with permission. Copyright 2024, Springer Nature.

Traditional methods involving high-refractive-index particles (such as TiO_2 nanoparticles) are investigated for comparison. PS films embedded with varying concentrations of TiO_2 nanoparticles (approximately 200 nm in diameter) were fabricated via drop-casting for optical analysis. The TiO_2 nanoparticles are conducted with surface modification to avoid aggregations. The transmittance and haze spectra of PS/TiO_2 films are depicted in **Figure 6.7**. As the loading of TiO_2 nanoparticles increases, the transmittance of the PS film decreases significantly. Additionally, owing to the high absorbance of TiO_2 nanoparticles in the low wavelength range, the transmittance spectra demonstrate a steep decrease in the deep blue spectral region. The haze of the PS/TiO_2 film steadily increases with the rising mass fraction of TiO_2 nanoparticles. Specifically, the TiO_2-20% sample demonstrates the highest haze value approaching 100%. However, its mean transmittance among the visible range is less than 40%.

A good balance of high transmittance and high scattering capability is difficult to achieve with the approach of embedding TiO_2 nanoparticles, due to their light absorption. In contrast, PS/PEG microporous film creates strong scattering based on the refractive index contrast between polymer and air without employing extra light-absorbing material. This enables a high retention of the transmittance. To prove the low light absorption of PEG polymer, a 5-μm-thick PEG thin film was coated onto a glass substrate to measure its transmittance. As a result, the PEG thin film (containing glass substrate) obtains an average transmittance of 90.3% across the visible wavelength range. It exhibits only a slight decrease in transmittance compared to the bare glass substrate, which has an average transmittance of 91.5%. This suggests a minor light absorption of PEG material.

For a detailed analysis of the scattering performance of the microporous PS/PEG films, an angular intensity distribution measurement of the transmitted light was conducted on the sample films with a laser beam serving as the testing light source. The angular distribution curves (normalized to the maximum value) are presented in **Figure 6.8**. The transmitted light through the PEG-0% sample highly concentrates at 0° angle, due to the lack of scattering. In contrast, a
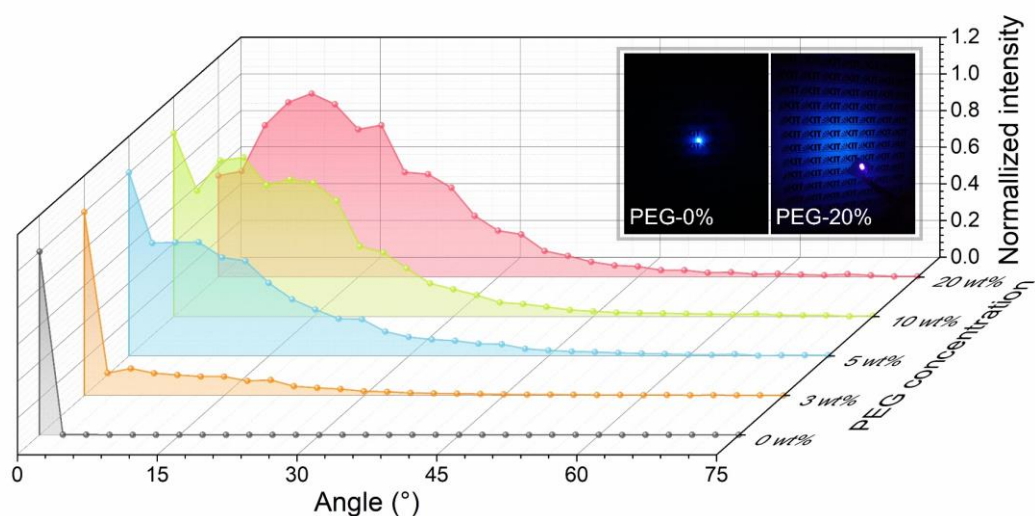
Figure 6.8 Normalized angular distribution of the transmittance intensity of a laser beam hitting microporous films with different PEG mass fractions. The inserts are the far-field transmission patterns of a blue laser beam passing through PEG-0% and PEG-20% samples, respectively.[164] Reproduced with permission. Copyright 2024, Springer Nature.

wider spreading angle of the transmitted light, indicative of superior scattering capability, is observed for films with higher PEG mass fractions. Moreover, as the concentration of PEG increases, the peak of the distribution curve shifts towards larger angles. The inserted photographs depict the far-field transmission patterns of a blue laser beam traversing a PEG-0% film (left) and a PEG-20% film (right). The distance from the sample film to the receiving plane is 15 cm. The pattern of the laser beam is significantly widened by the microporous structure, visually highlighting the superior scattering performance of the PEG-20% film.

6.3.2 Optical characterizations for microporous films with quantum dots

In this section, QDs are embedded into the PS/PEG microporous films to investigate the influence of the microporous structure. Before characterizing the luminescence performance of the QD films, the density distribution of QDs in the two polymer domains is first studied. For this, a PEG-50% thin film containing green QDs was fabricated by the spin-coating method at a spinning speed of 2000 rpm. A monolayer of the pore structure was obtained. Moreover, water was applied as the selective solvent to distinguish the two domains, as it can remove the PEG domains in the thin film but cannot dissolve the PS domains. The distribution of QDs can be observed by microscope with UV excitation. Microscopic images of the QD/PS/PEG thin film before and after water rinsing are presented in **Figure 6.9**. Due to its significantly lower thickness compared to drop-cast films, this thin film does not develop micropores with spherical shapes. Instead, it exhibits a two-dimensional phase-separating pattern. After 10 minutes of the water immersion process, the PEG domains are rinsed away, leaving PS composition with embedding QDs. From the image before water rinsing, a comparative analysis indicates that the fluorescence predominantly emanates from the PS domains. Therefore, it suggests that the majority of the QDs are distributed in PS domains after the phase separation.
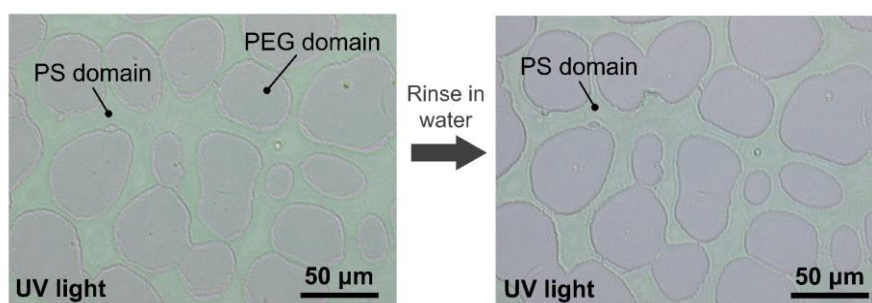
Figure 6.10 Microscopic images of a QD/PS/PEG thin film (PEG-50%) under 365 nm UV excitation before and after water rinsing, respectively.[164] Reproduced with permission. Copyright 2024, Springer Nature.

To demonstrate how the micropore structure impacts the photoluminescence intensity of the QD film in the color conversion process, we prepared and analyzed the optical properties, including PL intensity, absorption, and PLQY of multiple QD/polymer films. These films contained varying PEG mass fractions, ranging from 0 wt.% to 20 wt.%. For the preparation of the samples, dispersion of green-emitting CdSe/ZnS core-shell QDs (from Beida Jubang Co., Ltd) is equivalently added to a series of polymer blend solutions with corresponding PEG mass fractions. The concentration of QDs is 1 mg/ml and the total polymer concentration (PS and PEG) was 50 mg/ml in the prepared solution. These solutions were drop-cast onto glass substrates (16 mm × 16 mm) with consistent casting volumes. The resulting films had a thickness of approximately 25 µm after complete solvent volatilization. The characterizations of the films were conducted based on the 3M method for PLQY measurement,[130], [131] using an integrating sphere system with a blue laser (peak wavelength: 405 nm) as excitation. The power of the blue laser was 1.70 mW in the measurement.
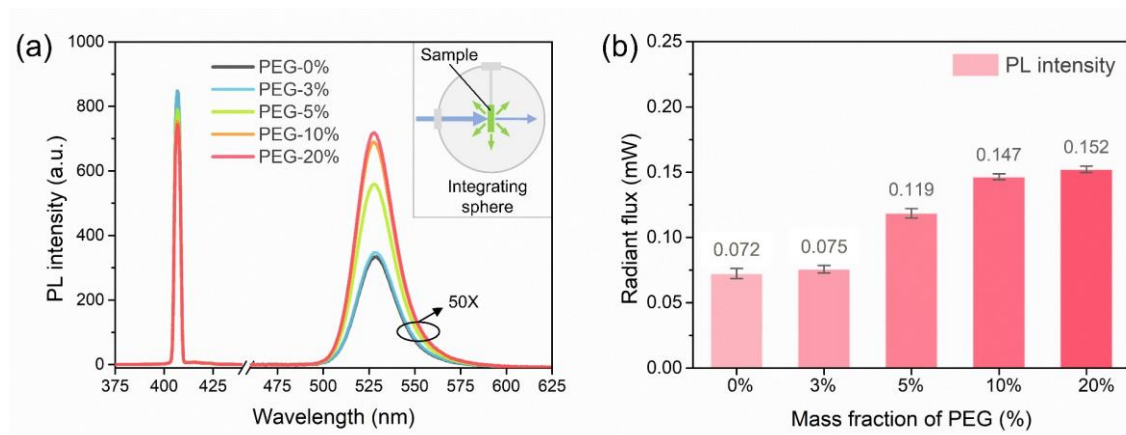
Figure 6.9 (a) PL spectra and (b) radiant fluxes of the emission peaks (475 nm-600 nm) of microporous QD/polymer films with different PEG mass fractions. The insert is the scheme for the PL measurement with an integrating sphere. [164] Reproduced with permission. Copyright 2024, Springer Nature.

As depicted in **Figure 6.10** (a), the peak value of the emission spectrum within the green range gradually increases with the rise in PEG mass fraction. In the measurement, the sample films are placed inside the integrating sphere and the overall emission is collected. In comparison to the PEG-0% sample, the enhancement observed in the PEG-3% sample is minimal due to the low density of micropores, which generate only slight light scattering. The enhancement in PL intensity becomes more noticeable when the PEG mass fraction lies within the range of 5 wt.% to 20 wt.%, attributed to a stronger scattering effect. Conversely, the peak value of retained excitation light in the blue spectral range gradually diminishes with increasing PEG mass fraction, owing to the improved light absorption of the QD film. The peak wavelength of the emission remains consistent across all samples, indicating that the phase separation process does not affect the emission properties of the QD material. By integrating the PL intensity over the wavelength range of 475-600 nm, the radiant fluxes of the emission peak of the QD films are calculated and depicted in **Figure 6.10** (b). The PEG-20% sample achieves the maximum radiant flux of 0.152 mW, representing a 110.0% increase compared to the PEG-0% reference sample (0.072 mW), demonstrating the profound enhancing effect of the microporous structure on the PL intensity.
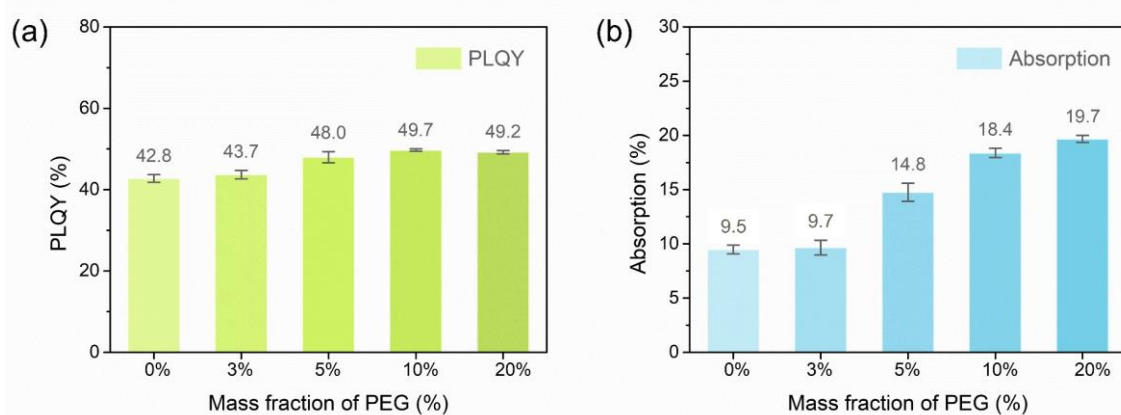
Figure 6.11 (a) PLQYs and (b) absorptions of microporous QD/polymer films with different PEG mass fractions. [164] Reproduced with permission. Copyright 2024, Springer Nature.

To elucidate the mechanism for the PL enhancement in detail, PLQYs and absorptions of the films are quantitatively studied. Here, absorption refers to the portion of the excitation light intensity absorbed by the QD nanoparticles to the total excitation light intensity. As shown in **Figure 6.11** (a), the PLQY initially rises with increasing PEG mass fraction slightly and then saturates when the PEG concentration is beyond 10%. This trend arises because the emission light from QDs experiences waveguiding within a dense encapsulating matrix, thereby causing a serious reabsorption effect within the matrix, suppressing the PLQY value.[96] Addressing this, micropores with an appropriate density in the film scatter the waveguided photons emitted by QDs and reorient them to a potential outcoupling direction, reducing the reabsorption of emitted light. However, excessive light scattering within the QD film also enhances light trapping and subsequent reabsorption. The overall effect on PLQY arises from the interplay between these two competitive mechanisms. In this case, the optimal balance is observed in the PEG-10% sample which exhibits the highest PLQY. In **Figure 6.11** (b), the film samples with higher PEG mass fractions demonstrate significantly greater absorption to the excitation. Besides, the absorption of the QD film shows a strong correlation with the radiant flux intensity of

the sample, suggesting that the increased absorption of QD film predominantly drives the PL enhancement. Additionally, the low light absorption of the PEG polymer has been demonstrated by transmittance characterization. This implies that the enhanced blue light absorption of the QD film stems from the strengthened scattering effect rather than the introduction and increased concentration of PEG polymer.
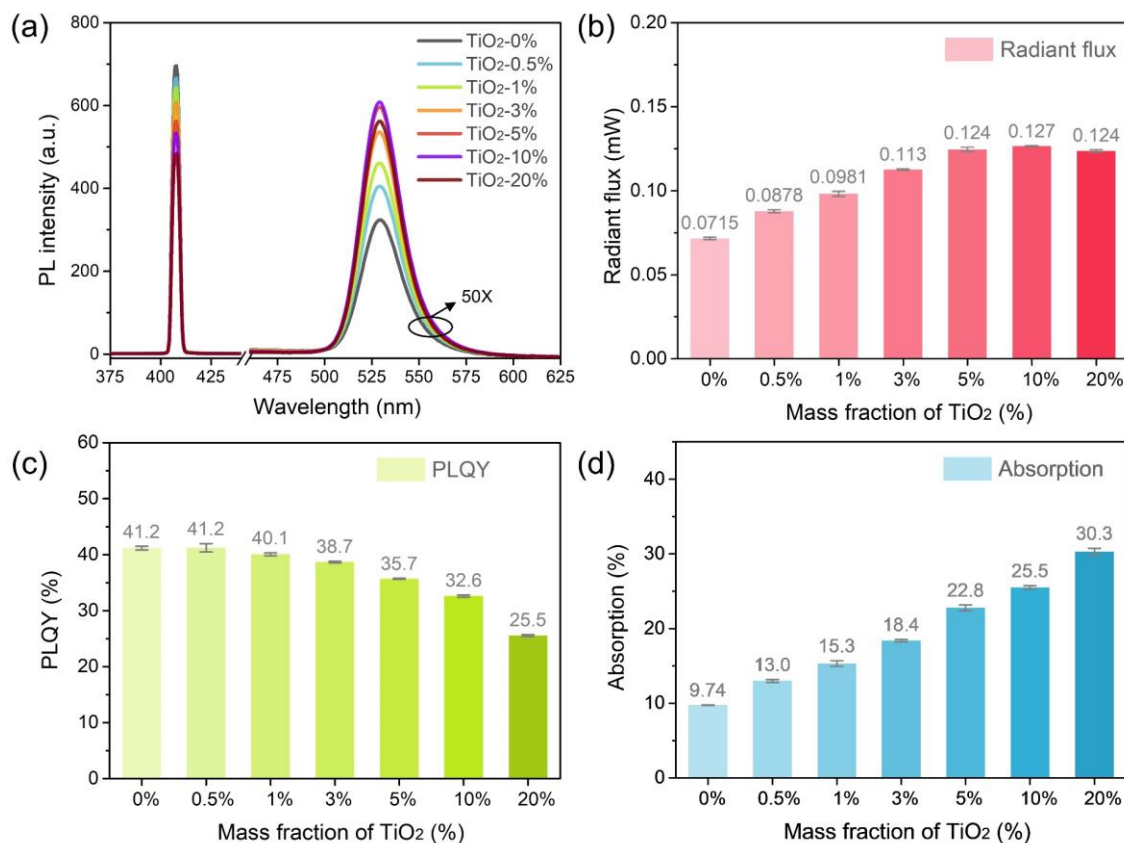
Figure 6.12 (a) PL spectra, (b) radiant fluxes of the emission, (c) PLQYs, and (d) absorptions of TiO_2 embedding QD/PS films with different mass fractions of TiO_2 nanoparticles.[164] Reproduced with permission. Copyright 2024, Springer Nature.

As a reference, QD films embedded with TiO_2 nanoparticles (diameter of around 200 nm) with varying concentrations were prepared and investigated with the same characterizations. The results are shown in **Figure 6.12**. The spectra of the samples exhibit a gradual decrease for the residual excitation peak in the blue wavelength range, indicating that the light absorption of the films is augmented with increasing concentration of TiO_2 nanoparticles. Compared to the QD film without embedding TiO_2, the samples containing TiO_2 obtain remarkable improvements in the emission peak, while the TiO_2-10% sample achieves the highest PL intensity. Furthermore, the emission peak of the TiO_2-20% sample is slightly lower than that of the TiO2-10% sample, attributed to TiO_2 overloading causing increased blue light absorption within the TiO_2 itself. Here, part of the excitation light absorbed by the TiO_2 nanoparticles cannot be converted to emitting light but generates extra heat, reducing the PLQY and stability of QD film. The PLQY and absorption diagrams reveal a clear trend: the increasing mass fraction of TiO_2 nanoparticles reduces the PLQY of the QD film while significantly enhancing light absorption. The overall emission intensity represents a compromise between diminished PLQY and heightened absorp-

71

tion for the excitation light. Consequently, the maximum radiant flux of the emission (475 nm to 600 nm) is achieved when the mass fraction of TiO_2 nanoparticles is 10%. Compared to the QD film without embedding TiO_2 nanoparticles, the maximum enhancement in radiant flux is calculated at 76.6%. The PL enhancement is lower than that of microporous PS/PEG/QD films.
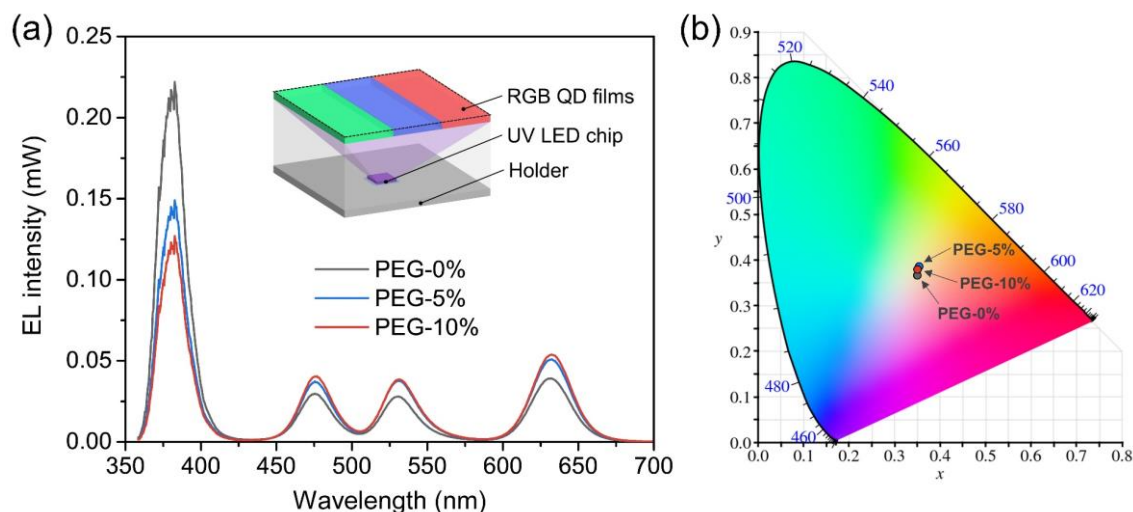
Figure 6.13 (a) EL spectrum of WLEDs incorporating QD films with different PEG mass fractions. The insert is the schematic of the architecture of the WLED. (b) Color coordinates of the WLEDs.[164] Reproduced with permission. Copyright 2024, Springer Nature.

To validate the adaptivity of the microporous structure in practical applications, we build and characterize various QD-WLED deceives, which consist of a UV LED chip as a pumping source and multi-color QD films as remote color conversion layers. In the preparation of the QD films, red, green, and blue (RGB) QDs are mixed with PS/PEG polymer blend solutions, respectively, and drop-cast on a glass substrate for acquiring multi-color QD films. These RGB QD films are integrated with a UV LED chip (365 nm, LG, UV-SMD-LED 3535) for generating white-emitting light. Three groups of RGB QD films are prepared with PEG mass fractions of 0%, 5%, and 10%, respectively. The spectral characterization is conducted at a voltage of 3.2 V and a driving current of 10 mA. Electroluminescence (EL) spectra of the WLEDs are shown in **Figure 6.13** (a). Compared to the PEG-0% sample, the EL spectra of PEG-5% and PEG-10% samples exhibited significant enhancements in the three emission peaks and a reduction in the remaining UV excitation, attributable to the enhanced UV absorption facilitated by the porous structure. The increased light absorption of the QD layer by enhanced scattering effect is beneficial to eliminating the retained excitation light for higher color purity in display applications.[181] Moreover, the EL intensity of the PEG-10% sample is only slightly higher than the PEG-5% sample, indicating its light scattering is nearly excessive. The luminous efficacies are measured 26.3 lm/W, 35.0 lm/W, and 36.4 lm/W for the PEG-0%, PEG-5%, and PEG-10% samples, respectively. A maximum enhancement of 38.4% is obtained. The results indicate that our concept is viable for QD films with different colors. **Figure 6.13** (b) exhibits the CIE color coordinates of WLED devices with various PEG mass fractions. The color coordinates of the WLEDs are similar, indicating the introduction of microporous structure effect barely to the color and hue of the devices.

6.4 Inkjet printing microporous quantum dot pixels

As a solution process, the phase separation method based on the PS/PEG polymer blend is highly compatible with the inkjet printing process for the patterning and pixelation of the QD color conversion layer. The polymer blend solution mixed with QDs can be conveniently adapted as inkjet printing ink. In addition, the microporous structure generated by the phase separation strategy causes little risk of nozzle clogging, as the porous structure is formed after leaving the printing nozzle. Compared to directly mixing nanoparticles as scatterers into inkjet printing ink, polymer blend solutions show superior homogeneity and less precipitation problem, potentially providing better production stability. Owing to the miniatured size and high velocity of the jetted ink droplets, the solidification of the polymer blend solution is significantly accelerated in the inkjet printing process. To address this issue, 1,2-dichlorobenzene with a high boiling point of 180.2 °C was applied as the solvent for the printing ink. The concentration of the polymer in the ink was reduced to 10 mg/ml as well to slow down the solidification.
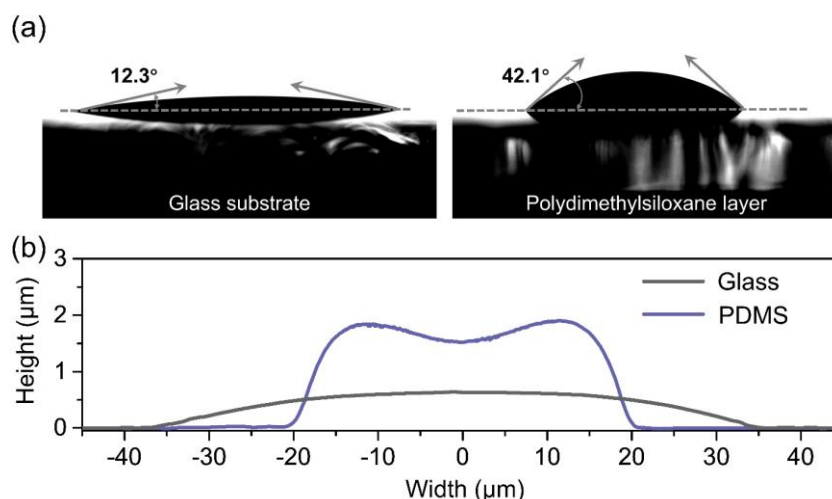
Figure 6.14 (a) Contact angle measurement (with 1,2-dichlorobenzene solvent) of a bare glass substrate (left) and a polydimethylsiloxane (PDMS) layer (right). (b) Profiles of the inkjet printing pixel on different substrates. [164] Reproduced with permission. Copyright 2024, Springer Nature.

The geometry of the inkjet-printed pixel is strongly affected by the surface tension of the substrate. To obtain a higher aspect ratio and smaller pixel size, a polydimethylsiloxane (PDMS) layer was introduced to the substrates for increasing surface tension. To evaluate the contact angle of the PDMS interlayer, polydimethylsiloxane and curing agent were mixed and spin-coated onto a glass substrate at 2000 rpm for 30 seconds and then cured on a hot plate at 100 °C to form a thin PDMS layer. For comparison, a bare glass substrate treated with 3 minutes of oxygen plasma was also included in the measurement. 1,2-dichlorobenzene with a droplet volume of 5 microliters was used for testing. As shown in **Figure 6.14** (a), the contact angle for the polydimethylsiloxane interlayer is 42.1°, which is much larger than that of the bare glass substrate (12.3°). The larger contact angle resulting a higher aspect ratio and smaller diameter for the inkjet-printed pixels. Profiles of the PEG-0% pixels printed on the two substrates (measured by Dektak XT) are compared in **Figure 6.14** (b). Pixel on PDMS substrate demonstrates a

reduced diameter and larger height. Thus, the PDMS interlayer is incorporated in the following printing process.
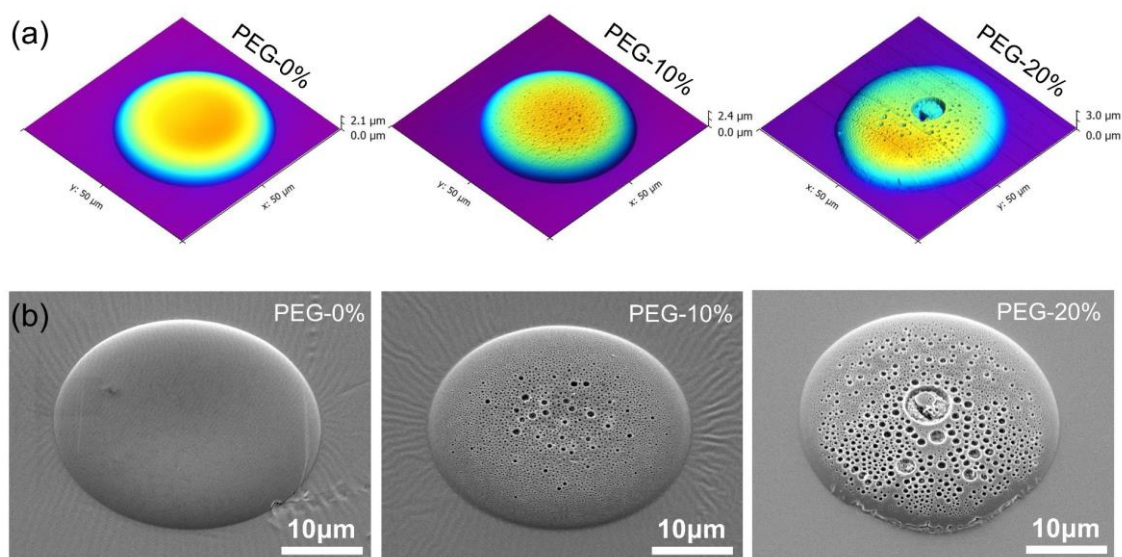
Figure 6.15 (a) AFM images and (b) SEM images (45° tilted) of inkjet-printed QD pixels with different PEG mass fractions.[164] Reproduced with permission. Copyright 2024, Springer Nature.

The AFM and SEM images of inkjet-printed QD pixels featuring various PEG mass fractions are exhibited in **Figure 6.15** (a) and (b). The PEG-0% pixel exhibits a smooth upper surface with a slight sag at its center. It originates from a slight coffee ring effect during the solvent evaporation. In contrast, the presence of PEG results in the formation of dense micropores on the surface of the PEG-10% pixel. Compared to the drop-cast PEG-10% film, the PEG-10% pixel shows a smaller overall pore size and higher pore density, attributed to accelerated solvent volatilization. Furthermore, the solvent volatilization speed at the edge region of the pixel is faster than that at the center region, leading to variations in pore size and morphological uniformity of the pixel. Smaller pores are observed at the edge, while larger ones occur towards the center. This effect is more pronounced in the PEG-20% pixel, where excessive coalescence of PEG domains results in a large void at the pixel center and lower regularity in pore distribution. SEM analysis reveals secondary porous structures on the inner surface of micropores, indicating a hierarchical pore arrangement within the pixel.

To demonstrate the capability of inkjet printing, a microscopic "LTI" pattern consisting of microporous QD pixels (PEG-10%) is presented in **Figure 6.16** (a) and (b). These QD pixels, approximately 30 μm in diameter, exhibit uniform round shapes. At higher magnification, dense and disordered micropores are visible. Uniform fluorescence intensities among the pixels can be observed with the excitation of UV radiation (365 nm) from beneath. Microscopic observation reveals heightened fluorescence intensity at micropore sites, with numerous bright circular spots indicative of enhanced light extraction. The spectral analysis of the QD pixel arrays is depicted in **Figure 6.16** (c), showcasing the PL spectra of printed samples with varying PEG mass fractions, all excited by a blue laser (405 nm) at a consistent power of 1.70 mW. Compared to the PEG-0% sample, the PEG-10% sample exhibits increased emission intensity by 35.3%. The PEG-20% sample shows diminished PL intensity, contrary to the observations in drop-cast films.
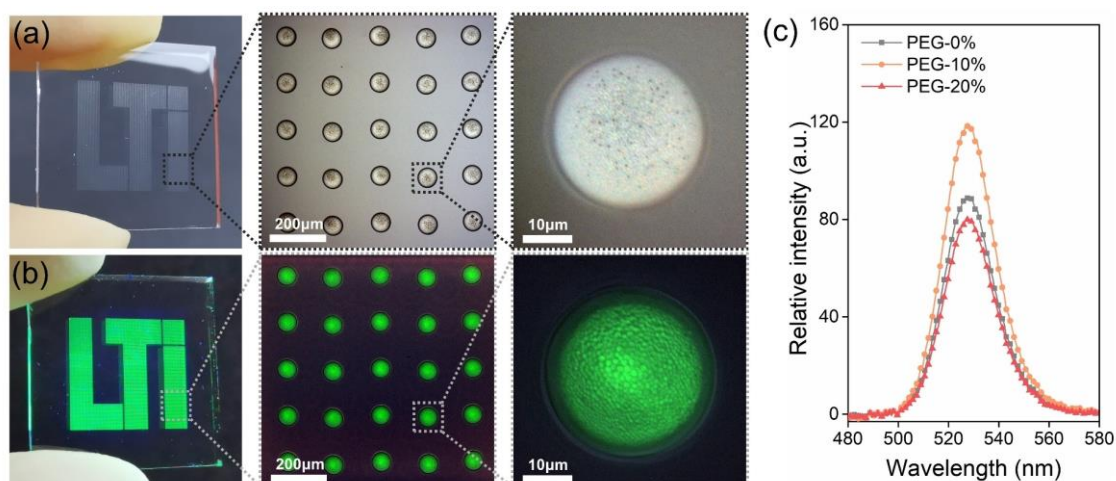
Figure 6.16 Photographs and optical microscopic images of the inkjet-printed microporous QD pixel array (PEG-10%) under (a) ambient light, and (b) UV excitation. (c) PL spectra of the QD pixel arrays with different PEG mass fractions.[164] Reproduced with permission. Copyright 2024, Springer Nature.

This discrepancy is attributed to accelerated solvent volatilization in inkjet printing, resulting in a denser micropore structure and intensified scattering despite equivalent PEG mass fractions. Hence, the reduced PL intensity is ascribed to excessive light scattering, potentially trapping emitted light within the pixel and causing significant reabsorption of QDs. The accelerated solvent volatilization also impacts pixel morphology. For instance, micropores at the edge region of a pixel may be smaller than the Mie scattering regime, generating inadequate scattering. Besides, the peak emission wavelengths of the samples remain the same, indicating that the printing process and PEG porogen do not impact the fluorescence property of QDs.
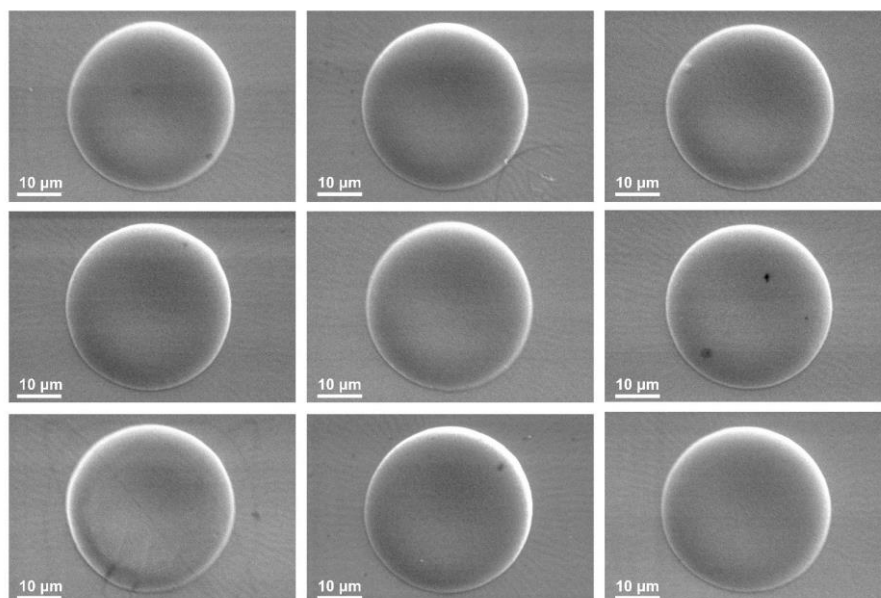
Figure 6.17 SEM images of the inkjet-printed QD pixels at 9 different spots of PEG-0% sample.[164] Reproduced with permission. Copyright 2024, Springer Nature.

To quantitatively assess the morphological consistency of inkjet-printed pixel arrays, SEM images of pixels from nine distinct locations on the PEG-0%, PEG-10%, and PEG-20% samples are presented in **Figure 6.17** to **Figure 6.19**, respectively. Micropore diameters on PEG-10% and PEG-20% samples were determined from these images, and the resulting statistics are depicted in the accompanying frequency distribution diagrams.
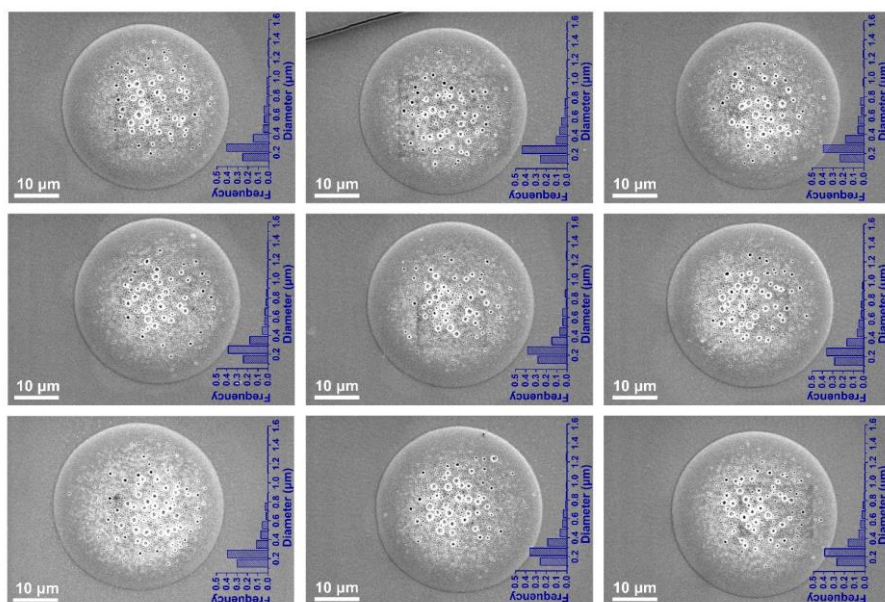
Figure 6.19 SEM images of the inkjet-printed microporous QD pixels at 9 different spots of PEG-10% sample. The inserts are the frequency distribution diagrams of the diameter of the micropores.[164] Reproduced with permission. Copyright 2024, Springer Nature.
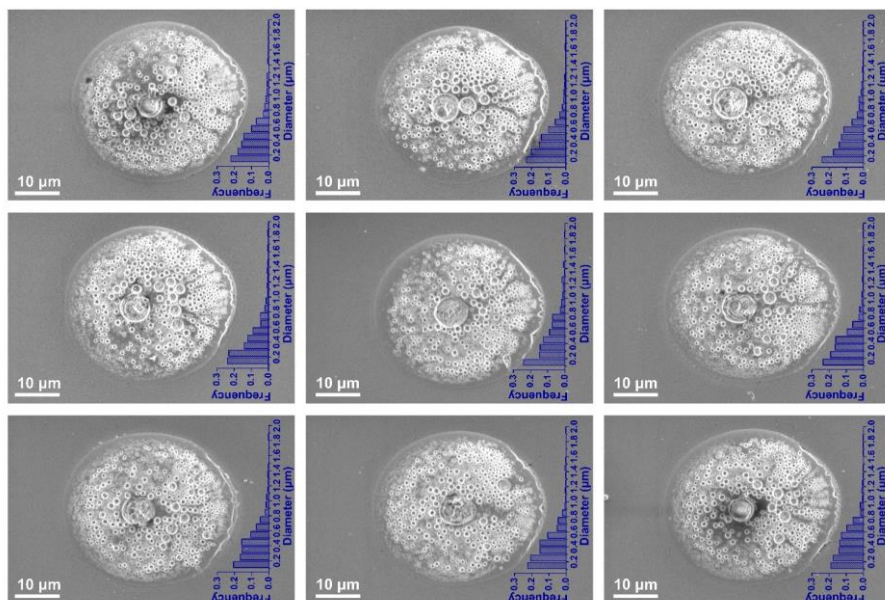
Figure 6.18 SEM images of the inkjet-printed microporous QD pixels at 9 different spots of PEG-20% sample. The inserts are the frequency distribution diagrams of the diameter of the micropores.[164] Reproduced with permission. Copyright 2024, Springer Nature.

Notably, all three samples exhibit good uniformity in pixel size. Furthermore, even though micropore distribution appears random within individual pixels, the PEG-10% sample displays a consistent frequency distribution of pore sizes across the nine pixels. Conversely, due to the higher PEG mass fraction and intensified micropore coalescence during phase separation, the PEG-20% sample demonstrates poorer morphological uniformity. Large pores can be observed at the centers of the pixels and a big diameter difference is shown between the center region and the edge region. Thus, an excessive PEG could lead to more defects in the morphology.
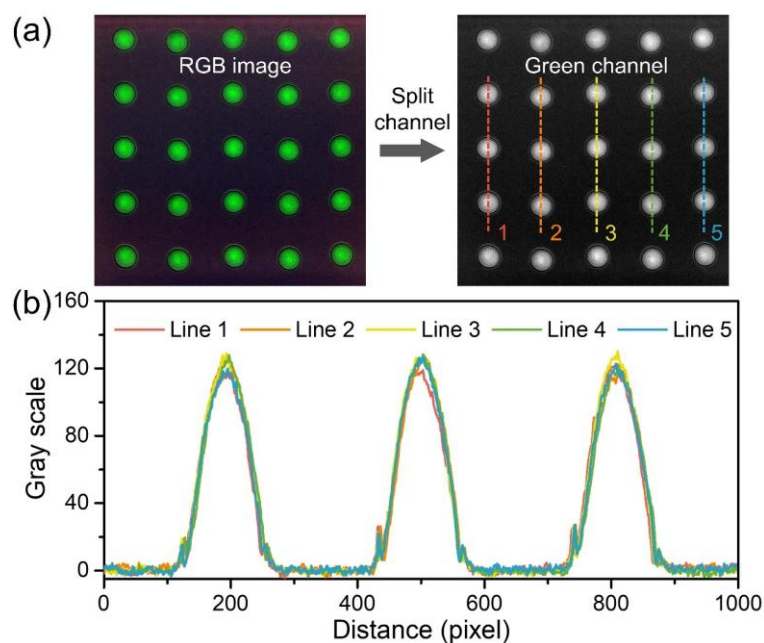
Figure 6.20 (a) Illustration of the channel splitting and extraction of the grayscale profiles. (b) Gray scale profile of the fluorescent image of the microporous pixel array (PEG-10%).[164] Reproduced with permission. Copyright 2024, Springer Nature.

To investigate the uniformity of the emission intensity among microporous QD pixels, the green color channel of the fluorescence microscopy image depicting the PEG-10% sample is split (via ImageJ software) and presented in **Figure 6.20**. The green color channel represents the emission intensity of QDs. The corresponding grayscale profiles across three QD pixels (identified by dashed lines each) are plotted as illustrated in the figure. By comparing the grayscale profiles of the green channel, uniformity of emission intensity can be demonstrated. The considerable overlap observed in the grayscale profiles indicates an adequate uniformity in the PL intensity of microporous QD pixels. The micropores on the QD pixels do not impact the emission uniformity in the macroscale.

A micro-spectroscopy setup was utilized to characterize the emission spectrum of individual QD pixels obtained by inkjet printing. The setup comprises a 405 nm laser source (Thorlabs, LP405-SF10), a spectrometer (Ocean Optics, HR2000CG-UV-NIR), and an optical microscope (Nikon, TE2000U). During the measurement, as depicted in **Figure 6.21** (a), the samples are positioned upside-down above the objective lens. A blue laser beam serves as the excitation light is directed and focused on a QD pixel through the microscope. The emitted light from the QD pixel is collected and directed to the spectrometer via the microscope. **Figure 6.21** (b)

shows a bright-field microscope image of a QD pixel solely excited, showcasing distinct green emission from the QD pixel while neighboring pixels remain non-luminescent. In this way, the spectrum of an individual QD pixel can be obtained for analysis.
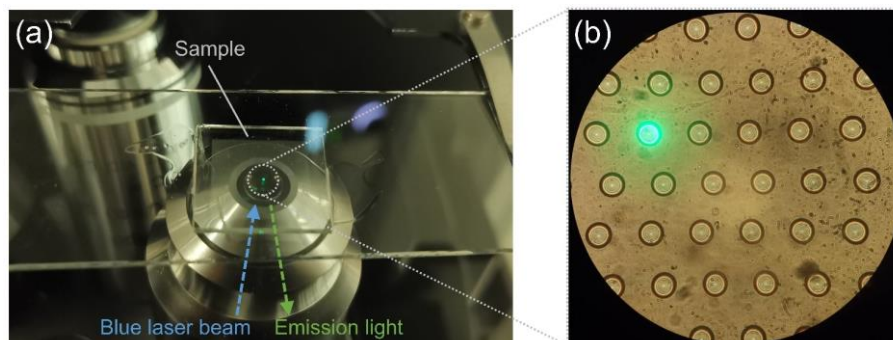
Figure 6.21 (a) Photograph of the micro-spectroscopy system with a measuring sample. (b) Bright-field microscope image of a QD pixel solely excited by a blue laser during the measurement.[164] Reproduced with permission. Copyright 2024, Springer Nature.

In the measurement, the power of the blue laser was set to 1.0 mW, and 20 pixels of each sample were individually characterized for comparison. The normalized emission spectra and corresponding color coordinates of pixels from PEG-0%, PEG-10%, and PEG-20% samples are illustrated in **Figure 6.22**. Consistent with morphological characterization, the normalized emission spectrum and color coordinates of PEG-0% and PEG-10% samples demonstrate significant overlapping and remarkable homogeneity, owing to their sound morphological uniformity and regular geometry of the micropores. PEG-20% exhibits poorer morphological uniformity and regularity, thus obtaining the least consistency in emission as well. Overall, a high color coordinate stability of the emission color of inkjet-printed pixels is manifested.
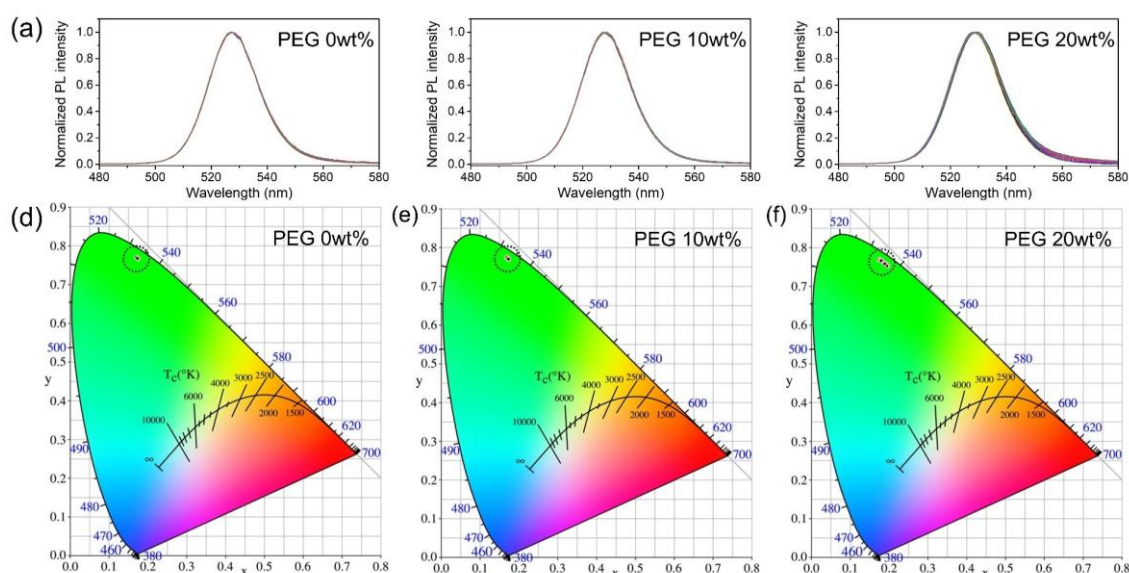
Figure 6.22 (a) Normalized emission spectra, and (b) color coordinates of the pixels of PEG-0%, PEG-10%, and PEG-20% samples, respectively.[164] Reproduced with permission. Copyright 2024, Springer Nature.

The optical characterizations for microporous polymer films and QD/polymer films systematically demonstrate the mechanisms of how the micropores improve the light scattering of the films, and how the strengthened light scattering effect enhances the PL intensity of the QD films. Moreover, inkjet printing microporous QD pixels with high luminescence intensity and high reproducibility are achieved. From the characterizations, the broad potential of this phase separation method is shown for the industrial production of QD-based color conversion films and QD pixel arrays.

6.5 Summary

In this chapter, we introduced a novel method for producing highly luminescent QD/polymer composites by incorporating a microporous structure optimized for optical scattering and light extraction. The fabrication method of the microporous structure was a self-assembly bottom-up approach, integrating the spontaneous phase separation of a polystyrene (PS) and polyethylene glycol (PEG) polymer blend system. The weight ratio between PS and PEG was the key parameter for controlling the morphology of the microporous network. The resulting structure enhanced light scattering within the QD film, thereby improving light absorption and outcoupling efficiency.

For polymer films devoid of QDs, the microporous networks exhibited haze values ranging from 2.4% to 97.6%, demonstrating the broad adjusting range and high controllability of this method to light scattering property. In the QD/polymer composite film, we observed a maximum 110% enhancement in PL intensity compared to a reference film lacking the microporous structure. By fine-tuning ink properties such as solvent and polymer concentration, we achieved uniform arrays of microporous QD pixels via inkjet printing, exhibiting regular round shapes and outstanding reproducibility. These porous QD pixels demonstrated a 35.3% increase in PL intensity compared to samples without micropores.

Our method is versatile and adaptable to various QD materials and micro-patterning techniques for QD-based display technologies. The high reproducibility of this method broadens the prospect for industrialization. Based on this research, the next objective could be developing a full-color display panel utilizing microporous QD pixels and practically combining the pixel layers with display devices, such as organic LED display panels and micro-LED panels.

7 Perovskite Quantum Dot Scintillators for X-ray imaging

This chapter focuses on developing a dual-organosilicon ligand system for metal halide perovskite quantum dots to improve compactness and reduce light scattering of the resulting films. The designed ligand system increases the molecular affinity among quantum dots and the encapsulation matrix, resulting in high quantum yield and outstanding long-term stability. The enhanced optical performance of the quantum dot film achieves a high spatial resolution in an X-ray imaging system. In Section 7.1, research background regarding encapsulation of perovskite quantum dots is introduced. Section 7.2 demonstrates the principle of ligand design and the corresponding synthesis process of the ligand. Section 7.3 presents the fabrication of the quantum dot film with the proposed ligand system. The optical performance and long-term stability of the quantum dot film are investigated in Section 7.4. Eventually, an X-ray imaging test in an indirect configuration is carried out incorporating the proposed quantum dot film in Section 7.5. A thorough study covering ligand design, film formation, optical characterization, and application of perovskite quantum dot film is conducted in this chapter.

Acknowledgements and Contributions

7.1 Introduction

All-inorganic CsPbX$_3$ (X = Cl, Br, or I) perovskite quantum dots (PQDs) have garnered significant attention due to their advantages of narrow emission bandwidth, broad variability of photoluminescence (PL) across 400-700 nm, and high PL quantum yield (PLQY).[214], [215], [216], [217] Given these promising features, CsPbX$_3$ QDs show huge potential for various optical and photonic applications, such as lasers,[218], [219] single-photon sources,[220], [221] light-emitting diodes (LEDs),[84], [222], [223] displays,[224], [225] and X-ray scintillators.[226], [227], [228] Moreover, the lead-halide PQDs exhibit relatively low formation energy and high tolerance to defects, facilitating the easy synthesis of highly luminescent materials at reduced temperatures with low expenses.[229] This aspect significantly expands their potential for mass production. However, their susceptibility to environmental stimuli such as heat, moisture, and UV radiation, stemming from their labile surface and metastable ionic structure, poses a challenge.[79], [230], [231]

Efforts to enhance the stability of PQDs have laid on three main strategies: composition engineering (e.g., forming heterojunction structures like CsPbBr$_3$/CsPb$_2$Br$_5$ composites),[232], [233] surface modification (e.g., employing multi-dentate surface ligands),[234], [235] and encapsulating within matrices (e.g., embedding PQDs in transparent inorganic oxides or organic polymers).[236], [237], [238], [239], [240] Of the abovementioned approaches, encapsulation utilizing a solid matrix offers efficient isolation of PQD materials from environmental stimuli such as moisture and oxygen, effectively enhancing their stability to a considerable extent. Polymers and inorganic oxides are the predominant matrices utilized for the solid-state encapsulation of PQDs.[74], [92] Encapsulation with inorganic oxides typically offers exceptional stability against heat and UV radiation due to the strong bonding energy of the oxide matrix.[241], [242] Nevertheless, PQDs encapsulated in an oxide matrix conventionally manifest as insoluble and crumbly powders, constraining their processability and application scope.[243], [244] Conversely, organic polymer matrices provide excellent solution-processability and film quality for PQDs. Yet, the conventionally employed long carbon chain ligands such as oleic acid (OA) and oleyl amine (OLA) are incompatible with polymer matrices due to the lack of molecular affinity, leading to significant PQD aggregations and deficient performance.[245], [246] Additionally, polymer-encapsulated PQDs exhibit inadequate thermal and photostability compared to oxide-encapsulated counterparts, as polymers are prone to aging and yellowing in harsh conditions.[247]

Organosilicon-based encapsulation offers an organic-inorganic hybrid approach, combining the advantages of both sides of inorganic oxides and organic polymers. This encapsulating matrix provides robust protection for PQDs meanwhile facilitating appealing processibility for the formation and patterning of PQD films.[248], [249] Compared to polymer encapsulation, the organosilicon matrix generates a stronger connection with PQDs owing to the massive O-Si-O bonds in the network, resulting in superior stability. Moreover, organosilicon molecules can crosslink via condensation reactions, enhancing the processability and compactness of the PQD films. However, current organosilicon-encapsulated PQD systems commonly incorporate inert long-chain ligands (e.g., OA) for the synthesis and stabilization of PQD dispersion, which hinders matrix crosslinking during film formation.[250] It leads to reduced transparency and increased surface roughness of the PQD film, limiting the full potential application of organosilicon-based encapsulation.[251], [252]

With addressing the challenges above, in this chapter, we develop a dual-organosilicon ligand system comprising (3-aminopropyl)triethoxysilane (APTES) and (3-aminopropyl)triethoxysilane with pentanedioic anhydride (APTES-PA) to fabricate high-performance PQD films. In this ligand system, inert long-carbon-chain ligands (such as OA and OLA) are replaced by APTES-PA ligands to improve the compatibility of the colloidal system. The APTES-PA molecule incorporates multiple silicon-based functional groups, facilitating its involvement in condensation reactions among silicate bonds for creating a well-crosslinked matrix. Meanwhile, it provides sufficient stabilization for the colloidal PQDs. Utilizing this designed ligand system, we successfully fabricate highly fluorescent PQD/silicone films with high transparency and reduced surface roughness. The compact encapsulation of the organosilicon matrix ensures decent stability of the resulting PQD films across various harsh environments. The optimized PQD films are subsequently applied as radioluminescence (RL) scintillators in an X-ray imaging system, achieving a remarkable spatial resolution exceeding 20 line pairs per millimeter (lp/mm).

7.2   Design and synthesis of organosilicon ligand

Aiming at achieving a high-resolution indirect X-ray imaging system based on PQDs, particular attention needs to be paid to the transparency and thickness of the PQD scintillator besides its light yield and stability. Indirect X-ray detection systems accomplish the imaging function by capturing the luminescence photograph of the scintillators. A high transparency of the scintillator enables a clear luminescence image due to the reduced disturbance from light scattering. The transparency of PQD film highly depends on the encapsulation strategy as the PQD nanoparticle itself causes rarely scattering and reflection owing to its small particle size. Particularly, the morphology of the encapsulating matrix, such as porosity and surface roughness, plays a key role in the overall transparency of the films. Thus, a compact and smooth film is desired for preparing the PQD scintillator. On the other hand, the increase of the scintillator thickness can cause significant blurring of the fluorescence image as well. As the captured luminescence photograph is the integration of the patterns among different thicknesses, the large thickness of the scintillator causes more serious blurring. To reduce the thickness of the PQD scintillator while maintaining sufficient X-ray absorption, a high concentration of PQD in the film is needed.

Addressing the concerns above, an encapsulating strategy based on the crosslinking of organosilicon ligands (e.g. APTES ligand) is selected for the fabrication of PQD films. Compared to the strategies that incorporate an extra encapsulating matrix to host PQDs and surface ligands, organosilicon-based encapsulation directly forms the barrier matrix by crosslinking among the surface ligands, free of introducing additional composition. It allows a higher PQD concentration in the resulting film. In this case, the thickness of the PQD scintillator can be reduced, improving the spatial resolution of the imaging system. However, existing organosilicon ligand systems for PQDs commonly contain inert long-carbon-chain ligands (e.g. OA) to provide adequate colloidal stability for PQD dispersion. As the inert ligands cannot participate in the crosslinking reaction, the existence of OA ligands consequently results in poor compactness and rough surface condition of the PQD films.

It is an ideal solution to replace the OA ligand with a new organosilicon ligand in the APTES-based encapsulation system to form a dual-organosilicon ligand group. Considered as a guideline for the design of the new ligand, this ligand molecule should contain a silicon-based functional group to participate in the condensation reaction for forming an encapsulation barrier. The size of the molecule needs to be relatively small to allow a high PQD concentration in the final solid film. To provide sufficient passivation and colloidal stability for the PQDs, the ligand molecule should be able to offer an anionic head group for anchoring on the PQD surface,[253], [254] as the APTES ligand has offered ammonium cation ($-NH_3^+$) head-group. Regarding the above requirements, the APTES molecule integrated with pentanedioic anhydride (APTES-PA) is designed, forming a dual-organosilicon ligand system together with APTES ligand for the passivation and encapsulation of PQDs.
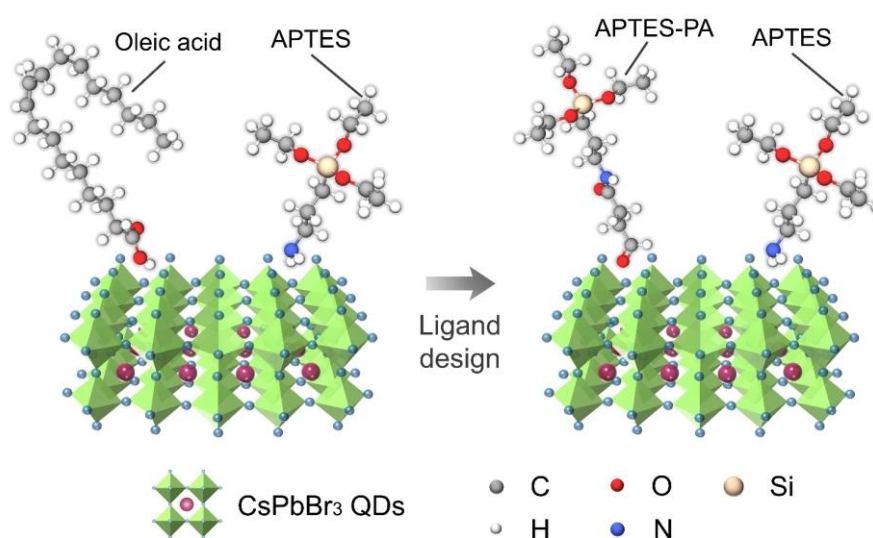
Figure 7.1 Illustrations of conventional APTES/OA ligand system (left) and proposed APTES/APTES-PA ligand system (right) on $CsPbBr_3$ QDs.[213] Reproduced with permission. Copyright 2024, American Chemical Society.

With the blueprint of the new ligand (named APTES-PA ligand), for better illustration, three-dimensional models of PQD crystals with different surface ligands were built. The PQD models capped with conventional APTES/OA ligand group and APTES/APTES-PA ligand group are illustrated in **Figure 7.1**. Compared to the OA ligand, the APTES-PA ligand shows a smaller molecule size and contains a carboxyl group (-COOH) as well. The smaller molecule size enables a higher PQD concentration and the carboxyl group is beneficial to the anchoring and passivation on the PQD surface.[255], [256] Moreover, the APTES-PA molecule contains a silicon-based functional group for the crosslinking reaction. By integrating the carboxyl group and silicon group in the molecule, the APTES-PA ligand can provide adequate colloidal stability as well as robust encapsulation to PQDs.
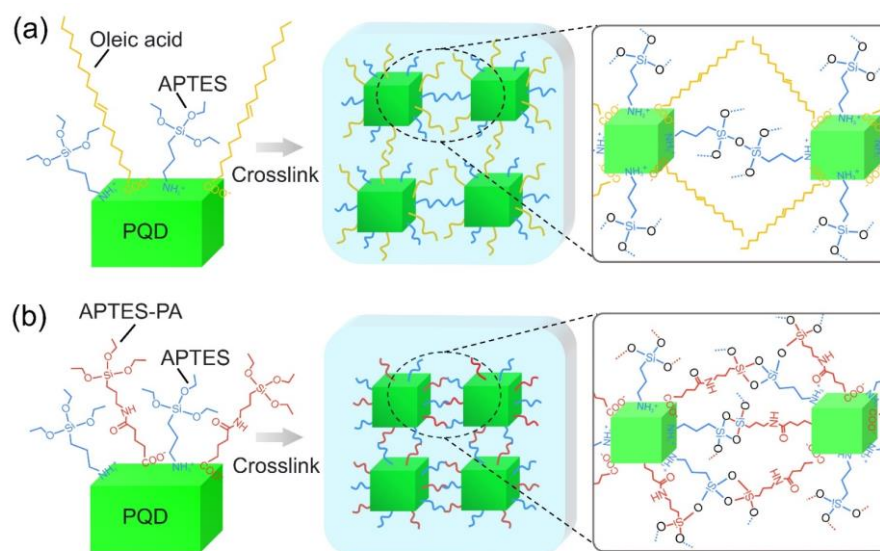
Figure 7.2 Schematics of the ligand molecules and illustrations of the condensation reactions of (a) conventional APTES/OA ligand system, and (b) proposed APTES/APTES-PA ligand system.[213] Reproduced with permission. Copyright 2024, American Chemical Society.

To demonstrate the advantages of the designed ligand system, schematics of the condensation reaction and film formation mechanism of the APTES/APTES-PA ligand group are illustrated in **Figure 7.2**, together with the conventional APTES/OA ligand group. For the APTES/OA ligand system, the long-chain OA ligands play a detrimental role in the condensation reaction for forming the solid organosilicon matrix due to their inertness. They mainly contribute to the surface passivation of the PQDs. Moreover, due to their large molecular length, the presence of OA molecules hinders the contacts among APTES ligands during condensation, resulting in insufficient crosslinking and inadequate compactness of the PQD/silicone film. In contrast, the designed APTES-PA molecule is relatively shorter than the OA molecule and it incorporates silicone functional groups. During the condensation process, the ethoxy-silane-ether groups that exist in both APTES and APTES-PA ligands are activated by trace water in the solvent or ambient air, facilitating the formation of extensive crosslinking Si-O-Si bonds and the solid matrix for $CsPbBr_3$ QDs.[257], [258] This dense crosslinking enhances the compactness and robustness of PQD film. Additionally, due to the reduced molecular size and higher crosslinking efficiency of APTES-PA ligands compared to OA ligands, fewer capping ligands are required to achieve an adequate encapsulation, potentially allowing for a higher PQD loading in the film.

The quality of surface passivation is another key performance to evaluate a ligand system for PQDs. As ligand debonding is a common problem for surface ligands, the performance of the capping ligands can be indicated by the binding energy between the ligand and the lattice surface of PQD.[256], [259] The theoretical binding energies of the ligand systems can be calculated via the density functional theory (DFT) method.[260], [261] The models of the ligand molecules and $CsPbBr_3$ crystal plane were built for the calculation, as depicted in **Figure 7.3** (a). The calculated charge density redistributions of the $PbBr_2$-rich (001) plane of $CsPbBr_3$ crystals attached with APTES/OA and APTES/APTES-PA ligands are shown in **Figure 7.3** (b). In both situations, the APTES ligands bind to the Pb atoms, exhibiting similar charge redistributions: electron accumulation space (depicted as yellow cloud) mainly located on the ammonium group and electron
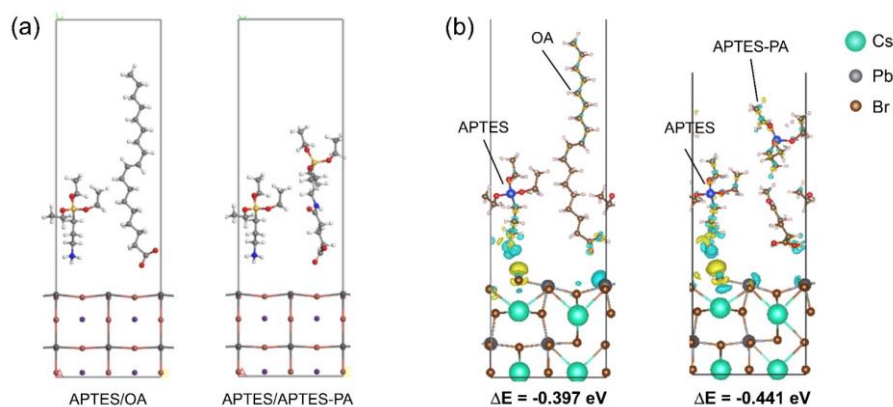
Figure 7.3 (a) Models of the ligand molecules and the CsPbBr$_3$ QD interface for DFT calculation. (b) Results of DFT calculation: charge density redistribution of the optimized CsPbBr$_3$-001 surfaces capped with APTES/OA and APTES/APTES-PA ligand groups, respectively.[213] Reproduced with permission. Copyright 2024, American Chemical Society.

dilution space (depicted as cyan cloud) along the surface Pb atoms. Notably, the APTES-PA ligand demonstrates a larger electron dilution cloud on the bottom of the molecule compared to the OA ligand when bound to the PQD surface. Consequently, the APTES/APTES-PA ligand group exhibits a higher total binding energy (-0.441 eV) compared to the APTES/OA ligand group (-0.397 eV) in absolute terms. This stronger binding of the proposed APTES-PA ligand to the PQD surface suggests superior surface passivation.
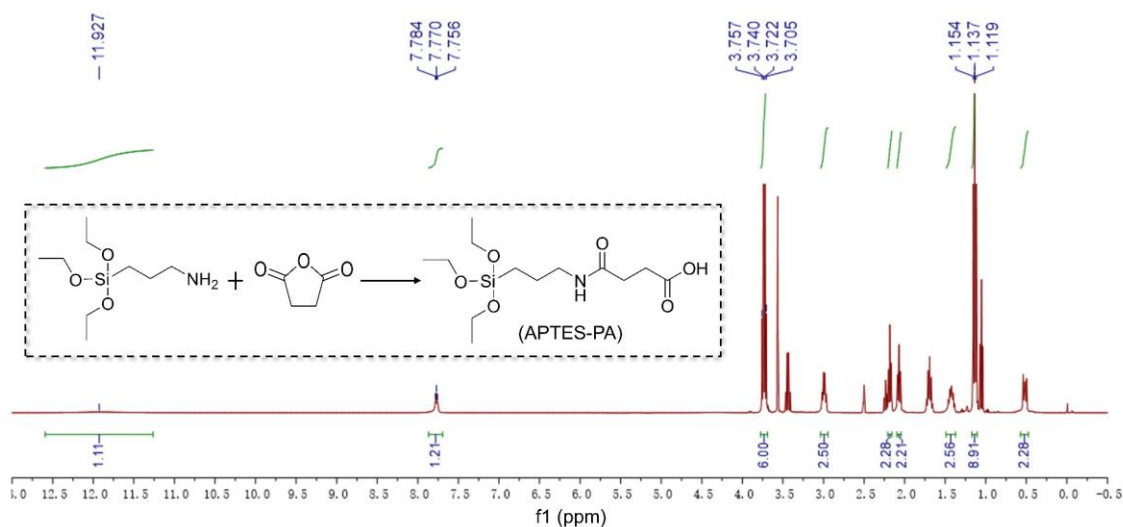
Figure 7.4 Hydrogen-1 nuclear magnetic resonance spectrum of the APTES-PA compound. The insert is the chemical equation of the synthesis of the APTES-PA ligand.[213] Reproduced with permission. Copyright 2024, American Chemical Society.

Lastly, to synthesize the designed APTES-PA ligand, a chemical reaction as shown in **Figure 7.4** was applied. In the practical synthesis process, we first dissolved 5 mmol of pentanedioic anhydride in 10 mL of tetrahydrofuran and then slowly added 5 mmol of APTES under stirring conditions at 65 °C. After a reaction duration of 12 h, the red crude product was obtained using a rotary evaporator. The amide reaction of primary ammonia and anhydride in the above process has a high yield (over 95%). Therefore, there is no further product purification. The whole

synthesis process of the APTES-PA ligand is efficient and simple. In addition, to certify the successful synthesis of the APTES-PA ligand, the hydrogen-1 nuclear magnetic resonance spectrum of the APTES-PA compound was measured and the result is shown in **Figure 7.4**. In the characterization, a portion of the synthesized APTES-PA compound was dissolved in deuterated DMSO solvent for the measurement. The nuclear magnetic resonance data obtained confirms the successful synthesis of the APTES-PA ligand which is consistent with the standard pattern and previously reported findings in the literature. [262], [263]

7.3   Fabrication of perovskite quantum dot film

The proposed APTES-PA ligand can be conveniently adopted into the ligand-assisted co-precipitation synthesis method for fabricating PQD dispersion.[44], [185] In the PQD dispersion, APTES and APTES-PA ligands play the roles of passivating the surface defects of PQDs and maintaining good dispersibility for the colloidal system. Through condensation reactions among the ligands, the PQD dispersion can directly form a solid PQD film without introducing extra material. Thus, the fabrication of the PQD film is a pure solution process, demonstrating good adaptability to numerous film-forming and pattering processes, such as spin-coating, drop-casting, spray-coating, and inkjet printing. As there is no patterning demand for scintillator film in X-ray imaging applications, a drop-casting strategy was chosen for the fabrication of PQD films due to its high usage rate for material and simple operation.
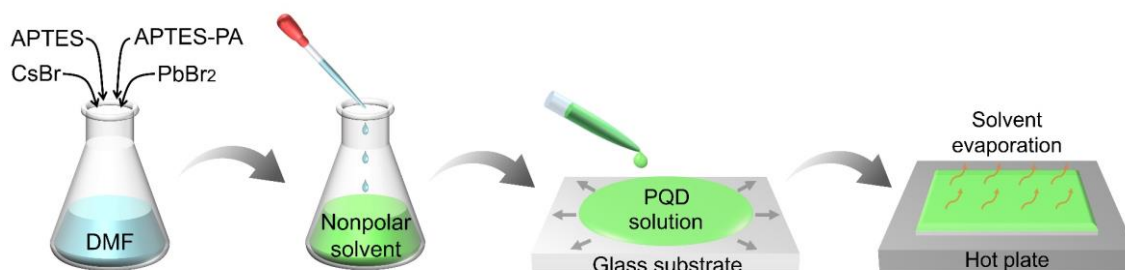
Figure 7.5 Illustration of the synthesis and film formation process of the PQD/silicone film based on APTES/APTES-PA ligands.[213] Reproduced with permission. Copyright 2024, American Chemical Society.

The illustrations of the synthesis of PQDs and the formation of PQD/silicone film are shown in **Figure 7.5**. In this fabrication process, CsBr, PbBr$_2$, APTES, and APTES-PA are first dissolved and mixed homogeneously in DMF solvent, followed by a rapid injection into the nonpolar solvent (e.g. toluene) for the recrystallization of CsPbBr$_3$ QDs. The capping ligands stabilize and passivate the PQDs in the solution while maintaining good dispersibility. The obtained PQD dispersion is then drop-cast on a cleaned glass substrate and subsequently heated at 65 °C in a vacuum environment for 10 min. The heating process induces the volatilization of solvent and the condensation reactions of the silicate bonds to generate a solid silicone-encapsulated PQD/silicone film on the substrate. With this method, by adjusting the drop-casting volume and the concentration of the PQD dispersion, the thickness of the resulting PQD film can be altered ranging from sub-micron scale to micron scale conveniently.
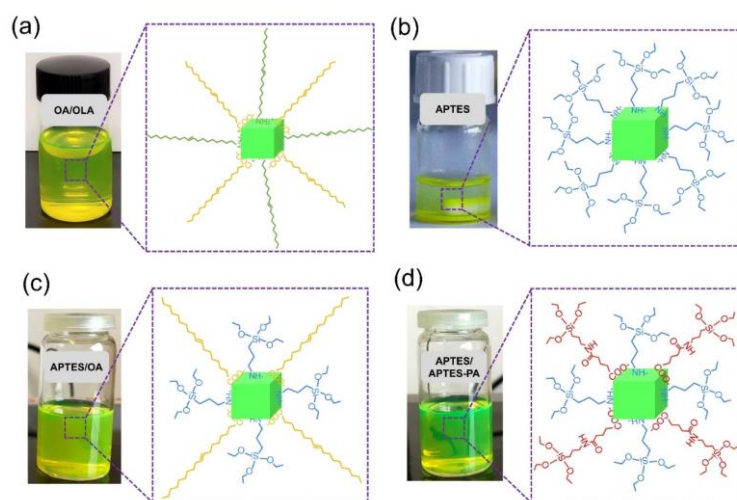
Figure 7.7 Photographs and illustrations of ligand capping of PQD toluene dispersions with different ligand groups.[213] Reproduced with permission. Copyright 2024, American Chemical Society.

Good dispersibility and colloidal stability of the PQD dispersion are required for the fabrication of PQD film. Note that the quality of the obtained $CsPbBr_3$ QD dispersion is crucial for the optical performance of the resulting PQD film. Problems of PQD aggregations and sediments might appear in the dispersion if the surface passivation of PQDs is insufficient, impairing the PLQY and processibility directly.[264] To demonstrate the dispersibility of the PQD dispersion with different ligand capping, photographs of PQD toluene dispersions with different ligand groups and the corresponding ligand schematics are depicted in **Figure 7.6**. The PQD dispersions containing OA/OLA, APTES/OA, and APTES/APTES-PA ligand combinations all exhibit clear appearances, indicating remarkable dispersibility in the solvent. However, the PQD dispersion solely capped by APTES ligands fails to sustain an adequate dispersibility of the PQD nanoparticles. Macroscale precipitation and stratification can be observed as the APTES ligand is unable to provide enough colloidal stability alone. Among them, the APTES/APTES-PA ligand pair is the only full-organosilicon ligand system with good maintenance of the dispersibility of PQDs.
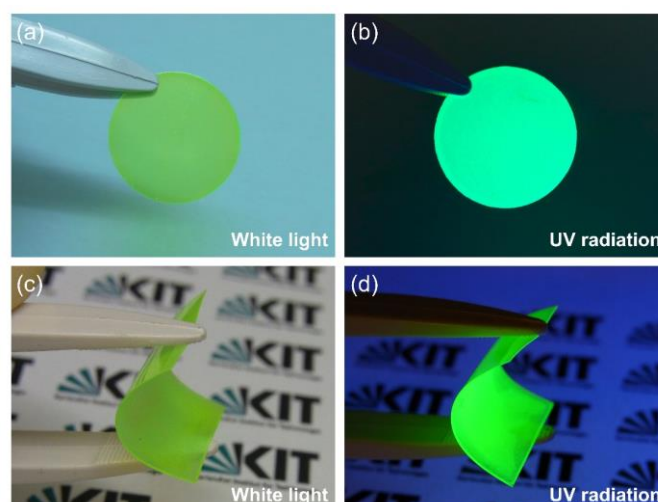
Figure 7.6 Photographs of (a)-(b) a PQD/silicone film on the glass substrate, and (c)-(d) a PQD/silicone film on flexible PET foil under white light and UV radiation (365 nm), respectively.[213] Reproduced with permission. Copyright 2024, American Chemical Society.

With the benefit of solution fabrication, the PQD/silicone composite is processable with a variety of substrates, such as glass slide and flexible polymer foil. **Figure 7.7** exhibits the photographs of the proposed PQD/silicone samples on a glass substrate and a flexible polyethylene terephthalate (PET) foil, respectively. The samples were prepared directly by drop-casting the PQD dispersion on different substrates. The PQD sample with glass substrate shows good uniformity and smooth surface while achieving bright fluorescence under UV excitation. The PQD sample deposited on PET foil demonstrates sound flexibility and strong adhesive to the foil after bending. Meanwhile, the corresponding curvature does not impair its high luminescence intensity.
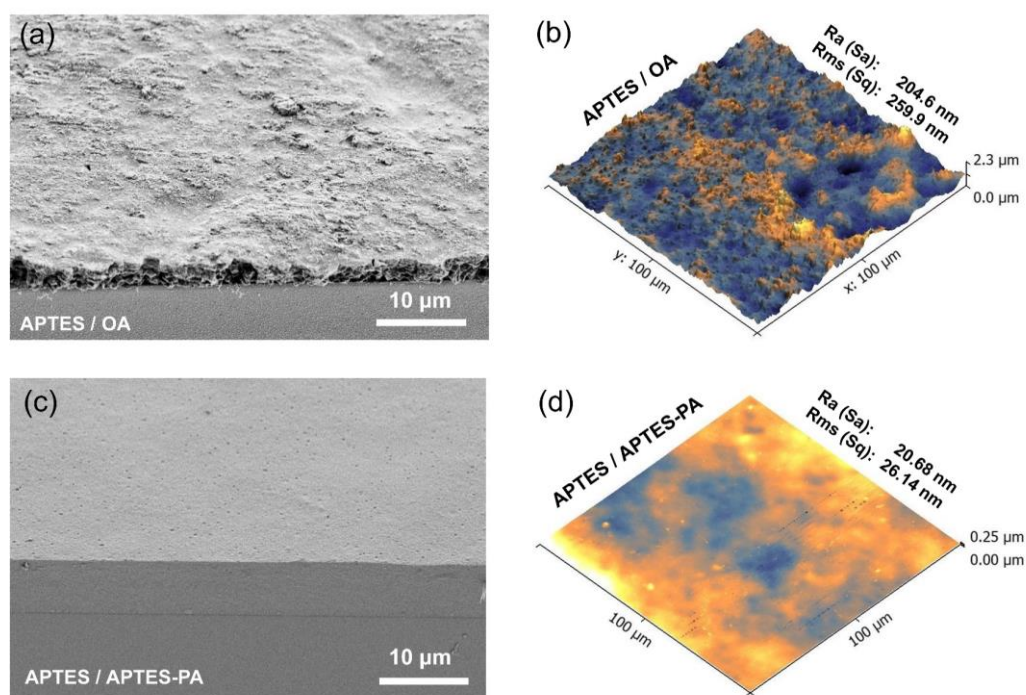
Figure 7.8 Cross-sectional SEM images (with a tilting angle of 45°) and AFM images of the PQD/silicone films with APTES/OA ligands and APTES/APTES-PA ligands, respectively.[213] Reproduced with permission. Copyright 2024, American Chemical Society.

The microscale morphology differs significantly between the PQD films with different ligand groups, resulting from the different molecular affinity between the ligand pairs. **Figure 7.8** shows the cross-sectional SEM images and the AFM images of the PQD films prepared with APTES/OA ligands and APTES/ APTES-PA ligands, respectively. For the conventional APTES/OA ligand system, owing to the relatively larger molecular size, the inclusion of long-chain OA molecules inhibits the interaction and bonding between APTES ligands during condensation. This leads to a rough surface texture and inadequate compactness in the PQD/silicone film. The inert OA ligand could potentially be embedded in the silicone matrix, resulting in an undesired porosity. Therefore, the sample shows a rough surface and crumbly encapsulating matrix in the images. A large surface roughness (Ra of 204.6 nm and Rms of 259.9 nm) is observed. As the APTES-PA ligand is thoroughly involved in the condensation reaction, the replacement of the OA molecule with the APTES-PA molecule profoundly improves the film quality and encapsulating efficiency with massive crosslinking. The SEM image of the APTES/APTES-PA sample

shows a smooth surface and a regular cross-section. As the sample film is mechanically broken for the characterization, neat cross-section of the film indicates a high compactness of the silicone matrix. The surface roughness of the APTES/APTES-PA sample is evaluated as 20.68 nm for Ra and 26.14 nm for Rms, respectively, which is significantly lower than that of the APTES/OA sample.
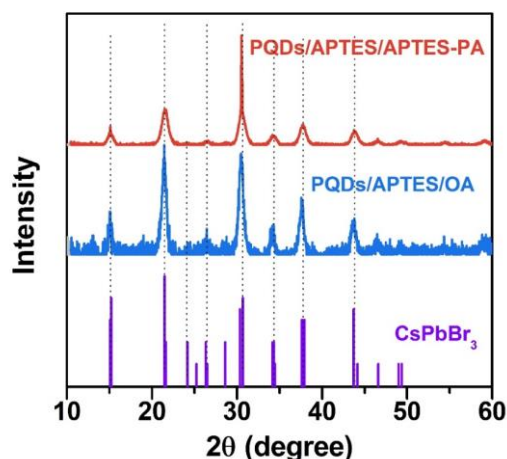
Figure 7.9 X-ray diffraction patterns of the obtained PQDs with APTES/APTES-PA ligands (red line) and APTES/OA ligands (blue line), as well as a standard pattern chart of $CsPbBr_3$.[213] Reproduced with permission. Copyright 2024, American Chemical Society.

Besides the morphology of the resulting PQD film, capping ligands significantly affect the crystal structure and optical performance of the PQDs as well. In the ligand-assisted co-precipitation approach for synthesizing PQDs, the perovskite nanocrystals start nucleating and growing when the precursor solution is injected into a poor solvent. The ligands capping on the crystal surface assist in the termination of crystal growth, playing a critical role in the crystal size and lattice structure. To further characterize the crystal quality of the synthesized PQDs with the proposed ligand group, X-ray diffraction (XRD) measurement is conducted on the PQDs with different ligand capping to demonstrate their crystal structures.[265], [266] The XRD patterns of PQDs with APTES/APTES-PA ligands (red line) and APTES/OA ligands (blue line) are shown in **Figure 7.9**, together with a standard pattern chart of $CsPbBr_3$. The XRD patterns of the two samples show similar diffraction peaks which are aligned with the expected standard pattern of $CsPbBr_3$. It indicates that there are no other non-luminescent phases synthesized with both APTES/APTES-PA and APTES/OA ligand systems.

The morphological properties of the PQD film, such as compactness and surface roughness, highly depend on the crosslinking efficiency of the ligands and the quality of the resulting silicone matrix. To evaluate the silicone matrix, Fourier transform infrared (FTIR) analyses were performed on the PQD/silicone films to certify the chemical bonds present inside.[267], [268] As depicted in **Figure 7.10**, the FTIR spectra demonstrate a significant increase in the wave-number ranges of Si-O-Si and Si-O-C bonds for APTES/OA and APTES/APTES-PA samples in comparison to the OLA/OA ligand group, confirming the sufficient hydrolysis reaction and effective encapsulation of the organosilicon-based ligands. Additionally, the APTES/APTES-PA sample exhibits a notable reduction in the characteristic peak of the C-H bond, which is

attributed to the absence of OA ligands. These results verify the intensive crosslinking of organosilicon ligands and the successful formation of the silicone matrix for encapsulating PQDs.
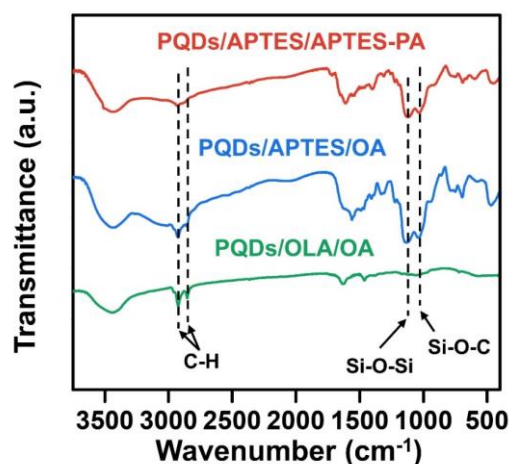
Figure 7.10 Fourier transform infrared (FTIR) spectra of the PQD composite films with different ligand groups.[213] Reproduced with permission. Copyright 2024, American Chemical Society.

7.4 Optical performance and stability of perovskite quantum dot film

Exceptional optical properties and adequate stability of the PQD film are the fundamentals for achieving high-performance X-ray imaging, as scintillation material. The development of a good ligand system should consider these two aspects.
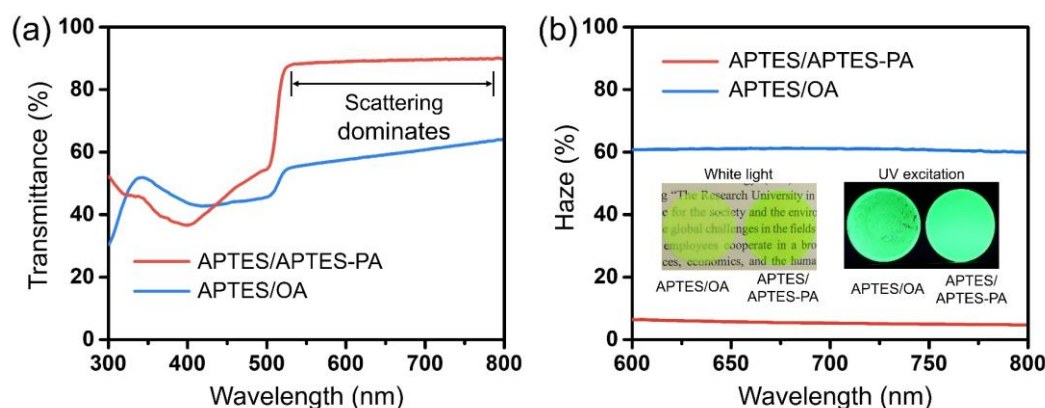
Figure 7.11 (a) Transmittance spectra, and (b) haze spectra of PQD/silicone films with APTES/APTES-PA ligands and APTES/OA ligands, respectively. The inserts are photographs of the corresponding sample films under white light and UV radiation.[213] Reproduced with permission. Copyright 2024, American Chemical Society.

Aiming at the application of indirect X-ray imaging, high transparency and low light scattering of the PQD film is able to improve the spatial resolution of the imaging system. The transmit-

tance and haze spectra of PQD films prepared with different ligand groups are shown in **Figure 7.11**. In this measurement, PQD films with a thickness of approximately 5 μm are deposited on glass substrates for analysis. The haze value is defined as the proportion of the diffused light (>5°) to the total transmitted light. The APTES/APTES-PA sample exhibits a significantly higher transmittance (with a mean value of 89%) than that of the APTES/OA sample (with a mean value of 59%) in the non-absorbing wavelength range (550-800 nm), indicating its remarkably high transparency. In the wavelength range below 500 nm, the transmittance values are inaccurate due to the disturbance of the color conversion effect. In addition, replacing the OA ligand with the APTES-PA ligand results in a remarkable reduction in the haze value for the PQD films from a mean value of 60% to 7%. The reduced light scattering can be visually demonstrated by the inserted photographs of the sample film. The letter pattern under the APTES/APTES-PA sample can be clearly read, meanwhile, the uniformity of the luminescence is enhanced. The deficient transmittance and high haze of the APTES/OA sample are attributed to the rough surface and microscale protrusions of the film which generate massive light scattering and reflection. In contrast, the APTES/APTES-PA sample with a dense matrix and smooth surface effectively reduces the scattering effect.
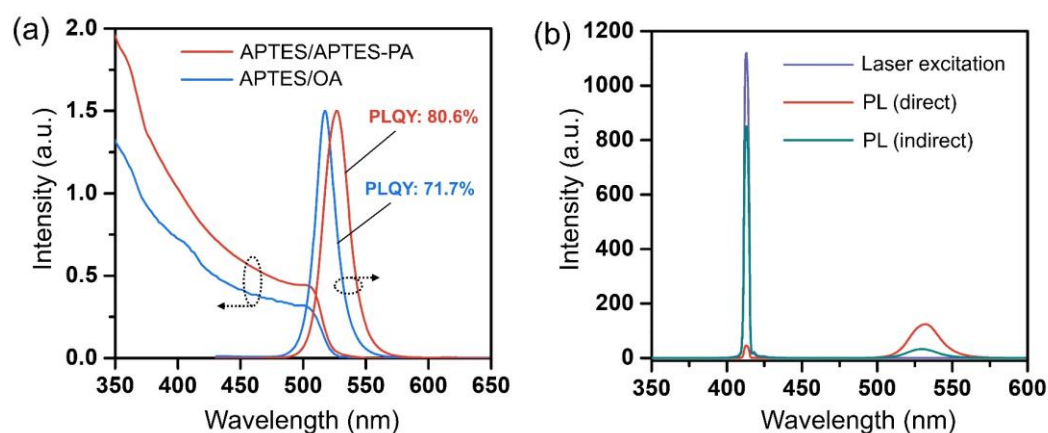
Figure 7.12 (a) Absorbance and emission spectra of the PQD composite films with different ligands. (b) Laser spectrum and PL spectra of a PQD film with APTES/APTES-PA ligands for the PLQY calculation.[213] Reproduced with permission. Copyright 2024, American Chemical Society.

The photoluminescence efficiency is another key performance of the PQD films. To investigate the luminescence property, spectroscopy characterization is conducted for the PQD films capped by different ligand groups with a thickness of around 5 μm and a QD concentration of 36 wt.%. As shown in **Figure 7.12** (a), the absorbance spectra of the composite films exhibit the classic characteristic profile of $CsPbBr_3$ QDs. Specifically, the PQD/APTES/APTES-PA film exhibits an emission peak centering at 526 nm with a full width at half maximum (FWHM) of 23 nm. This sample reaches a high PLQY of 80.6% with such a high PQD loading. In contrast, the APTES/OA sample with the same PQD loading exhibits a lower PLQY of 71.7% but a narrower FWHM of 20 nm. In **Figure 7.12** (b), the spectra for calculating the PLQY value of PQD/APTES/APTES-PA film are shown. A blue laser with a peak wavelength of 405 nm is applied as excitation. The diminished laser peak remaining in the blue band of the PL spectrum (red line) indicates a high PQD loading in the sample film. A high blue light absorption of 95%

is achieved with a low thickness of 5 μm, demonstrating an excellent color conversion capacity of the PQD film.

In the spectrum characterization, the high PLQY observed in the APTES/APTES-PA sample indicates effective surface passivation of the PQDs facilitated by the APTES/APTES-PA ligands. On the one hand, sufficient passivation enables a good dispersibility of the PQDs in the matrix and prevents PQD aggregations. It lightens the reabsorption effect of the emitted photons and thus increases the PLQY of the film. On the other hand, high-quality surface passivation inhibits non-luminescence recombination for PQD film, effectively elevating the luminescence efficiency. Besides a higher quantum yield, the APTES/APTES-PA sample exhibits a larger FWHM than the APTES/OA sample. The slightly broadened emission peak of this sample indicates a poorer size uniformity of the PQDs. It can be attributed to enhanced hydrolysis capability and efficiency of the ligands that potentially form undesired nano-capsules in the PQD dispersion, which will be elaborated on later.
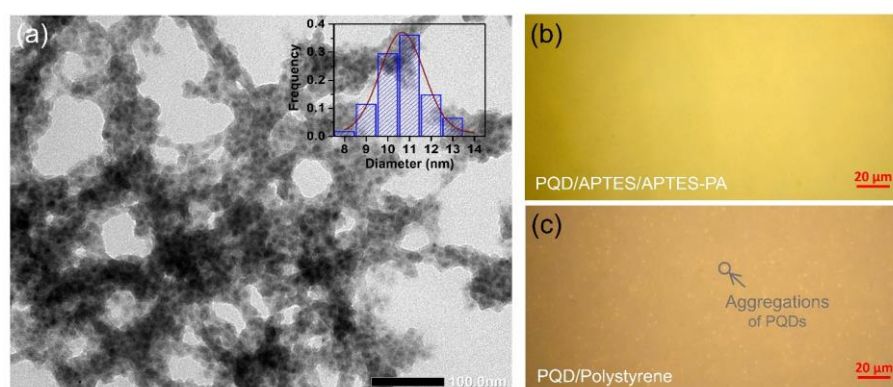
Figure 7.13 (a) Transmission electron microscopy (TEM) image of the PQD/silicone composite with APTES/APTES-PA ligands. The insert is the frequency distribution of the diameter of PQDs. Microscope images of (b) PQD/silicone film and (c) PQD/polystyrene film.[213] Reproduced with permission. Copyright 2024, American Chemical Society.

To investigate the distribution of the PQDs in the silicone matrix, transmission electron microscopy (TEM) and microscopy characterizations are conducted. **Figure 7.13** shows the TEM image and microscope image of the PQD/silicone film with APTES/APTES-PA as capping ligands. In the TEM image, the PQD/silicone composite showcases a uniform dispersion of PQDs without aggregation, even at a high loading of 36 wt.%. The shadows in the image are caused by the overlapping of the PQDs. The mean diameter of PQDs is calculated as around 11 nm. In the microscope images, a PQD film employing polystyrene (PS) polymer as an encapsulating matrix is incorporated as a reference. From the images, bare micrometer-scale aggregation is found for the PQD/silicone sample. The uniform and individual distribution of PQDs within the solid-state matrix is advantageous for preserving their optical properties and mitigating the reabsorption effect. In contrast, the PQDs encapsulated in PS polymer exhibit numerous aggregations on the micrometer scale, due to the poor molecular affinity between the capping ligands and polymer matrix.
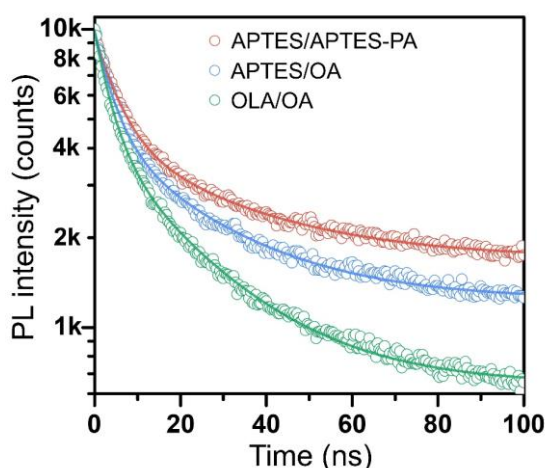
Figure 7.14 Time-resolved PL decay curves and the corresponding bi-exponential fitting curves of the PQD films with different ligand groups.[213] Reproduced with permission. Copyright 2024, American Chemical Society.

Besides the inhibited PQD aggregations, a high luminescence-recombination rate is another critical factor for achieving high PLQY. Addressing this, time-resolved PL decay measurements are conducted to investigate the charge-carrier dynamics within the PQDs. Corresponding bi-exponential fitting curves are presented and utilized to determine the average PL lifetime as well. As shown in **Figure 7.14**, the APTES/APTES-PA sample obtains the longest PL lifetime among the three samples. The intensity-averaged PL lifetimes obtained from fitting curves for the APTES/APTES-PA sample, the APTES/OA sample, and the OLA/OA sample were 22.7 ns, 20.0 ns, and 17.7 ns, respectively. Combining these results with the PLQY values, the radiative recombination rate (K_r) and nonradiative recombination rate (K_{nr}) of the films are calculated and summarized in **Table 7.1**. The longer average PL lifetime and lower K_{nr} observed in the APT-ES/APTES-PA sample, coupled with its high PLQY, indicate effective surface defect passivation facilitated by the proposed ligands within the organosilicon coating.

Table 7.1 Curve fitting parameters of the PL decays of the PQD films with different ligands.

	τ_1 (ns)	A_1 (%)	τ_2 (ns)	A_2 (%)	τ_{avg} (ns)	PLQY (%)	K_r	K_{nr}
APTES/APTES-PA	28.6	31.5	5.2	64.9	22.7	80.6	3.55×10^7	0.85×10^7
APTES/OA	24.5	37.4	4.2	62.6	20.0	71.7	3.58×10^7	1.41×10^7
OLA/OA	21.6	38.6	3.8	61.4	17.7	65.5	3.70×10^7	1.95×10^7

In the calculation, the PL decay curves are fitted with a double exponential decay function. τ_1 and τ_2 represent the fitted individual lifetimes while A_1 and A_2 represent the corresponding fractional contribution. The calculations of the average lifetime (τ_{avg}), the radiative recombination rate (K_r), and the non-radiative recombination rate (K_{nr}) are based on a double exponential fitting model.[269], [270]
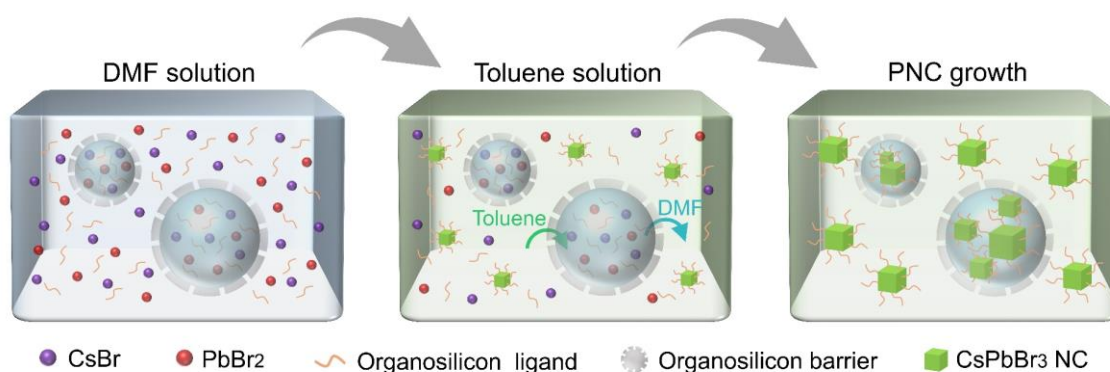
Figure 7.15 Schematic diagram of the synthesis process of PQDs with the dual-organosilicon ligand system and the formation of silicone nano-encapsules.[213] Reproduced with permission. Copyright 2024, American Chemical Society.

The superior hydrolysis efficiency of the dual-organosilicon ligand system also causes detrimental effects on the PQD film, such as the broadening of the emission peak. A higher FWHM of the emission spectrum normally indicates a poorer size uniformity of PQDs. This deficient uniformity of the PQD size should be attributed to the appearance of the undesired silicone nano-encapsules or nano-spheres that cause space confinement to the PQDs during crystal growth. Schematic illustrations about the details of the synthesis of PQDs and the formation of silicone nano-capsules are shown in **Figure 7.15**, to better demonstrate the principle. In the synthesis process, precursors and ligands are initially mixed in DMF solvent. The presence of trace water induces hydrolysis reactions of the organosilicon ligands. This can lead to the formation of silicone nano-encapsules which wrap the precursor solution inside. Subsequently, the solution is added into a poor solvent (e.g. toluene) under vigorous stirring to prompt immediate nucleation of PQDs. Once the PQDs have undergone complete crystal growth and stabilization, the synthesis of colloidal PQDs is finished. Notably, the nucleation and crystal growth of the PQDs is heavily influenced by the diffusion and mixing dynamics during the injection of precursor solution into the poor solvent. The silicone nano-capsules act as barriers, slowing down the diffusion rate of the encapsulated precursor solution and spatially confining the growth of PQD crystals, thus lowering the size uniformity of PQDs. In comparison to the conventional APTES/OA ligand system, the dual-organosilicon ligand system (APTES/APTES-PA) demonstrates higher efficiency and speed in hydrolysis reactions due to a higher density of crosslinkable molecules. Consequently, more undesired silicon nano-capsules are formed, resulting in a broader emission peak. To mitigate this effect, a solvent dehydration step or a nitrogen atmosphere could be incorporated into the synthesis process of PQDs with APTES/APTES-PA ligands.

Sufficient crosslinking of the capping ligands and the resulting compact encapsulation provides robust protection for PQDs, facilitating superior stability against environmental stimuli. **Figure 7.16** shows the normalized PL intensity of three different PQD films (PQD/APTES/APTES-PA, PQD/APTES/OA, PQD/PS) after heating to elevated temperatures and exposure to UV radiation, respectively. As a common encapsulation material, PS polymer packaged with CsPbBr$_3$ is incorporated in the test as a reference. The PQD concentration of all the PQD films here is 36 wt.%. For the thermal stability test, the heating process lasted 10 min for each temperature and the samples were cooled down to room temperature for PL intensity measurement. For the UV
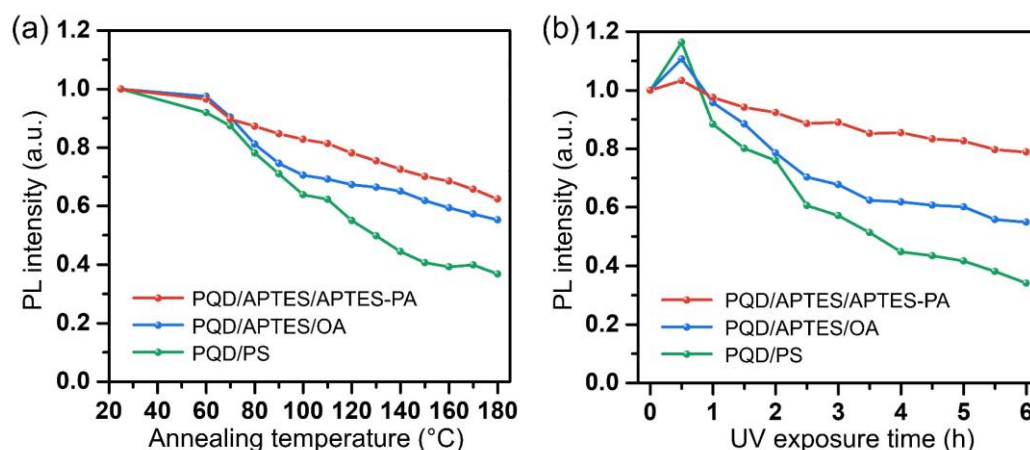
Figure 7.16 Normalized PL intensities of PQD/APTES/APTES-PA, PQD/APTES/OA, and PQD/PS films (a) after heating to different temperatures, and (b) under UV irradiation (365 nm) with the power of 1.5 mW/cm² for 6 h.[213] Reproduced with permission. Copyright 2024, American Chemical Society.

stability test, a UV radiation source (Proma 140007 UV exposer) with a power of 1.5 mW/cm² was used. As shown in **Figure 7.16** (a), the PQD/APTES/APTES-PA sample exhibits higher remaining PL intensity than the other two samples after heating. Specifically, the PQD/APTES/APTES-PA film maintains 62.3% of the initial PL intensity after the thermal treatment up to 180 °C, while only 36.8% and 55.2% of PL intensity are maintained for PQD/PS film and PQD/APTES/OA sample, respectively. The improved thermal stability can be attributed to the decent protection from the organosilicon matrix that suppresses the phase transition of PQDs at high temperatures.[271] Moreover, the thermal performance of the encapsulating matrix itself would affect the stability of PQD films as well.[186] As the glass transition temperature of the PS matrix is relatively low, morphology defects (such as air bubbles) are generated inside the PQD/PS film when the temperature is above 110 °C, resulting in severe impairment to the film quality. On the contrary, organosilicon-based encapsulation can prevent morphology defects and deformation in this condition. **Figure 7.16** (b) shows the temporal evolution of the PL intensities of the three types of PQD film under strong UV radiation. The PQD/APTES/APTES-PA sample reveals better photostability with a remaining PL intensity of 78.9% after 6 h of UV radiation, while the PL intensity of the PQD/PS sample reduces to 34.1% and the PL intensity of the PQD/APTES/OA diminishes to 55.0%. It indicates that the compact encapsulation of the silicone coating effectively inhibits the photodegradation of PQDs.

To investigate the water resistance of the PQD films, a water immersion test was conducted on PQD/APTES/APTES-PA and PQD/PS samples. In this test, the sample films were directly immersed in deionized water for degrading and taken out from the water for PL measurements. Due to the brittle nature and poor adhesion of the PQD/APTES/OA sample, part of the PQDs could be removed from the substrate during water immersion, impairing the measurement accuracy. Therefore, this sample was excluded from the immersion tests. As depicted in **Figure 7.17** (a), the fluorescence of the PQD/APTES/APTES-PA film remains stable during 6 hours of water immersion with a retained PL intensity of 99.3%, while the PL intensity of the PQD/PS film decreases to 71.7%. The reduction in PL intensity of the PQD/PS film can be attributed to incomplete encapsulation by the PS polymer, likely due to the high PQD loading. **Figure 7.17** (b) illustrates the remarkable resistance of the PQD/APTES/APTES-PA film to various organic
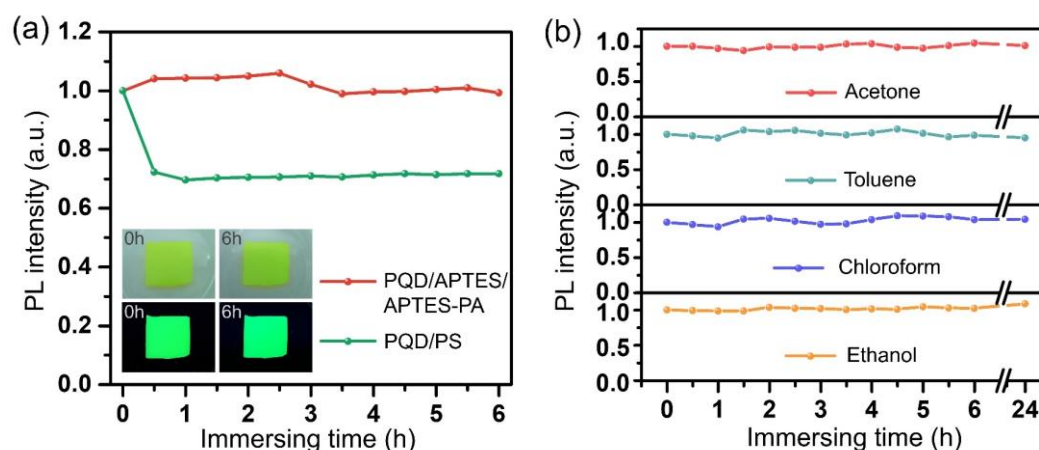
Figure 7.17 (a) Normalized PL intensity of PQD films after different immersing times in water. The inserts are the photographs of the PQD/APTES/APTES-PA sample before and after 6 h of water immersion under white light (upper row) and UV excitation (bottom row), respectively. (b) Normalized PL intensity of PQD/APTES/APTES-PA film after 24 h of immersion in acetone, toluene, chloroform, and ethanol, respectively.[213] Reproduced with permission. Copyright 2024, American Chemical Society.

solvents, including acetone, toluene, chloroform, and ethanol. In all the solvents, the PL intensity of the PQD/APTES/APTES-PA film shows barely diminishment after 24 hours of immersion, indicating effective protection of the PQDs by the organosilicon matrix. This exceptional resistance to organic solvents enables good adaptability of the material for the patterning processes that involve these solvents.

The comprehensive stability tests demonstrate the robustness of the PQD/silicone film with the designed ligand system, indicating its potential for practical applications in optical systems. Additionally, as shown in **Table 7.2**, a detailed summary of the PLQY and stability performance of PQD/organosilicon compounds from relevant literature is compiled for comparison and analysis.

Table 7.2. Summary of stability characterizations of PQDs with organosilicon encapsulation.

PQDs	Ligand materials	PLQY	Test condition	Retained PL	Ref
CsPbBr$_3$	OA/OLA/TMOS	72%	-Mixing with water, 3h; -UV radiation (365nm, 20W lamp with 10 cm distance), 5h;	95%; 72%;	[272]
CsPbBr$_3$	OA/OLA/TEOS	-	-In 75% humidity, 12h; -Heating at 60°C, 15h;	73.8%; 36.4%;	[249]
CsPbBr$_3$	OA/OLA/APTES	-	-Immersion in water, 6h; -Immersion in water, 48h;	59.0%; 35.8%;	[273]
CsPbBr$_3$	OA/APTES/ TMOS/TEOS	82%	-75% humidity, 6h; -UV radiation (80 mW/cm^2), 6h; -Immersion in ethanol;	90%; 81%; 85%;	[274]
CsPbBr$_3$	OA/OLA/ APTES/TEOS	89%	-UV irradiation (365 nm, 9 mW/cm^2),72h;	89%; 65%;	[271]

			-Heating at 100℃;		
$CsPbBr_3$	OA/OLA/ APTES	75%	-Heating at 80℃, 1h; -Mixing with ethanol, 30 min;	53%; 87%;	[275]
$CsPbBr_3$	APTES/ APTES-PA	80.6%	-Heating at 180℃, 10 min; -UV radiation (1.5 mW/cm^2), 6h; -Immersion in water, 6h; -Immersion in acetone, toluene, chloroform, and ethanol for 24h;	62.3%; 78.9%; ~100%; ~100%;	**This work**

7.5 Application of perovskite quantum dot scintillator for X-ray imaging

All-inorganic halide perovskite has been proven as a promising type of scintillation material, owing to its high absorption cross-section of X-ray, fast photo-response, and good solution-processibility.[228], [276] Compared to perovskite single crystal, PQDs have the advantages of high light yield at room temperature and rapid response down to ~1 ns.[219], [277] Based on these promising characteristics, the PQD films encapsulated with the proposed dual-organosilicon ligand system are eventually applied and investigated in an indirect X-ray imaging system as scintillators. In this section, all the PQD/silicone samples are prepared with APTES/APTES-PA ligands.
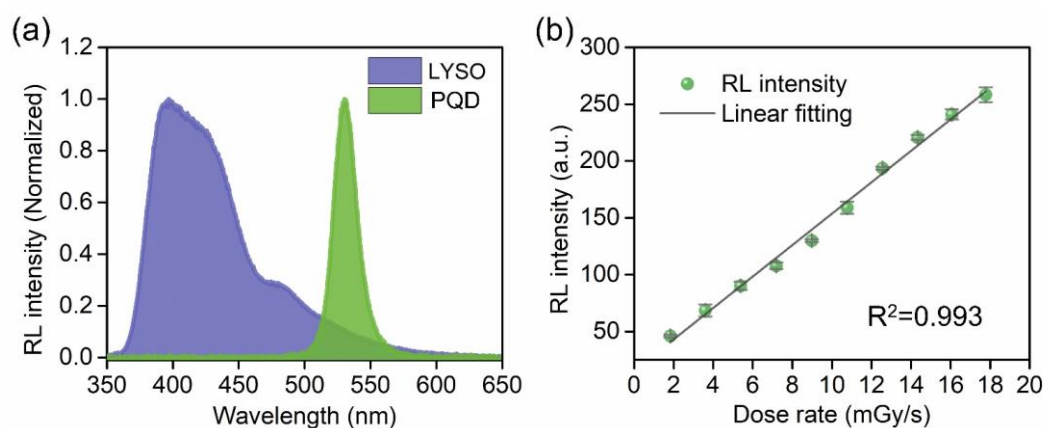
Figure 7.18 (a) Normalized radioluminescence (RL)spectra of a PQD/silicone film and a lutetium-yttrium oxyorthosilicate (LYSO) film under X-ray excitation. (b) Integrated RL intensity of PQD/silicone film as a function of the X-ray dose rate as well as its linear fitting.[213] Reproduced with permission. Copyright 2024, American Chemical Society.

To evaluate the performance of the proposed PQD/silicone film for X-ray scintillation and imaging applications, a series of characterizations are conducted utilizing a micro-focus X-ray tube (XT9160-DED, Viscom) as the radiation source. The thickness of the PQD/silicone film used was approximately 25 μm. **Figure 7.18** (a) illustrates the normalized radioluminescence (RL) spectra of the PQD/silicone film compared to a commonly utilized lutetium-yttrium oxy orthosilicate (LYSO) scintillator. Notably, the PQD/silicone film shows a narrow emission peak

with an FWHM of 21 nm, while the LYSO film exhibits a significantly broader RL peak. This narrow emission peak offers an advantage in achieving optimal read-out efficiency by matching the emission peak with the response peak of the photodetectors, such as photomultiplier tubes, photodiodes, and CCD or CMOS cameras.[278], [279] The integrated RL intensity of the PQD/silicone film as a function of the dose rate of X-ray excitation is depicted in **Figure 7.18** (b). A linear fitting line is derived from the measured data points, demonstrating high linearity with a coefficient of determination of 0.993. This linear response of the PQD/silicone film is fundamental for its practical use in X-ray detection and imaging, as the imaging is based on the intensity difference of the X-ray radiation impinging on the scintillator.

To characterize the performance of the PQD scintillator, an X-ray imaging system was con-
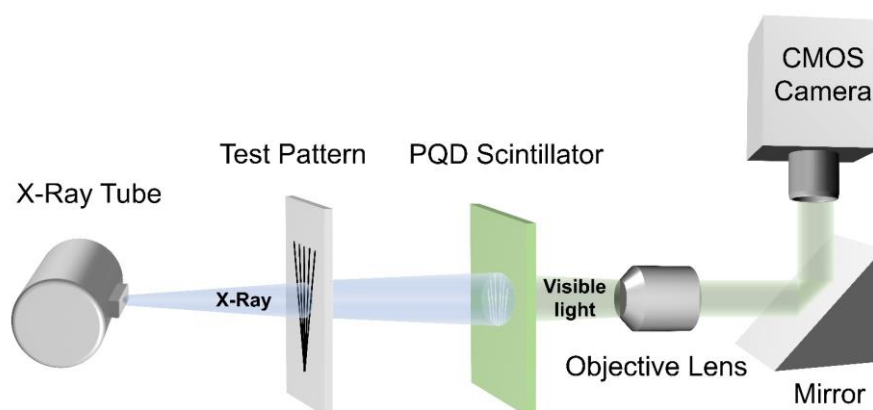
Figure 7.19 The schematic of the X-ray imaging system with PQD/silicone film as scintillator.[213] Reproduced with permission. Copyright 2024, American Chemical Society.

structed following the design in **Figure 7.19**. In this system, an X-ray tube (XT9160-DED, Viscom) is employed as the radiation source. The PQD scintillator film here plays the role of converting the high-energy X-ray to the low-energy photon in the visible wavelength range, which can be detected by the CMOS camera (DMK 21BZU04, Imaging Source). The testing sample is placed between the X-ray source and PQD scintillator film with alignment. Due to the X-ray absorption of the testing sample, the pattern of the sample can be exhibited by the fluorescence image on the PQD scintillator, further captured by the camera. The objective lens is included for adjusting the magnification of the imaging system. The setting of the mirror is for bending the optical path and keeping the CMOS camera away from the direct radiation of X-ray which can cause massive flashing dots on the image. With this setup, a standard X-ray line-pair test pattern (PTW L659035) is utilized as the testing pattern to evaluate the performance of the PQD scintillator and the spatial resolution of the system.

Figure 7.20 shows the X-ray images of the standard line-pair test pattern at different positions for characterizing the spatial resolution of the imaging system with the PQD scintillator. The imaging test is conducted with a tube voltage of 60 kV and a dose rate of 6.58 mGy/s. All the X-ray images in the test are darkfield-corrected. For the images of 6 lp/mm and 10 lp/mm, clear boundaries and contrast can be observed between the lines. The flashing white dots on the images are caused by the direct impinging of the X-ray radiation. For higher resolution, owing to the reduced light scattering and the low thickness of the PQD/silicone film,[280] the line pairs
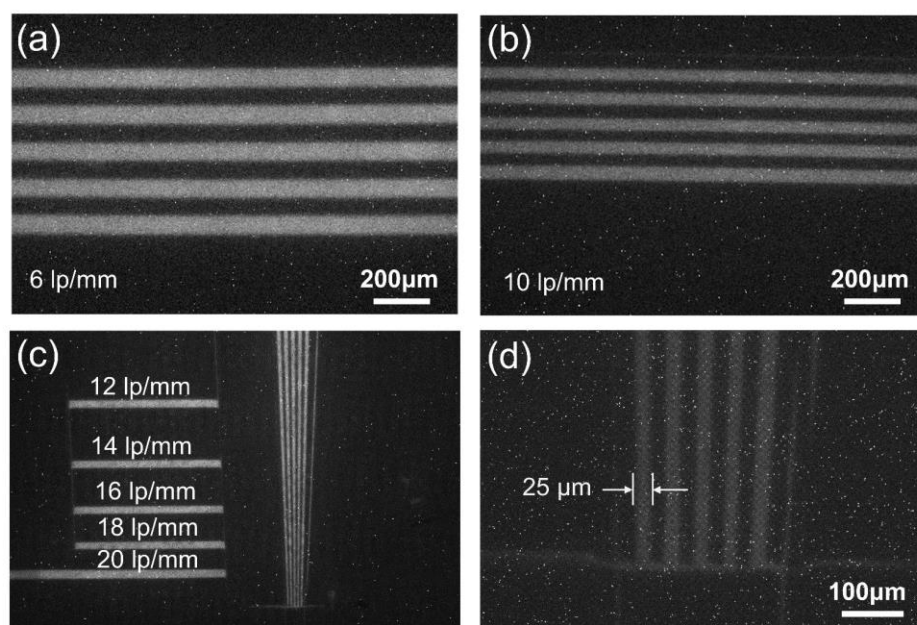
Figure 7.20 (a)-(c) X-ray images of a line-pair test pattern with the spatial resolution ranging from 6 lp/mm to 20 lp/mm. (d) X-ray image of the bottom part of the line-pair test pattern with higher magnification. The tube voltage of the X-ray source is 60 kV and the dose rate is 6.58 mGy/s in this imaging test.[213] Reproduced with permission. Copyright 2024, American Chemical Society.

at the positions with a spatial resolution of up to 20 lp/mm can be distinguished. Moreover, an enlarged view of the bottom part of the line pattern is acquired by using an objective lens with higher magnification. More details of the line pattern are presented in the enlarged image and the gaps between the lines can be easily distinguished. The results visually demonstrate the high spatial resolution of the imaging system.

By extracting the gray values across the line-pair pattern in the X-ray images, gray value pro-
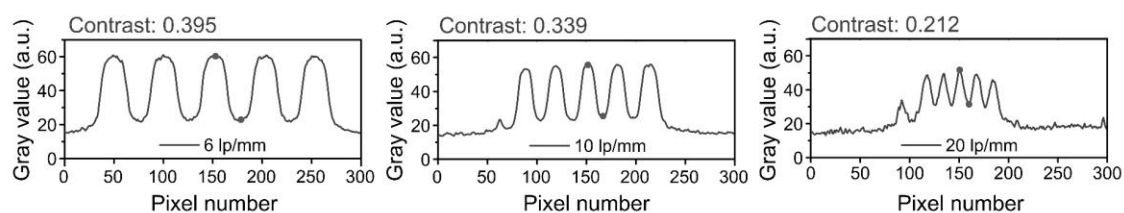
Figure 7.21 Gray-value profiles of the line-pair patterns extracted from the corresponding positions in the X-ray images and the calculated contrasts.[213] Reproduced with permission. Copyright 2024, American Chemical Society.

files of the line pairs featuring different spatial resolutions are obtained and illustrated in **Figure 7.21**. In the figure, distinct peaks and valleys of the profile curves are obvious up to the highest measured spatial resolution of 20 lp/mm. As the gaps between the lines decrease for higher resolution, the gray value contrast gradually diminishes. The contrast of the gray value image is calculated as the following equation:

Contrast = $(I_{max} - I_{min}) / (I_{max} + I_{min})$;

where the maximal and minimal intensity are marked on the profiles as gray dots. With the increase of the spatial resolution, the contrast of the profile gradually reduces. A contrast of the line-pair profile which is above 0.2 is normally regarded as clear enough to distinguish the lines. Thus, the imaging results suggest that the 25 μm thick PQD/silicone film can achieve a spatial resolution of at least 20 lp/mm with a contrast exceeding 0.2.
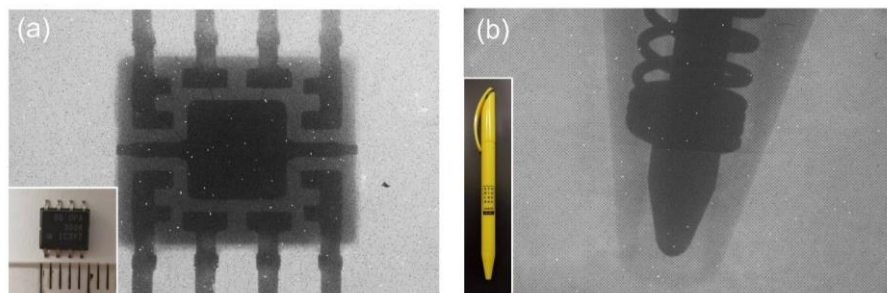
Figure 7.22 X-ray images of (a) a microelectronic chip, and (b) a ball-point pen (tube voltage: 30 kV, dose rate: 3.84 mGy/s). The inserts are photos of the respective samples.[213] Reproduced with permission. Copyright 2024, American Chemical Society.

X-ray imaging demonstrations are conducted utilizing the PQD/silicone scintillator to capture images of an amplifier chip (OPA 300A, Burr-Brown) and a ball-point pen. As shown in **Figure 7.22**, these images exhibit clear contrasts, delineating the plastic cover and metal components with precision. Within the package of the electronic chip, the thin metal wires measuring approximately 50 μm in thickness are distinctly visible, showcasing the high-resolution capabilities of the scintillator film.

Table 7.3 Performances comparisons of $CsPbBr_3$ PQD-based scintillators.

Scintillator	Matrix	Thickness (μm)	Spatial resolution (lp/mm)	Method	Ref
$CsPbBr_3$ NCs	PMMA	1620	9.8 (MTF=0.2)	UV-induced poly-merization	[227]
$CsPbBr_3$ NCs	PDMS	120	~5.0 (MTF=0.4)	Spin-coating	[226]
$CsPbBr_3$ NCs	Acrylate-based resin	200	4.0 (MTF=0.2)	Barrier film lamination	[281]
$CsPbBr_3$ NCs	PMMA	40	8.0 (MTF=0.2)	Template assembly	[282]
$CsPbBr_3$:Eu NCs	Glass	2000	15.0 (MTF=0.2)	Melt-quenching	[280]
$CsPbBr_3$:Lu^{3+} NCs	Glass	600	16.8 (MTF=0.2)	Melt-quenching	[283]
$CsPbBr_3$ NCs	Anodized aluminum oxide	20	211 (MTF=0.1)	Negative pressure filling	[284]

CsPbBr$_3$ nanowire	Anodized aluminum oxide	12-13	160 (MTF=0.1)	Template casting	[285]
CsPbBr$_3$ nanosheet	-	25	2.4 (feature size of 0.21 mm)	Drop-casting	[286]
CsPbBr$_3$ NCs	Organosilicon	25	~20 (Contrast of 0.2)	Drop-casting	**This work**

To provide a comparative analysis of the spatial resolution of the proposed PQD films, we compiled the encapsulating matrix types and various parameters of previously documented CsPbBr$_3$ PQD scintillators in **Table 7.3**. This summary table suggests that the PQD/silicone film proposed in this study demonstrates competitiveness with other PQD scintillators regarding high spatial resolution.
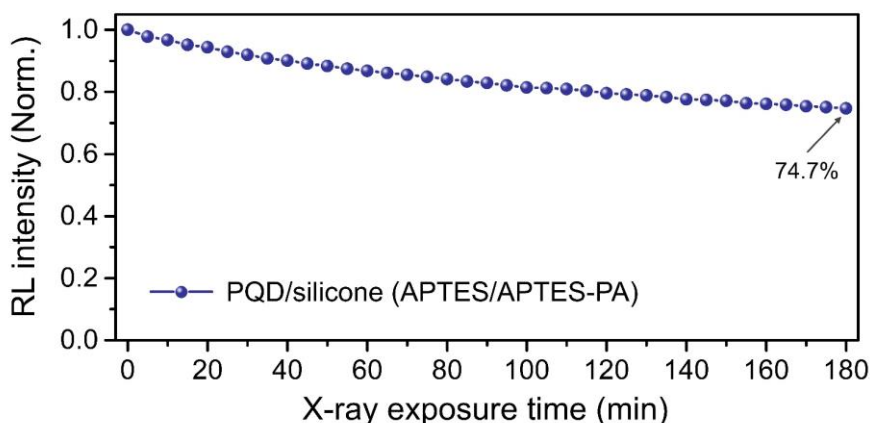
Figure 7.23 Normalized RL intensity of the PQD/silicone scintillator under continuous X-ray radiation with a tube voltage of 60 kV and dose rate of 24.7 mGy/s.[213] Reproduced with permission. Copyright 2024, American Chemical Society.

Additionally, a stability test for the PQD/silicone scintillator under continuous high-dose-rate X-ray radiation (tube voltage: 60 kV / dose rate: 24.7 mGy/s) is performed, to characterize the lifetime of the PQD scintillator in an imaging system. As depicted in **Figure 7.23**, the PQD/silicone sample shows a slow decrease in the X-rya exposure time and maintains 74.7% of its RL intensity after 180 minutes of X-ray radiation. It suggests a satisfactory stability of the PQD scintillator when exposed to X-rays. The degradation of the PQD/silicone film is attributed to the crystal decomposition caused by the continuous X-ray radiation.

Besides the X-ray imaging application, we conducted a characterization of the amplification of spontaneous emission (ASE) measurement of the PQD/silicone film, as the enhanced surface condition of the PQD/silicone film is beneficial to its ASE and lasing performance as well.[287], [288] In the measurement, the PQD/silicone film was pumped by a femtosecond laser peaking at 342 nm without cavity structure. The duration of the laser pulse was 270 fs and the frequency was 1 kHz. The illustration of the ASE process and the corresponding PL spectra are presented in **Figure 7.24**. When pumped with a femtosecond laser, the PQD/silicone film achieves a low

ASE threshold between 17.1 and 34.2 μJ/cm². This result highlights the large potential of the proposed high-performance PQD/silicone film, which is distinguished by its high transparency and exceptional stability, for various optical applications.
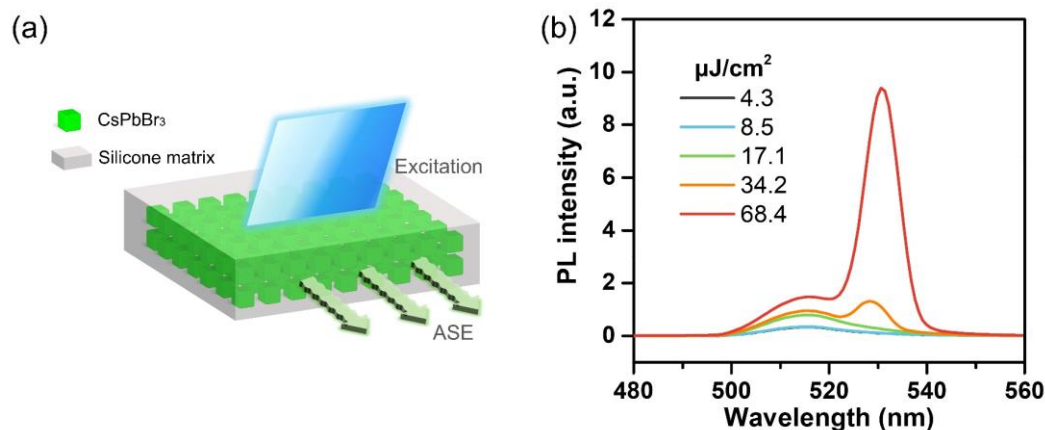
Figure 7.24 (a) Illustration of the amplification of spontaneous emission (ASE) of the PQD/silicone film with APTES/APTES-PA as capping ligands. (b) PL spectra of the PQD/silicone film with different pump intensities.[213] Reproduced with permission. Copyright 2024, American Chemical Society.

7.6 Summary

In summary, we introduced a comprehensive organosilicon-based ligand system designed for encapsulating CsPbBr$_3$ PQDs, enabling the successful fabrication of a high-performance fluorescent PQD/silicone film. The effectiveness of this system lay in its ability to create a toughly encapsulating matrix through ample crosslinking of the dual-organosilicon ligand combination. It resulted in improved transparency, reduced surface roughness, and enhanced stability of the PQD film while maintaining a high PLQY. The PQD films prepared with the proposed ligand system demonstrate a higher transmittance and reduced haze value. Furthermore, the proposed capping ligands endow a robust encapsulation and effective passivation for the PQD/silicone film. It showed superior stability compared to PQD films encapsulated with polystyrene, under harsh conditions such as high temperatures and intense UV radiation. Notably, the proposed PQD film exhibited excellent resistance to water and organic solvents. Detailed characterizations for the surface chemistry of the obtained PQD films were conducted to investigate the enhancing mechanism of the designed ligands. Given these promising properties, the PQD/silicone films were utilized as scintillators in X-ray imaging systems, achieving a high spatial resolution of over 20 lp/mm with commendable contrast.

Overall, the proposed ligand system offers a cost-effective solution for producing high-performance PQD films, compatible with a range of deposition and patterning techniques. The improved film quality and stability are beneficial to a variety of optoelectronic applications.

8   Conclusion and Outlook

In this chapter, comprehensive conclusions of the scientific work and advancements achieved in this research are presented. This research focuses on developing efficient light-managing approaches for optoelectronic devices based on quantum dots (QDs). It consists of three aspects, including the development of wavelength-selective reflectors, the self-assembly fabrication of microporous structures, and the design of an organosilicon-based ligand system for perovskite QDs (PQDs). Corresponding outlooks of each aspect are proposed for future development.

8.1   Conclusion

The rapid development of QDs facilitates their broad application in optoelectronic devices, including luminescent devices, energy-harvesting devices, and photodetectors. Light managing strategies toward these optoelectronic systems empower high efficiency and quality of the devices in practical use. It is a critical step to release the full potential of QD-based materials and meet the high demand of industrialization. This dissertation focused on the photoluminescent applications of QDs and demonstrated three approaches to improve the light management of QD-based optoelectronics. These approaches involved the fabrication of wavelength-selective reflectors on the macroscale, the fabrication of porous structures on the microscale, and the ligand design for QDs on the molecular scale. Systematic characterizations were conducted and validated the enhancing effect of these methods on the optical performance of the optoelectronic devices. The main findings and contributions of this thesis are presented below.

Wavelength-selective reflectors for enhancing forward emission

In photoluminescent applications of QDs, light trapping is a common problem that inhibits the efficiency of QD-based devices. Due to the isotropic emission of QDs, a large portion of the emitted photons from QDs are backward, which are hardly extracted and utilized in practical applications. To address this issue, *Chapter 5* introduced wavelength-selective reflectors based on a metallo-dielectric configuration for extracting the backward emission of QD layers. These reflectors consisted of a monolayer of silver nanoparticles and a coating layer of TiO_2. A high transmittance in the UV and blue wavelength range as well as a remarkable reflectance in the green and red wavelength range were shown by the reflectors. In addition, a solid-state dewetting method was developed to fabricate the monolayer of silver nanoparticles with low-coat. The processing parameters involved in this method, such as the initial thickness of the silver layer and dewetting temperature, allowed good controllability on the morphology of silver nanoparticles. The adjustment of the morphology of the wavelength-selective reflector enabled the manipulation of its transmittance and reflectance spectra. In this work, the optimized reflector demonstrated a peak transmittance of 79% in the UV range and a peak reflectance of 72% in the visible range. A double-integrating sphere system was applied to evaluate the light extraction improvement of the backward emission of QD layers quantitatively. Eventually, based on their optical characteristics, the reflectors were integrated into UV-pumped white light-emitting

diodes incorporating QD color conversion layers. A notable luminescence enhancement of 19.5% in radiant flux was achieved for the sample with the wavelength-selective reflector. The work on wavelength-selective reflectors provided an industrially applicable route to boost the performance of QD-based luminescent devices, including light-emitting diodes and display panels.

QD-based color converters with microporous structures

The photoluminescence process of QDs related to the absorption of excitation photons and the generation of emitted photons. The light absorption capability of QDs significantly affects their color conversion performance. The conventional strategy for enhancing the light absorption of QDs is by increasing the concentration of QDs in the color conversion layer. As an alternative, the introduction of microporous structures into QD layers is another effective solution. By generating sufficient light scattering inside the QD layers, the light absorption of QDs to excitation photons can be largely augmented, resulting in a high photoluminescence intensity.

In *Chapter 6*, a self-assembly method to fabricate light-scattering microporous structures was introduced to QD/polymer composites. This method was based on the phase separation of polystyrene (PS) and polyethylene glycol (PEG) polymer blends. The morphology of the micropores could be manipulated by the weight ratio of the two polymers, enabling precise control of the scattering capability. A broad range of the haze value of the microporous films across zero to nearly 100% was achieved. The improved light scattering facilitated the light absorption and the light out-coupling of the QD/polymer composites. For QD/polymer films, a maximum enhancement of 110% in photoluminescence intensity was realized by the sample with a microporous structure. Moreover, the phase separation method was a solution process with good adaptability to the inkjet printing technique for depositing QD pixels. The inkjet-printed QD pixel arrays exhibited high uniformity in pixel size and outstanding reproducibility even with the presence of microporous structures. It indicated that this method for fabricating porous structures was versatile and adaptable to various micro-patterning technologies. This work illustrated the profound enhancing effect of introducing light-scattering porous structure to QD color conversion layers and the versatility of the fabrication method based on phase separation. It offered a commercially feasible solution to promote the performance of QD-based color converters.

Ligand design for perovskite PQDs scintillators

The long-term stability against environmental stimuli is the main challenge for the wide-range application of PQDs. Developing a robust encapsulation for PQDs is one of the most efficient and straightforward strategies to elongate their lifetime in practical applications. In X-ray imaging systems with indirect configuration, PQDs serve as scintillation media that convert X-rays to visible light for detection by normal cameras. Besides outstanding long-term stability, PQD scintillators require high transparency and minimal scattering to realize a high spatial resolution of the imaging system.

To address this demand, *Chapter 7* proposed a dual-organosilicon ligand system for the encapsulation of $CsPbBr_3$ PQDs. Through the condensation reactions of the organosilicon-based capping ligands, a tough encapsulating matrix was formed without introducing an extra hosting material. It was advantageous for achieving a high loading of PQDs in the scintillators. The

ligand system contained massive silicon-based head groups to facilitate sufficient crosslinking, resulting in a robust barrier and excellent stability for PQDs. In addition, the compact encapsulating matrix brought improved transparency, reduced surface roughness, and lessened light scattering to PQD scintillators. The PQD films prepared with the proposed ligand system were testified with a high quantum yield of 81% and superior stability under harsh conditions such as high temperatures and solvent immersion. These merits further enabled high-performance X-ray imaging and detection. The X-ray imaging system equipped with the proposed PQD films achieved an outstanding spatial resolution of above 20 lp/mm. This work demonstrated a ligand system for the cost-effective production of high-performance PQD films, which promotes the commercialization of PQDs.

8.2 Outlook

In the current stage, despite the growing interest in QDs from scientific research, QD-based optoelectronics are facing challenges to large-scale manufacturing and commercialization. Cost-effective and productive fabrication techniques are yet needed to meet the high demand of the industry. The light-managing approaches developed in this work have demonstrated compelling results in improving the performance of QD-based devices. Aiming at promoting QD-based optoelectronics forward to industrialization, the following potentials are promising for future development:

Solution processing fabrication of wavelength-selective reflectors

The wavelength-selective reflectors proposed in this work are based on a solid-state dewetting method for the fabrication of silver nanoparticles. This method incorporates the deposition of silver thin film by gas-phase evaporation and a thermal annealing process, which shows poor compatibility with many patterning techniques, such as screen printing and inkjet printing. It limits their application in display technology that requires pixelation of the reflectors. Addressing this obstacle, developing a solution process to fabricate the reflectors is an ideal solution. The gas-phase evaporation process can be replaced by the inkjet printing of silver nanoparticles for depositing the silver thin film, enabling the patterning of the wavelength-selective reflectors. In this strategy, the rest of the fabrication steps remain the same. As alternatives, the solution-process fabrication can potentially be achieved by mixing the dispersions of silver nanoparticles and titanium dioxide nanoparticles or synthesizing core-shell nanoparticles of silver and titanium dioxide with the engineering of the particle geometry. The deposition of the reflector can be realized by spin-coating or inkjet printing these nanoparticle dispersions with a larger variety of configurations. The prospect of the proposed wavelength-selective reflector shall be extended by developing solution processing fabrications.

Color-filter-free QD color conversion layers for displays

In QD-enhanced micro-light-emitting diode (micro-LED) displays, QD layers (or micro-pixels) are commonly coated on the excitation source of blue or UV micro-LEDs for color conversion. Due to the incomplete absorption of the QD layer to the excitation light, color filters need to be incorporated in every subpixel to filter out the residual excitation that transmits the QD layer.

The color filters contribute to a high color gamut of display devices but largely increase the production cost. In *Chapter 6*, we emphasize the increase of photoluminescence intensity of QD layers caused by the light scattering effect of microporous structures. Meanwhile, another interesting effect is exhibited that the enhanced light scattering is beneficial to the reduction of residual excitation light. The successful suppression of the residual excitation enables color-filter-free display devices, which significantly decreases the fabrication cost. It can be potentially accomplished by increasing the concentration of QDs along with morphology optimization of the microporous structure for stronger light scattering. The density of the micropores and thickness of the QD layers shall be further increased to ensure the total absorption of the excitation photons. The processing parameters of the phase separation method have been investigated in this dissertation, establishing a guideline for the structural optimization of future development.

PQD inks for inkjet printing and direct laser writing

The dual-organosilicon ligand system proposed in this work has been testified with remarkable improvement to the optical performance and stability of PQDs. Adapting this solution system (containing PQDs and capping ligands) to serve as the ink for printing technologies can further broaden its prospect of application. Aiming at the inkjet printing technique, dispersion of PQD/silicone nanoparticles synthesized with the proposed ligand system would be an ideal printing ink. By introducing a polymer network (e.g. polystyrene, acrylate) to the synthesis process, spatial confinement for limiting the growth of PQD/silicone nanoparticles is generated. It brings a factor to control the size of the PQD/silicone nanoparticles to fit the demand of inkjet printing. The polymer network can either be removed through centrifugation after the synthesis or be left in ink as an adhesive for bonding the nanoparticles. Aiming at the direct laser writing technique, the proposed ligands can directly serve as thermal responsive media in the ink. As the crosslinking of the ligands would be accelerated profoundly by heating, the laser beam focus with appropriate thermal energy is able to trigger the solidification of the PQD/silicone composite. The patterning of the PQD layer shall be achieved by direct laser writing on a thin layer of PQD/ligand solution.

Bibliography

[1]   S. Neeleshwar *et al.*, "Size-dependent properties of CdSe quantum dots," *Phys. Rev. B*, vol. 71, no. 20, p. 201307, May 2005, doi: 10.1103/PhysRevB.71.201307.

[2]   H. Wang, Z. Bao, H. Tsai, A. Tang, and R. Liu, "Perovskite Quantum Dots and Their Application in Light-Emitting Diodes," *Small*, vol. 14, no. 1, p. 1702433, Jan. 2018, doi: 10.1002/smll.201702433.

[3]   F. P. García De Arquer, D. V. Talapin, V. I. Klimov, Y. Arakawa, M. Bayer, and E. H. Sargent, "Semiconductor quantum dots: Technological progress and future challenges," *Science*, vol. 373, no. 6555, p. eaaz8541, Aug. 2021, doi: 10.1126/science.aaz8541.

[4]   A. C. Arias, J. D. MacKenzie, I. McCulloch, J. Rivnay, and A. Salleo, "Materials and Applications for Large Area Electronics: Solution-Based Approaches," *Chem. Rev.*, vol. 110, no. 1, pp. 3–24, Jan. 2010, doi: 10.1021/cr900150b.

[5]   "The Nobel Prize in Chemistry 2023," NobelPrize.org. Accessed: Aug. 08, 2024. [Online]. Available: https://www.nobelprize.org/prizes/chemistry/2023/summary/

[6]   "Quantum Dot Market Size & Share – Trends Report, 2032," Global Market Insights Inc. Accessed: Aug. 08, 2024. [Online]. Available: https://www.gminsights.com/industry-analysis/quantum-dot-market

[7]   Z. Luo, Y. Chen, and S.-T. Wu, "Wide color gamut LCD with a quantum dot backlight," *Opt. Express*, vol. 21, no. 22, p. 26269, Nov. 2013, doi: 10.1364/OE.21.026269.

[8]   Y. Huang, E.-L. Hsiang, M.-Y. Deng, and S.-T. Wu, "Mini-LED, Micro-LED and OLED displays: present status and future perspectives," *Light Sci Appl*, vol. 9, no. 1, p. 105, Jun. 2020, doi: 10.1038/s41377-020-0341-9.

[9]   UbiGro, "Quantum Dots in Agriculture: Enhancing Growth," UbiGro. Accessed: Aug. 08, 2024. [Online]. Available: https://ubigro.com/quantum-dots-to-agriculture-questions/

[10]   Y. Wu, J. Feng, Z. Yang, Y. Liu, and S. (Frank) Liu, "Halide Perovskite: A Promising Candidate for Next-Generation X-Ray Detectors," *Advanced Science*, vol. 10, no. 1, p. 2205536, Jan. 2023, doi: 10.1002/advs.202205536.

[11]   M. Lutfullin, "Quantum Dot X-ray Image Sensors," Articles & Publications - Blog | Quantum Solutions. Accessed: Aug. 08, 2024. [Online]. Available: https://quantum-solutions.com/blog/quantum-dot-x-ray-detectors/

[12]   A. S. Rasal, S. Yadav, A. A. Kashale, A. Altaee, and J.-Y. Chang, "Stability of quantum dot-sensitized solar cells: A review and prospects," *Nano Energy*, vol. 94, p. 106854, Apr. 2022, doi: 10.1016/j.nanoen.2021.106854.

[13]   Q. Zhang *et al.*, "Light Out-Coupling Management in Perovskite LEDs—What Can We Learn from the Past?," *Adv Funct Materials*, vol. 30, no. 38, p. 2002570, Sep. 2020, doi: 10.1002/adfm.202002570.

[14]   Y. Zhan, C. Li, Z. Che, H. C. Shum, X. Hu, and H. Li, "Light management using photonic structures towards high-index perovskite optoelectronics: fundamentals, designing, and applications," *Energy Environ. Sci.*, vol. 16, no. 10, pp. 4135–4163, 2023, doi: 10.1039/D3EE00646H.

[15]   A. J. Nozik and O. I. Micic, "Colloidal Quantum Dots Of Ill-V Semiconductors," *MRS BULLETIN*, 1998.

[16]   T. Takagahara and K. Takeda, "Theory of the quantum confinement effect on excitons in quantum dots of indirect-gap materials," *Phys. Rev. B*, vol. 46, no. 23, pp. 15578–15581, Dec. 1992, doi: 10.1103/PhysRevB.46.15578.

[17]   Y. Shirasaki, G. J. Supran, M. G. Bawendi, and V. Bulović, "Emergence of colloidal quantum-dot light-emitting technologies," *Nature Photon*, vol. 7, no. 1, pp. 13–23, Jan. 2013, doi: 10.1038/nphoton.2012.328.

[18] C. R. Kagan, E. Lifshitz, E. H. Sargent, and D. V. Talapin, "Building devices from colloidal quantum dots," *Science*, vol. 353, no. 6302, p. aac5523, Aug. 2016, doi: 10.1126/science.aac5523.

[19] T. Jamieson, R. Bakhshi, D. Petrova, R. Pocock, M. Imani, and A. M. Seifalian, "Biological applications of quantum dots," *Biomaterials*, vol. 28, no. 31, pp. 4717–4732, Nov. 2007, doi: 10.1016/j.biomaterials.2007.07.014.

[20] V. G. Reshma and P. V. Mohanan, "Quantum dots: Applications and safety consequences," *Journal of Luminescence*, vol. 205, pp. 287–298, Jan. 2019, doi: 10.1016/j.jlumin.2018.09.015.

[21] Y. Yan *et al.*, "Recent Advances on Graphene Quantum Dots: From Chemistry and Physics to Applications," *Advanced Materials*, vol. 31, no. 21, p. 1808283, May 2019, doi: 10.1002/adma.201808283.

[22] D. Zherebetskyy *et al.*, "Hydroxylation of the surface of PbS nanocrystals passivated with oleic acid," *Science*, vol. 344, no. 6190, pp. 1380–1384, Jun. 2014, doi: 10.1126/science.1252727.

[23] S. Wang, B. R. Jarrett, S. M. Kauzlarich, and A. Y. Louie, "Core/Shell Quantum Dots with High Relaxivity and Photoluminescence for Multimodality Imaging," *J. Am. Chem. Soc.*, vol. 129, no. 13, pp. 3848–3856, Apr. 2007, doi: 10.1021/ja065996d.

[24] H. Zhu, N. Song, and T. Lian, "Controlling Charge Separation and Recombination Rates in CdSe/ZnS Type I Core−Shell Quantum Dots by Shell Thicknesses," *J. Am. Chem. Soc.*, vol. 132, no. 42, pp. 15038–15045, Oct. 2010, doi: 10.1021/ja106710m.

[25] P. Zrazhevskiy and X. Gao, "Multifunctional quantum dots for personalized medicine," *Nano Today*, vol. 4, no. 5, pp. 414–428, Oct. 2009, doi: 10.1016/j.nantod.2009.07.004.

[26] C. Bostedt *et al.*, "Strong quantum-confinement effects in the conduction band of germanium nanocrystals," *Applied Physics Letters*, vol. 84, no. 20, pp. 4056–4058, May 2004, doi: 10.1063/1.1751616.

[27] K. Shibuya, M. Koshimizu, H. Murakami, Y. Muroya, Y. Katsumura, and K. Asai, "Development of Ultra-Fast Semiconducting Scintillators Using Quantum Confinement Effect," *Jpn. J. Appl. Phys.*, vol. 43, no. No. 10B, pp. L1333–L1336, Sep. 2004, doi: 10.1143/JJAP.43.L1333.

[28] D. J. Norris and M. G. Bawendi, "Measurement and assignment of the size-dependent optical spectrum in CdSe quantum dots," *Phys. Rev. B*, vol. 53, no. 24, pp. 16338–16346, Jun. 1996, doi: 10.1103/PhysRevB.53.16338.

[29] A. I. Ekimov, "Quantum size effect in three-dimensional microscopic semiconductor crystals," *Jetp Lett.*, vol. 34, p. 345, 1981.

[30] R. Rossetti, S. Nakahara, and L. E. Brus, "Quantum size effects in the redox potentials, resonance Raman spectra, and electronic spectra of CdS crystallites in aqueous solution," *The Journal of Chemical Physics*, vol. 79, no. 2, pp. 1086–1088, Jul. 1983, doi: 10.1063/1.445834.

[31] C. B. Murray, D. J. Norris, and M. G. Bawendi, "Synthesis and characterization of nearly monodisperse CdE (E = sulfur, selenium, tellurium) semiconductor nanocrystallites," *J. Am. Chem. Soc.*, vol. 115, no. 19, pp. 8706–8715, Sep. 1993, doi: 10.1021/ja00072a025.

[32] R. E. Bailey, A. M. Smith, and S. Nie, "Quantum dots in biology and medicine," *Physica E: Low-dimensional Systems and Nanostructures*, vol. 25, no. 1, pp. 1–12, Oct. 2004, doi: 10.1016/j.physe.2004.07.013.

[33] V. L. Colvin, M. C. Schlamp, and A. P. Alivisatos, "Light-emitting diodes made from cadmium selenide nanocrystals and a semiconducting polymer," *Nature*, vol. 370, no. 6488, pp. 354–357, 1994.

[34] Z. A. Peng and X. Peng, "Formation of High-Quality CdTe, CdSe, and CdS Nanocrystals Using CdO as Precursor," *J. Am. Chem. Soc.*, vol. 123, no. 1, pp. 183–184, Jan. 2001, doi: 10.1021/ja003633m.

[35] Q. Shan *et al.*, "Perovskite Quantum Dots for the Next-Generation Displays: Progress and Prospect," *Adv Funct Materials*, p. 2401284, Mar. 2024, doi: 10.1002/adfm.202401284.

[36] Y. Wang, X. Li, J. Song, L. Xiao, H. Zeng, and H. Sun, "All-Inorganic Colloidal Perovskite Quantum Dots: A New Class of Lasing Materials with Favorable Characteristics," *Advanced Materials*, vol. 27, no. 44, pp. 7101–7108, Nov. 2015, doi: 10.1002/adma.201503573.

[37] D. A. Hanifi *et al.*, "Redefining near-unity luminescence in quantum dots with photothermal threshold quantum yield," *Science*, vol. 363, no. 6432, pp. 1199–1202, Mar. 2019, doi: 10.1126/science.aat3803.

[38] J. Hao *et al.*, "A facile route to synthesize CdSe/ZnS thick-shell quantum dots with precisely controlled green emission properties: towards QDs based LED applications," *Sci Rep*, vol. 9, no. 1, p. 12048, Aug. 2019, doi: 10.1038/s41598-019-48469-7.

[39] X. Jin *et al.*, "Cation exchange assisted synthesis of ZnCdSe/ZnSe quantum dots with narrow emission line widths and near-unity photoluminescence quantum yields," *Chem. Commun.*, vol. 56, no. 45, pp. 6130–6133, 2020, doi: 10.1039/D0CC01302A.

[40] B. Xu *et al.*, "One pot synthesis of thick shell blue emitting CdZnS/ZnS quantum dots with narrow emission line width," *Opt. Mater. Express*, vol. 10, no. 5, p. 1232, May 2020, doi: 10.1364/OME.389823.

[41] K. Kim *et al.*, "Zinc Oxo Clusters Improve the Optoelectronic Properties on Indium Phosphide Quantum Dots," *Chem. Mater.*, vol. 32, no. 7, pp. 2795–2802, Apr. 2020, doi: 10.1021/acs.chemmater.9b04309.

[42] Y.-H. Won *et al.*, "Highly efficient and stable InP/ZnSe/ZnS quantum dot light-emitting diodes," *Nature*, vol. 575, no. 7784, pp. 634–638, Nov. 2019, doi: 10.1038/s41586-019-1771-5.

[43] F. Huang, C. Bi, R. Guo, C. Zheng, J. Ning, and J. Tian, "Synthesis of Colloidal Blue-Emitting InP/ZnS Core/Shell Quantum Dots with the Assistance of Copper Cations," *J. Phys. Chem. Lett.*, vol. 10, no. 21, pp. 6720–6726, Nov. 2019, doi: 10.1021/acs.jpclett.9b02386.

[44] S.-W. Dai *et al.*, "Perovskite Quantum Dots with Near Unity Solution and Neat-Film Photoluminescent Quantum Yield by Novel Spray Synthesis," *Adv. Mater.*, vol. 30, no. 7, p. 1705532, Feb. 2018, doi: 10.1002/adma.201705532.

[45] C. Luo *et al.*, "Ultrafast Thermodynamic Control for Stable and Efficient Mixed Halide Perovskite Nanocrystals," *Adv Funct Materials*, vol. 30, no. 19, p. 2000026, May 2020, doi: 10.1002/adfm.202000026.

[46] Y. Cai *et al.*, "Trimethylsilyl Iodine-Mediated Synthesis of Highly Bright Red-Emitting CsPbI $_3$ Perovskite Quantum Dots with Significantly Improved Stability," *Chem. Mater.*, vol. 31, no. 3, pp. 881–889, Feb. 2019, doi: 10.1021/acs.chemmater.8b04049.

[47] A. Sengupta and C. K. Sarkar, Eds., *Introduction to Nano: Basics to Nanoscience and Nanotechnology*. in Engineering Materials. Berlin, Heidelberg: Springer Berlin Heidelberg, 2015. doi: 10.1007/978-3-662-47314-6.

[48] C. Y. Ngo, S. F. Yoon, W. J. Fan, and S. J. Chua, "Effects of size and shape on electronic states of quantum dots," *Phys. Rev. B*, vol. 74, no. 24, p. 245331, Dec. 2006, doi: 10.1103/PhysRevB.74.245331.

[49] X. Zhang, H. Dong, and W. Hu, "Organic Semiconductor Single Crystals for Electronics and Photonics," *Advanced Materials*, vol. 30, no. 44, p. 1801048, Nov. 2018, doi: 10.1002/adma.201801048.

[50] Al. L. Efros and M. Rosen, "The Electronic Structure of Semiconductor Nanocrystals," *Annu. Rev. Mater. Sci.*, vol. 30, no. 1, pp. 475–521, Aug. 2000, doi: 10.1146/annurev.matsci.30.1.475.

[51] N.-M. Park, C.-J. Choi, T.-Y. Seong, and S.-J. Park, "Quantum Confinement in Amorphous Silicon Quantum Dots Embedded in Silicon Nitride," *Phys. Rev. Lett.*, vol. 86, no. 7, pp. 1355–1357, Feb. 2001, doi: 10.1103/PhysRevLett.86.1355.

[52] Y. Zhai, Y. Dou, D. Zhao, P. F. Fulvio, R. T. Mayes, and S. Dai, "Carbon Materials for Chemical Capacitive Energy Storage," *Advanced Materials*, vol. 23, no. 42, pp. 4828–4850, Nov. 2011, doi: 10.1002/adma.201100984.

[53] M.-M. Titirici *et al.*, "Sustainable carbon materials," *Chem. Soc. Rev.*, vol. 44, no. 1, pp. 250–290, 2015, doi: 10.1039/C4CS00232F.

[54] W. J. Parak, L. Manna, and T. Nann, "Fundamental Principles of Quantum Dots," in *Nanotechnology*, 1st ed., Wiley-VCH Verlag GmbH & Co. KGaA, Ed., Wiley, 2010, pp. 73–96. doi: 10.1002/9783527628155.nanotech004.

[55] K. W. Böer and U. W. Pohl, *Semiconductor Physics*. Cham: Springer International Publishing, 2023. doi: 10.1007/978-3-031-18286-0.

[56] G. Konstantatos, *Colloidal quantum dot optoelectronics and photovoltaics*. Cambridge University Press, 2013.

[57] J. P. Foster and F. Weinhold, "Natural hybrid orbitals," *J. Am. Chem. Soc.*, vol. 102, no. 24, pp. 7211–7218, Nov. 1980, doi: 10.1021/ja00544a007.

[58] D. I. Khomskii and S. V. Streltsov, "Orbital Effects in Solids: Basics, Recent Progress, and Opportunities," *Chem. Rev.*, vol. 121, no. 5, pp. 2992–3030, Mar. 2021, doi: 10.1021/acs.chemrev.0c00579.

[59] R. L. Moon, G. A. Antypas, and L. W. James, "Bandgap and lattice constant of GaInAsP as a function of alloy composition," *JEM*, vol. 3, no. 3, pp. 635–644, Aug. 1974, doi: 10.1007/BF02655291.

[60] D. Luo, R. Su, W. Zhang, Q. Gong, and R. Zhu, "Minimizing non-radiative recombination losses in perovskite solar cells," *Nature Reviews Materials*, vol. 5, no. 1, pp. 44–60, 2020.

[61] C. Zhang and J. Lin, "Defect-related luminescent materials: synthesis, emission properties and applications," *Chem. Soc. Rev.*, vol. 41, no. 23, p. 7938, 2012, doi: 10.1039/c2cs35215j.

[62] M. A. Reshchikov and H. Morkoç, "Luminescence properties of defects in GaN," *Journal of Applied Physics*, vol. 97, no. 6, p. 061301, Mar. 2005, doi: 10.1063/1.1868059.

[63] C. Cohen-Tannoudji, B. Diu, and F. Laloë, *Quantum mechanics, volume 3: fermions, bosons, photons, correlations, and entanglement*. John Wiley & Sons, 2019.

[64] G. Grosso and G. P. Parravicini, *Solid state physics*. Academic press, 2013.

[65] A. D. Yoffe, "Semiconductor quantum dots and related systems: electronic, optical, luminescence and related properties of low dimensional systems," *Advances in physics*, vol. 50, no. 1, pp. 1–208, 2001.

[66] J. H. Davies, *The physics of low-dimensional semiconductors: an introduction*. Cambridge university press, 1998.

[67] E. F. Pinzón, L. C. Lopes, A. F. V. Fonseca, M. A. Schiavon, and P. R. Bueno, "Quantum rate as a spectroscopic methodology for measuring the electronic structure of quantum dots," *J. Mater. Chem. C*, vol. 12, no. 13, pp. 4606–4617, 2024, doi: 10.1039/D4TC00347K.

[68] R. W. Meulenberg, J. R. I. Lee, A. Wolcott, J. Z. Zhang, L. J. Terminello, and T. Van Buuren, "Determination of the Exciton Binding Energy in CdSe Quantum Dots," *ACS Nano*, vol. 3, no. 2, pp. 325–330, Feb. 2009, doi: 10.1021/nn8006916.

[69] G. T. Einevoll, "Confinement of excitons in quantum dots," *Phys. Rev. B*, vol. 45, no. 7, pp. 3410–3417, Feb. 1992, doi: 10.1103/PhysRevB.45.3410.

[70] J. Jasieniak, M. Califano, and S. E. Watkins, "Size-Dependent Valence and Conduction Band-Edge Energies of Semiconductor Nanocrystals," *ACS Nano*, vol. 5, no. 7, pp. 5888–5902, Jul. 2011, doi: 10.1021/nn201681s.

[71] J. Kwak, J. Lim, M. Park, S. Lee, K. Char, and C. Lee, "High-Power Genuine Ultraviolet Light-Emitting Diodes Based On Colloidal Nanocrystal Quantum Dots," *Nano Lett.*, vol. 15, no. 6, pp. 3793–3799, Jun. 2015, doi: 10.1021/acs.nanolett.5b00392.

[72] S. Goossens *et al.*, "Broadband image sensor array based on graphene–CMOS integration," *Nature Photon*, vol. 11, no. 6, pp. 366–371, Jun. 2017, doi: 10.1038/nphoton.2017.75.

[73] Y. Wang *et al.*, "Silver telluride colloidal quantum dot infrared photodetectors and image sensors," *Nat. Photon.*, vol. 18, no. 3, pp. 236–242, Mar. 2024, doi: 10.1038/s41566-023-01345-3.

[74] Y. Wei, Z. Cheng, and J. Lin, "An overview on enhancing the stability of lead halide perovskite quantum dots and their applications in phosphor-converted LEDs," *Chem. Soc. Rev.*, vol. 48, no. 1, pp. 310–350, 2019, doi: 10.1039/C8CS00740C.

[75] J. Kim, S.-H. Lee, J. H. Lee, and K.-H. Hong, "The Role of Intrinsic Defects in Methylammonium Lead Iodide Perovskite," *J. Phys. Chem. Lett.*, vol. 5, no. 8, pp. 1312–1317, Apr. 2014, doi: 10.1021/jz500370k.

[76] H. Dong, C. Ran, W. Gao, M. Li, Y. Xia, and W. Huang, "Metal Halide Perovskite for next-generation optoelectronics: progresses and prospects," *eLight*, vol. 3, no. 1, p. 3, Jan. 2023, doi: 10.1186/s43593-022-00033-z.

[77] A. J. Houtepen, Z. Hens, J. S. Owen, and I. Infante, "On the Origin of Surface Traps in Colloidal II–VI Semiconductor Nanocrystals," *Chem. Mater.*, vol. 29, no. 2, pp. 752–761, Jan. 2017, doi: 10.1021/acs.chemmater.6b04648.

[78] H. J. Queisser and E. E. Haller, "Defects in Semiconductors: Some Fatal, Some Vital," *Science*, vol. 281, no. 5379, pp. 945–950, Aug. 1998, doi: 10.1126/science.281.5379.945.

[79] H. Huang, M. I. Bodnarchuk, S. V. Kershaw, M. V. Kovalenko, and A. L. Rogach, "Lead Halide Perovskite Nanocrystals in the Research Spotlight: Stability and Defect Tolerance," *ACS Energy Lett.*, vol. 2, no. 9, pp. 2071–2083, Sep. 2017, doi: 10.1021/acsenergylett.7b00547.

[80] J. Kang and L.-W. Wang, "High Defect Tolerance in Lead Halide Perovskite CsPbBr$_3$," *J. Phys. Chem. Lett.*, vol. 8, no. 2, pp. 489–493, Jan. 2017, doi: 10.1021/acs.jpclett.6b02800.

[81] M. V. Kovalenko, L. Protesescu, and M. I. Bodnarchuk, "Properties and potential optoelectronic applications of lead halide perovskite nanocrystals," *Science*, vol. 358, no. 6364, pp. 745–750, Nov. 2017, doi: 10.1126/science.aam7093.

[82] C. C. Stoumpos *et al.*, "Crystal Growth of the Perovskite Semiconductor CsPbBr$_3$: A New Material for High-Energy Radiation Detection," *Crystal Growth & Design*, vol. 13, no. 7, pp. 2722–2727, Jul. 2013, doi: 10.1021/cg400645t.

[83] J. De Roo *et al.*, "Highly Dynamic Ligand Binding and Light Absorption Coefficient of Cesium Lead Bromide Perovskite Nanocrystals," *ACS Nano*, vol. 10, no. 2, pp. 2071–2081, Feb. 2016, doi: 10.1021/acsnano.5b06295.

[84] J. Chen, Q. Zhao, B. Yu, and U. Lemmer, "A Review on Quantum Dot-Based Color Conversion Layers for Mini/Micro-LED Displays: Packaging, Light Management, and Pixelation," *Advanced Optical Materials*, p. 2300873, Aug. 2023, doi: 10.1002/adom.202300873.

[85] J. Cho, J. H. Park, J. K. Kim, and E. F. Schubert, "White light-emitting diodes: History, progress, and future," *Laser & Photonics Reviews*, vol. 11, no. 2, p. 1600147, Mar. 2017, doi: 10.1002/lpor.201600147.

[86] T. Guner and M. M. Demir, "A Review on Halide Perovskites as Color Conversion Layers in White Light Emitting Diode Applications," *Physica Status Solidi (a)*, vol. 215, no. 13, p. 1800120, Jul. 2018, doi: 10.1002/pssa.201800120.

[87] J. Yang *et al.*, "Toward Full-Color Electroluminescent Quantum Dot Displays," *Nano Lett.*, vol. 21, no. 1, pp. 26–33, Jan. 2021, doi: 10.1021/acs.nanolett.0c03939.

[88] J. Kim, J. Roh, M. Park, and C. Lee, "Recent Advances and Challenges of Colloidal Quantum Dot Light-Emitting Diodes for Display Applications," *Advanced Materials*, vol. 36, no. 20, p. 2212220, May 2024, doi: 10.1002/adma.202212220.

[89] A. R. Puente-Santiago and D. Rodríguez-Padrón, Eds., *Surface-modified Nanobiomaterials for Electrochemical and Biomedicine Applications*. in Topics in Current Chemistry Collections. Cham: Springer International Publishing, 2020. doi: 10.1007/978-3-030-55502-3.

[90] A. Kim, A. Hosseinmardi, P. K. Annamalai, P. Kumar, and R. Patel, "Review on Colloidal Quantum Dots Luminescent Solar Concentrators," *ChemistrySelect*, vol. 6, no. 20, pp. 4948–4967, May 2021, doi: 10.1002/slct.202100674.

[91] Y. A/P Chowmasundaram, T. L. Tan, R. Nulit, M. Jusoh, and S. A. Rashid, "Recent developments, applications and challenges for carbon quantum dots as a photosynthesis enhancer in agriculture," *RSC Adv.*, vol. 13, no. 36, pp. 25093–25117, 2023, doi: 10.1039/D3RA01217D.

[92] W. Lv *et al.*, "Improving the Stability of Metal Halide Perovskite Quantum Dots by Encapsulation," *Adv. Mater.*, vol. 31, no. 28, p. 1900682, Jul. 2019, doi: 10.1002/adma.201900682.

[93] S. J. Lim, L. Ma, A. Schleife, and A. M. Smith, "Quantum dot surface engineering: Toward inert fluorophores with compact size and bright, stable emission," *Coordination Chemistry Reviews*, vol. 320–321, pp. 216–237, Aug. 2016, doi: 10.1016/j.ccr.2016.03.012.

[94] N. Ming *et al.*, "Mode-locked Er-doped fiber laser based on PbS/CdS core/shell quantum dots as saturable absorber," *Opt. Express*, vol. 26, no. 7, p. 9017, Apr. 2018, doi: 10.1364/OE.26.009017.

[95] J.-S. Li, Y. Tang, Z.-T. Li, X.-R. Ding, L.-S. Rao, and B.-H. Yu, "Effect of Quantum Dot Scattering and Absorption on the Optical Performance of White Light-Emitting Diodes," *IEEE Trans. Electron Devices*, vol. 65, no. 7, pp. 2877–2884, Jul. 2018, doi: 10.1109/TED.2018.2830798.

[96] J.-S. Li, Y. Tang, Z.-T. Li, K. Cao, C.-M. Yan, and X.-R. Ding, "Full spectral optical modeling of quantum-dot-converted elements for light-emitting diodes considering reabsorption and reemission effect," *Nanotechnology*, vol. 29, no. 29, p. 295707, Jul. 2018, doi: 10.1088/1361-6528/aac1b0.

[97] R.-H. Horng, H.-Y. Chien, F.-G. Tarntair, and D.-S. Wuu, "Fabrication and Study on Red Light Micro-LED Displays," *IEEE J. Electron Devices Soc.*, vol. 6, pp. 1064–1069, 2018, doi: 10.1109/JEDS.2018.2864543.

[98] A. Paranjpe, J. Montgomery, S. M. Lee, and C. Morath, "45-2: *Invited Paper:* Micro-LED Displays: Key Manufacturing Challenges and Solutions," *Symp Digest of Tech Papers*, vol. 49, no. 1, pp. 597–600, May 2018, doi: 10.1002/sdtp.12414.

[99] J. Xiong, E.-L. Hsiang, Z. He, T. Zhan, and S.-T. Wu, "Augmented reality and virtual reality displays: emerging technologies and future perspectives," *Light Sci Appl*, vol. 10, no. 1, p. 216, Oct. 2021, doi: 10.1038/s41377-021-00658-8.

[100] E.-L. Hsiang, Z. Yang, Q. Yang, P.-C. Lai, C.-L. Lin, and S.-T. Wu, "AR/VR light engines: perspectives and challenges," *Adv. Opt. Photon.*, vol. 14, no. 4, p. 783, Dec. 2022, doi: 10.1364/AOP.468066.

[101] T. Wu *et al.*, "Mini-LED and Micro-LED: Promising Candidates for the Next Generation Display Technology," *Applied Sciences*, vol. 8, no. 9, p. 1557, Sep. 2018, doi: 10.3390/app8091557.

[102] R. S. Cok *et al.*, "Inorganic light-emitting diode displays using micro-transfer printing," *J Soc Info Display*, vol. 25, no. 10, pp. 589–609, Oct. 2017, doi: 10.1002/jsid.610.

[103] B. Corbett, R. Loi, W. Zhou, D. Liu, and Z. Ma, "Transfer print techniques for heterogeneous integration of photonic components," *Progress in Quantum Electronics*, vol. 52, pp. 1–17, Mar. 2017, doi: 10.1016/j.pquantelec.2017.01.001.

[104] L.-C. Chen, C.-H. Tien, D.-F. Chen, Z.-T. Ye, and H.-C. Kuo, "High-Uniformity Planar Mini-Chip-Scale Packaged LEDs with Quantum Dot Converter for White Light Source," *Nanoscale Res Lett*, vol. 14, no. 1, p. 182, Dec. 2019, doi: 10.1186/s11671-019-2993-z.

[105] X. Fan *et al.*, "Recent developments of quantum dot based micro-LED based on non-radiative energy transfer mechanism," *OEA*, vol. 4, no. 4, pp. 210022–210022, 2021, doi: 10.29026/oea.2021.210022.

[106] S.-W. H. Chen *et al.*, "Full-color micro-LED display with high color stability using semipolar (20-21) InGaN LEDs and quantum-dot photoresist," *Photon. Res.*, vol. 8, no. 5, p. 630, May 2020, doi: 10.1364/PRJ.388958.

[107] A. V. Malko, A. A. Mikhailovsky, M. A. Petruska, J. A. Hollingsworth, and V. I. Klimov, "Interplay between Optical Gain and Photoinduced Absorption in CdSe Nanocrystals," *J. Phys. Chem. B*, vol. 108, no. 17, pp. 5250–5255, Apr. 2004, doi: 10.1021/jp037699q.

[108] T. Han, Y. Yuan, X. Liang, Y. Zhang, C. Xiong, and L. Dong, "Colloidal stable quantum dots modified by dual functional group polymers for inkjet printing," *J. Mater. Chem. C*, vol. 5, no. 19, pp. 4629–4635, 2017, doi: 10.1039/C7TC00452D.

[109] F. Fang *et al.*, "Atomic Layer Deposition Assisted Encapsulation of Quantum Dot Luminescent Microspheres toward Display Applications," *Advanced Optical Materials*, vol. 8, no. 12, p. 1902118, Jun. 2020, doi: 10.1002/adom.201902118.

[110] D.-H. Jiang *et al.*, "Novel ultra-stable and highly luminescent white light-emitting diodes from perovskite quantum dots—Polymer nanofibers through biaxial electrospinning," *APL Materials*, vol. 7, no. 11, p. 111105, Nov. 2019, doi: 10.1063/1.5124880.

[111] Y. Li *et al.*, "One-Step Preparation of Long-Term Stable and Flexible CsPbBr$_3$ Perovskite Quantum Dots/Ethylene Vinyl Acetate Copolymer Composite Films for White Light-Emitting Diodes," *ACS Appl. Mater. Interfaces*, vol. 10, no. 18, pp. 15888–15894, May 2018, doi: 10.1021/acsami.8b02857.

[112] M. J. Smith *et al.*, "Robust, Uniform, and Highly Emissive Quantum Dot–Polymer Films and Patterns Using Thiol–Ene Chemistry," *ACS Appl. Mater. Interfaces*, vol. 9, no. 20, pp. 17435–17448, May 2017, doi: 10.1021/acsami.7b03366.

[113] Z.-T. Li, C.-J. Song, X.-W. Du, J. Xuan, J.-S. Li, and Y. Tang, "Study on the Photoluminescence Intensity, Thermal Performance, and Color Purity of Quantum Dot Light-Emitting Diodes Using a Pumping-Light Absorber," *IEEE Trans. Electron Devices*, vol. 67, no. 6, pp. 2418–2424, Jun. 2020, doi: 10.1109/TED.2020.2990728.

[114] Z.-T. Li, J.-X. Li, Z.-H. Deng, J.-Y. Liang, and J.-S. Li, "Unraveling the Origin of Low Optical Efficiency for Quantum Dot White Light-Emitting Diodes From the Perspective of Aggregation-Induced Scattering Effect," *IEEE Trans. Electron Devices*, vol. 68, no. 4, pp. 1738–1745, Apr. 2021, doi: 10.1109/TED.2021.3060698.

[115] Y. Tang, Z. Li, Z.-T. Li, J.-S. Li, S.-D. Yu, and L.-S. Rao, "Enhancement of Luminous Efficiency and Uniformity of CCT for Quantum Dot-Converted LEDs by Incorporating With ZnO Nanoparticles," *IEEE Trans. Electron Devices*, vol. 65, no. 1, pp. 158–164, Jan. 2018, doi: 10.1109/TED.2017.2771785.

[116] H. Lee, Y. H. Kim, Y. Lim, J. Jang, S. Kang, and B. Bae, "Flexible but Mechanically Robust Hazy Quantum Dot/Glass Fiber Reinforced Film for Efficiently Luminescent Surface Light Source," *Advanced Optical Materials*, vol. 8, no. 10, p. 1902178, May 2020, doi: 10.1002/adom.201902178.

[117] J. Shen, Y. Wang, Y. Zhu, Y. Gong, and C. Li, "A polymer-coated template-confinement CsPbBr$_3$ perovskite quantum dot composite," *Nanoscale*, vol. 13, no. 13, pp. 6586–6591, 2021, doi: 10.1039/D1NR00201E.

[118] S. Yu *et al.*, "Enhanced Photoluminescence in Quantum Dots–Porous Polymer Hybrid Films Fabricated by Microcellular Foaming," *Advanced Optical Materials*, vol. 7, no. 12, p. 1900223, Jun. 2019, doi: 10.1002/adom.201900223.

[119] G. Y. Kim *et al.*, "Order-of-Magnitude, Broadband-Enhanced Light Emission from Quantum Dots Assembled in Multiscale Phase-Separated Block Copolymers," *Nano Lett.*, vol. 19, no. 10, pp. 6827–6838, Oct. 2019, doi: 10.1021/acs.nanolett.9b01941.

[120] A. K. Tobias and M. Jones, "Metal-Enhanced Fluorescence from Quantum Dot-Coupled Gold Nanoparticles," *J. Phys. Chem. C*, vol. 123, no. 2, pp. 1389–1397, Jan. 2019, doi: 10.1021/acs.jpcc.8b09108.

[121] S. Yu *et al.*, "Butterfly-inspired micro-concavity array film for color conversion efficiency improvement of quantum-dot-based light-emitting diodes," *Opt. Lett.*, vol. 42, no. 23, p. 4962, Dec. 2017, doi: 10.1364/OL.42.004962.

[122] J. Lee, K. Min, Y. Park, K. Cho, and H. Jeon, "Photonic Crystal Phosphors Integrated on a Blue LED Chip for Efficient White Light Generation," *Advanced Materials*, vol. 30, no. 3, p. 1703506, Jan. 2018, doi: 10.1002/adma.201703506.

[123] H.-V. Han *et al.*, "Resonant-enhanced full-color emission of quantum-dot-based micro LED display technology," *Opt. Express*, vol. 23, no. 25, p. 32504, Dec. 2015, doi: 10.1364/OE.23.032504.

[124] M. Duan *et al.*, "Inkjet-Printed Micrometer-Thick Patterned Perovskite Quantum Dot Films for Efficient Blue-to-Green Photoconversion," *Adv Materials Technologies*, vol. 4, no. 12, p. 1900779, Dec. 2019, doi: 10.1002/admt.201900779.

[125] L. Shi *et al.*, "In Situ Inkjet Printing Strategy for Fabricating Perovskite Quantum Dot Patterns," *Adv Funct Materials*, vol. 29, no. 37, p. 1903648, Sep. 2019, doi: 10.1002/adfm.201903648.

[126] H. Kim, M. Ryu, J. H. J. Cha, H. S. Kim, T. Jeong, and J. Jang, "Ten micrometer pixel, quantum dots color conversion layer for high resolution and full color active matrix micro-LED display," *J Soc Info Display*, vol. 27, no. 6, pp. 347–353, Jun. 2019, doi: 10.1002/jsid.782.

[127] W. Zhan, L. Meng, C. Shao, X. Wu, K. Shi, and H. Zhong, "In Situ Patterning Perovskite Quantum Dots by Direct Laser Writing Fabrication," *ACS Photonics*, vol. 8, no. 3, pp. 765–770, Mar. 2021, doi: 10.1021/acsphotonics.1c00118.

[128] T.-H. Kim *et al.*, "Full-colour quantum dot displays fabricated by transfer printing," *Nature Photon*, vol. 5, no. 3, pp. 176–182, Mar. 2011, doi: 10.1038/nphoton.2011.12.

[129] M. K. Choi *et al.*, "Wearable red–green–blue quantum dot light-emitting diode array using high-resolution intaglio transfer printing," *NATURE COMMUNICATIONS*, 2015.

[130] J. C. De Mello, H. F. Wittmann, and R. H. Friend, "An improved experimental determination of external photoluminescence quantum efficiency," *Adv. Mater.*, vol. 9, no. 3, pp. 230–232, Mar. 1997, doi: 10.1002/adma.19970090308.

[131] D. O. Faulkner, J. J. McDowell, A. J. Price, D. D. Perovic, N. P. Kherani, and G. A. Ozin, "Measurement of absolute photoluminescence quantum yields using integrating spheres – Which way to go?," *Laser & Photonics Reviews*, vol. 6, no. 6, pp. 802–806, Nov. 2012, doi: 10.1002/lpor.201200077.

[132] J. Chen *et al.*, "Silver-Nanoparticle-Based Metallodielectric Wavelength-Selective Reflectors for Quantum-Dot-Enhanced White-Light-Emitting Diodes," *ACS Appl. Nano Mater.*, vol. 5, no. 1, pp. 87–93, Jan. 2022, doi: 10.1021/acsanm.1c02885.

[133] Y. Liu *et al.*, "Transparent Ceramics Enabling High Luminous Flux and Efficacy for the Next-Generation High-Power LED Light," *ACS Appl. Mater. Interfaces*, vol. 11, no. 24, pp. 21697–21701, Jun. 2019, doi: 10.1021/acsami.9b02703.

[134] I. Jaadane *et al.*, "Retinal damage induced by commercial light emitting diodes (LEDs)," *Free Radical Biology and Medicine*, vol. 84, pp. 373–384, Jul. 2015, doi: 10.1016/j.freeradbiomed.2015.03.034.

[135] Th. Gessmann and E. F. Schubert, "High-efficiency AlGaInP light-emitting diodes for solid-state lighting applications," *Journal of Applied Physics*, vol. 95, no. 5, pp. 2203–2216, Mar. 2004, doi: 10.1063/1.1643786.

[136] M. Qu, H. Li, Y. Zhao, and X.-M. Zhang, "Single-Component Color-Tunable Gd(pic) $_3$: Eu $^{3+}$ Phosphor Based on a Metal–Organic Framework for Near-UV White-Light-Emitting Diodes," *ACS Omega*, vol. 4, no. 2, pp. 3593–3600, Feb. 2019, doi: 10.1021/acsomega.8b02692.

[137] X. Wang, Z. Bao, Y.-C. Chang, and R.-S. Liu, "Perovskite Quantum Dots for Application in High Color Gamut Backlighting Display of Light-Emitting Diodes," *ACS Energy Lett.*, vol. 5, no. 11, pp. 3374–3396, Nov. 2020, doi: 10.1021/acsenergylett.0c01860.

[138] M. Richter, A. Carmele, A. Sitek, and A. Knorr, "Few-Photon Model of the Optical Emission of Semiconductor Quantum Dots," *Phys. Rev. Lett.*, vol. 103, no. 8, p. 087407, Aug. 2009, doi: 10.1103/PhysRevLett.103.087407.

[139] X. Liu *et al.*, "Competition between Local Field Enhancement and Nonradiative Resonant Energy Transfer in the Linear Absorption of a Semiconductor Quantum Dot Coupled to a Metal Nanoparticle," *J. Phys. Chem. C*, vol. 120, no. 32, pp. 18220–18227, Aug. 2016, doi: 10.1021/acs.jpcc.6b03637.

[140] E. Hwang, I. I. Smolyaninov, and C. C. Davis, "Surface Plasmon Polariton Enhanced Fluorescence from Quantum Dots on Nanostructured Metal Surfaces," *Nano Lett.*, vol. 10, no. 3, pp. 813–820, Mar. 2010, doi: 10.1021/nl9031692.

[141] J.-S. Li *et al.*, "Toward 200 Lumens per Watt of Quantum-Dot White-Light-Emitting Diodes by Reducing Reabsorption Loss," *ACS Nano*, vol. 15, no. 1, pp. 550–562, Jan. 2021, doi: 10.1021/acsnano.0c05735.

[142] H.-J. Song, B. G. Jeong, J. Lim, D. C. Lee, W. K. Bae, and V. I. Klimov, "Performance Limits of Luminescent Solar Concentrators Tested with Seed/Quantum-Well Quantum Dots in a Selective-Reflector-Based Optical Cavity," *Nano Lett.*, vol. 18, no. 1, pp. 395–404, Jan. 2018, doi: 10.1021/acs.nanolett.7b04263.

[143] H. C. Yoon, H. Lee, H. Kang, J. H. Oh, and Y. R. Do, "Highly efficient wide-color-gamut QD-emissive LCDs using red and green perovskite core/shell QDs," *J. Mater. Chem. C*, vol. 6, no. 47, pp. 13023–13033, 2018, doi: 10.1039/C8TC04537B.

[144] H. Jin *et al.*, "Vertically stacked RGB LEDs with optimized distributed Bragg reflectors," *Opt. Lett.*, vol. 45, no. 24, p. 6671, Dec. 2020, doi: 10.1364/OL.408416.

[145] J. H. Oh, S. J. Yang, Y.-G. Sung, and Y. R. Do, "Improved color coordinates of green monochromatic pc-LED capped with a band-pass filter," *Opt. Express*, vol. 21, no. 4, p. 4539, Feb. 2013, doi: 10.1364/OE.21.004539.

[146] M. Song *et al.*, "Colors with plasmonic nanostructures: A full-spectrum review," *Applied Physics Reviews*, vol. 6, no. 4, p. 041308, Dec. 2019, doi: 10.1063/1.5110051.

[147] J. S. Clausen *et al.*, "Plasmonic Metasurfaces for Coloration of Plastic Consumer Products," *Nano Lett.*, vol. 14, no. 8, pp. 4499–4504, Aug. 2014, doi: 10.1021/nl5014986.

[148] S. N. Chowdhury *et al.*, "Lithography-Free Plasmonic Color Printing with Femtosecond Laser on Semicontinuous Silver Films," *ACS Photonics*, vol. 8, no. 2, pp. 521–530, Feb. 2021, doi: 10.1021/acsphotonics.0c01506.

[149] S. J. Tan *et al.*, "Plasmonic Color Palettes for Photorealistic Printing with Aluminum Nanostructures," *Nano Lett.*, vol. 14, no. 7, pp. 4023–4029, Jul. 2014, doi: 10.1021/nl501460x.

[150] A. Kristensen *et al.*, "Plasmonic colour generation," *Nat Rev Mater*, vol. 2, no. 1, p. 16088, Nov. 2016, doi: 10.1038/natrevmats.2016.88.

[151] P. Mao *et al.*, "Disorder-Induced Material-Insensitive Optical Response in Plasmonic Nanostructures: Vibrant Structural Colors from Noble Metals," *Advanced Materials*, vol. 33, no. 23, p. 2007623, Jun. 2021, doi: 10.1002/adma.202007623.

[152] H. Bertin *et al.*, "Correlated Disordered Plasmonic Nanostructures Arrays for Augmented Reality," *ACS Photonics*, vol. 5, no. 7, pp. 2661–2668, Jul. 2018, doi: 10.1021/acsphotonics.8b00168.

[153] P. Mao, C. Liu, F. Song, M. Han, S. A. Maier, and S. Zhang, "Manipulating disordered plasmonic systems by external cavity with transition from broadband absorption to reconfigurable reflection," *Nat Commun*, vol. 11, no. 1, p. 1538, Mar. 2020, doi: 10.1038/s41467-020-15349-y.

[154] R. R. Sahu *et al.*, "Single-step fabrication of liquid gallium nanoparticles via capillary interaction for dynamic structural colours," *Nat. Nanotechnol.*, vol. 19, no. 6, pp. 766–774, Jun. 2024, doi: 10.1038/s41565-024-01625-1.

[155] J. Chen *et al.*, "Broadband and Spectrally Selective Photothermal Conversion through Nanocluster Assembly of Disordered Plasmonic Metasurfaces," *Nano Lett.*, vol. 23, no. 15, pp. 7236–7243, Aug. 2023, doi: 10.1021/acs.nanolett.3c01328.

[156] F. Leroy *et al.*, "How to control solid state dewetting: A short review," *Surface Science Reports*, vol. 71, no. 2, pp. 391–409, Jun. 2016, doi: 10.1016/j.surfrep.2016.03.002.

[157] T. Das Gupta *et al.*, "Self-assembly of nanostructured glass metasurfaces via templated fluid instabilities," *Nat. Nanotechnol.*, vol. 14, no. 4, pp. 320–327, Apr. 2019, doi: 10.1038/s41565-019-0362-9.

[158] S. Morawiec, M. J. Mendes, S. Mirabella, F. Simone, F. Priolo, and I. Crupi, "Self-assembled silver nanoparticles for plasmon-enhanced solar cell back reflectors: correlation between structural and optical properties," *Nanotechnology*, vol. 24, no. 26, p. 265601, Jul. 2013, doi: 10.1088/0957-4484/24/26/265601.

[159] A. Kumar, P. Choudhary, A. Kumar, P. H. C. Camargo, and V. Krishnan, "Recent Advances in Plasmonic Photocatalysis Based on TiO_2 and Noble Metal Nanoparticles for Energy Conversion, Environmental Remediation, and Organic Synthesis," *Small*, vol. 18, no. 1, p. 2101638, Jan. 2022, doi: 10.1002/smll.202101638.

[160] S. K. Cushing *et al.*, "Controlling Plasmon-Induced Resonance Energy Transfer and Hot Electron Injection Processes in Metal@TiO_2 Core–Shell Nanoparticles," *J. Phys. Chem. C*, vol. 119, no. 28, pp. 16239–16244, Jul. 2015, doi: 10.1021/acs.jpcc.5b03955.

[161] M. Kneissl, T.-Y. Seong, J. Han, and H. Amano, "The emergence and prospects of deep-ultraviolet light-emitting diode technologies," *Nat. Photonics*, vol. 13, no. 4, pp. 233–244, Apr. 2019, doi: 10.1038/s41566-019-0359-9.

[162] K.-C. Lee, S.-J. Lin, C.-H. Lin, C.-S. Tsai, and Y.-J. Lu, "Size effect of Ag nanoparticles on surface plasmon resonance," *Surface and Coatings Technology*, vol. 202, no. 22–23, pp. 5339–5342, Aug. 2008, doi: 10.1016/j.surfcoat.2008.06.080.

[163] M. M. Miller and A. A. Lazarides, "Sensitivity of Metal Nanoparticle Surface Plasmon Resonance to the Dielectric Environment," *J. Phys. Chem. B*, vol. 109, no. 46, pp. 21556–21565, Nov. 2005, doi: 10.1021/jp054227y.

[164] J. Chen *et al.*, "Enhanced photoluminescence of a microporous quantum dot color conversion layer by inkjet printing," *Nano Res.*, May 2024, doi: 10.1007/s12274-024-6671-9.

[165] M. J. Smith, C. H. Lin, S. Yu, and V. V. Tsukruk, "Composite Structures with Emissive Quantum Dots for Light Enhancement," *Advanced Optical Materials*, vol. 7, no. 4, p. 1801072, Feb. 2019, doi: 10.1002/adom.201801072.

[166] Y. Shu, X. Lin, H. Qin, Z. Hu, Y. Jin, and X. Peng, "Quantum Dots for Display Applications," *Angew Chem Int Ed*, vol. 59, no. 50, pp. 22312–22323, Dec. 2020, doi: 10.1002/anie.202004857.

[167] A. Park, A. Goudarzi, P. Yaghmaie, V. J. Thomas, and E. Maine, "Rapid response through the entrepreneurial capabilities of academic scientists," *Nat. Nanotechnol.*, Apr. 2022, doi: 10.1038/s41565-022-01103-6.

[168] A. R. Anwar, M. T. Sajjad, M. A. Johar, C. A. Hernández-Gutiérrez, M. Usman, and S. P. Łepkowski, "Recent Progress in Micro-LED-Based Display Technologies," *Laser & Photonics Reviews*, vol. 16, no. 6, p. 2100427, Jun. 2022, doi: 10.1002/lpor.202100427.

[169] Z. Liu *et al.*, "Micro-light-emitting diodes with quantum dots in display technology," *Light Sci Appl*, vol. 9, no. 1, p. 83, May 2020, doi: 10.1038/s41377-020-0268-1.

[170] C. Wei *et al.*, "A Universal Ternary-Solvent-Ink Strategy toward Efficient Inkjet-Printed Perovskite Quantum Dot Light-Emitting Diodes," *Advanced Materials*, vol. 34, no. 10, p. 2107798, Mar. 2022, doi: 10.1002/adma.202107798.

[171] H. Roh *et al.*, "Enhanced Performance of Pixelated Quantum Dot Light-Emitting Diodes by Inkjet Printing of Quantum Dot–Polymer Composites," *Advanced Optical Materials*, vol. 9, no. 11, p. 2002129, Jun. 2021, doi: 10.1002/adom.202002129.

[172] D. Yang and Z. Ye, "Quantum simulator comes in pairs," *Nat. Nanotechnol.*, vol. 17, no. 9, pp. 902–903, Sep. 2022, doi: 10.1038/s41565-022-01191-4.

[173] S. Myeong, B. Chon, S. Kumar, H.-J. Son, S. O. Kang, and S. Seo, "Quantum dot photolithography using a quantum dot photoresist composed of an organic–inorganic hybrid coating layer," *Nanoscale Adv.*, vol. 4, no. 4, pp. 1080–1087, 2022, doi: 10.1039/D1NA00744K.

[174] X. Li, J. Liu, G. Jiang, X. Lin, J. Wang, and Z. Li, "Self-supported CsPbBr3/Ti3C2Tx MXene aerogels towards efficient photocatalytic CO2 reduction," *Journal of Colloid and Interface Science*, vol. 643, pp. 174–182, Aug. 2023, doi: 10.1016/j.jcis.2023.04.015.

[175] F. Meinardi *et al.*, "Large-area luminescent solar concentrators based on 'Stokes-shift-engineered' nanocrystals in a mass-polymerized PMMA matrix," *Nature Photon*, vol. 8, no. 5, pp. 392–399, May 2014, doi: 10.1038/nphoton.2014.54.

[176] H. Yang *et al.*, "Enhanced light emission of quantum dot films by scattering of poly(zinc methacrylate) coating CdZnSeS/ZnS quantum dots and high refractive index BaTiO $_3$ nanoparticles," *RSC Adv.*, vol. 10, no. 53, pp. 31705–31710, 2020, doi: 10.1039/D0RA05389A.

[177] D. Theobald, S. Yu, G. Gomard, and U. Lemmer, "Design of Selective Reflectors Utilizing Multiple Scattering by Core–Shell Nanoparticles for Color Conversion Films," *ACS Photonics*, vol. 7, no. 6, pp. 1452–1460, Jun. 2020, doi: 10.1021/acsphotonics.0c00117.

[178] B. Yu *et al.*, "Luminous efficacy enhancement for LED lamps using highly reflective quantum dot-based photoluminescent films," *Opt. Express*, vol. 29, no. 18, p. 29007, Aug. 2021, doi: 10.1364/OE.431345.

[179] M. Yin *et al.*, "Color-stable WRGB emission from blue OLEDs with quantum dots-based patterned down-conversion layer," *Organic Electronics*, vol. 62, pp. 407–411, Nov. 2018, doi: 10.1016/j.orgel.2018.08.036.

[180] J. Li, Y. Tang, Z. Li, X. Ding, B. Yu, and L. Lin, "Largely Enhancing Luminous Efficacy, Color-Conversion Efficiency, and Stability for Quantum-Dot White LEDs Using the Two-Dimensional Hexagonal Pore Structure of SBA-15 Mesoporous Particles," *ACS Appl. Mater. Interfaces*, vol. 11, no. 20, pp. 18808–18816, May 2019, doi: 10.1021/acsami.8b22298.

[181] B.-R. Hyun, C.-W. Sher, Y.-W. Chang, Y. Lin, Z. Liu, and H.-C. Kuo, "Dual Role of Quantum Dots as Color Conversion Layer and Suppression of Input Light for Full-Color Micro-LED Displays," *J. Phys. Chem. Lett.*, vol. 12, no. 29, pp. 6946–6954, Jul. 2021, doi: 10.1021/acs.jpclett.1c00321.

[182] G. Liang *et al.*, "Polystyrene-Fiber-Rod Hybrid Composite Structure for Optical Enhancement in Quantum-Dot-Converted Light-Emitting Diodes," *ACS Appl. Polym. Mater.*, vol. 4, no. 1, pp. 91–99, Jan. 2022, doi: 10.1021/acsapm.1c01022.

[183] Y. Li, S. Yu, J. G. C. Veinot, J. Linnros, L. Berglund, and I. Sychugov, "Luminescent Transparent Wood," *Advanced Optical Materials*, vol. 5, no. 1, p. 1600834, Jan. 2017, doi: 10.1002/adom.201600834.

[184] P. Kumar, N. Ganesh, and K. S. Narayan, "Electrospun Fibers Containing Emissive Hybrid Perovskite Quantum Dots," *ACS Appl. Mater. Interfaces*, vol. 11, no. 27, pp. 24468–24477, Jul. 2019, doi: 10.1021/acsami.9b08409.

[185] S. Wang, A. A. Yousefi Amin, L. Wu, M. Cao, Q. Zhang, and T. Ameri, "Perovskite Nanocrystals: Synthesis, Stability, and Optoelectronic Applications," *Small Structures*, vol. 2, no. 3, p. 2000124, Mar. 2021, doi: 10.1002/sstr.202000124.

[186] J. Li, Z. Li, J. Qiu, and J. Li, "Photothermal Optimization of Quantum Dot Converters for High-Power Solid-State Light Sources," *Advanced Optical Materials*, vol. 10, no. 8, p. 2102201, Apr. 2022, doi: 10.1002/adom.202102201.

[187] Z. Hu *et al.*, "Inkjet printed uniform quantum dots as color conversion layers for full-color OLED displays," *Nanoscale*, vol. 12, no. 3, pp. 2103–2110, 2020, doi: 10.1039/C9NR09086J.

[188] P. Yang, L. Zhang, D. J. Kang, R. Strahl, and T. Kraus, "High-Resolution Inkjet Printing of Quantum Dot Light-Emitting Microdiode Arrays," *Advanced Optical Materials*, vol. 8, no. 1, p. 1901429, Jan. 2020, doi: 10.1002/adom.201901429.

[189] Q. Zhang *et al.*, "Fabrication of Microlens Arrays with High Quality and High Fill Factor by Inkjet Printing," *Advanced Optical Materials*, vol. 10, no. 14, p. 2200677, Jul. 2022, doi: 10.1002/adom.202200677.

[190] Y. J. Donie *et al.*, "Phase-Separated Nanophotonic Structures by Inkjet Printing," *ACS Nano*, vol. 15, no. 4, pp. 7305–7317, Apr. 2021, doi: 10.1021/acsnano.1c00552.

[191] J.-K. Kim, K. Taki, and M. Ohshima, "Preparation of a Unique Microporous Structure via Two Step Phase Separation in the Course of Drying a Ternary Polymer Solution," *Langmuir*, vol. 23, no. 24, pp. 12397–12405, Nov. 2007, doi: 10.1021/la7013896.

[192] J. Kim, K. Taki, S. Nagamine, and M. Ohshima, "Preparation of a polymeric membrane with a fine porous structure by dry casting," *J of Applied Polymer Sci*, vol. 111, no. 5, pp. 2518–2526, Mar. 2009, doi: 10.1002/app.29348.

[193] J. Wu *et al.*, "Porous Polymers as Multifunctional Material Platforms toward Task-Specific Applications," *Advanced Materials*, vol. 31, no. 4, p. 1802922, Jan. 2019, doi: 10.1002/adma.201802922.

[194] F. Wang, P. Altschuh, L. Ratke, H. Zhang, M. Selzer, and B. Nestler, "Progress Report on Phase Separation in Polymer Solutions," *Advanced Materials*, vol. 31, no. 26, p. 1806733, Jun. 2019, doi: 10.1002/adma.201806733.

[195] S. Yu, J. Chen, G. Gomard, H. Hölscher, and U. Lemmer, "Recent Progress in Light-Scattering Porous Polymers and Their Applications," *Advanced Optical Materials*, vol. 11, no. 13, p. 2203134, Jul. 2023, doi: 10.1002/adom.202203134.

[196] D. Chen, K. Gao, J. Yang, and L. Zhang, "Functionally graded porous structures: Analyses, performances, and applications – A Review," *Thin-Walled Structures*, vol. 191, p. 111046, Oct. 2023, doi: 10.1016/j.tws.2023.111046.

[197] S. Dou *et al.*, "Bioinspired Microstructured Materials for Optical and Thermal Regulation," *Advanced Materials*, vol. 33, no. 6, p. 2000697, Feb. 2021, doi: 10.1002/adma.202000697.

[198] Y. Pang, Y. Cao, W. Zheng, and C. B. Park, "A comprehensive review of cell structure variation and general rules for polymer microcellular foams," *Chemical Engineering Journal*, vol. 430, p. 132662, Feb. 2022, doi: 10.1016/j.cej.2021.132662.

[199] G. Wang, J. Liu, J. Zhao, S. Li, G. Zhao, and C. B. Park, "Structure-gradient thermoplastic polyurethane foams with enhanced resilience derived by microcellular foaming," *The Journal of Supercritical Fluids*, vol. 188, p. 105667, Sep. 2022, doi: 10.1016/j.supflu.2022.105667.

[200] J. Syurik *et al.*, "Bio-inspired, large scale, highly-scattering films for nanoparticle-alternative white surfaces," *Sci Rep*, vol. 7, no. 1, p. 46637, Apr. 2017, doi: 10.1038/srep46637.

[201] D. Li *et al.*, "Scalable and hierarchically designed polymer film as a selective thermal emitter for high-performance all-day radiative cooling," *Nat. Nanotechnol.*, vol. 16, no. 2, pp. 153–158, Feb. 2021, doi: 10.1038/s41565-020-00800-4.

[202] H. Zhong *et al.*, "Hierarchically Hollow Microfibers as a Scalable and Effective Thermal Insulating Cooler for Buildings," *ACS Nano*, vol. 15, no. 6, pp. 10076–10083, Jun. 2021, doi: 10.1021/acsnano.1c01814.

[203] L. Zhou *et al.*, "Sustainable and Inexpensive Polydimethylsiloxane Sponges for Daytime Radiative Cooling," *Advanced Science*, vol. 8, no. 23, p. 2102502, Dec. 2021, doi: 10.1002/advs.202102502.

[204] Y. Weng, W. Zhang, Y. Jiang, W. Zhao, and Y. Deng, "Effective daytime radiative cooling via a template method based PDMS sponge emitter with synergistic thermo-optical activity," *Solar Energy Materials and Solar Cells*, vol. 230, p. 111205, Sep. 2021, doi: 10.1016/j.solmat.2021.111205.

[205] J. Syurik, G. Jacucci, O. D. Onelli, H. Hölscher, and S. Vignolini, "Bio-inspired Highly Scattering Networks via Polymer Phase Separation," *Adv Funct Materials*, vol. 28, no. 24, p. 1706901, Jun. 2018, doi: 10.1002/adfm.201706901.

[206] Y. J. Donie *et al.*, "Light trapping in thin film silicon solar cells *via* phase separated disordered nanopillars," *Nanoscale*, vol. 10, no. 14, pp. 6651–6659, 2018, doi: 10.1039/C8NR00455B.

[207] Y. Tang *et al.*, "Bioinspired high-scattering polymer films fabricated by polymerization-induced phase separation," *Opt. Lett.*, vol. 45, no. 10, p. 2918, May 2020, doi: 10.1364/OL.390639.

[208] J. Mandal *et al.*, "Hierarchically porous polymer coatings for highly efficient passive daytime radiative cooling," *Science*, vol. 362, no. 6412, pp. 315–319, Oct. 2018, doi: 10.1126/science.aat9513.

[209] W. F. Yong and H. Zhang, "Recent advances in polymer blend membranes for gas separation and pervaporation," *Progress in Materials Science*, vol. 116, p. 100713, Feb. 2021, doi: 10.1016/j.pmatsci.2020.100713.

[210] D. Mrđenović, D. Abbott, V. Mougel, W. Su, N. Kumar, and R. Zenobi, "Visualizing Surface Phase Separation in PS-PMMA Polymer Blends at the Nanoscale," *ACS Appl. Mater. Interfaces*, vol. 14, no. 21, pp. 24938–24945, Jun. 2022, doi: 10.1021/acsami.2c03857.

[211] Y. Kawamura, J. Brooks, J. J. Brown, H. Sasabe, and C. Adachi, "Intermolecular Interaction and a Concentration-Quenching Mechanism of Phosphorescent Ir(III) Complexes in a Solid Film," *Phys. Rev. Lett.*, vol. 96, no. 1, p. 017404, Jan. 2006, doi: 10.1103/PhysRevLett.96.017404.

[212] K. Tai, W. Lü, I. Umezu, and A. Sugimura, "Inter-Dot Distance Dependence of Photoluminescence Properties in CdSe Quantum Dot Systems," *Appl. Phys. Express*, vol. 3, no. 3, p. 035202, Mar. 2010, doi: 10.1143/APEX.3.035202.

[213] J. Chen *et al.*, "Organosilicon-Based Ligand Design for High-Performance Perovskite Nanocrystal Films for Color Conversion and X-ray Imaging," *ACS Nano*, vol. 18, no. 14, pp. 10054–10062, Apr. 2024, doi: 10.1021/acsnano.3c11991.

[214] L. Protesescu *et al.*, "Nanocrystals of Cesium Lead Halide Perovskites (CsPbX$_3$, X = Cl, Br, and I): Novel Optoelectronic Materials Showing Bright Emission with Wide Color Gamut," *Nano Lett.*, vol. 15, no. 6, pp. 3692–3696, Jun. 2015, doi: 10.1021/nl5048779.

[215] Q. A. Akkerman, A. L. Abdelhady, and L. Manna, "Zero-Dimensional Cesium Lead Halides: History, Properties, and Challenges," *J. Phys. Chem. Lett.*, vol. 9, no. 9, pp. 2326–2337, May 2018, doi: 10.1021/acs.jpclett.8b00572.

[216] C.-Y. Huang *et al.*, "Inorganic Halide Perovskite Quantum Dots: A Versatile Nanomaterial Platform for Electronic Applications," *Nano-Micro Lett.*, vol. 15, no. 1, p. 16, Dec. 2023, doi: 10.1007/s40820-022-00983-6.

[217] S. Chang, Z. Bai, and H. Zhong, "In Situ Fabricated Perovskite Nanocrystals: A Revolution in Optical Materials," *Advanced Optical Materials*, vol. 6, no. 18, p. 1800380, Sep. 2018, doi: 10.1002/adom.201800380.

[218] H. Zhang *et al.*, "Stable continuous-wave lasing from discrete cesium lead bromide quantum dots embedded in a microcavity," *Nanoscale Horiz.*, p. 10.1039.D3NH00139C, 2023, doi: 10.1039/D3NH00139C.

[219] J. Chen *et al.*, "Perovskite quantum dot lasers," *InfoMat*, vol. 2, no. 1, pp. 170–183, Jan. 2020, doi: 10.1002/inf2.12051.

[220] C. Zhu *et al.*, "Room-Temperature, Highly Pure Single-Photon Sources from All-Inorganic Lead Halide Perovskite Quantum Dots," *Nano Lett.*, vol. 22, no. 9, pp. 3751–3760, May 2022, doi: 10.1021/acs.nanolett.2c00756.

[221] G. Rainò *et al.*, "Underestimated Effect of a Polymer Matrix on the Light Emission of Single $CsPbBr_3$ Nanocrystals," *Nano Lett.*, vol. 19, no. 6, pp. 3648–3653, Jun. 2019, doi: 10.1021/acs.nanolett.9b00689.

[222] Q. Wan *et al.*, "Ultrathin Light-Emitting Diodes with External Efficiency over 26% Based on Resurfaced Perovskite Nanocrystals," *ACS Energy Lett.*, vol. 8, no. 2, pp. 927–934, Feb. 2023, doi: 10.1021/acsenergylett.2c02802.

[223] B. Zhao *et al.*, "Light management for perovskite light-emitting diodes," *Nat. Nanotechnol.*, Aug. 2023, doi: 10.1038/s41565-023-01482-4.

[224] S. Liao *et al.*, "A Hierarchical Structure Perovskite Quantum Dots Film for Laser-Driven Projection Display," *Adv Funct Materials*, vol. 33, no. 1, p. 2210558, Jan. 2023, doi: 10.1002/adfm.202210558.

[225] H. Hu, I. Levchuk, F. Kalkowski, J. Elia, A. Osvet, and C. J. Brabec, "Engineering Stable Perovskite Quantum Dot Films for High Color Purity Display Applications," *ACS Energy Lett.*, pp. 4380–4385, Sep. 2023, doi: 10.1021/acsenergylett.3c01812.

[226] Q. Chen *et al.*, "All-inorganic perovskite nanocrystal scintillators," *Nature*, vol. 561, no. 7721, pp. 88–93, Sep. 2018, doi: 10.1038/s41586-018-0451-1.

[227] J. H. Heo, D. H. Shin, J. K. Park, D. H. Kim, S. J. Lee, and S. H. Im, "High-Performance Next-Generation Perovskite Nanocrystal Scintillator for Nondestructive X-Ray Imaging," *Adv. Mater.*, vol. 30, no. 40, p. 1801743, Oct. 2018, doi: 10.1002/adma.201801743.

[228] Y. Zhou, J. Chen, O. M. Bakr, and O. F. Mohammed, "Metal Halide Perovskites for X-ray Imaging Scintillators and Detectors," *ACS Energy Lett.*, vol. 6, no. 2, pp. 739–768, Feb. 2021, doi: 10.1021/acsenergylett.0c02430.

[229] J. Shamsi, A. S. Urban, M. Imran, L. De Trizio, and L. Manna, "Metal Halide Perovskite Nanocrystals: Synthesis, Post-Synthesis Modifications, and Their Optical Properties," *Chem. Rev.*, vol. 119, no. 5, pp. 3296–3348, Mar. 2019, doi: 10.1021/acs.chemrev.8b00644.

[230] M. Liu *et al.*, "Suppression of temperature quenching in perovskite nanocrystals for efficient and thermally stable light-emitting diodes," *Nat. Photonics*, vol. 15, no. 5, pp. 379–385, May 2021, doi: 10.1038/s41566-021-00766-2.

[231] S. Huang *et al.*, "Morphology Evolution and Degradation of $CsPbBr_3$ Nanocrystals under Blue Light-Emitting Diode Illumination," *ACS Appl. Mater. Interfaces*, vol. 9, no. 8, pp. 7249–7258, Mar. 2017, doi: 10.1021/acsami.6b14423.

[232] X. Zhang *et al.*, "All-Inorganic Perovskite Nanocrystals for High-Efficiency Light Emitting Diodes: Dual-Phase $CsPbBr_3$-$CsPb_2Br_5$ Composites," *Adv. Funct. Mater.*, vol. 26, no. 25, pp. 4595–4600, Jul. 2016, doi: 10.1002/adfm.201600958.

[233] C. Jia, H. Li, X. Meng, and H. Li, "CsPbX$_3$/Cs$_4$PbX$_6$ core/shell perovskite nanocrystals," *Chem. Commun.*, vol. 54, no. 49, pp. 6300–6303, 2018, doi: 10.1039/C8CC02802H.

[234] S. Wang, L. Du, Z. Jin, Y. Xin, and H. Mattoussi, "Enhanced Stabilization and Easy Phase Transfer of CsPbBr$_3$ Perovskite Quantum Dots Promoted by High-Affinity Polyzwitterionic Ligands," *J. Am. Chem. Soc.*, vol. 142, no. 29, pp. 12669–12680, Jul. 2020, doi: 10.1021/jacs.0c03682.

[235] J. Pan *et al.*, "Bidentate Ligand-Passivated CsPbI$_3$ Perovskite Nanocrystals for Stable Near-Unity Photoluminescence Quantum Yield and Efficient Red Light-Emitting Diodes," *J. Am. Chem. Soc.*, vol. 140, no. 2, pp. 562–565, Jan. 2018, doi: 10.1021/jacs.7b10647.

[236] M. N. An *et al.*, "Low-Temperature Molten Salts Synthesis: CsPbBr$_3$ Nanocrystals with High Photoluminescence Emission Buried in Mesoporous SiO$_2$," *ACS Energy Lett.*, vol. 6, no. 3, pp. 900–907, Mar. 2021, doi: 10.1021/acsenergylett.1c00052.

[237] Z. Li, L. Kong, S. Huang, and L. Li, "Highly Luminescent and Ultrastable CsPbBr$_3$ Perovskite Quantum Dots Incorporated into a Silica/Alumina Monolith," *Angew. Chem.*, vol. 129, no. 28, pp. 8246–8250, Jul. 2017, doi: 10.1002/ange.201703264.

[238] K. J. Babu, G. Kaur, L. Biswal, G. De, and H. N. Ghosh, "Ultrafast Charge Delocalization Dynamics of Ambient Stable CsPbBr$_3$ Nanocrystals Encapsulated in Polystyrene Fiber," *Chemistry A European J*, vol. 27, no. 2, pp. 683–691, Jan. 2021, doi: 10.1002/chem.202003254.

[239] Z. Wang *et al.*, "One-Step Polymeric Melt Encapsulation Method to Prepare CsPbBr$_3$ Perovskite Quantum Dots/Polymethyl Methacrylate Composite with High Performance," *Adv Funct Materials*, vol. 31, no. 22, p. 2010009, May 2021, doi: 10.1002/adfm.202010009.

[240] G. Jiang *et al.*, "Highly Luminescent and Water-Resistant CsPbBr$_3$ –CsPb$_2$Br$_5$ Perovskite Nanocrystals Coordinated with Partially Hydrolyzed Poly(methyl methacrylate) and Polyethylenimine," *ACS Nano*, vol. 13, no. 9, pp. 10386–10396, Sep. 2019, doi: 10.1021/acsnano.9b04179.

[241] H. C. Yoon, S. Lee, J. K. Song, H. Yang, and Y. R. Do, "Efficient and Stable CsPbBr$_3$ Quantum-Dot Powders Passivated and Encapsulated with a Mixed Silicon Nitride and Silicon Oxide Inorganic Polymer Matrix," *ACS Appl. Mater. Interfaces*, vol. 10, no. 14, pp. 11756–11767, Apr. 2018, doi: 10.1021/acsami.8b01014.

[242] F. Carulli, M. He, F. Cova, A. Erroi, L. Li, and S. Brovelli, "Silica-Encapsulated Perovskite Nanocrystals for X-ray-Activated Singlet Oxygen Production and Radiotherapy Application," *ACS Energy Lett.*, vol. 8, no. 4, pp. 1795–1802, Apr. 2023, doi: 10.1021/acsenergylett.3c00234.

[243] H.-C. Wang *et al.*, "Mesoporous Silica Particles Integrated with All-Inorganic CsPbBr$_3$ Perovskite Quantum-Dot Nanocomposites (MP-PQDs) with High Stability and Wide Color Gamut Used for Backlight Display," *Angew. Chem. Int. Ed.*, vol. 55, no. 28, pp. 7924–7929, Jul. 2016, doi: 10.1002/anie.201603698.

[244] Z. Li *et al.*, "Highly Efficient and Water-Stable Lead Halide Perovskite Quantum Dots Using Superhydrophobic Aerogel Inorganic Matrix for White Light-Emitting Diodes," *Adv Materials Technologies*, vol. 5, no. 2, p. 1900941, Feb. 2020, doi: 10.1002/admt.201900941.

[245] H. Kim *et al.*, "Polymer Zwitterions for Stabilization of CsPbBr$_3$ Perovskite Nanoparticles and Nanocomposite Films," *Angewandte Chemie*, vol. 132, no. 27, pp. 10894–10898, Jun. 2020, doi: 10.1002/ange.201916492.

[246] L. Xi, C. B. Boothroyd, T. Salim, S. Borghardt, Y. M. Lam, and B. E. Kardynał, "Facile in situ synthesis of stable luminescent organic–inorganic lead halide perovskite nanoparticles in a polymer matrix," *J. Mater. Chem. C*, vol. 5, no. 29, pp. 7207–7214, 2017, doi: 10.1039/C7TC02109G.

[247] R. Tian, K. Li, Y. Lin, C. Lu, and X. Duan, "Characterization Techniques of Polymer Aging: From Beginning to End," *Chem. Rev.*, vol. 123, no. 6, pp. 3007–3088, Mar. 2023, doi: 10.1021/acs.chemrev.2c00750.

[248] L. Xu *et al.*, "Double-Protected All-Inorganic Perovskite Nanocrystals by Crystalline Matrix and Silica for Triple-Modal Anti-Counterfeiting Codes," *ACS Appl. Mater. Interfaces*, vol. 9, no. 31, pp. 26556–26564, Aug. 2017, doi: 10.1021/acsami.7b06436.

[249] Z. Hu *et al.*, "Enhanced Two-Photon-Pumped Emission from In Situ Synthesized Nonblinking CsPbBr$_3$/SiO$_2$ Nanocrystals with Excellent Stability," *Advanced Optical Materials*, vol. 6, no. 3, p. 1700997, Feb. 2018, doi: 10.1002/adom.201700997.

[250] G. Almeida *et al.*, "Role of Acid–Base Equilibria in the Size, Shape, and Phase Control of Cesium Lead Bromide Nanocrystals," *ACS Nano*, vol. 12, no. 2, pp. 1704–1711, Feb. 2018, doi: 10.1021/acsnano.7b08357.

[251] S. Jeon *et al.*, "All-Solution Processed Multicolor Patterning Technique of Perovskite Nanocrystal for Color Pixel Array and Flexible Optoelectronic Devices," *Advanced Optical Materials*, vol. 8, no. 17, p. 2000501, Sep. 2020, doi: 10.1002/adom.202000501.

[252] C. K. Trinh, H. Lee, M. G. So, and C.-L. Lee, "Synthesis of Chemically Stable Ultrathin SiO$_2$-Coated Core–Shell Perovskite QDs via Modulation of Ligand Binding Energy for All-Solution-Processed Light-Emitting Diodes," *ACS Appl. Mater. Interfaces*, vol. 13, no. 25, pp. 29798–29808, Jun. 2021, doi: 10.1021/acsami.1c06097.

[253] M. Imran *et al.*, "Simultaneous Cationic and Anionic Ligand Exchange For Colloidally Stable CsPbBr$_3$ Nanocrystals," *ACS Energy Lett.*, vol. 4, no. 4, pp. 819–824, Apr. 2019, doi: 10.1021/acsenergylett.9b00140.

[254] J. Ye, M. M. Byranvand, C. O. Martínez, R. L. Z. Hoye, M. Saliba, and L. Polavarapu, "Defect Passivation in Lead-Halide Perovskite Nanocrystals and Thin Films: Toward Efficient LEDs and Solar Cells," *Angew Chem Int Ed*, vol. 60, no. 40, pp. 21636–21660, Sep. 2021, doi: 10.1002/anie.202102360.

[255] F. Zhang *et al.*, "Synergetic Effect of the Surfactant and Silica Coating on the Enhanced Emission and Stability of Perovskite Quantum Dots for Anticounterfeiting," *ACS Appl. Mater. Interfaces*, vol. 11, no. 31, pp. 28013–28022, Aug. 2019, doi: 10.1021/acsami.9b07518.

[256] Y. Geng *et al.*, "Large-Scale Production of Ligand-Engineered Robust Lead Halide Perovskite Nanocrystals by a Droplet-Based Microreactor System," *Small*, vol. 18, no. 19, p. 2200740, May 2022, doi: 10.1002/smll.202200740.

[257] C. Sun *et al.*, "Efficient and Stable White LEDs with Silica-Coated Inorganic Perovskite Quantum Dots," *Adv. Mater.*, vol. 28, no. 45, pp. 10088–10094, Dec. 2016, doi: 10.1002/adma.201603081.

[258] B. Luo *et al.*, "Organolead Halide Perovskite Nanocrystals: Branched Capping Ligands Control Crystal Size and Stability," *Angew. Chem. Int. Ed.*, vol. 55, no. 31, pp. 8864–8868, Jul. 2016, doi: 10.1002/anie.201602236.

[259] F. Krieg *et al.*, "Colloidal CsPbX$_3$ (X = Cl, Br, I) Nanocrystals 2.0: Zwitterionic Capping Ligands for Improved Durability and Stability," *ACS Energy Lett.*, vol. 3, no. 3, pp. 641–646, Mar. 2018, doi: 10.1021/acsenergylett.8b00035.

[260] P. Makkar and N. N. Ghosh, "A review on the use of DFT for the prediction of the properties of nanomaterials," *RSC Adv.*, vol. 11, no. 45, pp. 27897–27924, 2021, doi: 10.1039/D1RA04876G.

[261] X. Jing *et al.*, "Enhanced Photoluminescence and Photoresponsiveness of Eu^{3+} Ions-Doped CsPbCl$_3$ Perovskite Quantum Dots under High Pressure," *Adv Funct Materials*, vol. 31, no. 31, p. 2100930, Aug. 2021, doi: 10.1002/adfm.202100930.

[262] J. Schartner *et al.*, "Universal Method for Protein Immobilization on Chemically Functionalized Germanium Investigated by ATR-FTIR Difference Spectroscopy," *J. Am. Chem. Soc.*, vol. 135, no. 10, pp. 4079–4087, Mar. 2013, doi: 10.1021/ja400253p.

[263] M. A. Vargas, M. Scheubner, and G. Guthausen, "Reaction kinetics of polyfurfuryl alcohol bioresin and nanoparticles by [1] H-NMR transverse relaxation measurements," *Polymer Composites*, vol. 39, no. 9, pp. 3280–3288, Sep. 2018, doi: 10.1002/pc.24342.

[264] L. Chouhan, S. Ghimire, and V. Biju, "Blinking Beats Bleaching: The Control of Superoxide Generation by Photo-ionized Perovskite Nanocrystals," *Angew. Chem. Int. Ed.*, vol. 58, no. 15, pp. 4875–4879, Apr. 2019, doi: 10.1002/anie.201900061.

[265] J. Di *et al.*, "Reveal the Humidity Effect on the Phase Pure CsPbBr$_3$ Single Crystals Formation at Room Temperature and Its Application for Ultrahigh Sensitive X-Ray Detector," *Advanced Science*, vol. 9, no. 2, p. 2103482, Jan. 2022, doi: 10.1002/advs.202103482.

[266] X. Du *et al.*, "High-quality CsPbBr$_3$ perovskite nanocrystals for quantum dot light-emitting diodes," *RSC Adv.*, vol. 7, no. 17, pp. 10391–10396, 2017, doi: 10.1039/C6RA27665B.

[267] N. Majoul, S. Aouida, and B. Bessaïs, "Progress of porous silicon APTES-functionalization by FTIR investigations," *Applied Surface Science*, vol. 331, pp. 388–391, Mar. 2015, doi: 10.1016/j.apsusc.2015.01.107.

[268] D. H. Lee and R. A. Condrate, "FTIR spectral characterization of thin film coatings of oleic acid on glasses: I. Coatings on glasses from ethyl alcohol," 1998.

[269] E. V. Péan, S. Dimitrov, C. S. De Castro, and M. L. Davies, "Interpreting time-resolved photoluminescence of perovskite materials," *Phys. Chem. Chem. Phys.*, vol. 22, no. 48, pp. 28345–28358, 2020, doi: 10.1039/D0CP04950F.

[270] S. Chen *et al.*, "Light Illumination Induced Photoluminescence Enhancement and Quenching in Lead Halide Perovskite," *Solar RRL*, vol. 1, no. 1, p. 1600001, Jan. 2017, doi: 10.1002/solr.201600001.

[271] L. Qiu *et al.*, "Highly efficient and stable CsPbBr$_3$ perovskite quantum dots by encapsulation in dual-shell hollow silica spheres for WLEDs," *Inorg. Chem. Front.*, vol. 7, no. 10, pp. 2060–2071, 2020, doi: 10.1039/D0QI00208A.

[272] F. Zhang *et al.*, "Silica coating enhances the stability of inorganic perovskite nanocrystals for efficient and stable down-conversion in white light-emitting devices," *Nanoscale*, vol. 10, no. 43, pp. 20131–20139, 2018, doi: 10.1039/C8NR07022A.

[273] W. Song *et al.*, "Super stable CsPbBr3@SiO2 tumor imaging reagent by stress-response encapsulation," *Nano Res.*, vol. 13, no. 3, pp. 795–801, Mar. 2020, doi: 10.1007/s12274-020-2697-9.

[274] C. Meng, D. Yang, Y. Wu, X. Zhang, H. Zeng, and X. Li, "Synthesis of single CsPbBr$_3$ @SiO$_2$ core–shell particles *via* surface activation," *J. Mater. Chem. C*, vol. 8, no. 48, pp. 17403–17409, 2020, doi: 10.1039/D0TC03932B.

[275] H. Guan, S. Zhao, H. Wang, D. Yan, M. Wang, and Z. Zang, "Room temperature synthesis of stable single silica-coated CsPbBr3 quantum dots combining tunable red emission of Ag–In–Zn–S for High-CRI white light-emitting diodes," *Nano Energy*, vol. 67, p. 104279, Jan. 2020, doi: 10.1016/j.nanoen.2019.104279.

[276] S. Deumel *et al.*, "High-sensitivity high-resolution X-ray imaging with soft-sintered metal halide perovskites," *Nat Electron*, vol. 4, no. 9, pp. 681–688, Sep. 2021, doi: 10.1038/s41928-021-00644-3.

[277] G. Rainò *et al.*, "Ultra-narrow room-temperature emission from single CsPbBr3 perovskite quantum dots," *Nat Commun*, vol. 13, no. 1, p. 2587, May 2022, doi: 10.1038/s41467-022-30016-0.

[278] X. Wang *et al.*, "Color-tunable X-ray scintillation based on a series of isotypic lanthanide–organic frameworks," *Chem. Commun.*, vol. 56, no. 2, pp. 233–236, 2020, doi: 10.1039/C9CC08114C.

[279] W. Zhao, Y. Wang, Y. Guo, Y. D. Suh, and X. Liu, "Color-Tunable and Stable Copper Iodide Cluster Scintillators for Efficient X-Ray Imaging," *Advanced Science*, vol. 10, no. 5, p. 2205526, Feb. 2023, doi: 10.1002/advs.202205526.

[280] W. Ma *et al.*, "Highly Resolved and Robust Dynamic X-Ray Imaging Using Perovskite Glass-Ceramic Scintillator with Reduced Light Scattering," *Advanced Science*, vol. 8, no. 15, p. 2003728, Aug. 2021, doi: 10.1002/advs.202003728.

[281] F. Maddalena *et al.*, "Stable and Bright Commercial $CsPbBr_3$ Quantum Dot-Resin Layers for Apparent X-ray Imaging Screen," *ACS Appl. Mater. Interfaces*, vol. 13, no. 49, pp. 59450–59459, Dec. 2021, doi: 10.1021/acsami.1c16171.

[282] B. Wang *et al.*, "Template Assembled Large-Size $CsPbBr_3$ Nanocomposite Films toward Flexible, Stable, and High-Performance X-Ray Scintillators," *Laser & Photonics Reviews*, vol. 16, no. 7, p. 2100736, Jul. 2022, doi: 10.1002/lpor.202100736.

[283] H. Zhang *et al.*, "Reproducible X-ray Imaging with a Perovskite Nanocrystal Scintillator Embedded in a Transparent Amorphous Network Structure," *Advanced Materials*, vol. 33, no. 40, p. 2102529, Oct. 2021, doi: 10.1002/adma.202102529.

[284] H. Li *et al.*, "Ultrahigh Spatial Resolution, Fast Decay, and Stable X-Ray Scintillation Screen through Assembling $CsPbBr_3$ Nanocrystals Arrays in Anodized Aluminum Oxide," *Advanced Optical Materials*, vol. 9, no. 24, p. 2101297, Dec. 2021, doi: 10.1002/adom.202101297.

[285] Z. Zhang *et al.*, "Single-Crystalline Perovskite Nanowire Arrays for Stable X-ray Scintillators with Micrometer Spatial Resolution," *ACS Appl. Nano Mater.*, vol. 5, no. 1, pp. 881–889, Jan. 2022, doi: 10.1021/acsanm.1c03575.

[286] Y. Zhang *et al.*, "Metal Halide Perovskite Nanosheet for X-ray High-Resolution Scintillation Imaging Screens," *ACS Nano*, vol. 13, no. 2, pp. 2520–2525, Feb. 2019, doi: 10.1021/acsnano.8b09484.

[287] Y. Liang, Q. Shang, M. Li, S. Zhang, X. Liu, and Q. Zhang, "Solvent Recrystallization-Enabled Green Amplified Spontaneous Emissions with an Ultra-Low Threshold from Pinhole-Free Perovskite Films," *Adv Funct Materials*, vol. 31, no. 48, p. 2106108, Nov. 2021, doi: 10.1002/adfm.202106108.

[288] C. Cho, A. Palatnik, M. Sudzius, R. Grodofzig, F. Nehm, and K. Leo, "Controlling and Optimizing Amplified Spontaneous Emission in Perovskites," *ACS Appl. Mater. Interfaces*, vol. 12, no. 31, pp. 35242–35249, Aug. 2020, doi: 10.1021/acsami.0c08870.

List of Figures

List of Tables

Acronyms and Abbreviations

AFM   atomic force microscope

ALD   atomic layer deposition

APTES   aminopropyltriethoxysilicone

APTES-PA   aminopropyltriethoxysilicone with pentanedioic anhydride

ASE   amplification of spontaneous emission

CMOS   complementary metal–oxide–semiconductor

DCM   methylene chloride

DFT   density functional theory

DMF   N, N-dimethylformamide

EL   electroluminescence

EVA   ethylene vinyl acetate

FTIR   Fourier transform infrared

FWHM   full width at half maximum

Knr   nonradiative recombination rate

Kr   radiative recombination rate

LED   light-emitting diodes

LYSO   lutetium-yttrium oxyorthosilicate

MTF   modulation transfer function

NC   nanocrystal

NIR   near infrared

OA   oleic acid

OLA   oleyl amine

PA   pentanedioic anhydride

PDMS	polydimethylsiloxane
PEG	polyethylene glycol
PET	polyethylene terephthalate
PhC	photonic crystal
PL	photoluminescence
PLQY	photoluminescence quantum yield
PMMA	poly (methyl methacrylate)
PQD	perovskite quantum dot
PS	polystyrene
QD	quantum dot
Ra	roughness average
RGB	red-green-blue
RL	radioluminescence
Rms	root mean square
SEM	scanning electron microscope
SPR	surface plasmon resonances
THF	tetrahydrofuran
UV	ultraviolet
WLED	white light-emitting diode
WSR	wavelength-selective reflector
XRD	X-ray diffraction
τ_{avg}	average lifetime

Acknowledgements

Looking back on the summer of 2019, the beginning of the story, the memories of that time remain so vivid still. I can remember the feelings of anticipation and anxiety at that time when I imagined the future. Now, imagination has become a past. All the things that I have experienced and encountered, good and bad, have become an integral part of me. I am very glad to have had this journey. Thus, I want to give my last thanks to myself at that time for making this choice.